國立臺灣大學電機資訊學院電信工程學研究所

博士論文

Graduate Institute of Communication Engineering
College of Electrical Engineering & Computer Science
National Taiwan University

Doctoral Dissertation

寬頻縮小化電磁能隙結構於電源完整性設計之應用

Miniaturized and Stopband-Enhanced Electromagnetic Bandgap Structures for Power Integrity Design

王春得

Chuen-De Wang

指導教授：吳宗霖 博士

Advisor: Tzong-Lin Wu, Ph.D.

中華民國 102 年 3 月

March, 2013

國立臺灣大學博士學位論文
口試委員會審定書

寬頻縮小化電磁能隙結構於電源完整性設計之應用

Miniaturized and Stopband-Enhanced Electromagnetic Bandgap Structures for Power Integrity Design

本論文係王春得君（F95942079）在國立臺灣大學電信工程學研究所完成之博士學位論文，於民國 102 年 03 月 27 日承下列考試委員審查通過及口試及格，特此證明

口試委員：吳宗霖（簽名）

（指導教授）

楊成發　毛紹綱

林丁丙

馬誠

張子聖

所　長　吳宗霖（簽名）

誌謝

博士學位與論文得以順利完成，我要特別感謝我的指導老師吳宗霖教授。感謝吳教授的指導與鼓勵，在這段求學過程中，著實給予我很大的幫助，不僅是訓練我如何嚴謹的思考，如何有效率的組織，也幫助我解決研究上的瓶頸，更鼓勵我能再更進一步的創新。讓我這一路上能有機會接觸各種研究、計畫不同方面的挑戰，能尋找明確的方向，以及能掌握正確的方法，並藉由這多方的磨練，得以學習獨立思考，學習協調合作，學習整合系統，學習管理規劃，也學習如何成長與學習。感謝台大電信所電波組的各位教授，能提供各式課程、軟體與設備，讓我得以學習電波領域的專業知識與技能。感謝電波組瞿大雄教授、季先生、以及陳君朋學長與網管們的維護與管理，讓我能夠順利使用各樣軟、硬體，學習運用專業的工具。感謝口試委員毛紹綱教授、楊成發教授、馬自莊教授、林丁丙教授、洪子聖教授的建議，讓此論文得以完整與完善。

感謝電磁相容實驗室的學長姊、同學、學弟妹的幫助。謝謝挺光學長、子偉學長給我論文研究領域上的教導與啟發。謝謝仲豪、冠宗、書榮、佑勳、森貴、惠玲、皓翔、麵包、志穎，很高興在這段過程中能夠有機會與你們切磋，也謝謝你們長時間的陪伴，更感謝你們常常聽我的情緒抒發，在這段時間我們一起上課、一起討論、一起分工合作；也一起運動、一起出遊、一起分享生活；一起 café 8、一起 5 Senses、一起 cama；一起樂麵屋、一起小飯館、一起 22 盎司；一起去韓國 KAIST、一起去美國 EMCS、一起外島”莊蕭”遙；一起籃球、一起羽球、一起拔河拿獎牌。這一路上謝謝你們，有這麼多好同伴才讓我有勇氣能走得更遠。感謝碩班學弟妹嘉原、郁雯、雅欣、志榮、育豪、俊翔、逸賢、逸民、紹佑、景睿、博凱、泰禹、睿志、余任、齊軒、佑任、求致、翠微、佟鴻，雖然與你們相處的時間較短，但也感謝這段時間你們給我的幫助，特別是逸民、紹佑、泰禹、佑任，很抱歉討論時總是嚴格地要求你們，感謝你們對我的容忍，與你們的相處也讓我學習了很多。祺凱、揚智、英誠三位明日之星，很高興能在最後的階段認識你們，也祝福你們入寶山能滿載而歸、順利畢業。謝謝吳執行長手下大將詠守，我們同梯進台大也同梯出台大，同梯受訓也同梯替代役，謝謝你總以一口啤酒與一曲 men's talk 相挺，謝謝你陪我努力撐下去。

感謝我的家人，總是在背後給予我最大的支持、鼓勵與包容，不論何時都願意接納我的任性，特別是來不及看我畢業的爸爸。感謝這段時間因緣際會給予幫助的每個人，感謝讓我成長的每個機會，感謝加給我力量的，感謝神。

中文摘要

本論文著重於電磁能隙結構之等效電路模型、原理以及設計於抑制接地彈跳雜訊之應用，並藉以提出一縮小與寬頻化之電磁能隙結構。首先，我們提出計算電磁能隙之低頻與高頻截止頻率的方法。此方法不僅可幫助我們預測低頻與高頻的截止頻率，也提供我們了解電磁能隙的產生原理。低頻與高頻截止頻率可藉由單位元與適合之邊界條件的共振頻率求得而不用解其色散關係。基於此方法，我們分別針對一維與二維電磁能隙結構發展其等效電路模型的建構方法。針對一維電磁能隙結構，我們利用傳輸線段建立單位元之等效電路模型。至於二維電磁能隙結構，我們利用單位元及其相對應低頻、高頻截止頻率之邊界條件建立其等效電路模型，而其中之個別元件值則可利用所推導的共振腔模型求得。這些等效電路模型可給我們較清楚的物理觀點來連結電磁能隙結構之幾何形狀與電磁能隙的關係。

此論文提出兩種新穎電磁能隙結構之設計。首先是多連通柱電磁能隙結構。此結構之低頻與高頻截止頻率已可被解釋。藉由調整連通柱的間距，我們可以發現此多連通柱電磁能隙結構有最大頻寬比例之最佳化設計。在相同的幾何大小的條件之下與蘑菇型電磁能隙結構相比，多連通柱電磁能隙結構可改善絕對頻寬與頻寬比例的特性。另一種為以交錯型電磁能隙結構達成較大寬頻與較小面積之設計。藉由縮小電源/接地連通柱對之間距，此電磁能隙結構的低頻與高頻截止頻率可同時被改善，並利用此設計概念，多電源/接地連通柱對的設計可更進一步的增加頻寬。以單一電源/接地連通柱對為例，其單位元邊長的電氣大小與頻寬比例分別為 0.071 λ_{gL} 以及 139 %，與過去文獻上之蘑菇型電磁能隙結構相比較，此設計多增加 51.1 %的頻寬並同時節省 61.2 %的面積。至於四對電源/接地連通柱對為例，其頻寬則可多增加 115.2 %並同時減少 30.5 %的面積。

關鍵字：電磁能隙結構、接地彈跳雜訊、電源完整度。

ABSTRACT

This dissertation focuses on the equivalent circuit model, mechanism, and design of the electromagnetic bandgap (EBG) structures for the suppression of ground bounce noise. Developing a miniaturized and stopband-enhanced EBG structure is the main goal of this dissertation. In the beginning, we propose a method for determining the lower- and upper-bound cutoff frequencies of bandgaps. The method helps us not only to predict where the bandgap is but also to understand what mechanisms of the lower- and upper-bound cutoff frequencies are. Instead of solving the dispersion relation, we propose that the lower- and upper-bound cutoff frequencies can be determined by the resonant frequencies of the unit cell with appropriate boundary conditions. Based on the proposed method, two approaches are developed for constructing the physics-based models of one- and two-dimensional EBG structures, respectively. For the case of one-dimensional EBG structure, we can use an equivalent circuit model consisting of transmission-line sections to electrically characterize the electromagnetic behavior of a unit cell. As regards the two-dimensional EBG structure, an equivalent circuit model for the unit cell is developed to predict the lower- and upper-bound cutoff frequencies. The values of the circuit elements can be extracted by using the derived cavity models. The equivalent circuit models can provide us a design concept for relating the geometry of the EBG structure to the corresponding bandgap behavior.

Two novel designs of EBG structures are proposed in this dissertation. The first one is the multiple vias EBG structures. The mechanisms of lower- and upper-bound cutoff behaviors and the corresponding frequencies of the EBG structure are investigated and explained. By sweeping the via pitch of the multiple vias EBG

structure, we can find an optimized design for achieving the maximum bandwidth ratio. Under the assumption of the same dimension, the absolute bandwidth and bandwidth ratio are enhanced by the multiple vias EBG structure when compared with the mushroom EBG structure. The other design is the interleaved EBG structure for the wider bandwidth and smaller area. The improvements on lower- and upper-bound cutoff frequencies of the interleaved EBG structure can be achieved at the same time by reducing the pitch of power/ground vias pair. Based on the design concept, the interleaved EBG structures with multiple pairs of power/ground vias are also proposed to enhance the bandwidth of bandgap further. For the interleaved EBG structure with single pair of power/ground vias as an example, the electrical size of the unit-cell length, which is normalized to the wavelength in the substrate, and bandwidth ratio are 0.071 λ_{gL} and 139 %, respectively. Compared with the conventional mushroom EBG structure proposed in the past literatures, the interleaved EBG structure with single pair of power/ground vias simultaneously shows substantial improvements on bandwidth of 51.1 % and miniaturization of 61.2 %. With regard to the interleaved EBG structure with four pairs of power/ground vias, the bandwidth has an increase of 115.2 % wider than that of the conventional mushroom EBG structure and the required layout area can be reduced by 30.5 % simultaneously.

Index Terms —Electromagnetic bandgap (EBG) structure, ground bounce noise (GBN), power integrity (PI),

CONTENTS

口試委員會審定書 ..... #

誌謝 i

中文摘要 iii

ABSTRACT v

CONTENTS vii

LIST OF FIGURES xi

LIST OF TABLES xix

ACRONYMS xx

Chapter 1 Introduction 1

1.1 Research Motivation 1

1.2 Coupling Mechanism of Ground Bounce Noise 2

1.3 Traditional Solutions for GBN Suppression 5

1.3.1 Decoupling Method: Decoupling Capacitors 5

1.3.2 Isolation Method: Power Plane Segmentation 7

1.4 Electromagnetic Bandgap Structure for GBN Isolation 8

1.4.1 Photonic Crystal Power/Ground Layer 9

1.4.2 Coplanar EBG Structures 10

1.4.3 Mushroom EBG Structures 12

1.4.4 Design Challenge on PDN with EBG Structure 16

1.5 Contributions 20

1.6 Chapter Outlines 21

Chapter 2 Electromagnetic Bandgap Prediction 23

2.1 One-Dimensional EBG Analysis 23
2.1.1 One-Dimensional Dispersion Relation 26
2.1.2 Lower- and Upper-Bound Cutoff Frequencies Prediction 29
2.1.3 One-Dimensional Mushroom EBG Structure 34
2.2 Two-Dimensional EBG Analysis 40
2.2.1 Two-Dimensional Dispersion Diagram 40
2.2.2 Resonant Cavity Modeling 44
2.2.3 Two-Dimensional Mushroom EBG Structure 57
2.3 Summary 64
Chapter 3 Optimized Multiple Vias EBG Power/Ground Planes 66
3.1 Geometry and Design Concept 66
3.1.1 Design Concept of Multiple Vias EBG Structure 66
3.1.2 Optimum Design Based on Via Arrangement 74
3.2 One-Dimensional Bandgap Prediction 77
3.3 Two-Dimensional Bandgap Prediction 83
3.3.1 Resonant Cavity Modeling 84
3.3.2 Lower- and Upper-Bound Cutoff Frequencies Prediction 88
3.4 Experiment Results 92
3.5 Summary 96
Chapter 4 Miniaturized and Stopband-Enhanced Interleaved EBG Power/Ground Planes 98
4.1 Interleaved EBG Structure 98
4.1.1 Geometry and Design Concept 98
4.1.2 One-Dimensional Equivalent Circuit Model and Bandgap Analysis 102
4.2 Interleaved EBG Structure with Multiple Pairs of Power/Ground Vias 112

4.3 Two-Dimensional Bandgap Prediction 119
4.3.1 Resonant Cavity Modeling with Even- and Odd-Mode Analysis 119
4.3.2 Two-Dimensional Equivalent Circuit Model of Interleaved EBG Structure 121
4.4 Comparison and Measurement 131
4.4.1 Comparison 131
4.4.2 Measurement 135
4.5 Summary 137
Chapter 5 Conclusion 139
REFERENCE 141
PUBLICATION LIST 148

LIST OF FIGURES

Fig. 1.1 Simplified equivalent circuit model of PDN. 2

Fig. 1.2 Conductive coupling in the shared PDN. 3

Fig. 1.3 Crosstalk coupling between adjacent power islands. 3

Fig. 1.4 Electromagnetic radiated emissions caused by GBN. 4

Fig. 1.5 Power integrity issues for system design. 5

Fig. 1.6 Concept of decoupling method. 5

Fig. 1.7 Equivalent series inductance of a capacitor mounted on power/ground planes. 6

Fig. 1.8 Power plane segmentation (a) without and (b) with DC path. 8

Fig. 1.9 Photonic crystal power/ground layer. 10

Fig. 1.10 Coplanar EBG power/ground planes. 11

Fig. 1.11 Different types of coplanar EBG structures. (a) LPC-EBG, (b)AI-EBG (c) L-bridged EBG, and (d) meander-*L* bridge EBG structure. 12

Fig. 1.12 (a) Mushroom EBG power/ground planes and (b) its concept. 13

Fig. 1.13 (a) Cascading mushroom EBG structures and (b) double-stacked EBG structure. 14

Fig. 1.14 Inductance-enhanced EBG structures (a) proposed in [41] and (b) in [42]. ..15

Fig. 1.15 Capacitance-enhanced EBG structure using high dielectric constant layer. ..15

Fig. 1.16 Examples of (a) power trace and (b) power plane with mushroom EBG structure. 16

Fig. 1.17 Magnitudes of S_{21} of the examples including the 1-D power trance and 2-D power plane with and without mushroom EBG structures as shown in Fig.

1.16. 17

Fig. 1.18 Power plane with (a) EBG fence and (b) partial EBG structure.....18

Fig. 1.19 Electric field intensity at far field (3 m) for the EBG fence and magnitudes of S_{21} for the partial EBG structure. 19

Fig. 2.1 Equivalent circuit model for the unit cell of mushroom EBG structure.....24

Fig. 2.2 Transmission coefficients of series *LC* resonator and 5 cascaded unit cells.25

Fig. 2.3 Equivalent circuit model of periodic structure. 26

Fig. 2.4 Dispersion diagram of unit cell shown in Fig. 2.1.....28

Fig. 2.5 (a) Two-port symmetrical network, (b) even-mode half circuit, and (c) odd-mode half circuit.....29

Fig. 2.6 (a) Type-I, (b) Type-II, (c) Type-III, and (d) Type-IV half resonators with corresponding boundary conditions.....31

Fig. 2.7 (a) Type-I, (b) Type-II, (c) Type-III, and (d) Type-IV half resonators of the unit cell shown in Fig. 2.1. 32

Fig. 2.8 Left-hand and right-hand sides of (2.24) and (2.26).....33

Fig. 2.9 (a) Geometry of 1-D mushroom EBG structure and (b) corresponding equivalent circuit model. 35

Fig. 2.10 Dispersion diagram of 1-D mushroom EBG structure from full-wave simulation and equivalent circuit model.....36

Fig. 2.11 (a) Type-III half resonator and (b) Type-I half resonator for solving lower- and upper-bound cutoff frequencies of 1-D mushroom EBG structure, respectively. 38

Fig. 2.12 Two-dimensional periodic structure with square lattice in (a) space and (b) spectral domains. 41

Fig. 2.13 A two-dimensional dispersion diagram. 43

Fig. 2.14 A parallel-pate structure with a specific boundary condition. 44

Fig. 2.15 A parallel-plate structure with four PMC side walls around its periphery. ..47

Fig. 2.16 A circuit representation of cavity model with four PMC side walls.....49

Fig. 2.17 A parallel-plate structure with a via connecting with the bottom plane. 51

Fig. 2.18 Input impedance of parallel-plate structure shown in Fig. 2.17 (a) calculated by full-wave simulation and (2.52) and (b) approximated by (2.58).....52

Fig. 2.19 Parallel-plate structure with 4 PEC walls around its periphery. 54

Fig. 2.20 Input impedance of parallel-plate structure shown in Fig. 2.19 (a) calculated by full-wave simulation and (2.66) and (b) approximated by (2.67).....56

Fig. 2.21 (a) Unit cell of two-dimensional mushroom EBG structure and (b) its top view.....57

Fig. 2.22 Dispersion diagram of 2-D mushroom EBG structure. 58

Fig. 2.23 (a) Magnetic field intensity, (b) equivalent surface current density, and (c) electric field intensity of a mushroom EBG structure at lower-bound cutoff frequency.....59

Fig. 2.24 An equivalent circuit model for unit cell of two-dimensional mushroom EBG structure for lower-bound cutoff frequency. 61

Fig. 2.25 (a) Magnetic field intensity, (b) equivalent surface current density, and (c) electric field intensity of a mushroom EBG structure at upper-bound cutoff frequency.....62

Fig. 2.26 An equivalent circuit model for unit cell of two-dimensional mushroom EBG structure for upper-bound cutoff frequency. 63

Fig. 3.1 (a) 3-D view and (b) top view of unit cell of multiple vias EBG structure. .67

Fig. 3.2 Dispersion diagram of the multiple vias EBG structure with v = 8 mm and mushroom EBG structure. 68

Fig. 3.3 Top views of (a) multiple vias EBG and (b) mushroom EBG P/G planes. ..69

Fig. 3.4 $|S_{21}|$ of multiple vias EBG, mushroom EBG, and bared power/ground planes.70

Fig. 3.5 Current path from patch, ground plane to power plane of (a) multiple vias EBG and (b) mushroom EBG structures. 71

Fig. 3.6 Distribution of electrical field intensity (magnitude) on bottom plane for (a) multiple vias EBG P/G planes and (b) corresponding simplified structure..73

Fig. 3.7 Distribution of electrical field intensity (magnitude) on bottom plane for (a) mushroom EBG P/G planes and (b) corresponding simplified structure. 73

Fig. 3.8 Distribution of electrical field intensity (magnitude) on bottom plane for multiple vias EBG P/G planes with (a) v = 6 mm, (b) v =10 mm, and (c) v = 14 mm. 75

Fig. 3.9 Lower- and upper-bound cutoff frequencies and bandwidth ratio of multiple vias EBG structure with different via pitch v. 76

Fig. 3.10 (a) Geometry of 1-D multiple vias EBG structure and (b) corresponding equivalent circuit model. 78

Fig. 3.11 Half resonators for (a) lower- and (b) upper-bound cutoff frequencies of one-dimensional multiple vias EBG structure.....80

Fig. 3.12 Estimated and simulated lower- and upper-bound cutoff frequencies of 1-D multiple vias EBG structure and mushroom EBG structure (v = 0 mm).....82

Fig. 3.13 Error of lower- and upper-bound cutoff frequencies from derived formulas and full-wave simulation. 82

Fig. 3.14 Resonators for (a) lower- and (b) upper-bound cutoff frequencies of multiple vias EBG structure and quartered model for (c) lower- and (d) upper-bound cutoff frequencies. 83

Fig. 3.15 Parallel-plate structure surrounded by two PMC walls along x- and y-axis

and two PEC walls on the other two sides.....85

Fig. 3.16 Parallel-plate structure with a via connecting with the bottom plane surrounded by two PMC walls along *x*- and *y*-axis and two PEC walls on the other two sides. 86

Fig. 3.17 Input impedance of parallel-plate structure shown in Fig. 3.16 (a) calculated by full-wave simulation and (3.8) and (b) approximated by (3.9).....87

Fig. 3.18 Equivalent circuit model of quartered model for (a) lower- and (b) upper-bound cutoff frequencies. 89

Fig. 3.19 Estimated and simulated lower- and upper-bound cutoff frequencies of 2-D multiple vias EBG structure and mushroom EBG structure (v = 0 mm).....91

Fig. 3.20 Error of lower- and upper-bound cutoff frequencies from derived formulas and full-wave simulation. 91

Fig. 3.21 (a) Photo of multiple vias EBG test vehicle using PTH vias fabrication. (b) Simulated *S*-parameter of multiple vias EBG structure for PTH and blind vias. 93

Fig. 3.22 Measured and simulated results of multiple vias EBG structure with v =1 mm, v= 5mm, and v = 8mm and (b) comparison of bared board, mushroom EBG, and multiple vias EBG structures. 95

Fig. 4.1 (a) Geometry of unit cell of interleaved EBG structure in (b) side view and (c) top view. 99

Fig. 4.2 Dispersion diagram of Interleaved EBG structure with (a, p, v, r_v, h) = (10 mm, 9.4 mm, 1 mm, 0.1 mm, 0.2 mm). 100

Fig. 4.3 Dispersion diagrams of interleaved EBG structures with different via pitches of 1 mm, 3 mm, and 5 mm. 101

Fig. 4.4 Geometry of one-dimensional interleaved EBG structure.....102

Fig. 4.5 One-dimensional equivalent circuit model of interleaved EBG structure using transmission-line sections. 103

Fig. 4.6 Equivalent circuit model with (a) even-mode field pattern, which can be bisected into two identical (b) even-mode half circuits. 104

Fig. 4.7 Equivalent circuit model with (a) odd-mode field pattern, which can be bisected into two identical (b) odd-mode half circuits. 105

Fig. 4.8 Half resonators for determining (a) lower- and (b) upper-bound cutoff frequencies of interleaved EBG structure. 107

Fig. 4.9 (a) Behavior of half resonators for determining lower-bound cutoff frequency and (b) equivalent capacitance of the interleaved and mushroom EBG structure. 108

Fig. 4.10 Influence of via pitch on upper-bound cutoff frequency of interleaved EBG structure nearly determining by peak frequency of $|Z_{inRS}|$. 110

Fig. 4.11 Right-hand part of half resonator for upper-bound cutoff frequency is divided into (a) part *A* and (b) part *B*. 110

Fig. 4.12 Current distribution of interleaved EBG structure at upper-bound cutoff frequency. 111

Fig. 4.13 Lower- and upper-bound cutoff frequencies of 1-D interleaved EBG structure from full wave simulation and proposed model. 112

Fig. 4.14 (a) Geometry of unit cell of interleaved EBG structure with two pairs of power/ground vias in (b) top view. 113

Fig. 4.15 Dispersion diagram of interleaved EBG structure with two pairs of power/ground vias. Geometric parameters are (a, p, v, r_v, h) = (10 mm, 9.4 mm, 1 mm, 0.1 mm, 0.2 mm). 114

Fig. 4.16 Lower-, upper-bound cutoff frequencies and bandwidth ratio of interleaved

EBG structure with two pairs of power/ground vias with respect to via pitch v. 115

Fig. 4.17 (a) Geometry of unit cell of interleaved EBG structure with four pairs of power/ground vias in (b) top view. 116

Fig. 4.18 Dispersion diagram of interleaved EBG structure with four pairs of power/ground vias. Geometric parameters are (a, p, v, r_v, h, d) = (10 mm, 9.4 mm, 1 mm, 0.1 mm, 0.2 mm, 1.2 mm). 117

Fig. 4.19 Lower-, upper-bound cutoff frequencies and bandwidth ratio of interleaved EBG structure with four pairs of power/ground vias with respect to d. 118

Fig. 4.20 Top views of (a) original and (b) extended rectangular structures and (c) original and (d) extended isosceles right triangle structures. 120

Fig. 4.21 (a) Boundary condition and (b) equivalent circuit model for lower-bound cutoff frequency of interleaved EBG structure and top views of parallel-plate structures for extraction of (c) L_{eqL1} and (d) L_{eqL2}. 122

Fig. 4.22 (a) Boundary condition and (b) equivalent circuit model for upper-bound cutoff frequency of interleaved EBG structure and top views of parallel-plate structures for extraction of (c) L_{eqU1} and (d) L_{eqU2}. 124

Fig. 4.23 (a) Equivalent circuit model for f_L of interleaved EBG structure with two pairs of P/G vias, (b) simplified model, and (c) top views of parallel-plate structures for extraction of L_{eqL1} and L_{eqL2}. 125

Fig. 4.24 (a) Simplified model of interleaved EBG structure with two pairs of P/G vias for f_U and (b) top views of parallel-plate structures for extraction of L_{eqU1} and L_{eqU2}. 126

Fig. 4.25 Equivalent circuit model for f_L of interleaved EBG structure with four pairs of power/ground vias. 127

Fig. 4.26 Equivalent circuit model for f_U of interleaved EBG structure with four pairs of power/ground vias. 128

Fig. 4.27 Estimated and simulated lower-, upper-bound cutoff frequencies, and errors between the two methods for interleaved EBG structure with (a) single (b) two, and (c) four pairs of P/G vias....130

Fig. 4.28 Dispersion diagram of interleaved EBG structure with single pair of power/ground vias. The geometric parameters are (a, p, v, r_v, h) = (4 mm, 3.8 mm, 0.21 mm, 37.5 μm, 45 μm). 132

Fig. 4.29 Side views of (a) mushroom and (b) double-stacked EBG structures and (c) corresponding dispersion diagram. 133

Fig. 4.30 Dispersion diagrams of interleaved EBG structure with two and four pairs of power/ground vias. 134

Fig. 4.31 Test board with interleaved EBG structure....135

Fig. 4.32 Simulated and measured results of interleaved EBG structures with single pair of power/ground vias. 136

Fig. 4.33 Simulated and measured results of interleaved EBG structures with two and four pairs of power/ground vias....137

LIST OF TABLES

Table 2.1 Physical and circuit parameters of 1-D mushroom EBG structure.....36

Table 4.1 Maximum errors for f_L and f_U of interleaved EBG structures.....131

Table 4.2 Comparison of EBG structures.....134

ACRONYMS

SiP	:	System In A Package
RFI	:	Radio Frequency Interference
PI	:	Power Integrity
PDN	:	Power Distribution Networks
DC	:	Direct Current
VRM	:	Voltage Regulator Module
GBN	:	Ground Bounce Noise
SSN	:	Simultaneously Switching Noise
SI	:	Signal Integrity
SMT	:	Surface Mount Technology
ESL	:	Equivalent Series Inductance
EBG	:	Electromagnetic Bandgap
PMC	:	Perfect Magnetic Conductor
PCPL	:	Photonic Crystal Power/Ground Layer
PCB	:	Printed Circuit Board
LPC-EBG	:	Long-Periodic-Coplanar Electromagnetic Bandgap
AS-EBG	:	Artificial Substrate Electromagnetic Bandgap
PEC	:	Perfect Electric Conductor

Chapter 1 Introduction

1.1 Research Motivation

As the technology keeps developing rapidly, wireless voice/data communications, such as wireless local area network (WLAN), long term evolution (LTE), bluetooth, global positioning system (GPS), 3G mobile telecommunication, digital television (DTV), have become one of the most important features of the consumer electronics. Because the trend is going toward an all-in-one scheme, system in a package (SiP) is one of the popular solutions for providing a platform integrating both the computing and wireless functionalities.

This trend will be a great challenge for the SiP designers to combine the computers and communications circuits in a compact system due to radio frequency interference (RFI). In general, the wireless communication devices operate in the radio frequency (RF) from 800 MHz up to 10 GHz in the near future. The data rate of digital circuits, such as microprocessor, memory and high speed I/O, also operate from at least hundreds of Mbps to up to several Gbps, and the digital signal energy will distribute in a wide spectrum. The noise coupled from the digital systems to the RF systems will cause RFI problem and degrade the communication quality.

To guarantee the systems in a stable operation, power integrity (PI) design is becoming a major challenge under the trend toward low voltage level and high speed operation [1], [2]. Power distribution networks (PDN) for direct current (DC) power delivery consist of voltage regulator modules (VRMs) , planar power/ground planes, on-chip power/ground grids, and various vertical interconnects, such as plated-through-hole vias, wire bonding, microbumps, through silicon vias (TSVs). All

of the interconnections contribute considerable inductive parasitic effects. Fig. 1.1 shows a simplified equivalent circuit model of PDN. The voltage fluctuation will be induced when the transient switching current of the digital transistors flows through all the inductive parasitics of the PDN [3]. The noise problem, referred to ground bounce noise (GBN) or simultaneously switching noise (SSN), could be significant owing to the simultaneously switching effect. The GBN contains broad noise spectrum due to the transistor switching randomly in different speeds.

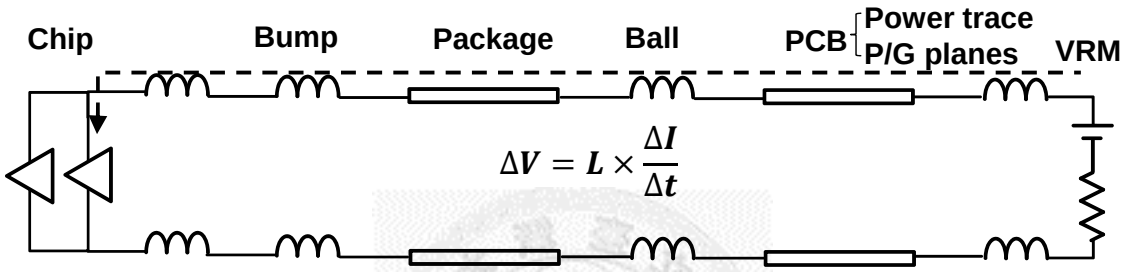

Fig. 1.1 Simplified equivalent circuit model of PDN.

1.2 Coupling Mechanism of Ground Bounce Noise

The three main coupling mechanisms of ground bounce noise are briefly described as follow：

1) Generally, the integrated circuits (ICs) biased at the same DC voltage level are connected to a power plane as shown in Fig. 1.2. For the case of the ICs using a shared power plane, the noise can propagate from one to another without obstruction in the parallel-plate transmission line structure formed by the power/ground planes.
2) The other case is the ICs biased at different DC voltage levels. To supply different DC voltages, the power plane is segmented to several power islands with surrounding slots as shown in Fig. 1.3. The noise without conducted path between power islands is isolated well in near DC frequency. But in the higher frequency

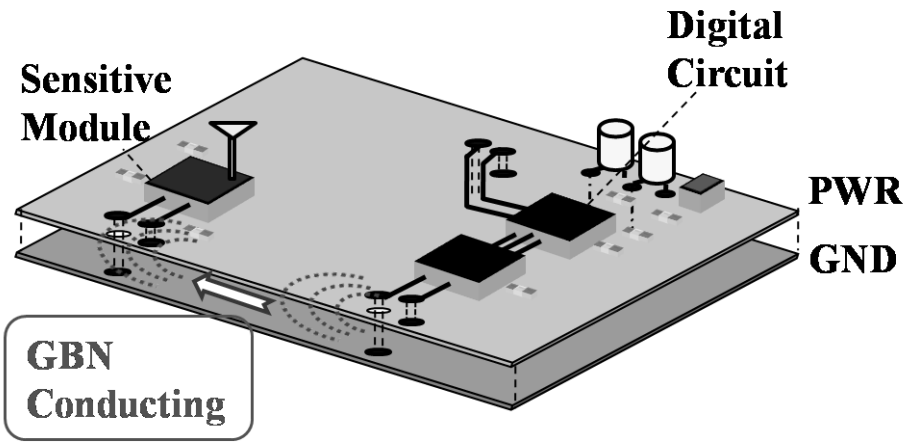

Fig. 1.2 Conductive coupling in the shared PDN.

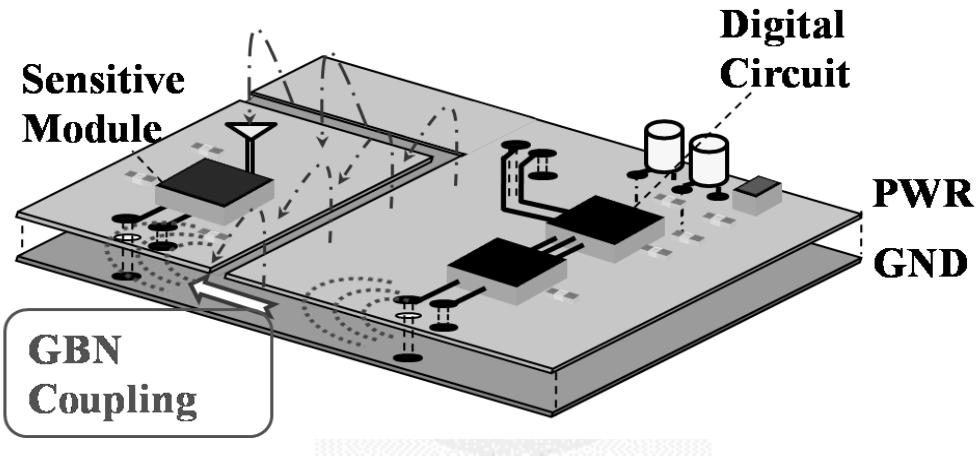

Fig. 1.3 Crosstalk coupling between adjacent power islands.

range, the noise coupling between different power planes is getting strong due to the capacitive or inductive coupling. Especially, the individual power and ground planes pair forms an open-end parallel-plate cavity. There are many resonances in the frequency range of RF band we concerned. The noise can couple easily between adjacent power planes at these resonant frequencies.

3) In addition, the PDN noise also causes the radiated emission issues. The mechanism of the emissions is due to the GBN propagating to the edge of the power/ground

planes and radiating toward outside as shown in Fig. 1.4. In particular, the emission problems will get more serious at the resonant frequencies of the power/ground cavity. The electric field around the edge of power/ground plane can be regarded as the equivalent magnetic current. It acts as the radiation of the patch antenna toward surrounding environment.

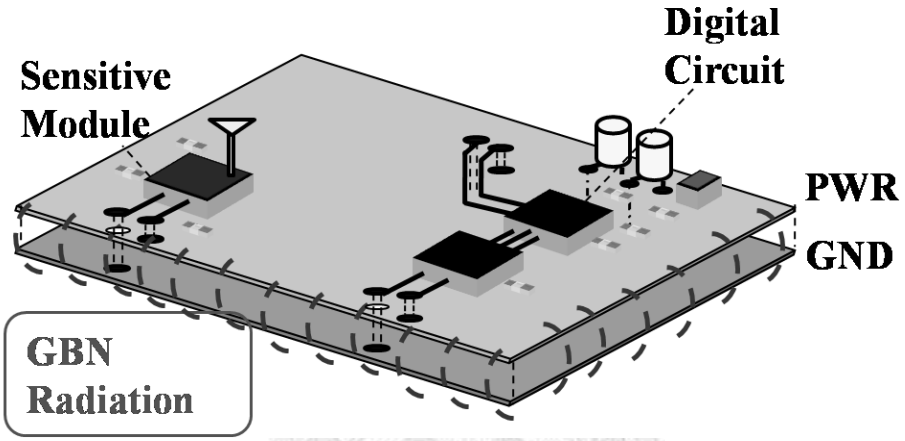

Fig. 1.4 Electromagnetic radiated emissions caused by GBN.

In summary, Fig. 1.5 shows the power integrity issues for system design. Several integrated circuits with different functions are integrated in a SiP. When the digital circuits are switching, the SSN will be induced. The voltage drop will degrade the output signals of the digital circuits. The eye diagram of the digital circuit, especially for the timing jitter, will become worse due to the SSN. It is a signal integrity (SI) issue. Owing to the noise coupling in the shared PDN, the quality and sensitivity of the analog/RF output signal will be distorted seriously [4], [5]. Moreover, PDN always keep in a planar structure (power or ground plane) with relatively large dimension, which could be a good radiator. The planar PDN may be excited by GBN and radiate into the surrounding environment [6], [7].

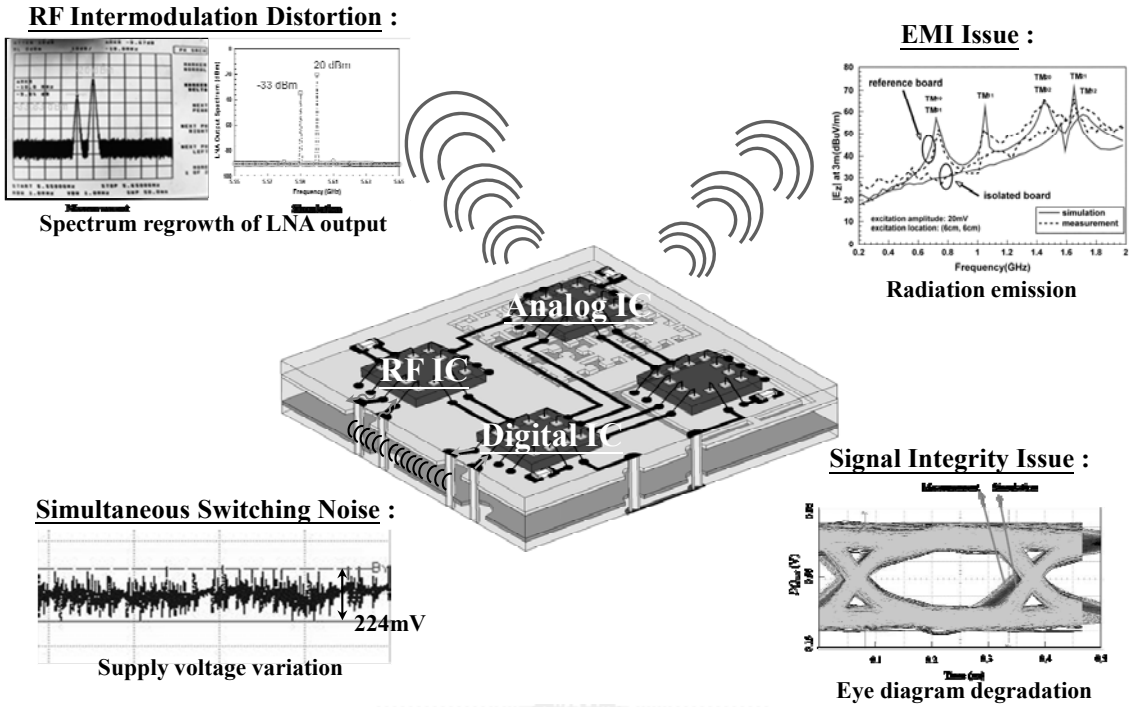

Fig. 1.5 Power integrity issues for system design.

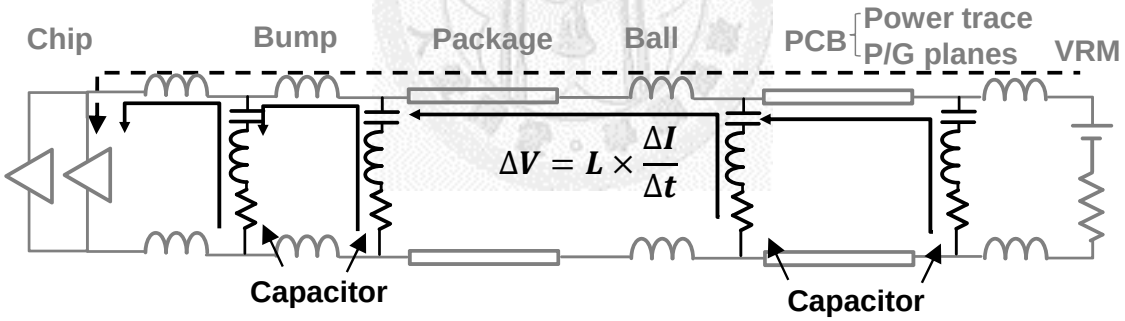

Fig. 1.6 Concept of decoupling method.

1.3 Traditional Solutions for GBN Suppression

There are two approaches, decoupling and isolation, to reduce the GBN coupling.

1.3.1 Decoupling Method: Decoupling Capacitors

The concept of the decoupling method is shown in Fig. 1.6. As mentioned above,

the voltage fluctuation will be serious when the current is drawn from the VRM because the current will flow through all of the inductive parasitics. In order to mitigate the SSN, the multiple capacitors with various capacitances can be connected in parallel with the hierarchical PDN. The transient current will be provided by the nearby capacitors rather than by the far VRM. Therefore, the current path and thus the inductive effects will be reduced and the noise can be decoupled.

One of the traditional solutions for realizing the decoupling method is adding surface mount technology (SMT) capacitors [8], [9] between power and ground planes. The concept of decoupling approach in frequency domain is to keep the impedance of the PDN low in a wideband frequency range. Thus, the capacitors provide a shorting path for the GBN. However, they will behave inductive above the self-resonance frequency formed by the capacitance and equivalent series inductance (ESL) as shown in Fig. 1.7. The ESL results from the current flowing through the power/ground planes, vias, pads, and SMT capacitor itself. The useful frequency range of the SMT capacitors is limited below gigahertz frequency.

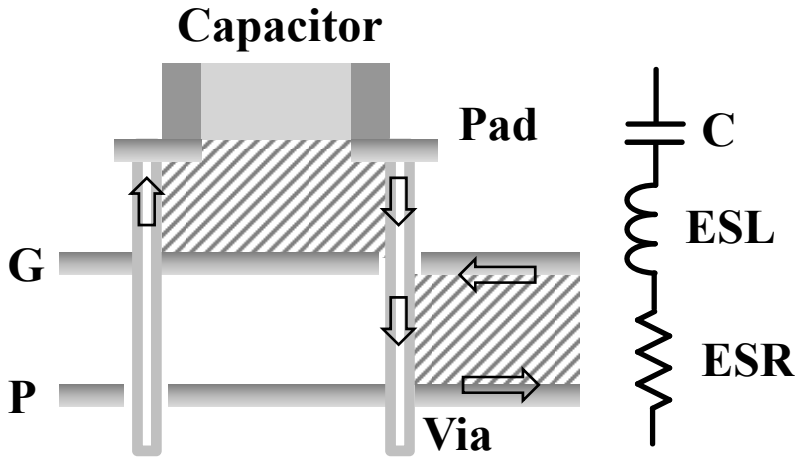

Fig. 1.7 Equivalent series inductance of a capacitor mounted on power/ground planes.

There are two approaches for reducing the ESL of the capacitors, [10], [11]. One is to embed the discrete capacitor into the substrate, and thus the current loop can be reduced. The other is using the embedded capacitor with a thin thickness and high permittivity substrate between the power and ground planes, but the planes still allow noise to propagate at some specific resonance frequencies in the gigahertz range. Both of them will increase manufacture cost.

1.3.2 Isolation Method: Power Plane Segmentation

The other is the isolation method. The concept of the isolation method is keeping part of the PDN with high impedance to mitigate the GBN propagation. The concept can be implemented by ensuring the transfer impedance Z_{21} as low as possible in a wide frequency range. The transfer impedance is defined as

$$Z_{21} = \left.\frac{V_2}{I_1}\right|_{I_i=0,\ i\neq 1} \tag{1.1}$$

, where I_1 represents transient current excited at port 1 and V_2 represents voltage perturbation induced at port 2.

Power plane segmentation is the conventional approach for realizing the isolation of the GBN coupling [12]. The method is to split the power plane for isolating the victim circuits from the noisy circuits. As shown in Fig. 1.8, the power island is surrounded by slots. There is no conductive path for the noise coupling. The method can be effective below gigahertz range. However, the crosstalk coupling could degrade the noise isolation capability in the high frequency range. In addition, to keep the same DC voltage in the power island, a small bridge would be typically used to connect the two metal planes as shown in Fig. 1.8(b). In this way, the performance will be significantly degraded because of the additional coupling path. A novel isolation method accounting for the high frequency range will be introduced in the following section.

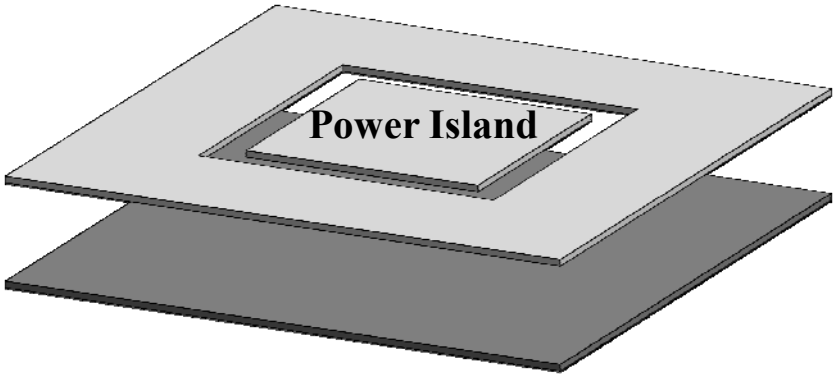

(a)

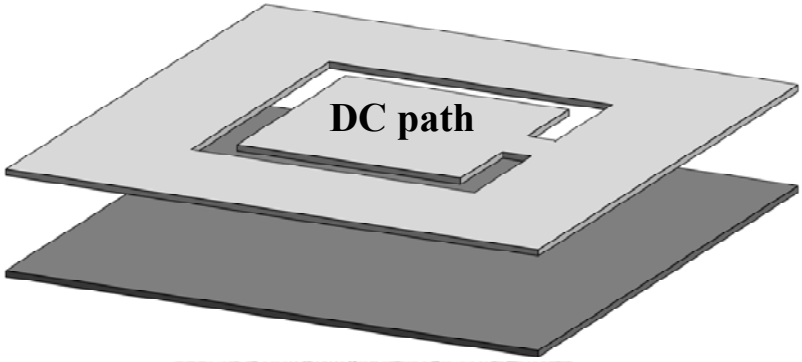

(b)

Fig. 1.8 Power plane segmentation (a) without and (b) with DC path.

1.4 Electromagnetic Bandgap Structure for GBN Isolation

In recent years, there are a lot of literatures for applying electromagnetic bandgap (EBG) structures to suppress the GBN coupling. The EBG structures have many useful unique features, such as slow-wave effect, equivalence of perfect magnetic conductor (PMC), and bandgap. These characteristics have many benefits for the microwave applications. The slow-wave effect means that the physical wavelength in the EBG structures can be smaller than the guided wavelength in the dielectric substrate. Therefore, this effect benefits the miniaturization of microwave devices, of which size is typically designed based on relative wavelength [13]-[17]. In terms of the equivalence

of perfect magnetic conductor, it does not directly exist in nature. The reflection phase characteristic of the EBG structure can behave like a perfect magnetic conductor surface in a specific frequency range. This feature can be applied to waveguide and antenna designs [18]-[20]. Electromagnetic bandgap structure, the focused characteristic of this thesis, can be used to forbid the electromagnetic wave propagating within a certain frequency range. The EBG structure was first proposed for suppressing the unwanted surface wave to enhance the gain of antenna [18], [21]-[22]. The forbidden-transmission behavior for wave is suitable for solving the GBN coupling problem by implementing the EBG structures within power/ground planes.

To isolate the GBN coupling above the GHz frequency range , three prototypes of periodic structures have been investigated in the literatures, such as photonic crystal power/ground layer (PCPL) [23]-[25], coplanar EBG structure [26]-[34], and mushroom EBG structure [35]-[43]. The unique characteristic of the EBG power/ground planes is employed to mitigate the GBN omni-directionally within the desired bandgap.

1.4.1 Photonic Crystal Power/Ground Layer

Photonic crystal power/ground layer is implemented by periodically embedding the material rods with high dielectric constant into original power/ground layers [23] as shown in Fig. 1.9. The rods with higher dielectric constant are located periodically in *x*- and *y*-direction and are embedded inside the original substrate with lower dielectric constant. Thus, the two-dimensional photonic crystal is formed because the different dielectric constants are distributed periodically in two dimensional spaces. The bandgaps will appear to suppress the coupling of GBN.

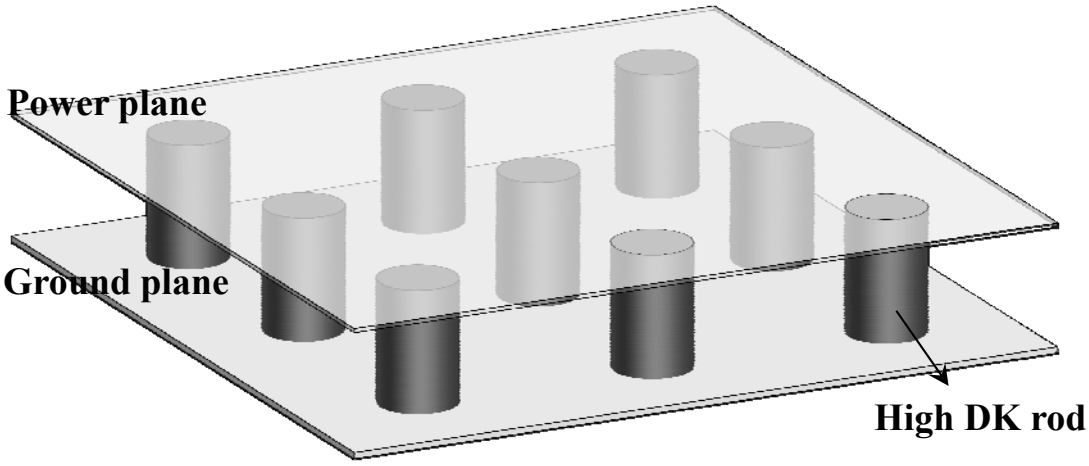

Fig. 1.9 Photonic crystal power/ground layer.

The PCPL can have good SI performance in multi-layer structure because the solid power/ground planes provide good paths for the return currents of the signals. Although the PCPL shows good performance for PI and SI, the fabrication and cost issues of the high dielectric constant rods are two challenges for widely using the PCPL concept. Some researches are recently proposed to improve the drawback of the PCPL. The high dielectric constant rods can be considered as SMT-type components connecting to power/ground planes on the printed circuit board (PCB) or package substrate. It can accomplish the implementation of PCPL in a standard PCB or package fabrication process [24]. On the other hand, in [24], the optimization design of PCPL has been proposed. Nevertheless, the demand of the high dielectric constant rods is the main constraint on the application of PCPL.

1.4.2 Coplanar EBG Structures

The coplanar EBG structure is a two-layer EBG structure which is implemented by periodically etching the power plane into a particular pattern as shown in Fig. 1.10. A number of etching patterns have been proposed including long-periodic-coplanar EBG (LPC-EBG) [26], alternating impedance EBG (AI-EBG) [28], *L*-bridge EBG [29], and

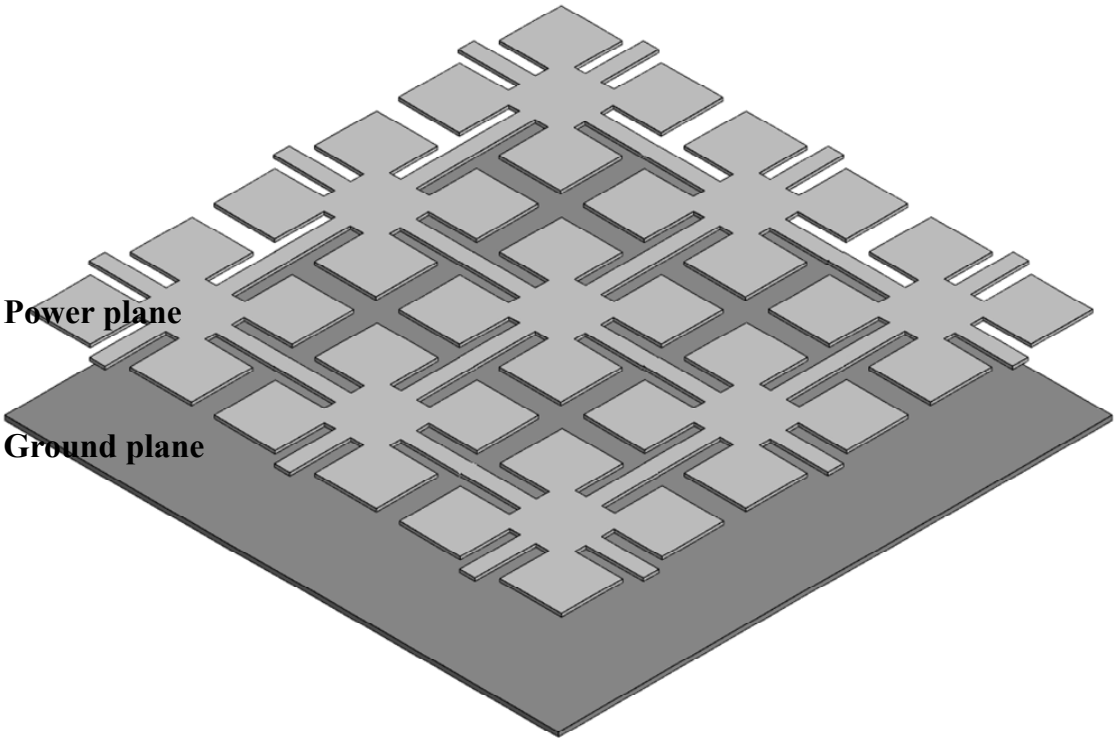

Fig. 1.10 Coplanar EBG power/ground planes.

meander-*L* bridge EBG structure [30] as shown in Fig. 1.11(a)-(d). The coplanar EBG structure can be regarded as an alternate cascade of high- and low-impedance transmission lines. The transmission lines with high impedance are contributed from the thin lines and can be modeled as an equivalent inductor. The low-impedance transmission lines are contributed from the patch and can be modeled as a capacitor. The lower-bound cutoff frequency of the coplanar EBG structure is determined by the equivalent inductance and capacitance. The upper-bound cutoff frequency is limited by the cavity resonance of unit cell [31]. Three approaches for improving the bandwidth are proposed by hybrid-planar-type EBG [31], artificial substrate EBG (AS-EBG) [32], and ground surface perturbation lattice (GSPL) EBG structure [33]. The concept of the hybrid-planar-type EBG structure is using SMT inductors and capacitors. The AS-EBG

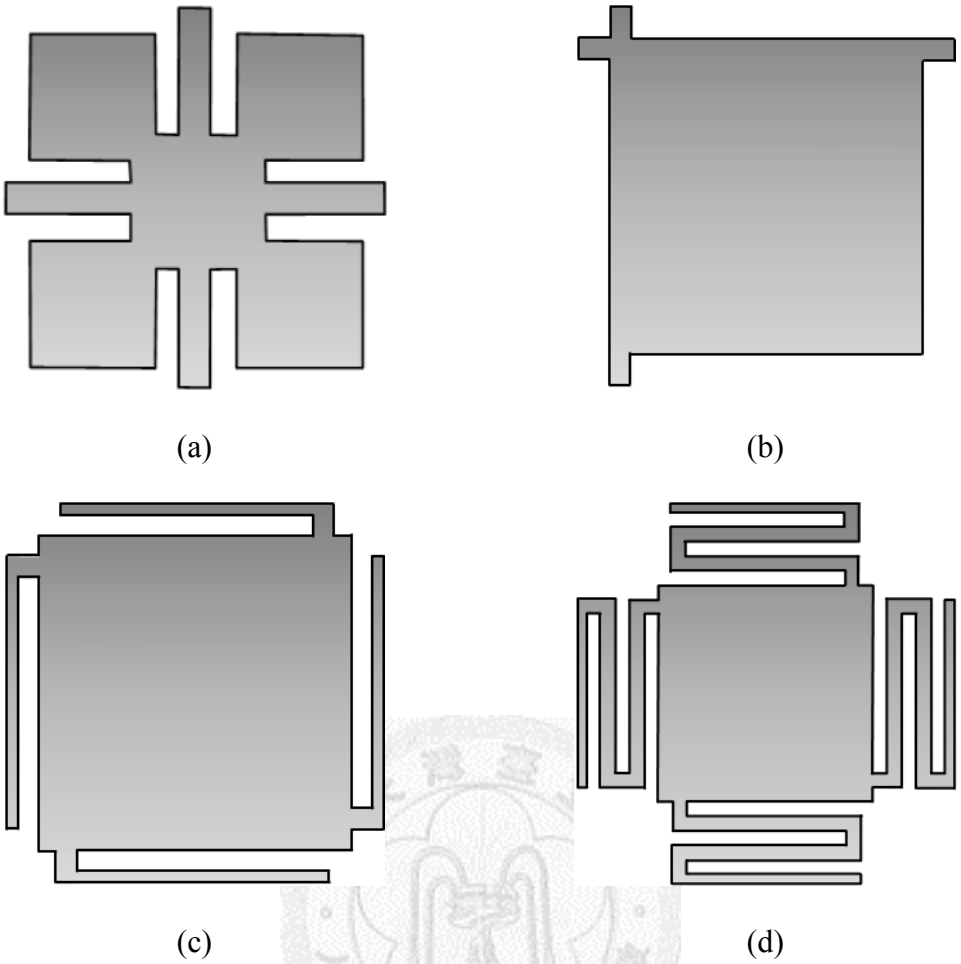

Fig. 1.11 Different types of coplanar EBG structures. (a) LPC-EBG, (b)AI-EBG (c) L-bridged EBG, and (d) meander-*L* bridge EBG structure.

structure is embedding air rods and rods with higher dielectric constant into the original substrate. The GSPL structure is using perturbation lattice on the ground plane for replacing the high dielectric constant rods in AS-EBG structure.

1.4.3 Mushroom EBG Structures

This prototype of EBG structure is realized by periodically embedding the metal patch between power/ground planes and connecting the patches with the ground plane through vias [35]-[37] as shown in Fig. 1.12(a). The design concept of the mushroom EBG structure can be considered as periodically terminating the series connections of

capacitance and inductance between power/ground planes as shown in Fig. 1.12(b). The capacitance is formed between the power plane and patch and the inductance results from the current path along patch, connecting via, and bottom plate. Hence, the stopband is regarded as the shorting ability of the series *LC* resonance.

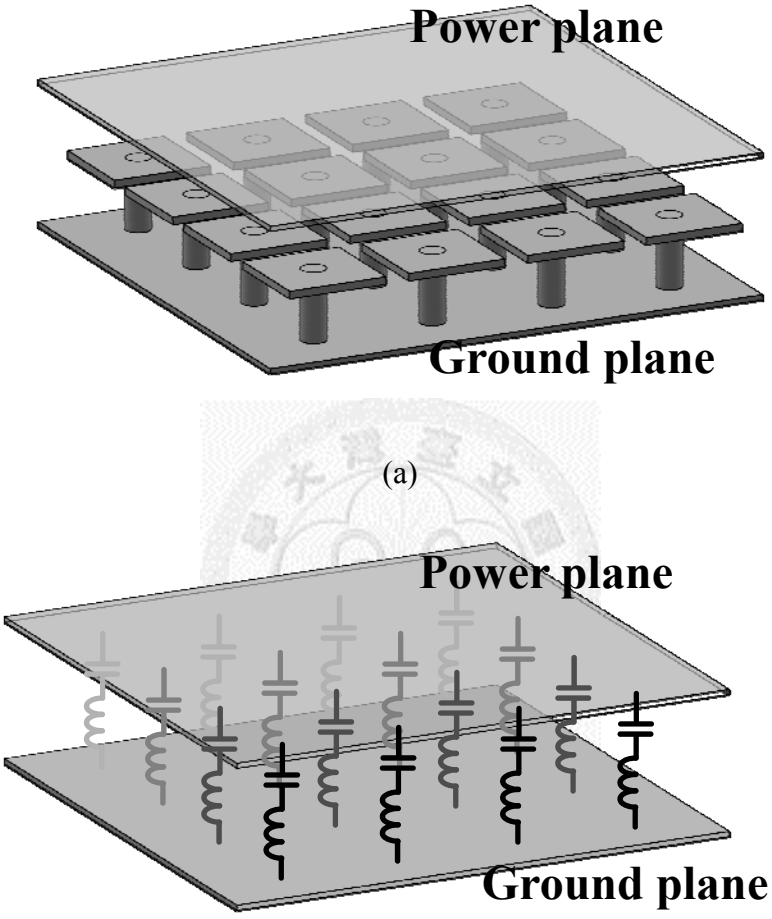

Fig. 1.12 (a) Mushroom EBG power/ground planes and (b) its concept.

Without the need of the high permittivity material for the photonic crystal and the IR-drop issue of the coplanar EBG structure [34], the mushroom EBG structure is suitable for the multilayer package or PCB standard fabrication. Nevertheless, the drawbacks of occupying larger area and narrower stopband bandwidth for the

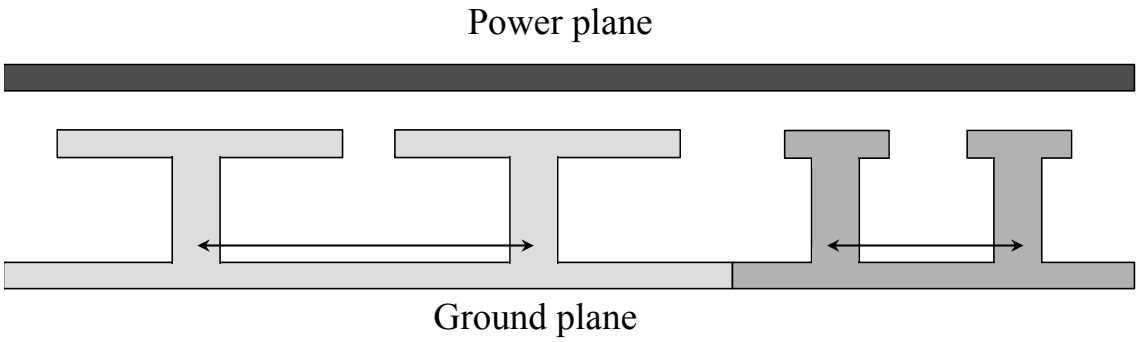

(a)

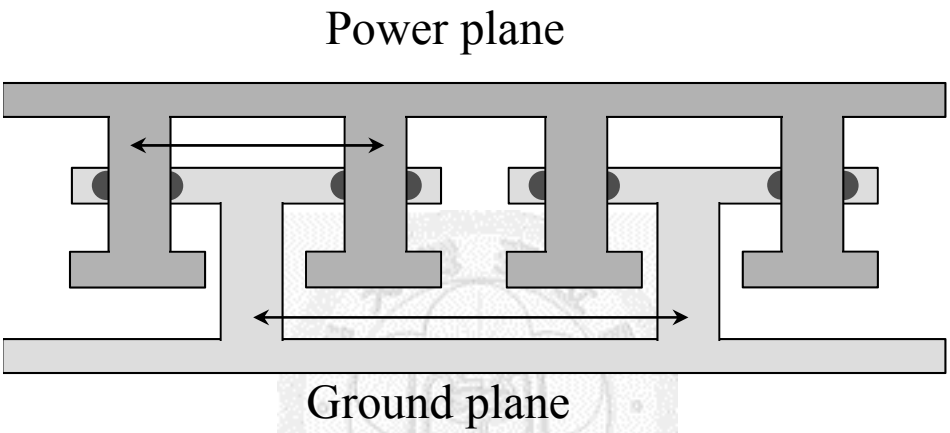

(b)

Fig. 1.13 (a) Cascading mushroom EBG structures and (b) double-stacked EBG structure.

mushroom EBG structure still need to be improved.

As shown in Fig. 1.13(a), the intuitive way to enhance the stopband is cascading EBG structures of different unit-cell size with different bandgaps [38]. This method needs large layout area. Double-stacked EBG structure [39] has been proposed by embedding two mushroom EBG structures with different sizes, and thus different bandgaps, into single unit cell, as shown in Fig. 1.13(b). However, the lower-bound cutoff frequency of the first bandgap is not improved and still determined by the size of

the larger mushroom EBG structure. The mushroom EBG structure with multiple vias has been proposed with wider bandwidth, but the original design is not optimized and the bandwidth moves toward high frequency range [40]. Besides that, several works for improving mushroom EBG structure have also been proposed and are classified into two types, inductance- [41], [42] and capacitance-enhanced EBG structures [43]. Although the former, as shown in Fig. 1.14, with enhanced via inductance improves the lower-bound cutoff frequency and thus decreases the required area, there is a decrease of stopband bandwidth. Without shrinking the bandwidth, the latter type implemented by embedded high permittivity material between power plane and patches reduces the area and enhances the bandwidth simultaneously, but high permittivity material with higher cost is required.

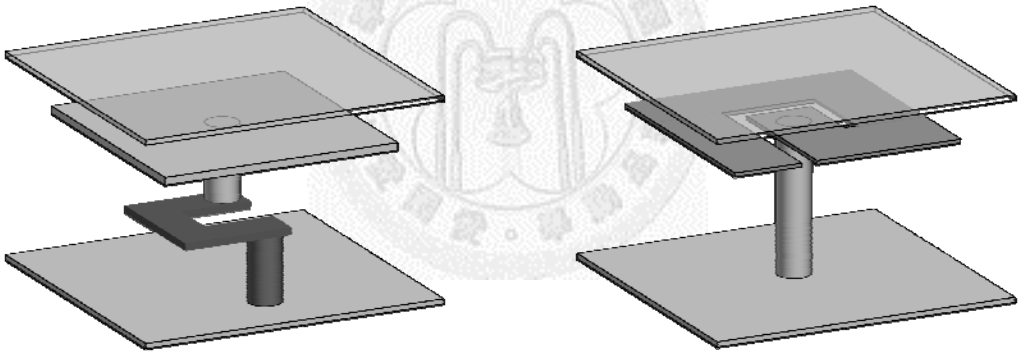

(a) (b)

Fig. 1.14 Inductance-enhanced EBG structures (a) proposed in [41] and (b) in [42].

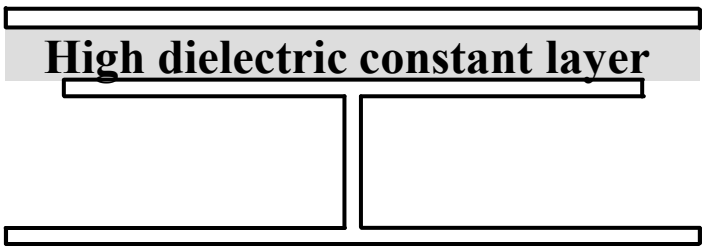

Fig. 1.15 Capacitance-enhanced EBG structure using high dielectric constant layer.

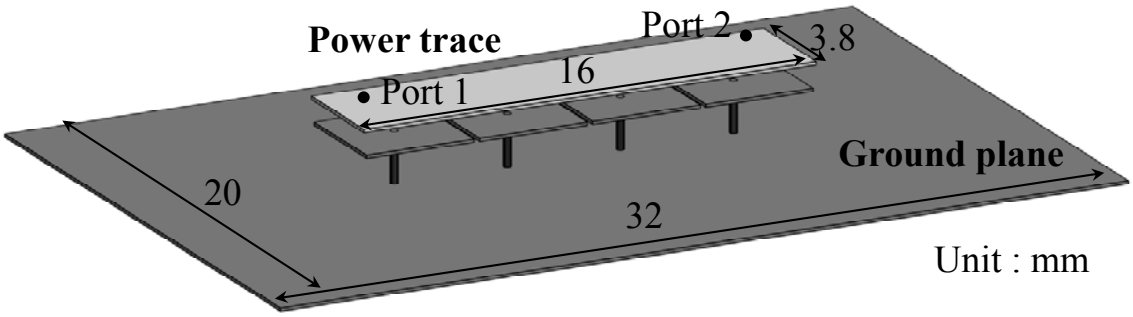

(a)

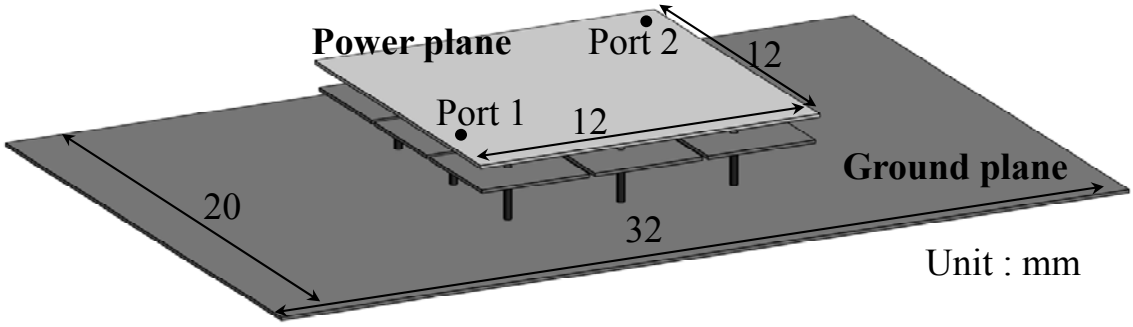

(b)

Fig. 1.16 Examples of (a) power trace and (b) power plane with mushroom EBG structure.

1.4.4 Design Challenge on PDN with EBG Structure

The mushroom EBG structure is taken as an example for introducing the PDN with EBG structure for power integrity design. The PDN in PCB or package is usually in the shapes of traces or planes. For the power trace, the one-dimensional (1-D) EBG structure can be implemented. As shown in Fig. 1.16(a), there are a power trace with dimension of 3.8 mm in width and 16 mm in length and a ground plane with dimension of 20 mm in width and 30 mm in length. In the situation, the mushroom EBG structures can be distributed in one-dimensional direction. As regards the case of power plane, the

mushroom EBG structure is distributed in two-dimensional (2-D) directions. As shown in Fig. 1.16(b), the power plane is 12 mm by 12 mm and the 3 by 3 mushroom EBG structures are embedded between the power and ground planes. Fig. 1.17 shows the simulated magnitudes of S_{21} of the two cases. The results of the bared boards, without mushroom EBG structures, are also shown in this figure. From the comparison of the bared board and EBG board, it can be found that there is a stopband where the noise coupling ($|S_{21}|$) between the two test ports, as shown in Fig. 1.16, can be significantly suppressed by the EBG board. For the 1-D power trace and 2-D power plane, the stopbands are a little different.

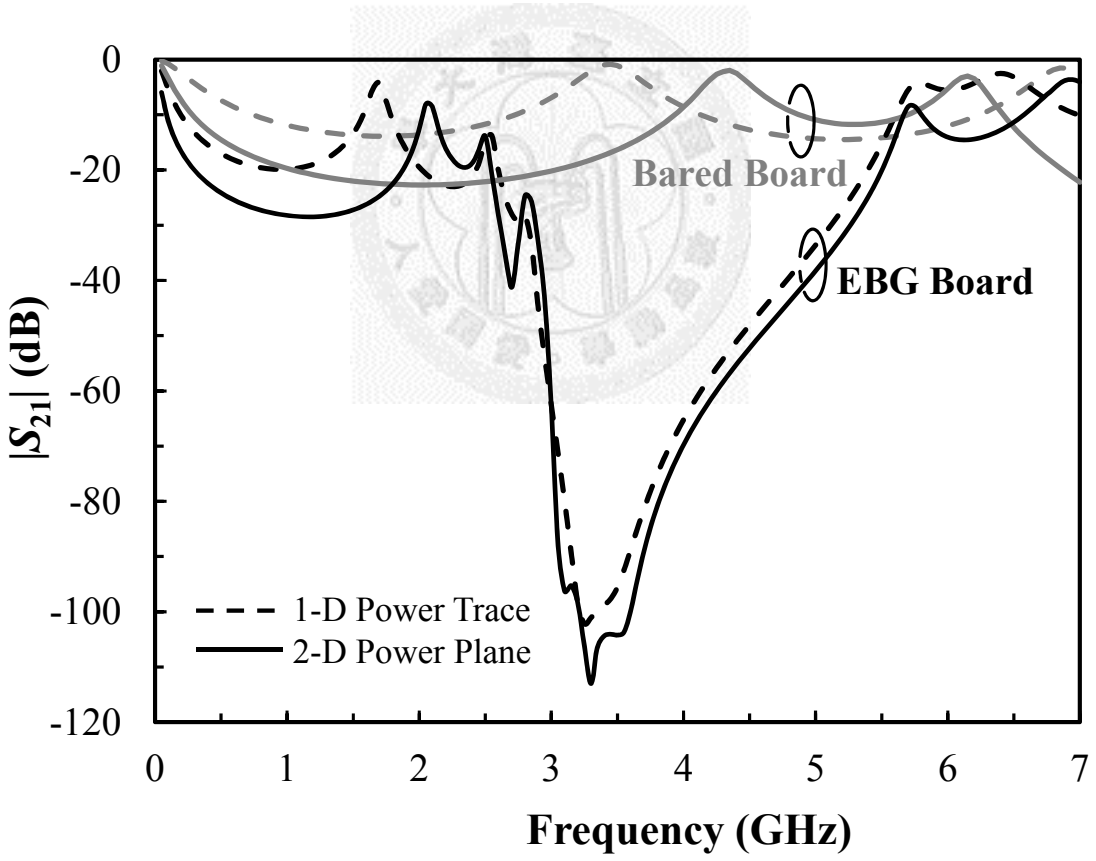

Fig. 1.17 Magnitudes of S_{21} of the examples including the 1-D power trance and 2-D power plane with and without mushroom EBG structures as shown in Fig. 1.16.

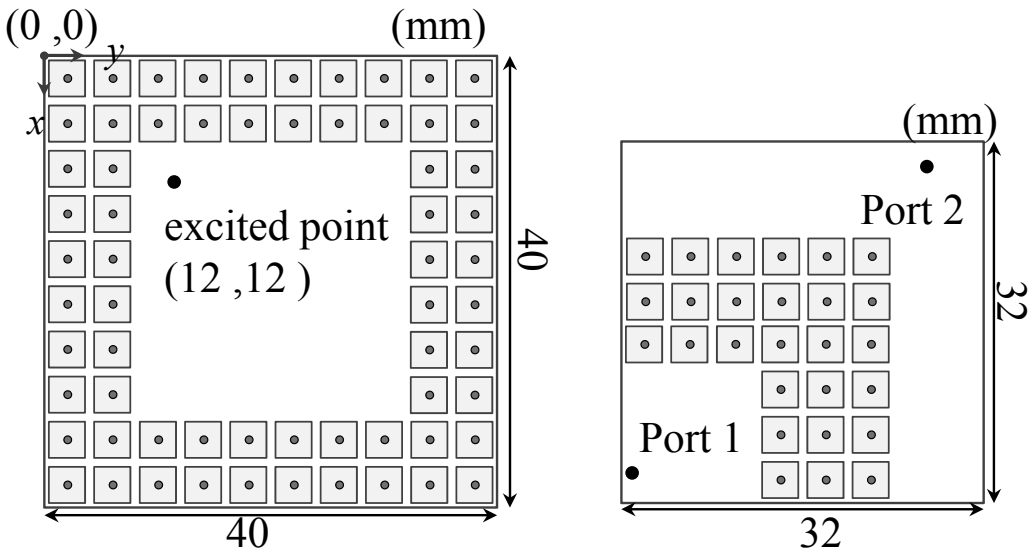

(a) (b)

Fig. 1.18 Power plane with (a) EBG fence and (b) partial EBG structure.

In the real situation of the package or PCB, the layout area is always the concern of the implement of the EBG structures. Fortunately, the EBG structures are not necessary occupied all the area of the power plane. For example, Fig. 1.18(a) shows the top view of the power plane with EBG fence for the suppression of EMI and Fig. 1.18(b) shows the top view of the power plane with partial EBG structure for the GBN isolation between port 1 and port 2. For the case of the EBG fence, there are two rows of the mushroom EBG structure embedded around the periphery of the power/ground plane. The simulated maximum electric fields at 3 meters distance, radiated by the power plane without and with the EBG structures, are illustrated in Fig. 1.19. The radiated emission excited at the point shown in Fig. 1.18(a) is suppressed by the mushroom EBG fence in the stopband. Although there are several resonant frequencies within bandgaps formed by the resonance of the area without embedded any EBG structure, the peaks can be eliminated by increasing the rows of the implemented EBG structure.

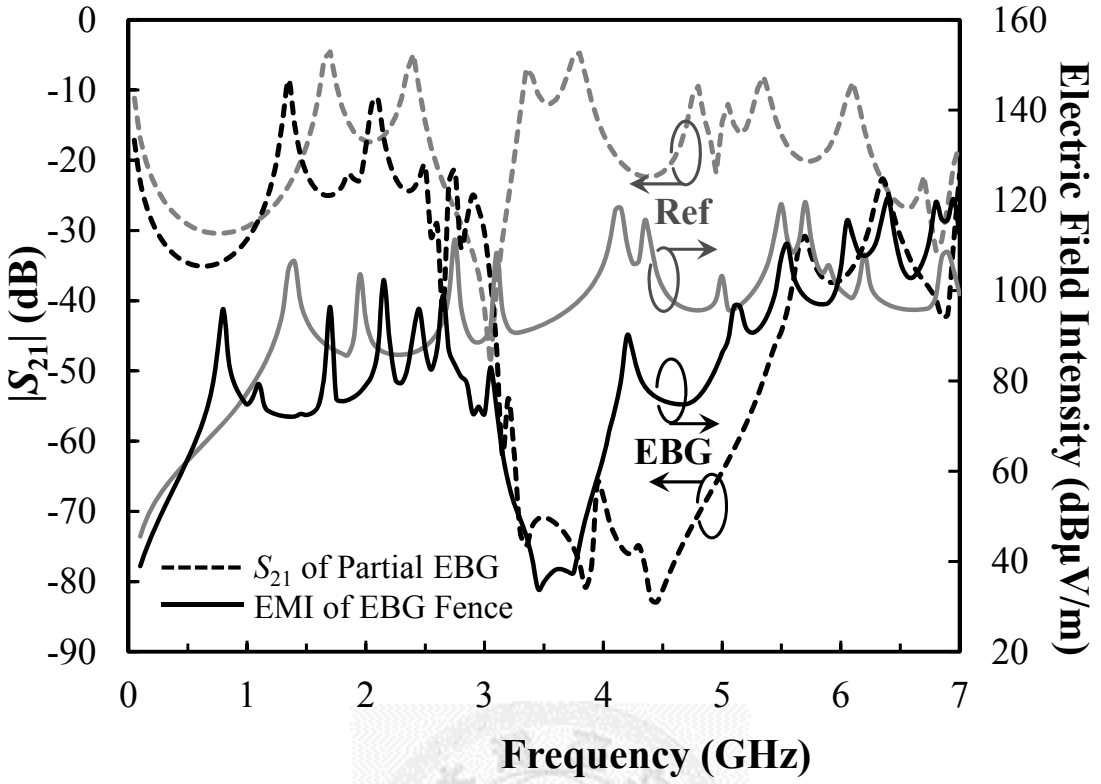

Fig. 1.19 Electric field intensity at far field (3 m) for the EBG fence and magnitudes of S_{21} for the partial EBG structure.

As regards the partial EBG structure shown in Fig. 1.18(b), the port 1 is surrounded by three rows of mushroom EBG structures. Hence, the noise coupling can be isolated from the area outside the partial EBG structure, for example, port 2. Fig. 1.19 also shows the simulated S_{21} of the case. Comparing with the reference board without EBG structures, the partial EBG board can achieve enough good capability for GBN isolation.

Although the EBG fence or partial EBG structure can achieve good performance for isolation, the occupied area is still a big issue in the real case. The design challenge in this field is how to reduce the layout area and widen the bandwidth at the same time. How to reduce the size of the unit cell of EBG structure is equivalent to how to lower

the lower-bound cutoff frequency. Therefore, an efficient prediction method for the lower- and upper-bound cutoff frequencies of the EBG structures is important. The bandgap was conventionally determined from full-wave simulation [44]. This approach is time-consuming. The bandgap predictions have been proposed based on one-dimensional analysis only [31], [33], [37]. However, the fast prediction for two-dimensional EBG structure is not found in the literatures.

1.5 Contributions

The three main contributions are briefly described as follow：

1) A novel method for predicting the lower- and upper-bound cutoff frequencies of the EBG structure is proposed based on determining the resonant frequency of the unit cell with specific boundary conditions. Compared to the conventional approach by solving the dispersion relation, this method is more efficient with the same accuracy. This method can be applied to both one-dimensional and two-dimensional EBG structures. Based on this method, the corresponding equivalent circuit model can be established by using transmission-line sections for the one-dimensional EBG structure and by resonant cavity models for the one-dimensional EBG structure.
2) A multiple vias EBG structure, which is the mushroom EBG structure with multiple vias, is proposed to enhance the bandwidth of the bandgap for the power/ground (P/G) noise suppression. By using four shorting vias and optimizing their arrangement, the multiple vias EBG structure has the wider bandwidth of the bandgap compared to the conventional mushroom EBG structure.
3) A novel interleaved EBG structure is proposed to be with both compact size and wide stopband bandwidth for suppressing the ground bounce noise in the power

distribution network. As an example of the interleaved EBG structure with single pair of power/ground vias, the electrical size, which is normalized to the wavelength in the substrate, and bandwidth ratio are 0.071 λ_{gL} and 139 %, respectively. Unlike other works with trade-off between size and bandwidth, the interleaved EBG structure with one pair of power/ground vias can simultaneously achieve substantial improvements on bandwidth of 51.1 % and on miniaturization of 61.2 % compared with the conventional mushroom EBG structure. As regards the interleaved EBG structure with four pairs of power/ground vias, the bandwidth has an increase of 115.2 % wider than that of the conventional mushroom EBG structure and the required layout area can also be reduced by 30.5 % simultaneously.

1.6 Chapter Outlines

The dissertation is organized as follow. In chapter 2, we will propose a novel methodology to efficiently predict the lower-bound and upper-bound cutoff frequencies of the bandgap. Based on this methodology, physics-based models with specific boundary conditions are proposed for the unit cell of the EBG structure. The cutoff frequencies are then solved for the resonant frequencies of the models. The mushroom EBG structure is taken as an example to illustrate the methodology. An equivalent circuit model using the transmission-line sections is proposed for the one-dimensional EBG structure. As regards the two-dimensional EBG structure, the *LC* circuit models are developed based on the resonant cavity models. This method provides a clear physical insight of the cutoff frequency of the bandgap.

In Chapter 3, a multiple vias EBG structure, which is a mushroom EBG structure with multiple vias, is proposed to enhance the bandwidth of the bandgap. By using four

shorting vias and optimizing their arrangement, the multiple vias EBG structure presents the wider bandwidth of the bandgap when comparing to the conventional mushroom EBG structure. In addition, both the design concept and the mechanism of the bandwidth enhancement are also studied based on the optimization of vias location. Two approaches are then used to predict the one- and two-dimensional bandgaps, respectively. Test vehicles are manufactured on FR4 substrate to compare the measured results and the numerical ones. Good agreements can be found to verify the new design.

In Chapter 4, a four-layer EBG structure with interleaved two identical patches and location-variable power/ground vias is proposed. The electromagnetic bandgap characteristic is different from that of the mushroom and double-stacked EBG structures, even though the interleaved EBG structure looks similar to them. Using the concept of the interleaved EBG structure, both the electrical size, which is normalized to the wavelength in the substrate, and the bandwidth ratio are improved. Miniaturization is achieved by additional shunt capacitance of the interleaved patches, and bandwidth is enhanced by the optimum location of power/ground vias. The design of multiple pairs of power/ground vias is also proposed for wider bandwidth. Finally, the comparison and measurement are given to demonstrate the design concept.

Chapter 5 concludes the main points of the dissertation.

Chapter 2 Electromagnetic Bandgap Prediction

Electromagnetic bandgaps are one of the most interesting unique characteristics resulting from the periodic structures. How to know the bandwidth of the bandgap and thus how to design the geometry of the EBG structure are important topics in the fields of EBG applications. In this chapter, we will propose a methodology to efficiently predict the lower-bound (f_L) and upper-bound (f_U) cutoff frequencies of the bandgap. The mushroom EBG structure is taken as an example to illustrate the methodology. Two approaches are proposed for modeling the unit cells arranged in the one-dimensional (1-D) and two-dimensional (2-D) distributions, respectively. An equivalent circuit model is proposed for the 1-D EBG structure using the transmission-line sections. As regards the 2-D EBG structure, the equivalent circuit models are developed for the lower- and upper-bound cutoff frequencies based on the resonant cavity models.

2.1 One-Dimensional EBG Analysis

As described in Chapter 1, the mushroom EBG structure was conventionally considered as series *LC* resonators embedded between power and ground planes periodically. It is supposed that there is an equivalent circuit model of the unit cell of the EBG structure shown in Fig. 2.1. It consists of two sections of transmission lines and a series *LC* resonant circuit. The transmission lines are with characteristic impedance of Z_0 and length of $\frac{1}{2}a$. The phase constant of the transmission line β_{TL} is dependent on frequency (f) as

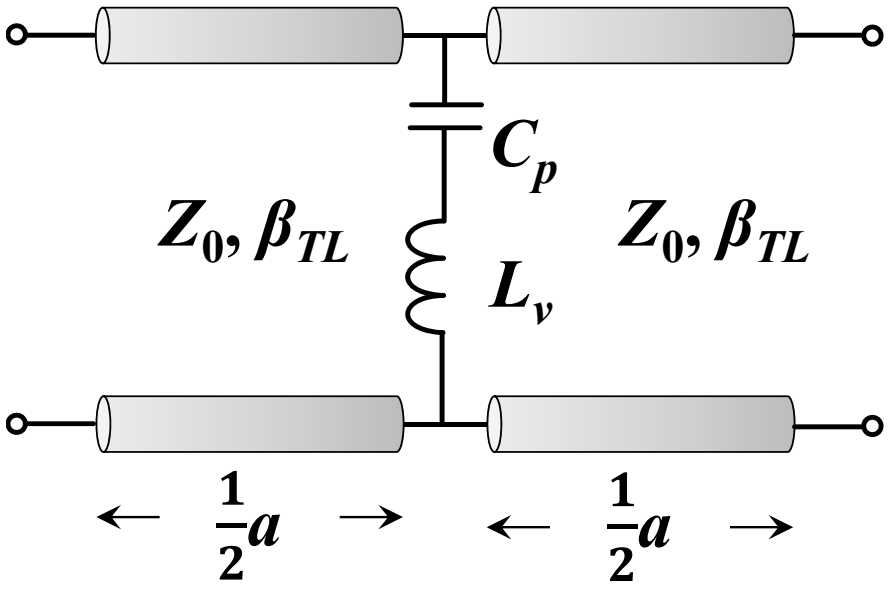

Fig. 2.1 Equivalent circuit model for the unit cell of mushroom EBG structure.

$$\beta_{TL} = \frac{2\pi f}{c_0}\sqrt{\varepsilon_r} \tag{2.1}$$

, where c_0 is the speed of light in vacuum and ε_r is the dielectric constant of material. The series *LC* resonant circuit is comprised of a capacitor with parallel-plate capacitance of C_p and an inductor with via inductance of L_v. Thus, the bandgap results from the transmission zero of the series *LC* resonator. This understanding gives us an intuitive design concept for relating the center frequency (f_0) and bandwidth (*BW*) of the *LC* resonator to those of the bandgap by [40], [44]

$$f_0 \propto \frac{1}{\sqrt{L_v C_p}} \tag{2.2}$$

and

$$BW \propto \sqrt{\frac{C_p}{L_v}}. \tag{2.3}$$

Further, they can be relative to the geometry of the EBG structure, which includes the sizes of the patch and via.

However, the lower- and upper-bound cutoff frequencies of the bandgap may not

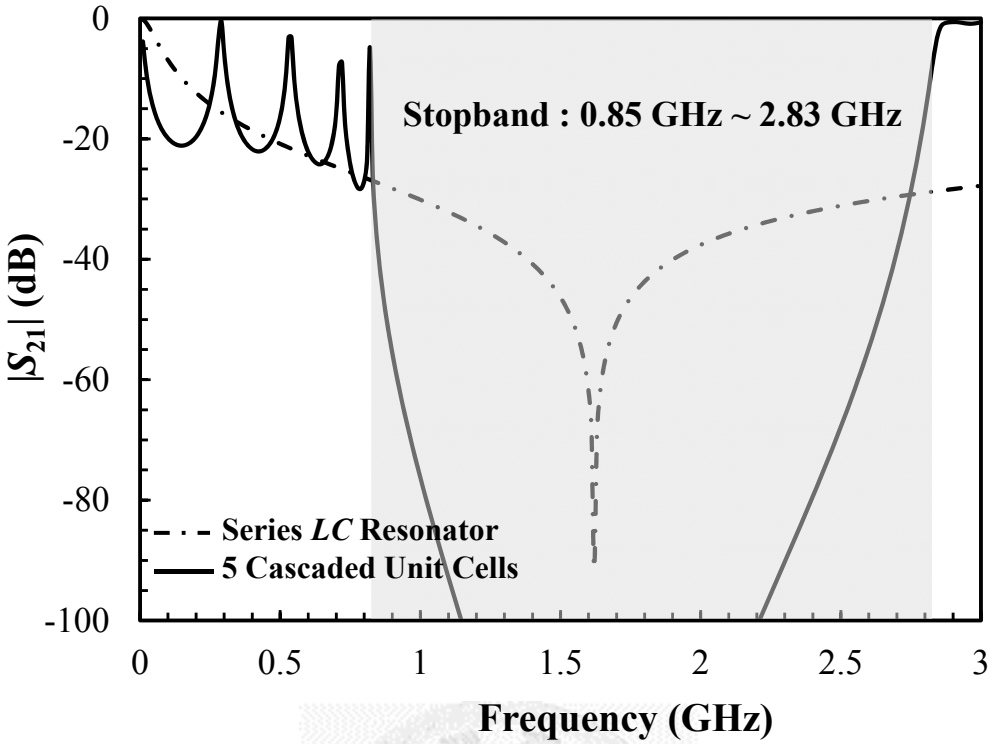

Fig. 2.2 Transmission coefficients of series *LC* resonator and 5 cascaded unit cells.

directly result from the transmission zero of the *LC* resonator. For example, it is assumed there is an EBG structure of which equivalent circuit model for the unit cell is the same as the one shown in Fig. 2.1. We choose a = 20 mm, ε_r = 4.4, Z_0 = 5.39 Ω, L_v = 76.4 pH, and C_p = 126 pF. The transmission coefficient (S_{21}) of the series *LC* resonator has a transmission zero at 1.62 GHz as shown in Fig. 2.2. However, a stopband appears between 0.85 GHz and 2.83 GHz when the five unit cells are cascaded. It is hard to predict the bandwidth of the stopband just from the characteristic of the series *LC* resonator. In addition, the transmission zero is not necessary located at the center of the stopband. Based on the above reasons, it is shown that (2.2) and (2.3) are not qualified for predicting center frequency and bandwidth of the bandgap. Hence, a method is required to relate the lower- and upper-bound cutoff frequencies to the geometry of the EBG structure.

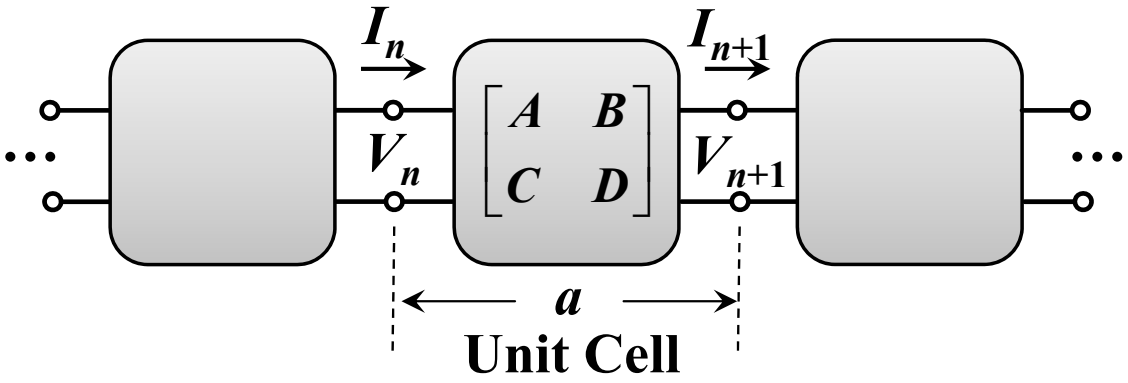

Fig. 2.3 Equivalent circuit model of periodic structure.

2.1.1 One-Dimensional Dispersion Relation

In order to analyze the periodic structure, a dispersion relation can be calculated by constructing the equivalent circuit model of the unit cell and applying the periodic boundary condition. As shown in Fig. 2.3, the periodic structure is considered as infinite unit cells cascaded by identical equivalent circuit models. The equivalent circuit model of the unit cell with length of a can be described as a two-port network represented by *ABCD* matrix [45]. The voltages and currents of the nth two-port network can be related by

$$\begin{bmatrix} V_n \\ I_n \end{bmatrix} = \begin{bmatrix} A & B \\ C & D \end{bmatrix} \begin{bmatrix} V_{n+1} \\ I_{n+1} \end{bmatrix}. \tag{2.4}$$

On the other hand, for the periodic structure, the voltage V_{n+1} and current I_{n+1} can also be the V_n and I_n just multiplied by a propagation term $e^{-\gamma a}$, respectively, where γ is the complex propagation constant defined as $\gamma = \alpha + j\beta$. The real part α is the attenuation constant and the imaginary part β is the phase constant. Thus, the relations of voltages and currents are

$$\begin{bmatrix} V_{n+1} \\ I_{n+1} \end{bmatrix} = e^{-\gamma a} \begin{bmatrix} V_n \\ I_n \end{bmatrix}. \tag{2.5}$$

Substituting the periodic boundary condition (2.5) into (2.4), we have

$$\begin{bmatrix} A - e^{\gamma a} & B \\ C & D - e^{\gamma a} \end{bmatrix} \begin{bmatrix} V_{n+1} \\ I_{n+1} \end{bmatrix} = 0. \tag{2.6}$$

For the nontrivial solution of both V_{n+1} and I_{n+1} being not zeros, the determinant of the above matrix must be zero and can be expressed as

$$e^{2\gamma a} - (A + D)e^{\gamma a} + AD - BC = 0. \tag{2.7}$$

The propagation constant can thus be solved as

$$\gamma = \frac{1}{a} \cosh^{-1}\left(\frac{A + D}{2}\right) \tag{2.8}$$

under the reciprocal condition AD-BC = 1. For $\left|\frac{A + D}{2}\right| > 1$, γ is a nonzero real number which represents a stopband. For $\left|\frac{A + D}{2}\right| < 1$, we have

$$\beta = \frac{1}{a} \cos^{-1}\left(\frac{A + D}{2}\right), \tag{2.9}$$

which represents a passband.

Using (2.9), we can get the dispersion relation of the EBG structure shown in Fig. 2.1. First, the *ABCD* matrix of equivalent circuit model for unit cell is

$$\begin{bmatrix} A & B \\ C & D \end{bmatrix} = \begin{bmatrix} \cos\theta_h & jZ_0 \sin\theta_h \\ \frac{j}{Z_0}\sin\theta_h & \cos\theta_h \end{bmatrix} \begin{bmatrix} 1 & 0 \\ \frac{j\omega C_p}{1 - \omega^2 L_v C_p} & 1 \end{bmatrix} \begin{bmatrix} \cos\theta_h & jZ_0 \sin\theta_h \\ \frac{j}{Z_0}\sin\theta_h & \cos\theta_h \end{bmatrix} \tag{2.10}$$

where ω is radian frequency and $\theta_h = \frac{\beta_{TL} a}{2}$. Substituting (2.10) into (2.9), the dispersion relation can be derived as

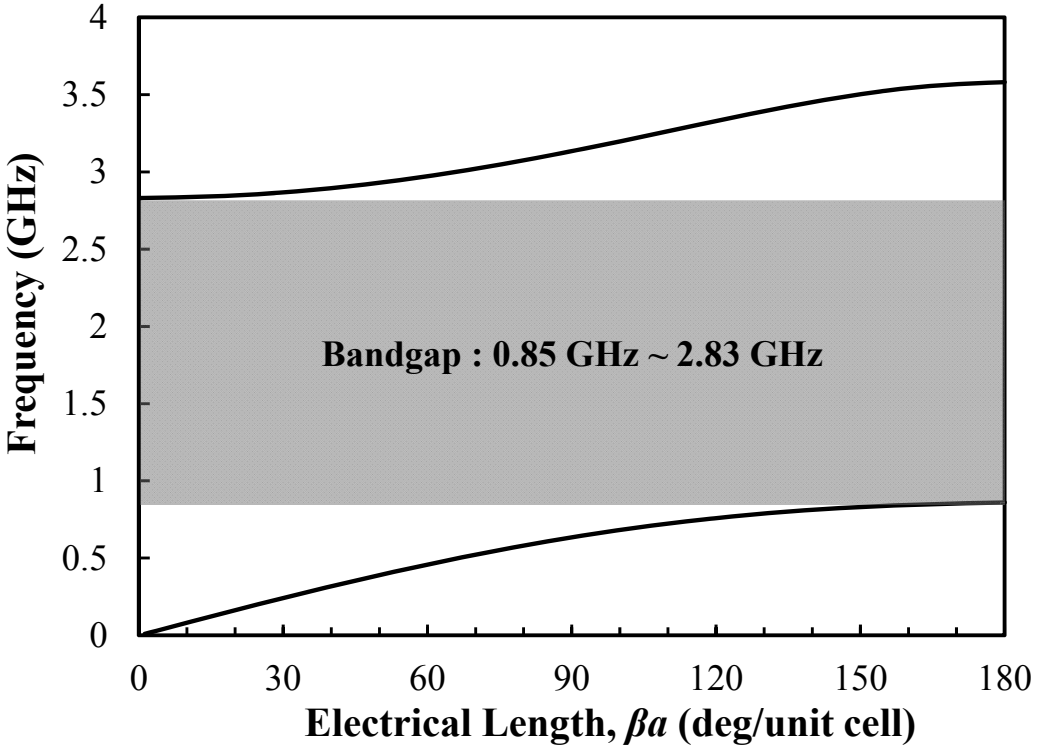

Fig. 2.4 Dispersion diagram of unit cell shown in Fig. 2.1.

$$\beta = \frac{1}{a}\cos^{-1}\left(\cos\left(\beta_{TL}a\right) - \frac{\omega C_p Z_0}{2\left(1-\omega^2 L_v C_p\right)}\sin\left(\beta_{TL}a\right)\right) \tag{2.11}$$

From (2.11), we can substitute each frequency into the right-hand side of (2.11), and thus the corresponding phase constant can be calculated. The dispersion diagram of the EBG structure can be plotted as shown in Fig. 2.4. As shown in this figure, we can find two propagation modes from 0 to 0.85 GHz and from 2.83 GHz to 3.57 GHz. There is a forbidden band between the two passbands, in which on propagation mode can be seen. The bandgap, between 0.85 GHz to 2.83 GHz, calculated from the dispersion relation is consistent with the stopband of five cascaded unit cells shown in Fig. 2.2.

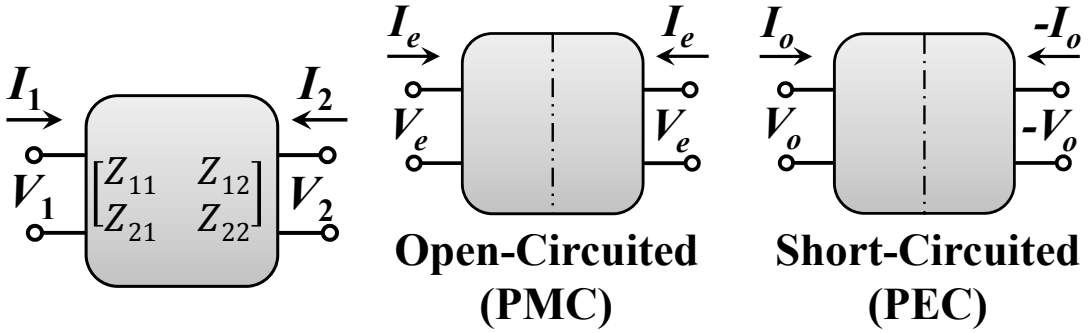

(a) (b) (c)

Fig. 2.5 (a) Two-port symmetrical network, (b) even-mode half circuit, and (c) odd-mode half circuit.

2.1.2 Lower- and Upper-Bound Cutoff Frequencies Prediction

As shown in Fig. 2.4, it is worth noting that the lower- and upper bound cutoff frequencies of the bandgap are determined by some specific phases, which are either zero or π. It implies that we may not need to solve the dispersion relation for all frequencies to obtain the cutoff frequencies. We will show that the cutoff frequencies of the bandgap will be decided and predicted by the half circuits of the equivalent circuit model with specific boundary conditions.

First, the two-port network of the unit cell, described by a *ABCD* matrix, can be replaced by using a *Z*-parameters matrix, which is shown in Fig. 2.5 (a) and defined as

$$\begin{bmatrix} V_1 \\ V_2 \end{bmatrix} = \begin{bmatrix} Z_{11} & Z_{12} \\ Z_{21} & Z_{22} \end{bmatrix} \begin{bmatrix} I_1 \\ I_2 \end{bmatrix}. \tag{2.12}$$

Thus, (2.9) can be rewritten as

$$\cos(\beta a) = \frac{A+D}{2} = \frac{Z_{11}+Z_{22}}{2Z_{21}} \tag{2.13}$$

Suppose the unit cell is symmetrical, based on even- and odd-mode excitation, the

two-port network can be decomposed into two identical half circuits as shown in Fig. 2.5 (b) and Fig. 2.5 (c) [46]. One is the even-mode half circuit with open-circuited (O.-C.) or perfect magnetic conductor (PMC) boundary condition along the symmetrical plane, when the equal magnitude and in phase sources are excited at port 1 and port 2 as shown in Fig. 2.5 (b). The other is odd-mode half circuit with short-circuited (S.-C.) or perfect electrical conductor (PEC) boundary condition along the symmetrical plane, when the equal magnitude but out-of-phase sources are excited at port 1 and port 2 as shown in Fig. 2.5 (c). Consequently, the response of the original two-port network can be represented by the superposition of the even- and odd-mode one-port network as

$$Z_{11} = \frac{V_1}{I_1}\Big|_{I_2=0} = \frac{V_e + V_o}{I_e + I_o}\Big|_{I_e - I_o=0} = \frac{1}{2}\left(\frac{V_e}{I_e} + \frac{V_o}{I_o}\right) = \frac{1}{2}(Z_{ine} + Z_{ino}) \tag{2.14}$$

and

$$Z_{21} = \frac{V_2}{I_1}\Big|_{I_2=0} = \frac{V_e - V_o}{I_e + I_o}\Big|_{I_e - I_o=0} = \frac{1}{2}\left(\frac{V_e}{I_e} - \frac{V_o}{I_o}\right) = \frac{1}{2}(Z_{ine} - Z_{ino}) \tag{2.15}$$

, where Z_{ine} and Z_{ino} are the even- and odd-mode input impedances, respectively. Substituting (2.14) and (2.15) into (2.13), we have

$$\cos(\beta a) = \frac{Z_{ine} + Z_{ino}}{Z_{ine} - Z_{ino}}. \tag{2.16}$$

When the right-hand side of (2.16) is between -1 to 1, βa can be solved as a real number between 0 to π, where a passband is present. Otherwise, there is a bandgap. The cutoff frequencies of the bandgaps are decided by the boundary frequencies of passband where βa equals either zero or π.

When βa equals zero, (2.16) can be expressed as

$$\frac{Z_{ine}(f) + Z_{ino}(f)}{Z_{ine}(f) - Z_{ino}(f)} = 1. \tag{2.17}$$

The solutions of (2.17) are the frequencies that satisfy

$$Z_{ine}(f) = \pm j\infty \tag{2.18}$$

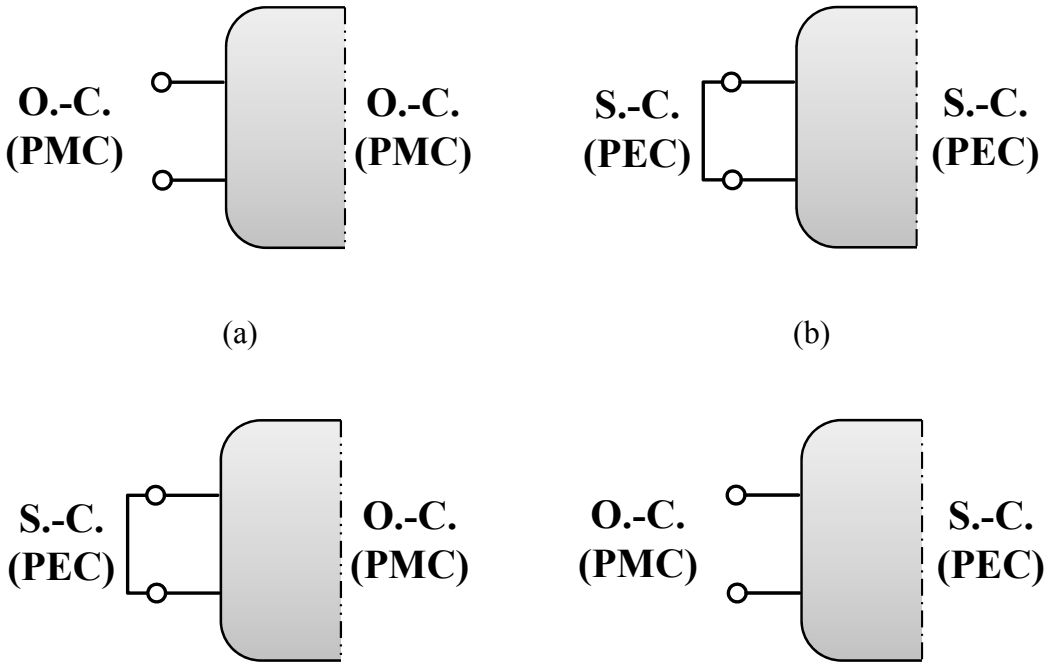

Fig. 2.6 (a) Type-I, (b) Type-II, (c) Type-III, and (d) Type-IV half resonators with corresponding boundary conditions.

or $$Z_{ino}(f) = 0. \tag{2.19}$$

It is worth noting that the solution frequencies of (2.18) also represent the resonant frequencies of the even-mode half circuit with open-circuited input port, which is denoted as the Type-I half resonator as shown in Fig. 2.6 (a). On the other hand, the solution frequencies of (2.19) are the resonant frequencies of the Type-II resonator, the odd-mode half circuit with short-circuited input port as shown in Fig. 2.6 (b).

In the case of βa equaling π, (2.16) can be rewritten as

$$\frac{Z_{ine}(f) + Z_{ino}(f)}{Z_{ine}(f) - Z_{ino}(f)} = -1. \tag{2.20}$$

The solutions of (2.20) are the frequencies that satisfy

$$Z_{ine}(f) = 0 \tag{2.21}$$

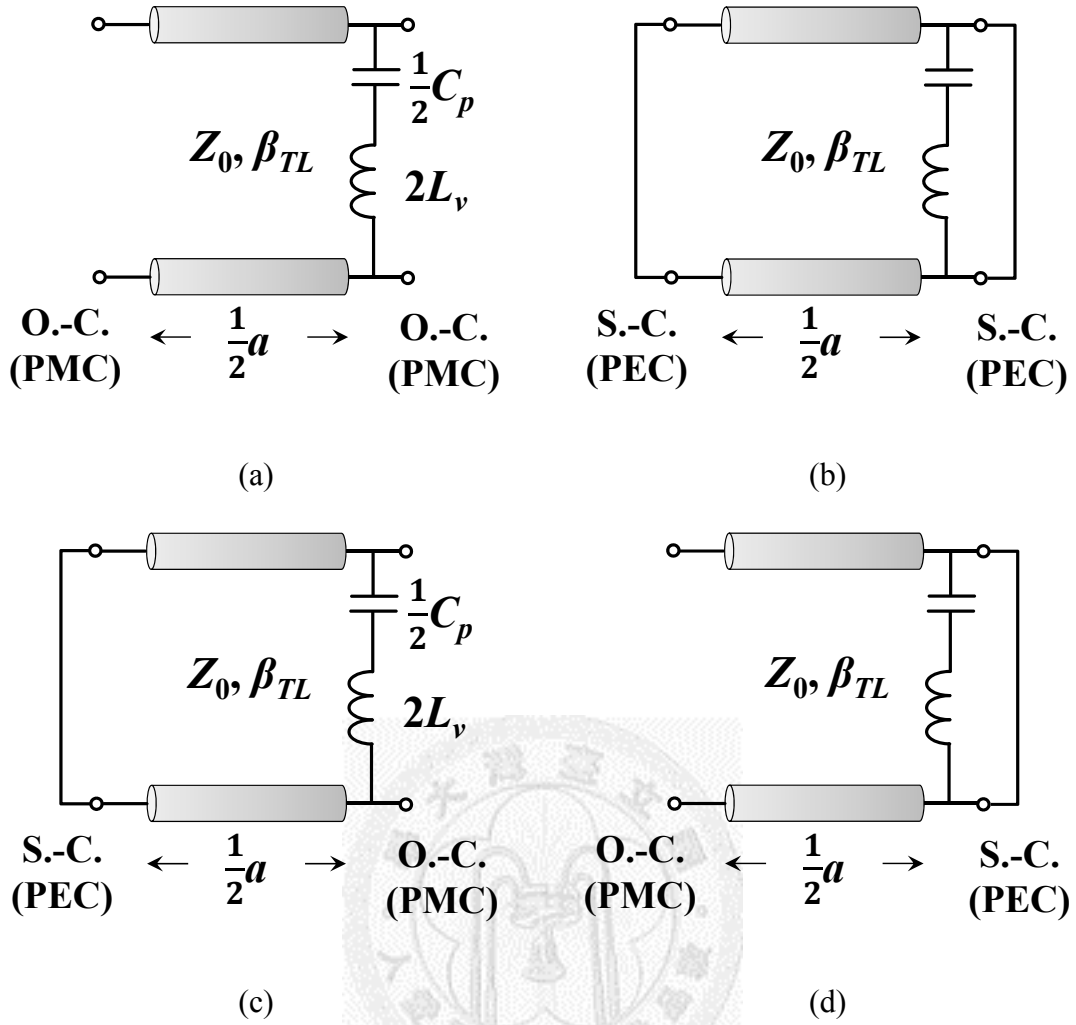

Fig. 2.7 (a) Type-I, (b) Type-II, (c) Type-III, and (d) Type-IV half resonators of the unit cell shown in Fig. 2.1.

or $$Z_{ino}(f) = \pm j\infty \tag{2.22}$$

The solution frequencies of (2.21) and (2.22) are the resonant frequencies of the Type-III resonator, even-mode half circuit with short-circuited input port as shown in Fig. 2.6 (c), and Type-IV resonator, odd-mode half circuit with open-circuited input port as shown in Fig. 2.6 (d), respectively.

It has been shown that applying periodic boundary condition with specific phases, 0 or π, can be replaced by solving resonant frequencies of four kinds of half resonators.

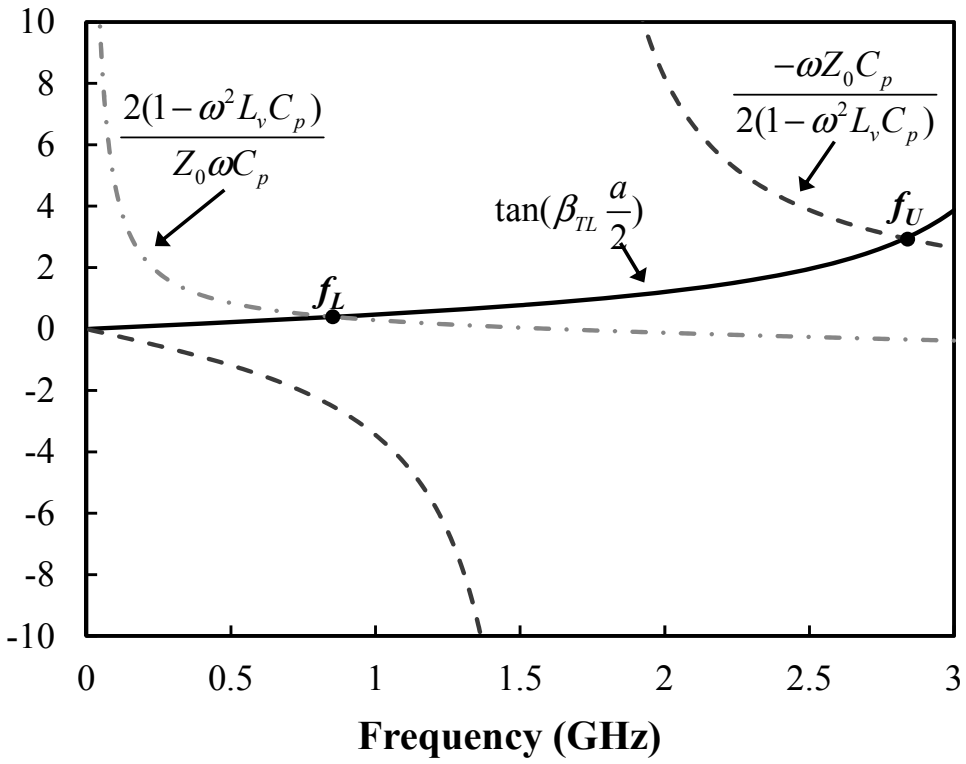

Fig. 2.8 Left-hand and right-hand sides of (2.24) and (2.26).

The lower- and upper-bound cutoff frequencies of the first bandgap will be decided by the lowest two resonant frequencies, except DC, of the four types of half resonators. Taking the unit cell shown in Fig. 2.1 as an example, the four types of half circuits are shown in Fig. 2.7 (a)-(d). It can be found that Type-III half resonator shown in Fig. 2.7 (c) has the lowest resonant frequency among the four kinds of resonators because the short-circuited line increases the total inductance of the resonance. So, the lower-bound cutoff frequency is decided by the first resonant frequency of the Type-III half resonator. To calculate the resonant frequency, we can have

$$jZ_0 \tan\left(\beta_{TL}\frac{a}{2}\right) + j2\omega L_v + \frac{2}{j\omega C_p} = 0. \tag{2.23}$$

The above equation (2.23) can be simplified as

$$\tan\left(\beta_{TL}\frac{a}{2}\right)=\frac{2(1-\omega^2 L_v C_p)}{Z_0\omega C_p}. \tag{2.24}$$

Both the left-hand side and right-hand side of (2.24) are shown in Fig. 2.8 and they intersect at 0.85 GHz, which is equal to the estimated lower-bound cutoff frequency using the dispersion relation as shown in Fig. 2.4.

With regard to the upper-bound cutoff frequency, it is the first non-zero resonant frequency of Type-I resonator and can be found by solving

$$-jZ_0\cot(\beta_{TL}\frac{a}{2})-j\frac{2}{\omega C_p}+j2\omega L_v=0, \tag{2.25}$$

which can be simplified as

$$\tan(\beta_{TL}\frac{a}{2})=\frac{-\omega Z_0 C_p}{2(1-\omega^2 L_v C_p)}. \tag{2.26}$$

The right-hand side of (2.26) is also shown in Fig. 2.8. The solution is found at 2.83 GHz, which is also consistent with that shown in Fig. 2.4. In addition, the first resonances of Type-IV and Type-II half resonators are corresponding to the half and one wavelength resonances of the unit cell, respectively. Hence the resonant frequencies of them will appear above the first bandgap.

2.1.3 One-Dimensional Mushroom EBG Structure

A case of one-dimensional mushroom EBG structure is discussed here. For the given geometric parameters, the dispersion diagram and bandgap of the mushroom EBG structure can be calculated by using commercial full-wave solver. A one-dimensional equivalent circuit model consisting of transmission-line sections is proposed for electrically characterizing the unit cell of the mushroom EBG structure. Applying the proposed prediction method, the estimated lower- and upper- bound cutoff frequencies can be consistent with the results from full-wave solver and used to predict the bandgap.

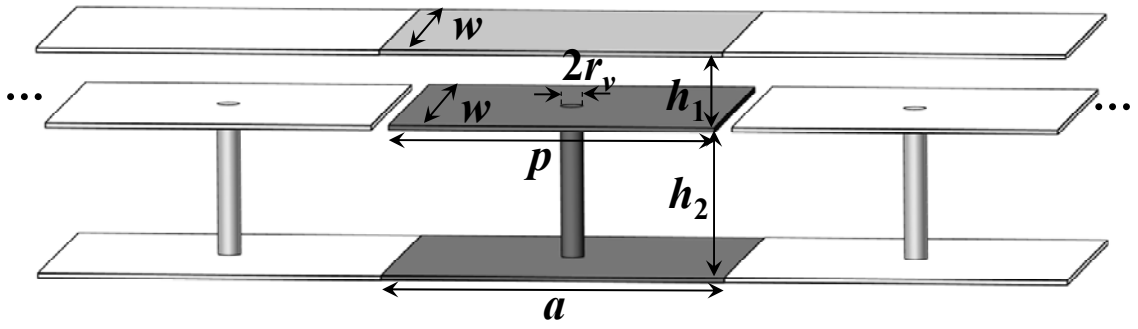

(a)

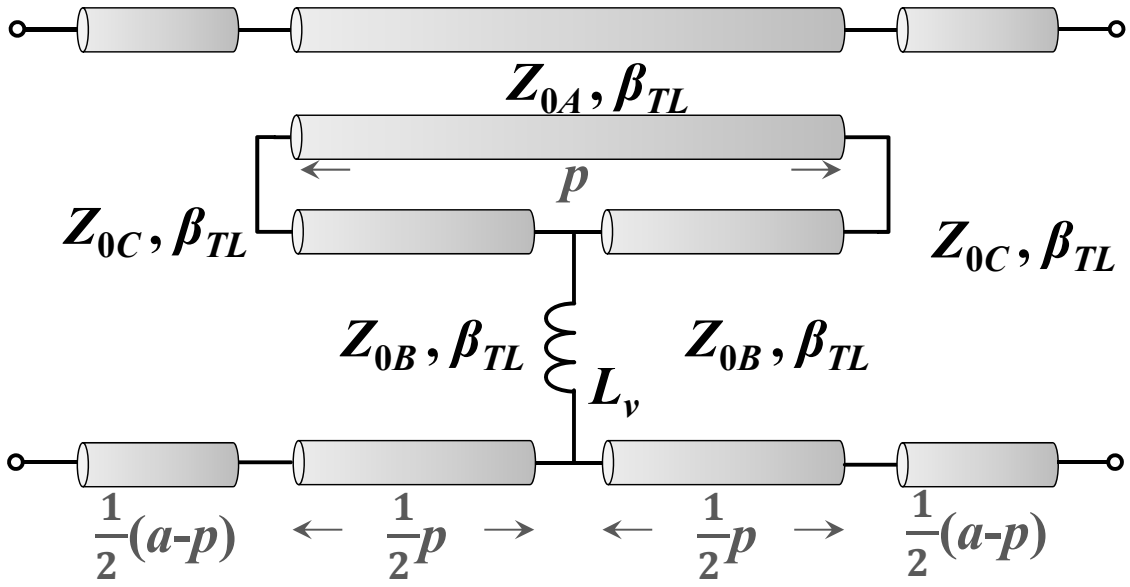

(b)

Fig. 2.9 (a) Geometry of 1-D mushroom EBG structure and (b) corresponding equivalent circuit model.

Fig. 2.9(a) shows the geometry of the one-dimensional mushroom EBG structure. The geometric parameters of the unit cell are: the length of the unit cell a, the width of the parallel plates w, the length of the patch p, the radius of the via r_v, and the separations between the patch and the top and bottom planes h_1 and h_2, respectively. The dielectric constant of the substrate is ε_r. An equivalent circuit model for the unit cell of the mushroom EBG structure is proposed as shown in Fig. 2.9(b). The equivalent circuit

Table 2.1 Physical and circuit parameters of 1-D mushroom EBG structure.

Physical Parameters		Circuit Parameters	
a = 20 (mm)	r_v = 0.15 (mm)	Z_{0A} = 1 (Ω)	L_v = 259.9 (pH)
w = 18 (mm)	h_1 = 0.1 (mm)	Z_{0B} = 5 (Ω)	
p = 18 (mm)	h_2 = 0.5 (mm)	Z_{0C} = 6 (Ω)	
ε_r = 4.4			

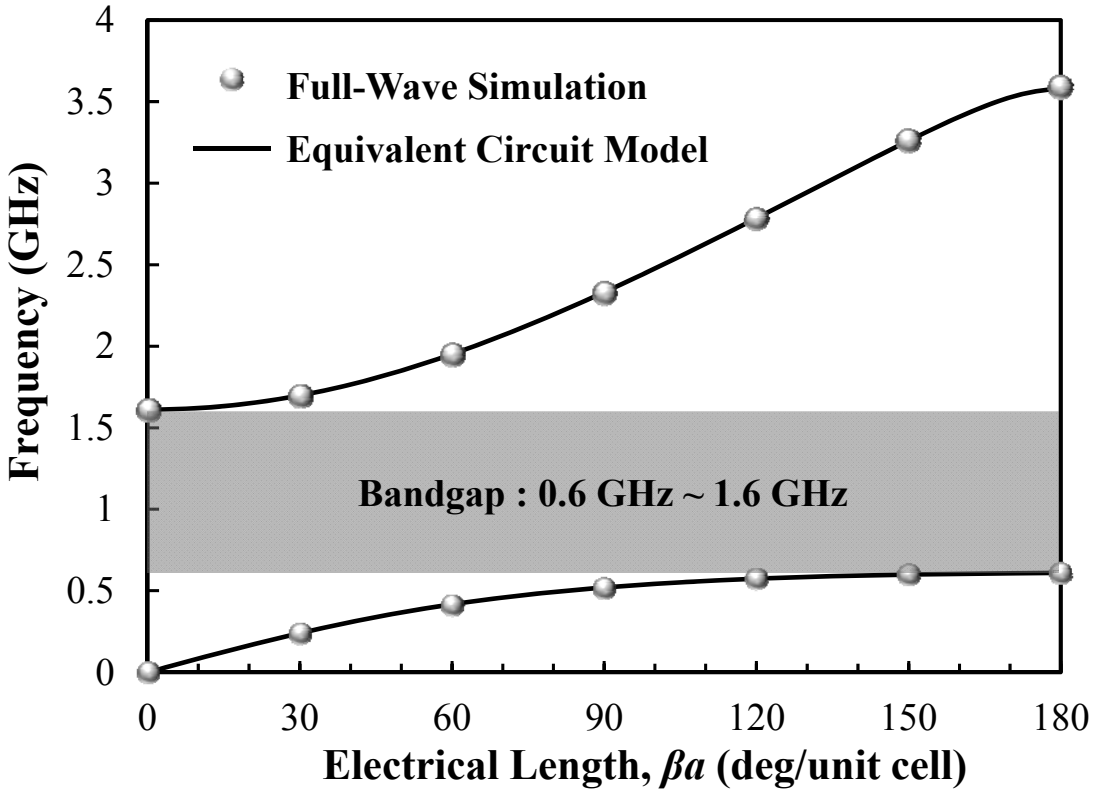

Fig. 2.10 Dispersion diagram of 1-D mushroom EBG structure from full-wave simulation and equivalent circuit model.

model is comprised of three different transmission-line sections and an inductor. Each pair of two adjacent parallel plates can be modeled by a parallel-plate transmission-line section with characteristic impedance

$$Z_0 = \frac{\eta_0}{\sqrt{\varepsilon_r}} \frac{h}{w} \tag{2.27}$$

, where η_0 is 377 Ω, h is the separation between the two plates, and w is the width of the plates.

Considering a case of physical parameters summarized in Table 2.1, we can calculate the circuit parameters, as summarized in Table 2.1, of the equivalent circuit model shown in Fig. 2.9(b), in which the characteristic impedance of the transmission lines is estimated using (2.27) and the via inductance L_v is extracted from full-wave simulation. Substituting the Z-parameters of the equivalent circuit model into (2.13), we can plot the one-dimensional dispersion diagram of the mushroom EBG structure as shown in Fig. 2.10. In order to verify the accuracy of the equivalent circuit model, the dispersion diagram calculated by full-wave simulation is also shown in Fig. 2.10. It can be seen that the results from the two methods agree well with each other. The equivalent circuit model using transmission-line sections takes the distributed effect into account and thus the accuracy can be guaranteed in the higher frequency range. The bandgap calculated by full-wave simulation is from 0.6 GHz to 1.6 GHz.

Besides the above method, solving the dispersion relation of the equivalent circuit model of the unit cell, the lower- and upper-bound cutoff frequencies can also be determined by solving the resonant frequencies of the Type-III and Type-I half resonators only. Fig. 2.11(a) shows the half circuit of the equivalent circuit model with Type-III boundary condition. The resonator can be divided into three parts, a short-circuited line with input impedance Z_{inCS}, an inductance-loaded line with input impedance Z_{inBL}, and an open-circuited line with input impedance Z_{inAO}, where

$$Z_{inCS} = jZ_{0C} \tan\left(\beta_{TL} \frac{a-p}{2}\right), \tag{2.28}$$

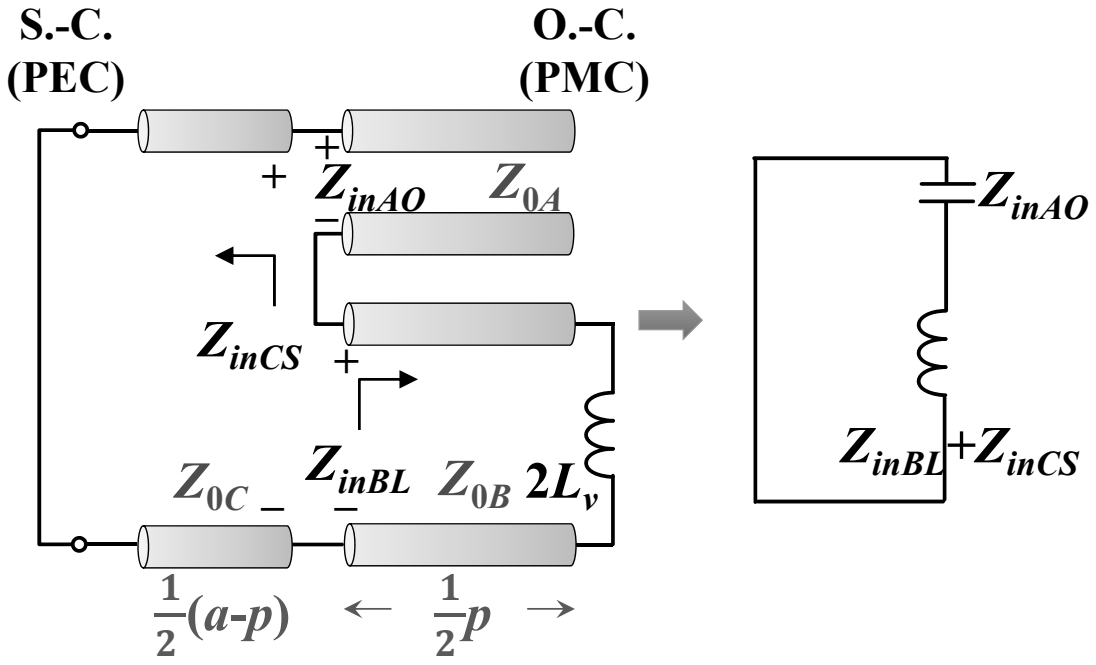

(a)

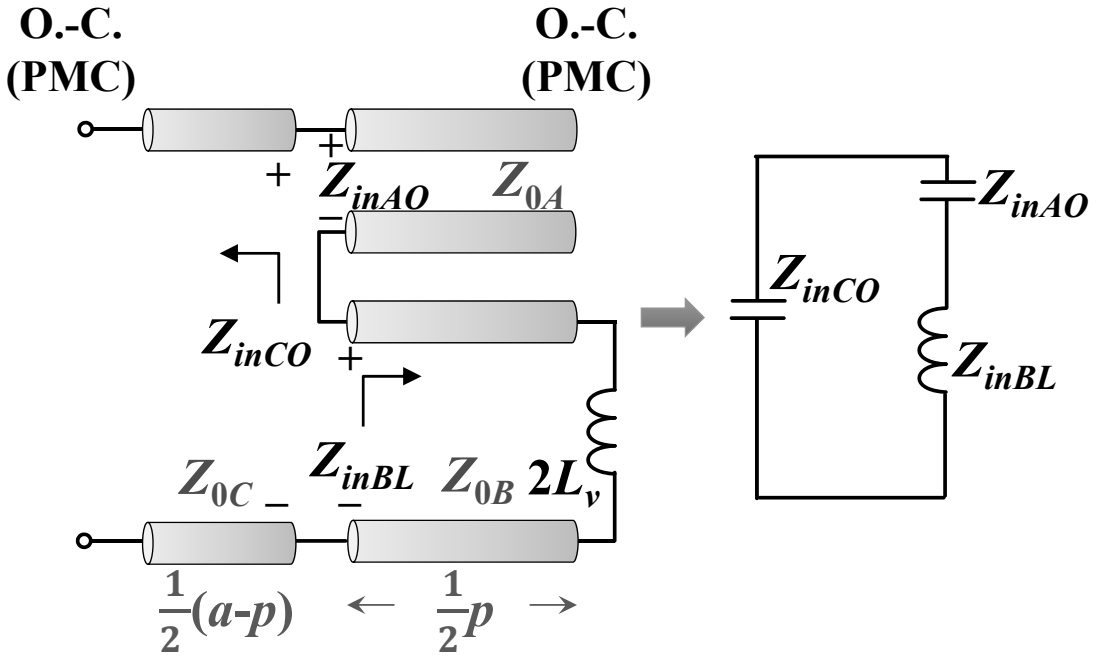

(b)

Fig. 2.11 (a) Type-III half resonator and (b) Type-I half resonator for solving lower- and upper-bound cutoff frequencies of 1-D mushroom EBG structure, respectively.

$$Z_{inBL} = j\frac{2\omega L_v + Z_{0B}\tan\left(\beta_{TL}\frac{p}{2}\right)}{1-\frac{2\omega L_v}{Z_{0B}}\tan\left(\beta_{TL}\frac{p}{2}\right)}, \tag{2.29}$$

and

$$Z_{inAO} = jZ_{0A}\cot\left(\beta_{TL}\frac{p}{2}\right). \tag{2.30}$$

Consequently, the resonant frequency must satisfy $Z_{inCS} + Z_{inBL} + Z_{inAO} = 0$, or

$$Z_{0C}\tan\left(\beta_{TL}\frac{a-p}{2}\right)+\frac{2\omega L_v + Z_{0B}\tan\left(\beta_{TL}\frac{p}{2}\right)}{1-\frac{2\omega L_v}{Z_{0B}}\tan\left(\beta_{TL}\frac{p}{2}\right)}+Z_{0A}\cot\left(\beta_{TL}\frac{p}{2}\right)=0. \tag{2.31}$$

The estimated first resonant frequency is 0.61 GHz, which agrees well with that from full-wave simulation. In this case, the series connection of Z_{inCS} and Z_{inBL} contributes the inductive impedance and the Z_{inAO} contributes the capacitive impedance. Because the impedance of the short-circuited line Z_{inCS} increases the total inductance, the Type-III half circuit has the lowest non-zero resonant frequency, which can be used to predict the lower-bound cutoff frequency. On the other hand, increasing the capacitance between power plane and patch or increasing via inductance is of benefit to lowering the cutoff frequency.

Fig. 2.11(b) shows the half circuit of the equivalent circuit model with Type-I boundary condition. The resonator can be divided into three parts, an open-circuited line with input impedance Z_{inCO}, an inductance-loaded line with input impedance Z_{inBL}, and an open-circuited line with input impedance Z_{inAO}, where

$$Z_{inCO} = jZ_{0C}\cot\left(\beta_{TL}\frac{a-p}{2}\right). \tag{2.32}$$

The resonant frequency can be decided by solving

$$Z_{0C}\cot\left(\beta_{TL}\frac{a-p}{2}\right)+\frac{2\omega L_v+Z_{0B}\tan\left(\beta_{TL}\frac{p}{2}\right)}{1-\frac{2\omega L_v}{Z_{0B}}\tan\left(\beta_{TL}\frac{p}{2}\right)}+Z_{0A}\cot\left(\beta_{TL}\frac{p}{2}\right)=0. \qquad (2.33)$$

The estimated first non-zero resonant frequency is 1.61 GHz, which agrees well with that from full-wave simulation. It is worth noting that the inductive part of the resonance is only contributed by Z_{inBL} and the capacitive part is the sum of Z_{inCO} and Z_{inAO}, which is almost dominated by Z_{inCO} because Z_{inAO} is usually much smaller than Z_{inCO}. Hence the series connection of Z_{inCO} and Z_{inAO} decreases the equivalent capacitance of the resonance and the thus resonant frequency is higher than that of Type-III half resonantor. On the other hand, increasing the capacitance between power plane and patch has little effect on the upper-bound cutoff frequency. However, the increasing via inductance will result in the lower upper-bound cutoff frequency and thus decrease the bandwidth of bandgap.

2.2 Two-Dimensional EBG Analysis

For a two-dimensional periodic structure, we propose a method to estimate its bandgap. First, we will introduce dispersion diagrams [47]. A resonant cavity model with particular boundary conditions is derived to estimate equivalent inductance for parallel-plate structures. A mushroom EBG structure is used to demonstrate the proposed equivalent circuit models and the prediction methods of the lower- and upper-bound cutoff frequencies of the bandgap.

2.2.1 Two-Dimensional Dispersion Diagram

Considering a wave propagating in a two-dimensional periodic structure, which is comprised of infinite identical unit cells distributing with two-dimensional translational

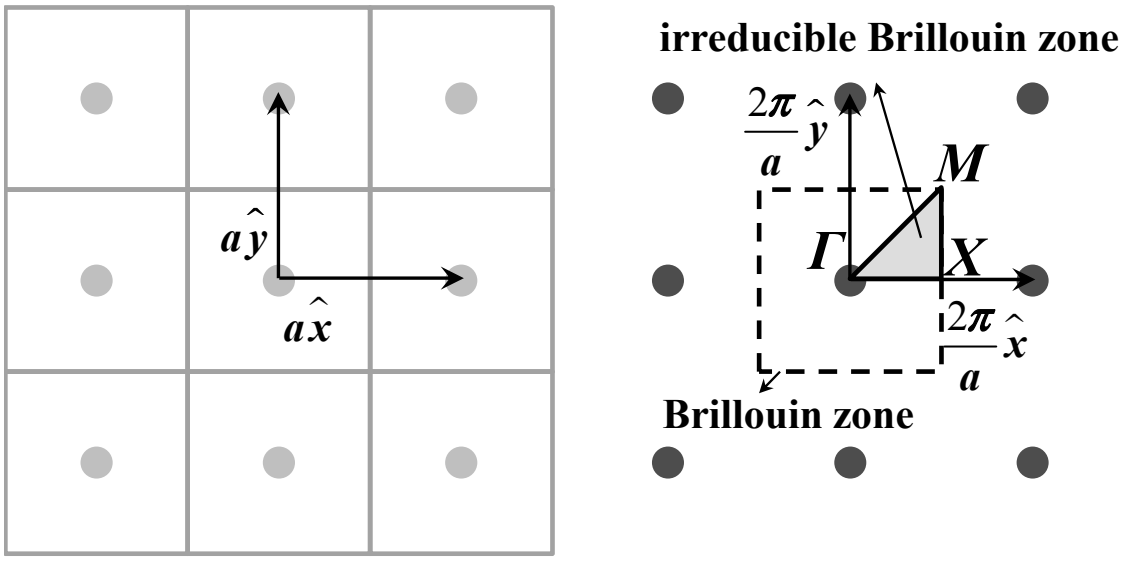

(a) (b)

Fig. 2.12 Two-dimensional periodic structure with square lattice in (a) space and (b) spectral domains.

symmetry, we find that, based on Bloch's theorem, the electrical field or magnetic field solved from Helmholtz's equation can be described by

$$\psi_k = e^{-j\vec{k}\cdot\vec{r}} u_k(\vec{r}) = e^{-j\vec{k}\cdot\vec{r}} u_k(\vec{r}+\vec{R}) \tag{2.34}$$

, where $\vec{k}$ is wave vector, $\vec{r}$ is observation point, $\vec{R}$ are lattice vectors (periodicity of unit cell in space domain), and $u_k(\vec{r})$ is a periodic function for field pattern. From (2.34), it is found that the electromagnetic modes with a wave vector $\vec{k}$ can be comprised of a plane wave modulated by a periodic function sharing the same periodicity of the lattice. Based on Bloch's theorem, different values of $\vec{k}$ may also lead to the same frequencies. For instance, a mode with wave vector $\vec{k}$ and a mode with vector $\vec{k}+\vec{G}$ are the same mode with the same frequency, if $\vec{G}$, reciprocal lattice vectors (periodicity of unit cell in spectral domain), satisfy

$$\vec{G}\cdot\vec{R} = 2\pi N \tag{2.35}$$

, where N is an integer. It is because the phase relationship between different cells, specified by the wave vector $\vec{k}$, will be incremented by $\vec{G} \cdot \vec{R}$ if the wave vector $\vec{k}$ is replaced by $\vec{k} + \vec{G}$. However, the increment of phase $2\pi N$ will not result in real phase difference at all. It implies us there are a lot of redundancies in $\vec{k}$ so that we can only focus on a finite region closest to $\vec{k} = 0$, so-called (first) Brillouin zone, in which there is no redundancy resulting from $\vec{G}$.

For example, Fig. 2.12(a) and (b) show a two-dimensional square lattice in space and spectral domain, respectively. The lattice vector is $ma\hat{x} + na\hat{y}$ and the reciprocal lattice vector is $p\frac{2\pi}{a}\hat{x} + q\frac{2\pi}{a}\hat{y}$, where m, n, p, and q are integers. The square region shown in Fig. 2.12(b) is the Brillouin zone related with the unit cell shown in Fig. 2.12(a). Furthermore, the Brillouin zone which needs to be taken into account can be reduced to a smallest region, so-called irreducible Brillouin zone, if the unit cell in space domain has other symmetries. For example, the square Brillouin zone shown in Fig. 2.12 (b) can be reduced to the triangular one because the unit cell in Fig. 2.12(a) has rotational and mirror symmetries. Three vertices of the triangle are Γ representing wave vector $(k_x, k_y) = (0, 0)$, X representing wave vector $(k_x, k_y) = (\pi/a, 0)$ and M representing wave vector $(k_x, k_y) = (\pi/a, \pi/a)$.

Based on the aforementioned, solving the Helmholtz's equation inside a corresponding irreducible Brillouin zone only is sufficient to describe the propagation behavior of electromagnetic wave in a certain two-dimensional periodic structure. In particular, in order to determine whether a bandgap exisits, only the wave vectors on the edge of the irreducible Brillouin zone should be taken into account. A dispersion diagram is usually used to illustrate the position of bandgap by plotting the solutions,

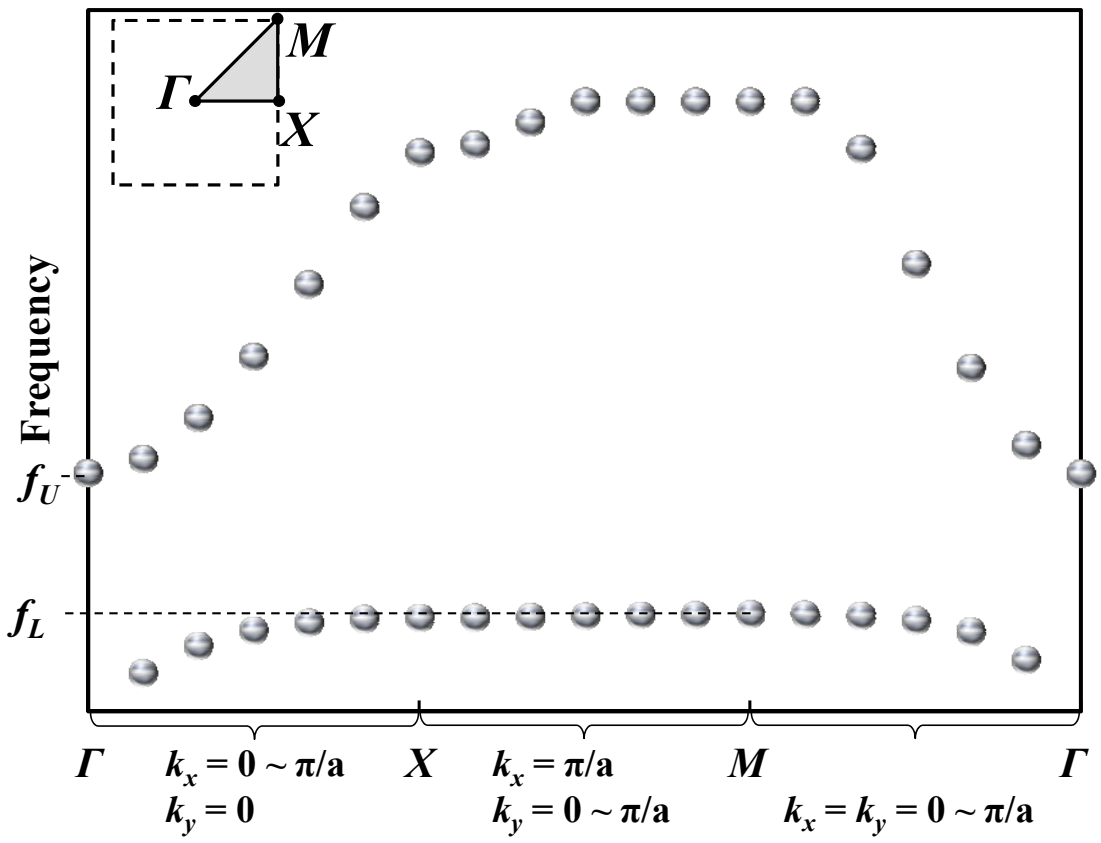

Fig. 2.13 A two-dimensional dispersion diagram.

eigenfrquencies, of the wave vectors tracing the edges of an irreducible Brillouin zone.

Fig. 2.13 shows an example of a two-dimensional dispersion diagram. The horizontal axis is divided into three sections. The first one is from Γ to X on the edge of the irreducible Brillouin zone, which means k_x is swept from 0 to π/a and k_y is kept as 0. The adjacent one is from X to M, which represents k_y is swept from 0 to π/a and k_x is kept as π/a. The last one is from M to Γ, which represents k_x and k_y are simultaneously swept from 0 to π/a. A bandgap exists, and the lower-bound cutoff frequency is located at M and upper-bound cutoff frequency is located at Γ. It will be illustrated the lower- and upper-bound cutoff frequencies can be decided by calculating the resonant frequencies of the unit cell with appropriate boundary conditions around its periphery.

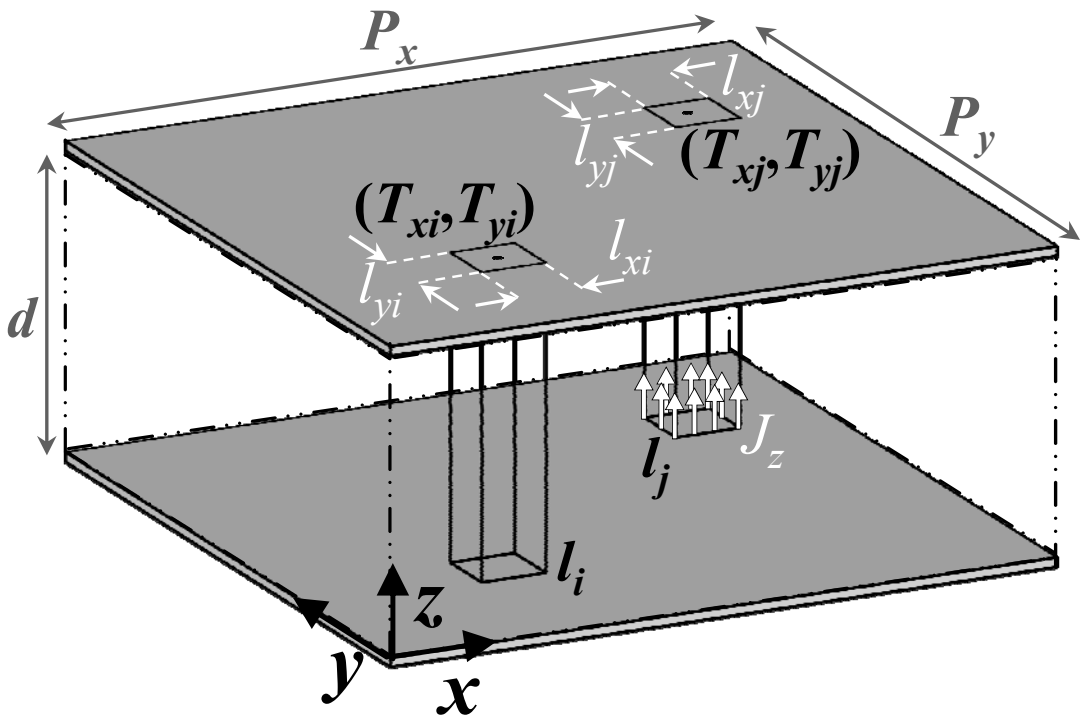

Fig. 2.14 A parallel-pate structure with a specific boundary condition.

2.2.2 Resonant Cavity Modeling

Before demonstrating how to establish an equivalent circuit model for predicting the lower- and upper-bound cutoff frequencies of the bandgap, we first derive analytic equations for estimating the equivalent inductances of parallel-plate structures with specific boundary conditions.

Fig. 2.14 shows a parallel-plate structure. A dielectric layer with relative permittivity ε_r is filled between two rectangular metal planes with side length P_x and P_y along the x- and y-direction, respectively. The normal magnetic fields and tangential electric fields are zero on the top and bottom planes because of the PEC boundaries. The separation between the two plates is d. At the frequencies of interest, the fields are uniform along the z direction because d is much smaller than the wavelength. The two

conditions support that only transverse magnetic (TM) mode, involving only H_x, H_y, and E_z, with mode number 0 to z-direction is survived in the parallel-plate structure.

As shown in Fig. 2.14, a source excitation with current density of J_z is impressed at port j along a periphery of a rectangle lj. The port j is with side length l_{xj} and l_{yj} (both l_{xj} and l_{yj} are much smaller than wavelength of interest) along the x- and y-direction, respectively, and located at (T_{xj}, T_{yj}). We are interesting in the voltage distribution excited by the current source in the parallel-plate structure with a specific boundary condition. For example, the average voltage on a port i along a periphery of a rectangle l_i is focused. The port i is with side length l_{xi} and l_{yi} (l_{xi} and l_{yi} are much smaller than wavelength of interest) along the x- and y-direction, respectively, and located at (T_{xi}, T_{yi}). Therefore, we can derive the self (input) impedance Z_{ii} and transfer impedances Z_{ij} defined as the ratio of average voltage on port i, V_i ,to total current on port j, I_j, for $i = j$ and $i \neq j$, respectively.

Such two-dimensional problem can be solved by using a resonant cavity model based on the eigenfunctions expansion of Green's function [48]-[50]. From Maxwell's equation, the target equation we want to solve is

$$\left(\nabla_T^2 + k^2\right)V = -j\omega\mu d J_z \tag{2.36}$$

, where $k = \omega\sqrt{\varepsilon_r}/c_0$ for the lossless case. (2.36) is valid inside the cavity and with a set of specific boundary condition on the four sides of the cavity. Before solving (2.36) directly, we can first consider the two-dimensional source-free Helmholtz's equation as

$$\left(\nabla_T^2 + k^2\right)\phi = 0 \tag{2.37}$$

with the same boundary condition of the original problem (2.36). In this problem, we suppose that there is a complete set of ϕ_{mn} and corresponding k_{mn} which satisfy

$$\nabla_T^2\phi_{mn} = -k_{mn}^2\phi_{mn}. \tag{2.38}$$

Substituting (2.38) in to (2.37), we get

$$\left(\nabla_T^2 + k^2\right)\phi_{mn} = -\left(k_{mn}^2 - k^2\right)\phi_{mn}. \tag{2.39}$$

Consequently, the green's function $G(x_i, y_i, x_j, y_j)$ of the original problem, which is defined as the solution of

$$\left(\nabla_T^2 + k^2\right)G(x_i, y_i, x_j, y_j) = -\delta\left(x - x_j, y - y_j\right) \tag{2.40}$$

with the same boundary condition of the original problem, can be expanded by the set of eigenfunctions and eigenvalues as

$$G(x_i, y_i, x_j, y_j) = \sum_m^\infty \sum_n^\infty \frac{\phi_{mn}(x_i, y_i)\phi_{mn}(x_j, y_j)}{k_{mn}^2 - k^2}. \tag{2.41}$$

Based on the concept of superposition, the solution of the original problem (2.36) is derived as

$$\begin{aligned} V &= \int_{l_j} G(x_i, y_i, x_j, y_j)\, j\omega\mu dJ_z dl_j \\ &= \int_{l_j} \sum_m^\infty \sum_n^\infty \frac{\phi_{mn}(x_i, y_i)\phi_{mn}(x_j, y_j)}{k_{mn}^2 - k^2} j\omega\mu dJ_z dl_j. \end{aligned} \tag{2.42}$$

The average voltage on port i can be derived by integrating the voltage along l_i and divided by the circumference as

$$V_i = \frac{1}{2(l_{xi} + l_{yi})} \int_{l_i}\int_{l_j} \sum_m^\infty \sum_n^\infty \frac{\phi_{mn}(x_i, y_i)\phi_{mn}(x_j, y_j)}{k_{mn}^2 - k^2} j\omega\mu dJ_z dl_i dl_j. \tag{2.43}$$

Dividing V_i in (2.43) by the total current $I_j = 2J_z\left(l_{xj} + l_{yj}\right)$, we can acquire the transfer impedance Z_{ij} as

$$Z_{ij} = \frac{j\omega\mu d}{4(l_{xi} + l_{yi})(l_{xj} + l_{yj})} \sum_m^\infty \sum_n^\infty \frac{1}{k_{mn}^2 - k^2} \int_{l_i}\int_{l_j} \phi_{mn}(x_i, y_i)\phi_{mn}(x_j, y_j) dl_i dl_j \tag{2.44}$$

and the self impedance Z_{ii} for $i = j$ as

$$Z_{ii} = \frac{j\omega\mu d}{4(l_{xi} + l_{yi})^2} \sum_m^\infty \sum_n^\infty \frac{1}{k_{mn}^2 - k^2} \left[\int_{l_i} \phi_{mn}(x_i, y_i) dl_i\right]^2. \tag{2.45}$$

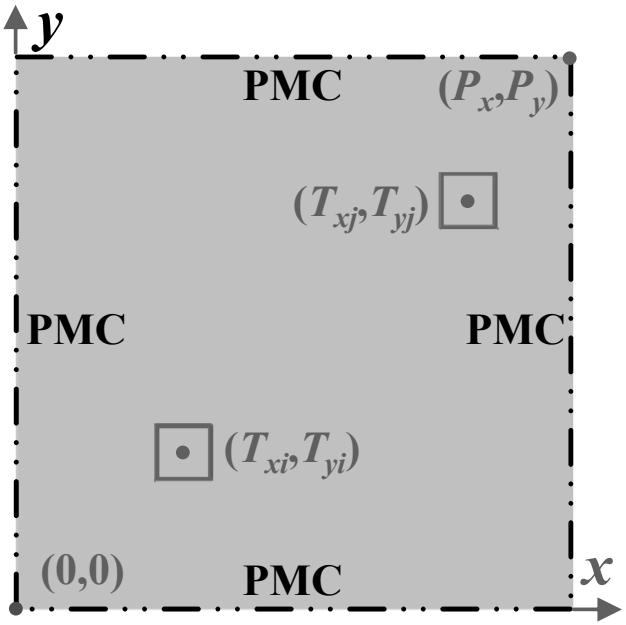

Fig. 2.15 A parallel-plate structure with four PMC side walls around its periphery.

Using (2.44) and (2.45) we can calculate the transfer and self impedance, respectively, of the parallel-plate structure with different boundary conditions. First, we start from (2.37) and consider the boundary conditions around the periphery of the cavity are all PMC walls, which is shown in Fig. 2.15. The boundary condition for ϕ, *z*-directed electrical field or voltage, can be expressed as

$$\begin{aligned}
&\frac{\partial\phi(x,0)}{\partial y}=0 \qquad \text{for } 0\le x\le P_x,\\
&\frac{\partial\phi(x,P_y)}{\partial y}=0 \qquad \text{for } 0\le x\le P_x,\\
&\frac{\partial\phi(0,y)}{\partial x}=0 \qquad \text{for } 0\le y\le P_y,\\
&\frac{\partial\phi(P_x,y)}{\partial x}=0 \qquad \text{for } 0\le y\le P_y.
\end{aligned} \tag{2.46}$$

From the above boundary condition, the eigenfunctions are given by

$$\phi_{mn}=\frac{C_mC_n}{\sqrt{P_xP_y}}\cos(k_mx)\cos(k_ny) \tag{2.47}$$

, where $k_m = \frac{m\pi}{P_x}$, $k_n = \frac{n\pi}{P_y}$ with m and n are mode numbers from zero to infinite (integers), $C_{m,n} = 1$ if $m,n = 0$, and $C_{m,n} = \sqrt{2}$ if $m,n \neq 0$. Substituting (2.47) into (2.45), we derive the self impedance Z_{ii} as

$$Z_{ii} = \frac{j\omega\mu d}{4(l_{xi}+l_{yi})^2}\sum_{m=0}^{\infty}\sum_{n=0}^{\infty}\frac{C_m^2 C_n^2}{P_x P_y (k_{mn}^2 - k^2)}\left[\int_{l_i}\cos(k_m x_i)\cos(k_n y_i)dl_i\right]^2. \quad (2.48)$$

, where $k_{mn}^2 = k_m^2 + k_n^2$. The integration in (2.48) can be calculated as [51]

$$\begin{aligned}\int_{l_i}\cos(k_m x_i)\cos(k_n y_i)dl_i &= 2\cos(k_m T_{xi})\cos(k_n T_{yi})\times \\ &(l_{xi}\mathrm{sinc}(k_m\frac{l_{xi}}{2})\cos(k_n\frac{l_{yi}}{2}) + l_{yi}\cos(k_m\frac{l_{xi}}{2})\mathrm{sinc}(k_n\frac{l_{yi}}{2})) \quad (2.49)\\ &= 2 f_{BC}(T_{xi},T_{yi}) f_P(l_{xi},l_{yi}).\end{aligned}$$

, where f_{BC} associated with the boundary condition of the cavity is a function of port location and f_p related to the port geometry is a function of port side length. They are expressed as

$$f_{BC}(T_{xi},T_{yi}) = \cos(k_m T_{xi})\cos(k_n T_{yi}) \quad (2.50)$$

and
$$f_P(l_{xi},l_{yi}) = l_{xi}\mathrm{sinc}(k_m\frac{l_{xi}}{2})\cos(k_n\frac{l_{yi}}{2}) + l_{yi}\cos(k_m\frac{l_{xi}}{2})\mathrm{sinc}(k_n\frac{l_{yi}}{2}). \quad (2.51)$$

Combing (2.48)-(2.51), the self impedance Z_{ii} is derived as

$$Z_{ii} = \frac{j\omega\mu d}{(l_{xi}+l_{yi})^2}\sum_{m=0}^{\infty}\sum_{n=0}^{\infty}\frac{C_m^2 C_n^2}{P_x P_y (k_{mn}^2 - k^2)}\left[f_{BC}(T_{xi},T_{yi})\times f_P(l_{xi},l_{yi})\right]^2 \quad (2.52)$$

Similarly, the transfer impedance can be derived as

$$\begin{aligned}Z_{ij} = &\frac{j\omega\mu d}{(l_{xi}+l_{yi})(l_{xj}+l_{yj})}\sum_{m=0}^{\infty}\sum_{n=0}^{\infty}\frac{C_m^2 C_n^2}{P_x P_y (k_{mn}^2 - k^2)}\times \\ &f_{BC}(T_{xi},T_{yi})\times f_P(l_{xi},l_{yi})\times f_{BC}(T_{xj},T_{yj})\times f_P(l_{xj},l_{yj}).\end{aligned} \quad (2.53)$$

(2.52) can be calculated by summing a double infinite series and rewritten in an equivalent circuit form. We can rewrite (2.52) as

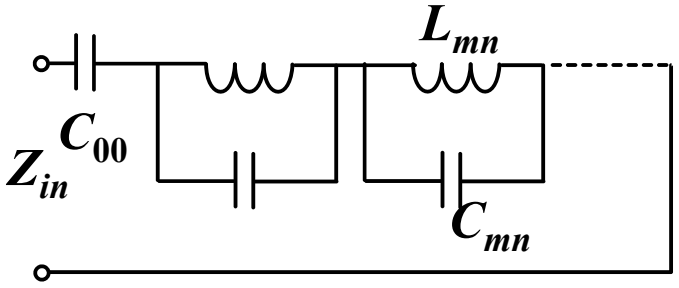

Fig. 2.16 A circuit representation of cavity model with four PMC side walls.

$$Z_{ii} = \frac{1}{j\omega\varepsilon\dfrac{P_x P_y}{d}} + \sum_{m=0}^{\infty}\sum_{n=0}^{\infty} \left. \frac{j\omega\mu d C_m^2 C_n^2 \left[f_{BC}(T_{xi}, T_{yi}) \times f_P(l_{xi}, l_{yi}) \right]^2}{(l_{xi} + l_{yi})^2 P_x P_y (k_{mn}^2 - k^2)} \right|_{(m,n)\neq(0,0)} \tag{2.54}$$

and give each term in (2.54) an equivalent circuit element as

$$\begin{aligned} Z_{ii} &= \frac{1}{j\omega\varepsilon\dfrac{P_x P_y}{d}} + \sum_{m=0}^{\infty}\sum_{n=0}^{\infty} \frac{j\omega}{1-\omega^2\mu\varepsilon/k_{mn}^2} \left. \frac{\mu d C_m^2 C_n^2 \left[f_{BC} \times f_P \right]^2}{(l_{xi} + l_{yi})^2 P_x P_y k_{mn}^2} \right|_{(m,n)\neq(0,0)} \\ &= \frac{1}{j\omega C_{00}} + \sum_{m=0}^{\infty}\sum_{n=0}^{\infty} \left. \frac{j\omega L_{mn}}{1-\omega^2 L_{mn} C_{mn}} \right|_{(m,n)\neq(0,0)} \end{aligned} \tag{2.55}$$

, where

$$\begin{aligned} L_{mn} &= \left. \frac{\mu d C_m^2 C_n^2 \left[f_{BC}(T_{xi}, T_{yi}) \times f_P(l_{xi}, l_{yi}) \right]^2}{(l_{xi} + l_{yi})^2 P_x P_y k_{mn}^2} \right|_{(m,n)\neq(0,0)}, \\ C_{mn} &= \left. \frac{\varepsilon (l_{xi} + l_{yi})^2 P_x P_y}{d C_m^2 C_n^2 \left[f_{BC}(T_{xi}, T_{yi}) \times f_P(l_{xi}, l_{yi}) \right]^2} \right|_{(m,n)\neq(0,0)}, \\ C_{00} &= \varepsilon \frac{P_x P_y}{d}. \end{aligned} \tag{2.56}$$

Fig. 2.16 shows the an equivalent circuit representation of (2.55). It can be found that each term in the series summation represents a resonant eigenmode of the cavity. The first term with wave number (m,n) = (0,0) refer to the static capacitance resulting from the parallel plates pair. Except the term of (m,n) = (0,0), each term for a given (m,n) can

be related to the impedance of the TM$_{mn}$ mode and modeled by an LC parallel tank of which resonant frequency is the same as that of the TM$_{mn}$ mode. The impedance is with inductive or capacitive contributions when the frequency is, respectively, below or above the cutoff frequency determined by

$$f_{mn} = \frac{c_0}{2\pi\sqrt{\varepsilon_r}}\sqrt{(\frac{m\pi}{P_x})^2 + (\frac{n\pi}{P_y})^2}. \tag{2.57}$$

Based on the equivalent circuit model, it is found that each term contributes inductive impedance if the frequency is below the first cutoff frequency, f_{10} or f_{01}. Especially, for the low frequency approximation, (2.55) can be approximated by [52]

$$\begin{aligned} Z_{ii} &\approx \frac{1}{j\omega\varepsilon\frac{P_x P_y}{d}} + \sum_{m=0}^{\infty}\sum_{n=0}^{\infty} j\omega \frac{\mu d C_m^2 C_n^2 \left[f_{BC}(T_{xi}, T_{yi}) \times f_P(l_{xi}, l_{yi}) \right]^2}{(l_{xi}+l_{yi})^2 P_x P_y k_{mn}^2}\Bigg|_{(m,n)\neq(0,0)} \\ &= \frac{1}{j\omega C_{00}} + j\omega L_{eq} \end{aligned} \tag{2.58}$$

, where

$$L_{eq} = \sum_{m=0}^{\infty}\sum_{n=0}^{\infty} \frac{\mu d C_m^2 C_n^2 \left[f_{BC}(T_{xi}, T_{yi}) \times f_P(l_{xi}, l_{yi}) \right]^2}{(l_{xi}+l_{yi})^2 P_x P_y k_{mn}^2}\Bigg|_{(m,n)\neq(0,0)} \tag{2.59}$$

According to (2.58) and (2.59), it is shown that inductive contributions are approximated as an inductance L_{eq} which is independent on frequency. The input impedance is thus modeled by a series connection of the inductance L_{eq} and capacitance C_{00}. The approximation can be figured out by substituting the condition $k_{mn}^2 - k^2 \approx k_{mn}^2$ into (2.54) or ignoring the capacitance terms C_{mn} in (2.55) shown in Fig. 2.16.

Fig. 2.17 shows a parallel-plate structure with a via connecting with the bottom plane. 4 PMC walls surround around the structure periphery. There is an opening (antipad) on the top plane to separate the top plane from the via. It is assumed that the induced voltage is cross the antipad and the impressed current flows through the via periphery. The input impedance of such structure can be calculated by (2.52) and

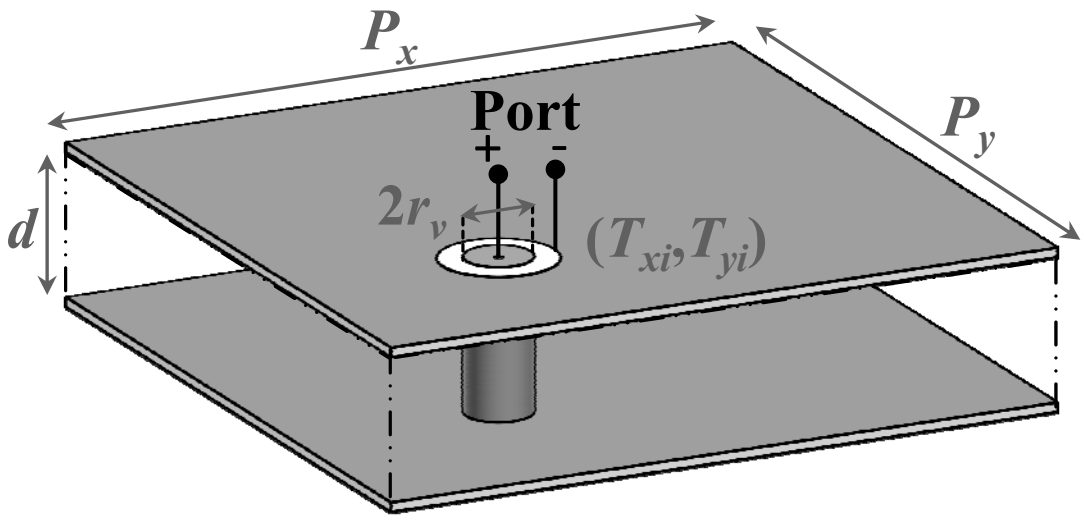

Fig. 2.17 A parallel-plate structure with a via connecting with the bottom plane.

approximated by (2.58). The geometrical parameters are $P_x = P_y = 10$ mm, $d = 0.73$ mm, and $r_v = 0.1$ mm. The equivalent side length of the port is assumed by a square with the same circumference of the cylindrical via:

$$l_{xi} = l_{yi} = \frac{\pi r_v}{2}. \tag{2.60}$$

Three cases for the port located at $T_{xi} = T_{yi} = \frac{1}{8}P_x$, $T_{xi} = T_{yi} = \frac{1}{4}P_x$, and $T_{xi} = T_{yi} = \frac{1}{2}P_x$ are calculated by full wave simulation, by (2.52), and by (2.58). Fig. 2.18(a) shows the comparison between the results by full-wave simulation and (2.52). Fig. 2.18(b) shows the ccomparison between the results by full-wave simulation and (2.58). From Fig. 2.18(a), the first resonance of the parallel-plate structure is TM_{10} or TM_{01} mode at 7.15 GHz as estimated by (2.57). The calculated results using resonant cavity model method agree well with those from full-wave simulation.

It is worth noting that the behavior of the parallel-plate structure can be considered as that of a *LC* series connection before the first TM_{10} or TM_{01} mode. There is a resonance with zero impedance contributed by the parallel-plate capacitance C_{00}

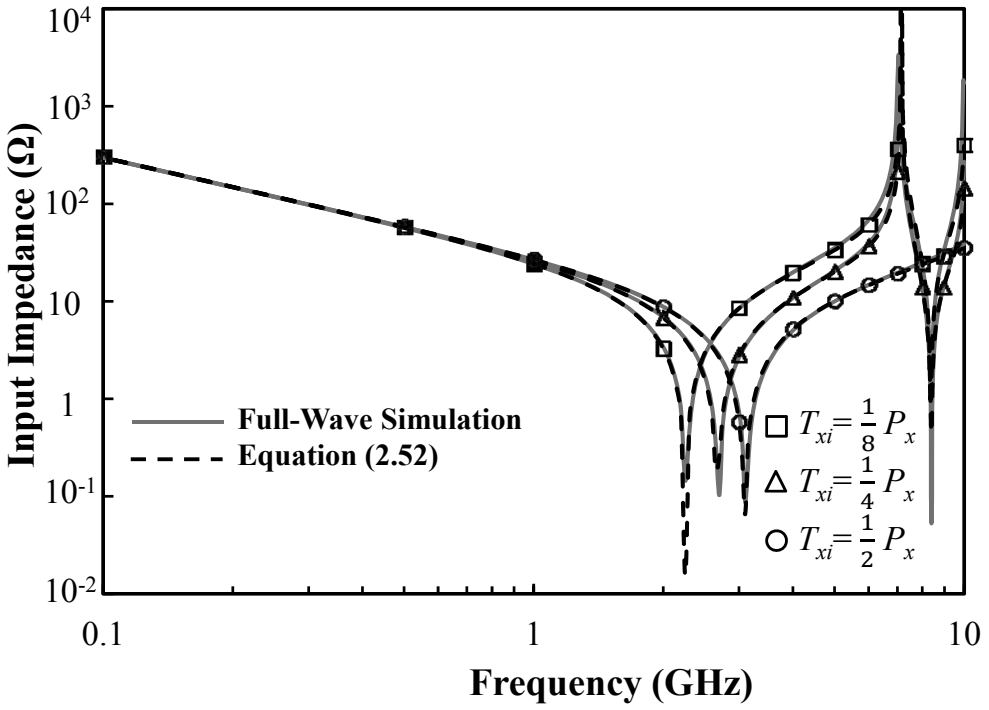

(a)

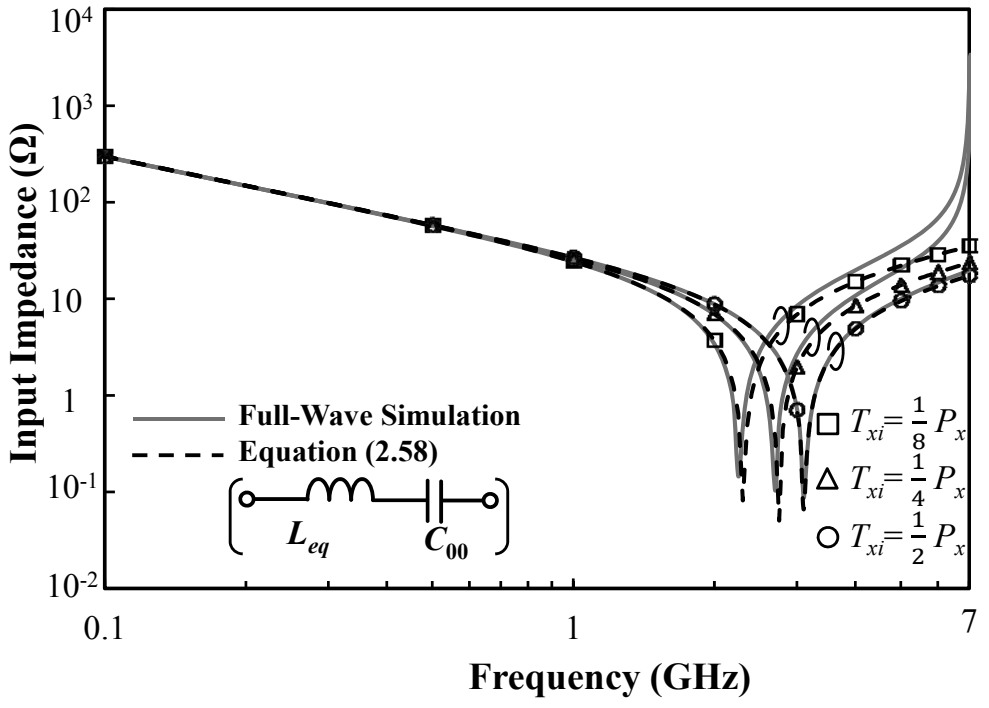

(b)

Fig. 2.18 Input impedance of parallel-plate structure shown in Fig. 2.17 (a) calculated by full-wave simulation and (2.52) and (b) approximated by (2.58).

connecting with the via-plate inductance, L_{eq} in series. For $T_{xi} = T_{yi} = \frac{1}{8}P_x$, $T_{xi} = T_{yi} = \frac{1}{4}P_x$, and $T_{xi} = T_{yi} = \frac{1}{2}P_x$, they are at 2.26 GHz, 2.69 GHz, and 3.11 GHz, respectively. Except near the resonant frequency of TM mode, the behavior can be characterized well by (2.58) and the zero frequency can be estimated as $\frac{1}{2\pi\sqrt{C_{00}L_{eq}}}$ as shown in Fig. 2.18(b). In this case, C_{00} is 5.329 pF and L_{eq} are 892.8 pH, 631.4 pH, and 491.2 pH for $T_{xi} = T_{yi} = \frac{1}{8}P_x$, $T_{xi} = T_{yi} = \frac{1}{4}P_x$, and $T_{xi} = T_{yi} = \frac{1}{2}P_x$, respectively. It is worth noting that the equivalent inductance L_{eq} increases when the via is moving away from the center of the plane because of the crowded current distribution.

Another case of the parallel-plate structure surrounded by 4 PEC walls is considered as shown in Fig. 2.19. The boundary condition can be expressed as

$$\begin{aligned} &\phi(x,0) = 0 \quad \text{for } 0 \le x \le P_x, \\ &\phi(x,P_y) = 0 \quad \text{for } 0 \le x \le P_x, \\ &\phi(0,y) = 0 \quad \text{for } 0 \le y \le P_y, \\ &\phi(P_x,y) = 0 \quad \text{for } 0 \le y \le P_y. \end{aligned} \tag{2.61}$$

From the above boundary condition, the eigenfunctions are given by

$$\phi_{mn} = \frac{C_m C_n}{\sqrt{P_x P_y}} \sin(k_m x) \sin(k_n y) \tag{2.62}$$

, where $k_m = \frac{m\pi}{P_x}$, $k_n = \frac{n\pi}{P_y}$, m and n are mode numbers (integers), and $C_m = C_n = \sqrt{2}$.

In this case, neither m nor n can be zero. Both of them are from one to infinite. By combing (2.41), (2.44), and (2.45), the transfer impedance Z_{ij} is derived as

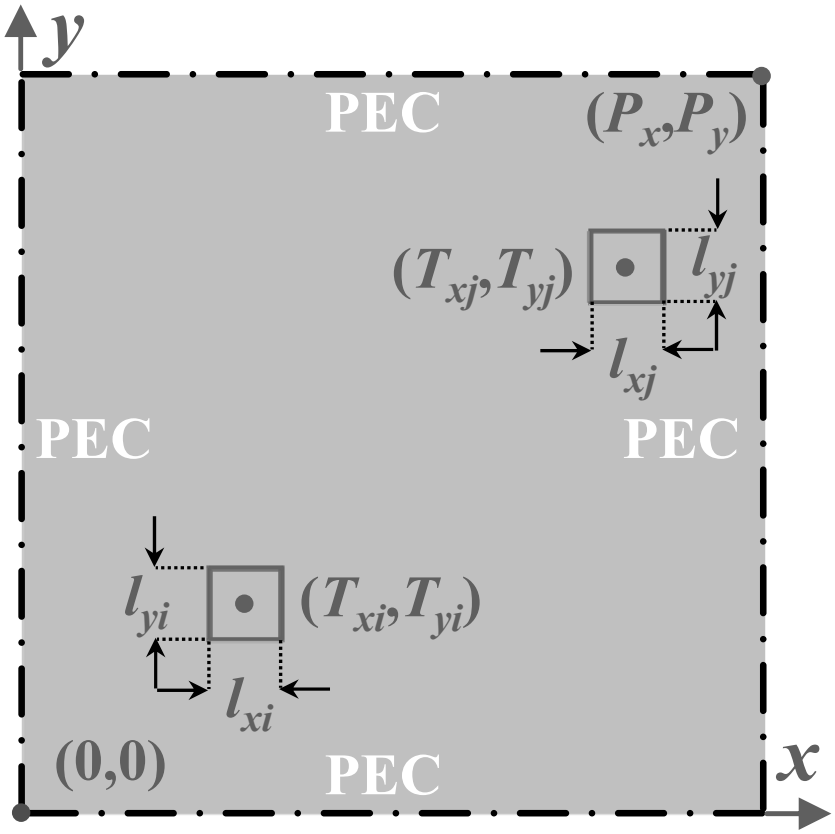

Fig. 2.19 Parallel-plate structure with 4 PEC walls around its periphery.

$$Z_{ij} = \frac{j\omega\mu d}{(l_{xi}+l_{yi})(l_{xj}+l_{yj})}\sum_{m=1}^{\infty}\sum_{n=1}^{\infty}\frac{C_m^2 C_n^2}{P_x P_y (k_{mn}^2 - k^2)}\times \\ f_{BC}(T_{xi},T_{yi})\times f_P(l_{xi},l_{yi})\times f_{BC}(T_{xj},T_{yj})\times f_P(l_{xj},l_{yj}) \tag{2.63}$$

, where

$$f_{BC}(T_{xi},T_{yi}) = \sin(k_m T_{xi})\sin(k_n T_{yi}) \tag{2.64}$$

and $$f_P(l_{xi},l_{yi}) = l_{xi}\text{sinc}(k_m \frac{l_{xi}}{2})\cos(k_n \frac{l_{yi}}{2}) + l_{yi}\cos(k_m \frac{l_{xi}}{2})\text{sinc}(k_n \frac{l_{yi}}{2}). \tag{2.65}$$

Similarly, the self impedance can be derived as

$$Z_{ii} = \frac{j\omega\mu d}{(l_{xi}+l_{yi})^2}\sum_{m=1}^{\infty}\sum_{n=1}^{\infty}\frac{C_m^2 C_n^2}{P_x P_y (k_{mn}^2 - k^2)}\left[f_{BC}(T_{xi},T_{yi})\times f_P(l_{xi},l_{yi})\right]^2 \tag{2.66}$$

and approximated as

$$Z_{ii} \approx \sum_{m=1}^{\infty}\sum_{n=1}^{\infty} j\omega \frac{\mu d C_m^2 C_n^2 \left[f_{BC}(T_{xi}, T_{yi}) \times f_P(l_{xi}, l_{yi}) \right]^2}{(l_{xi} + l_{yi})^2 P_x P_y k_{mn}^2} \\ = j\omega L_{eq} \tag{2.67}$$

, where

$$L_{eq} = \sum_{m=1}^{\infty}\sum_{n=1}^{\infty} \frac{\mu d C_m^2 C_n^2 \left[f_{BC}(T_{xi}, T_{yi}) \times f_P(l_{xi}, l_{yi}) \right]^2}{(l_{xi} + l_{yi})^2 P_x P_y k_{mn}^2} \tag{2.68}$$

The parallel-plate structure shown in Fig. 2.17 with 4 PEC walls is taken as an example to verify the accuracy of the close-form equation (2.66). The geometrical parameters are $P_x = P_y = 10$ mm, $d = 0.73$ mm, and $r_v = 0.1$ mm. Three cases for the port located at $T_{xi} = T_{yi} = \frac{1}{8} P_x$, $T_{xi} = T_{yi} = \frac{1}{4} P_x$, and $T_{xi} = T_{yi} = \frac{1}{2} P_x$ are calculated by full-wave simulation, by (2.66), and by (2.67). Fig. 2.20(a) shows the comparison of the results from full-wave simulation and (2.66). Fig. 2.20 (b) shows the comparison of the results from full-wave simulation and (2.67). From Fig. 2.20(a), it is shown the there is a resonant behavior near 10.01 GHz, the resonant frequency of the TM_{11} mode.

Below 10.01 GHz, the impedance is an inductive profile contributed by the via-plate inductance L_{eq}, which can be estimated by (2.68) as shown in Fig. 2.20(b). The inductive impedance results from the impressed current flowing through top plane, 4 PEC walls, bottom plane, and returning to the via. The pattern of the current loop with two-dimensional distribution on the planes can be characterized by the inductance L_{eq} below the first resonant frequency of the TM mode. The inductance L_{eq} are 429.3, 530.0, and 592.3 pH for $T_{xi} = T_{yi} = \frac{1}{8} P_x$, $T_{xi} = T_{yi} = \frac{1}{4} P_x$, and $T_{xi} = T_{yi} = \frac{1}{2} P_x$, respectively. The inductance L_{eq} depends on the location of the via and decreases when the via is near to the plane periphery. It is because the dominated current loop becomes small if the via becomes close to the 4 PEC walls.

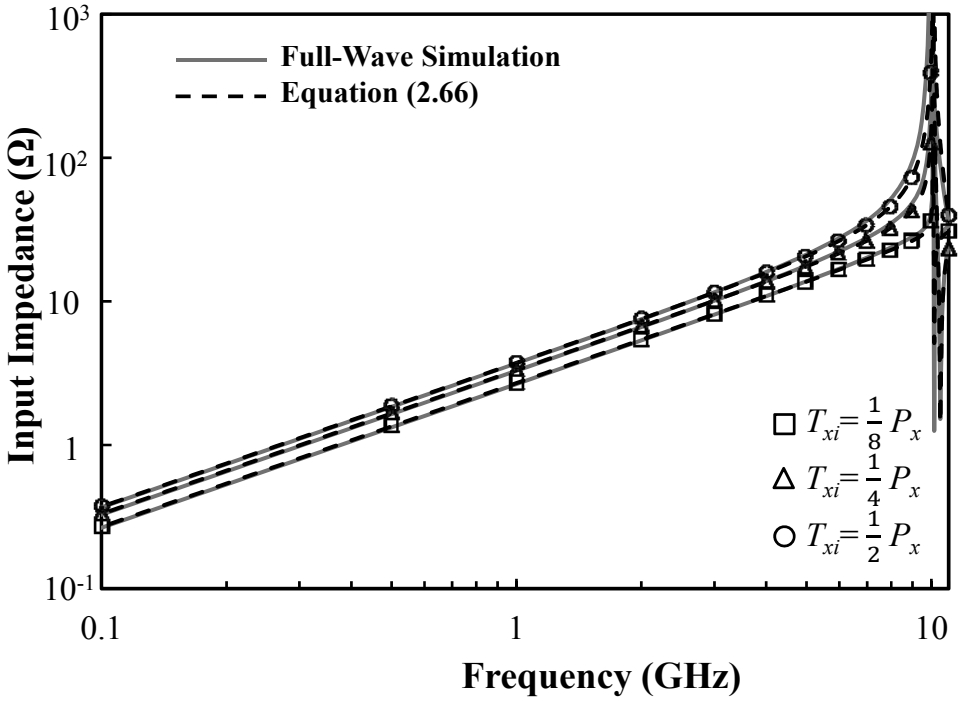

(a)

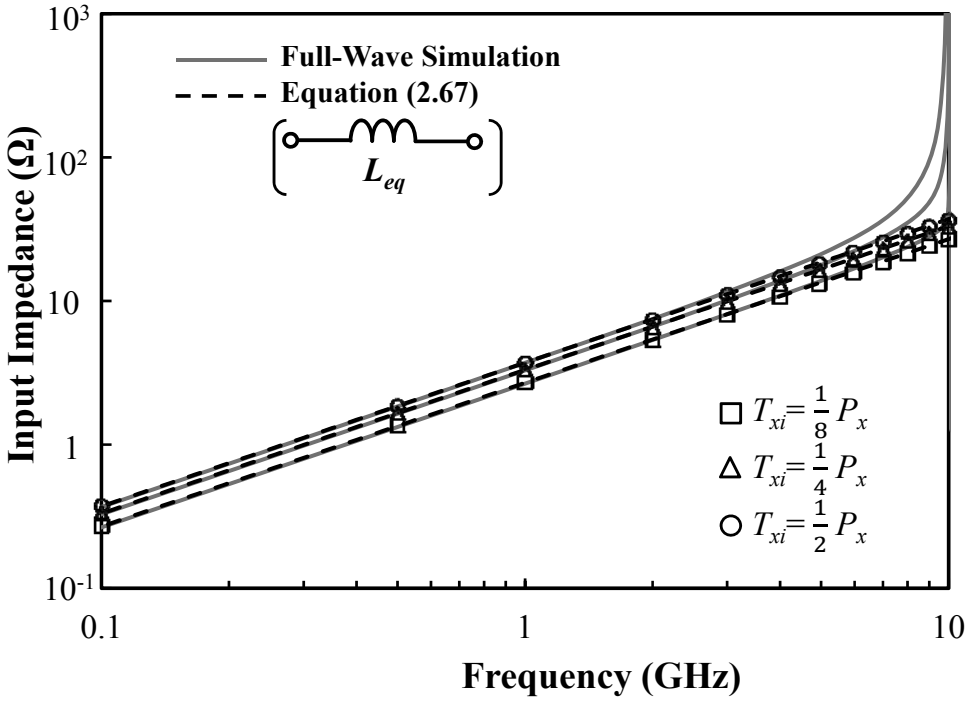

(b)

Fig. 2.20 Input impedance of parallel-plate structure shown in Fig. 2.19 (a) calculated by full-wave simulation and (2.66) and (b) approximated by (2.67).

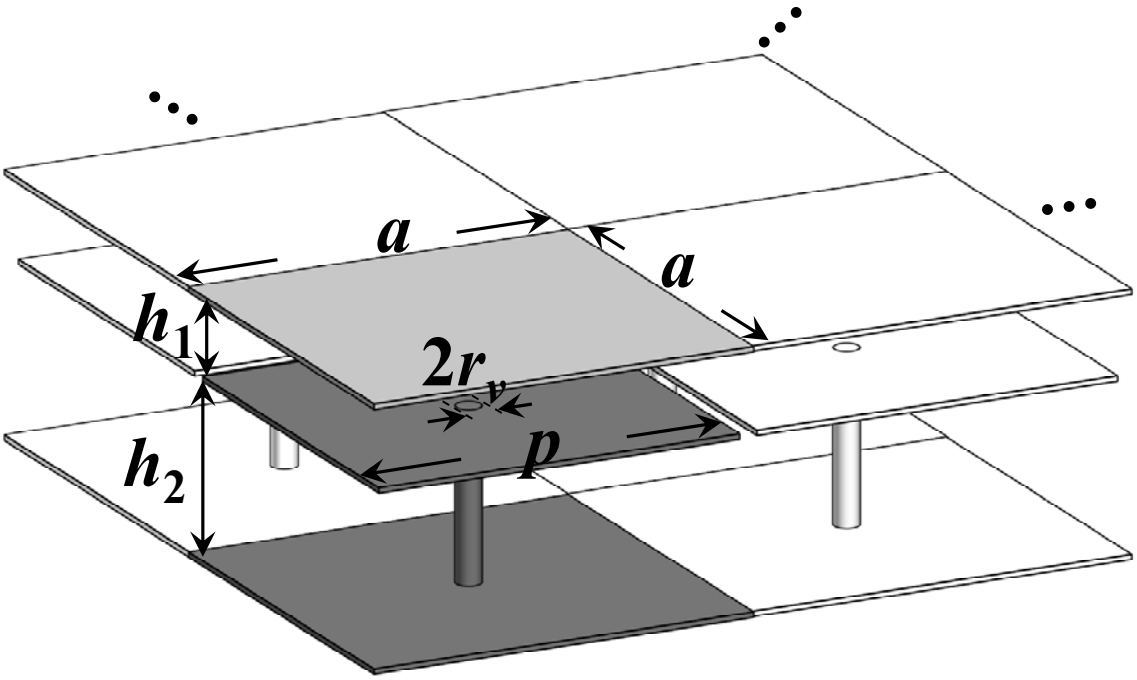

(a)

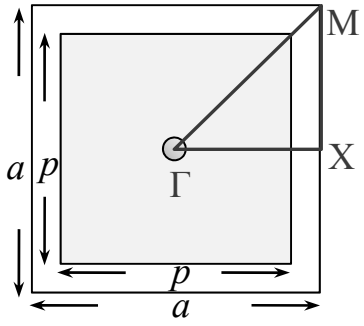

(b)

Fig. 2.21 (a) Unit cell of two-dimensional mushroom EBG structure and (b) its top view.

2.2.3 Two-Dimensional Mushroom EBG Structure

Fig. 2.21(a) shows the unit cell of two-dimensional mushroom EBG structure and its top view is shown in Fig. 2.21(b). The side length of the unit cell is a. The side length of the embedded patch is p. The separation between the top plane and embedded patch is h_1. There is a via with radius r_v connecting the bottom plane and embedded

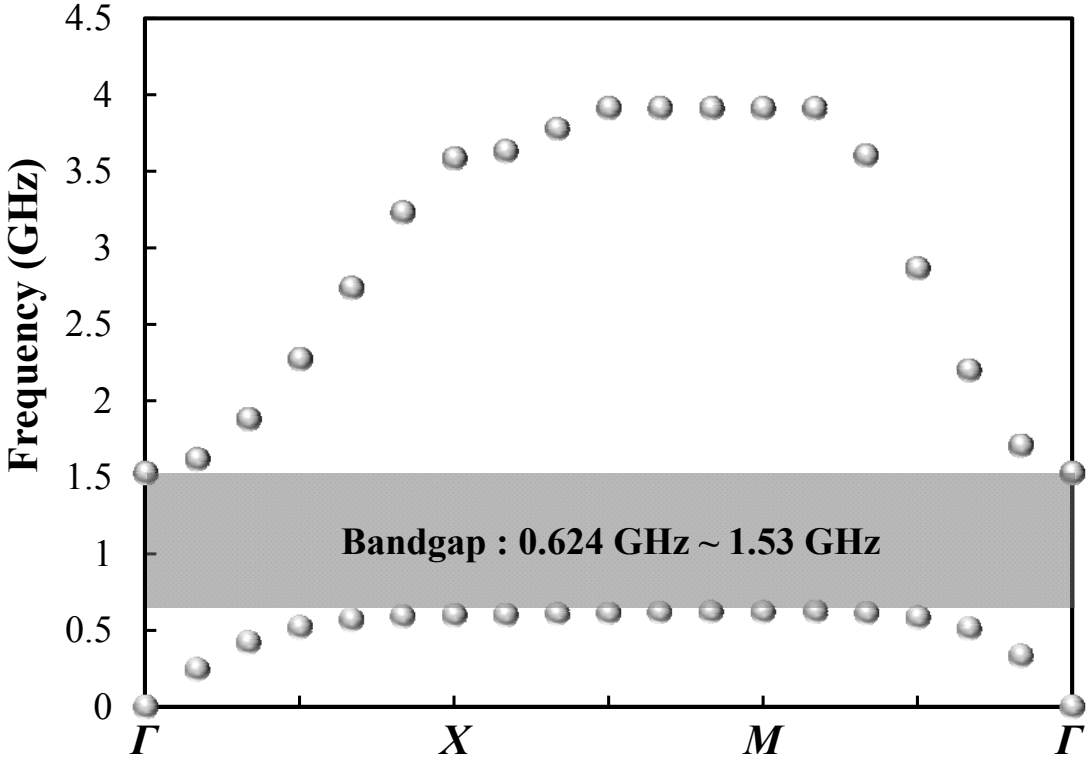

Fig. 2.22 Dispersion diagram of 2-D mushroom EBG structure.

patch. The separation between the patch and bottom plane is h_2.

Fig. 2.22 shows a dispersion diagram of the mushroom two-dimensional EBG structure. It is simulated by using full-wave simulator. The geometrical parameters are (a, p, r_v, h_1, h_2) = (20 mm, 18 mm, 0.15 mm, 0.1 mm, 0.5 mm). The dielectric constant of the substrate is ε_r = 4.4. There is a bandgap from 0.624 GHz to 1.53 GHz. The lower-bound cutoff frequency is decided by the frequency corresponding to the first mode at M point and the upper-bound cutoff frequency is determined by the frequency relating to the second mode at Γ point.

As discussed in section 2.2.1, the modes at M point represent the wave with wave vector π/a in both x- and y-direction. The phase difference of the wave between alternate cells is π. It implies the field patterns distributing in adjacent cells are with the same

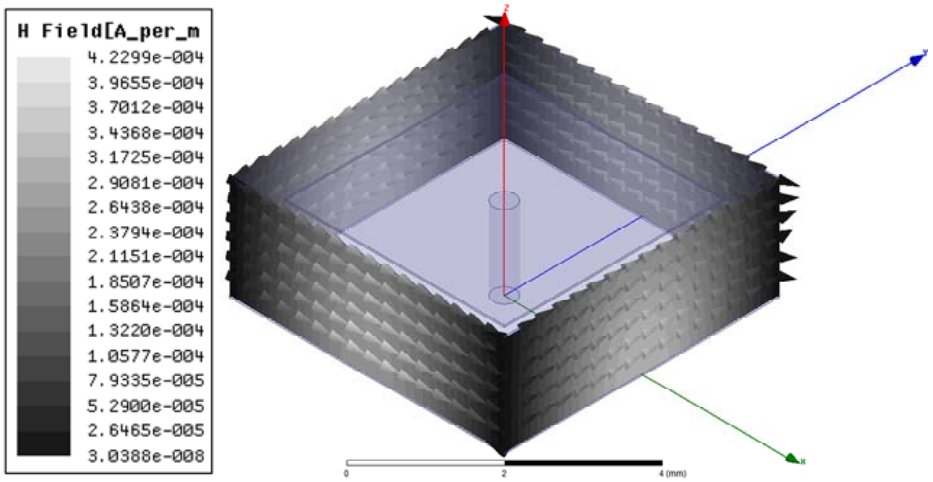

(a)

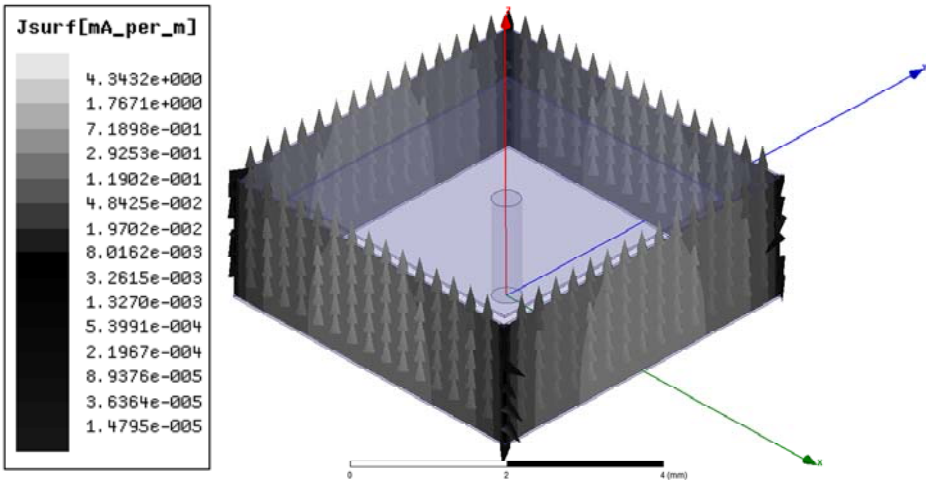

(b)

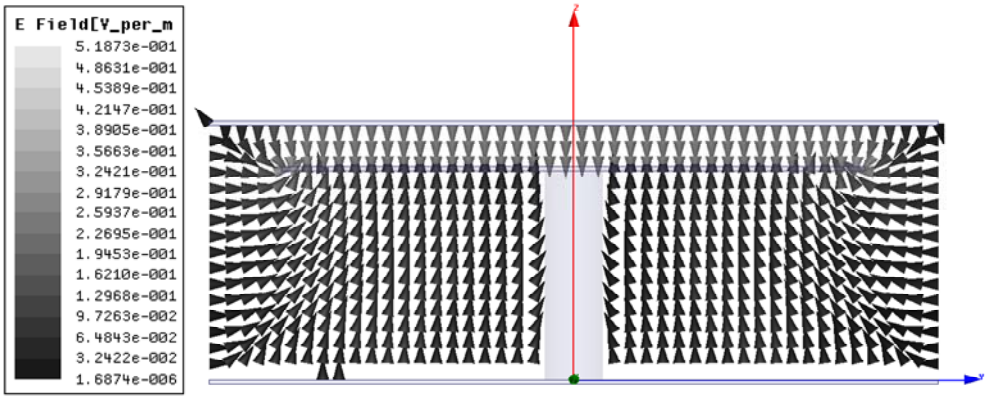

(c)

Fig. 2.23 (a) Magnetic field intensity, (b) equivalent surface current density, and (c) electric field intensity of a mushroom EBG structure at lower-bound cutoff frequency.

magnitude but out of phase. The field pattern behaves like a standing wave rather than a propagation wave. Equivalently, the field pattern of the periodic structure will be maintained if there are PEC walls on some particular symmetrical planes along the two directions. The 2-D model can be regarded as the extension from the 1-D model. For the unit cell shown in Fig. 2.21, the first mode at *M* point can be regarded as the resonance of the unit cell with 4 PEC side walls and the lower-bound cutoff frequency is the corresponding resonant frequency.

Fig. 2.23(a), (b), and (c) show the magnetic field intensity, equivalent surface current density, and electric field intensity distribution of a unit cell at the lower-bound cutoff frequency, respectively. The full-wave simulation is performed by applying the periodic boundary condition at *M* point. From Fig. 2.23(a), it is shown that the magnetic field intensity on the 4 side walls has only tangent component, and thus the equivalent surface current density which is defined as $\hat{n}\times\overline{H}$ can exist on the 4 side walls as shown in Fig. 2.23(b). In addition, the electric field intensity on the side walls is normal as shown in Fig. 2.23(c). The field patterns support that the boundary condition on the four side walls is PEC at lower-bound cutoff frequency.

Based on the mentioned above, an equivalent circuit model of the unit cell of the mushroom EBG structure for the lower-bound cutoff frequency can be established as shown in Fig. 2.24. As shown in Fig. 2.23(c), the distribution of electric field intensity is concentrated between the top plane and the embedded patch only. The effect is characterized by the parallel-plate capacitance C_p as

$$C_p = \varepsilon_0 \varepsilon_r \frac{p^2}{h_1}. \tag{2.69}$$

The effect of the current distribution, partially shown in Fig. 2.24, can be approximated by the inductance of a resonant cavity model with 4 PEC walls L_{eqL}, which is estimated

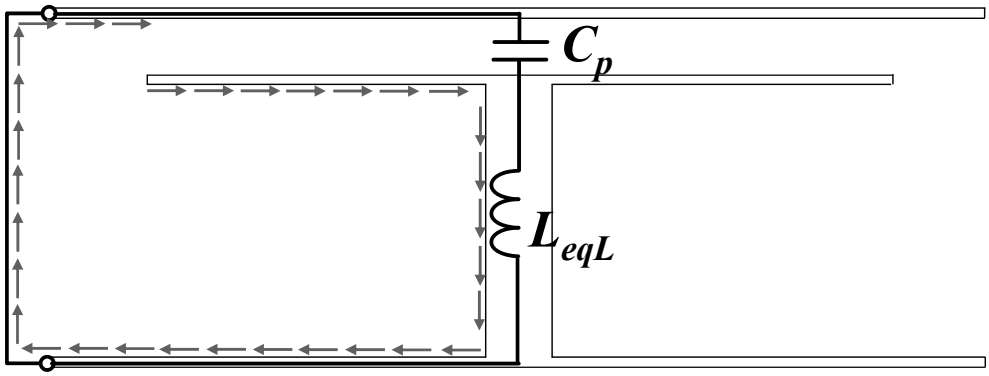

Fig. 2.24 An equivalent circuit model for unit cell of two-dimensional mushroom EBG structure for lower-bound cutoff frequency.

by (2.68) with a in side length, h_1+h_2 in height, and $T_{xi} = T_{yi} = \frac{a}{2}$. The lower-bound cutoff frequency is predicted by

$$f_L = \frac{1}{2\pi\sqrt{C_p L_{eqL}}}. \tag{2.70}$$

In this case, the C_p and L_{eqL} are 126.23 pF and 546.6 pH, respectively. The predicted lower-bound cutoff frequency is 606 MHz, which agrees well with the result from full-wave simulation 624 MHz. The error between the two methods is about 2.9 % only.

Similarly, the modes at Γ point represent the wave with wave vector 0 in both x- and y-direction. The phase difference of the wave between alternate cells is 0. It implies the field patterns distributing in adjacent cells are exactly the same. For the unit cell of mushroom EBG structure shown in Fig. 2.21, the second mode at Γ point, dominating the upper-bound cutoff frequency, can be considered as the resonant mode of the unit cell with 4 PMC walls on the periphery.

Fig. 2.25(a), (b), and (c) show the magnetic field intensity, equivalent surface current density, and electric field intensity distribution of a unit cell at the upper-bound cutoff frequency,respectively. The simulation is performed by applying the periodic

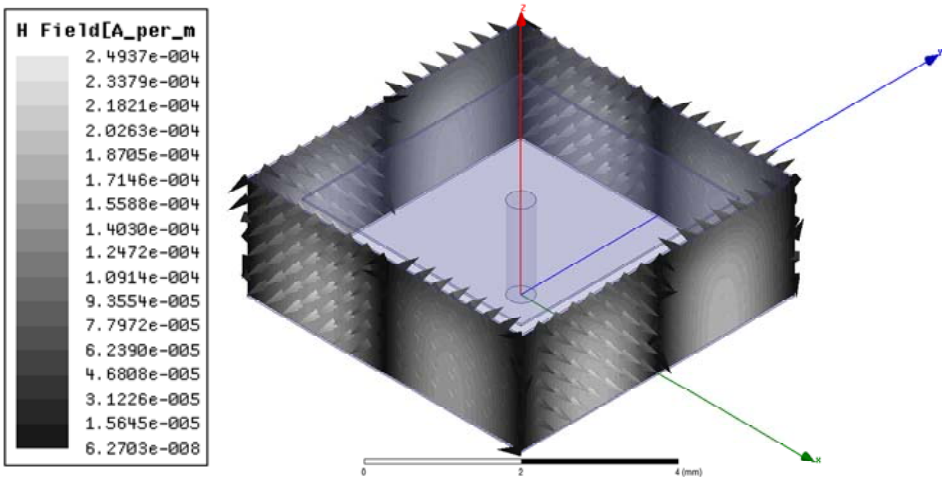

(a)

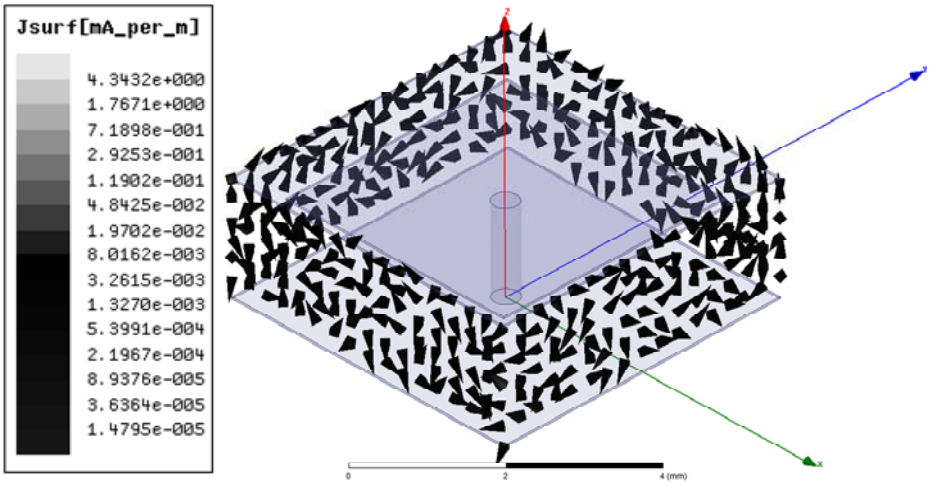

(b)

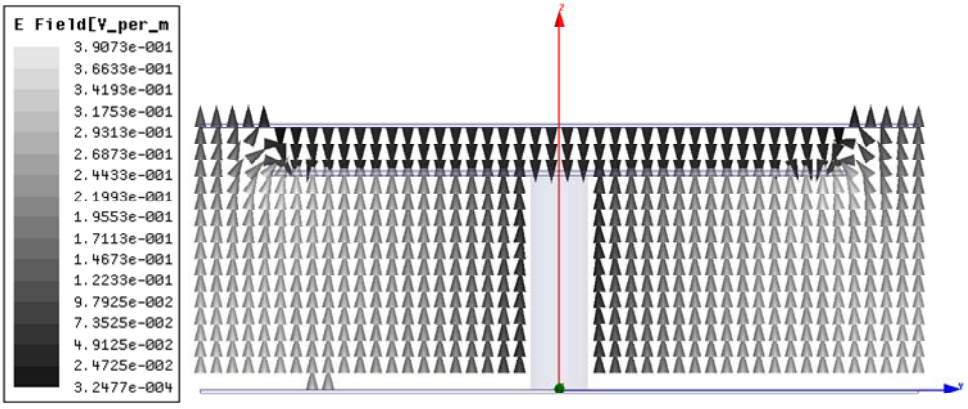

(c)

Fig. 2.25 (a) Magnetic field intensity, (b) equivalent surface current density, and (c) electric field intensity of a mushroom EBG structure at upper-bound cutoff frequency.

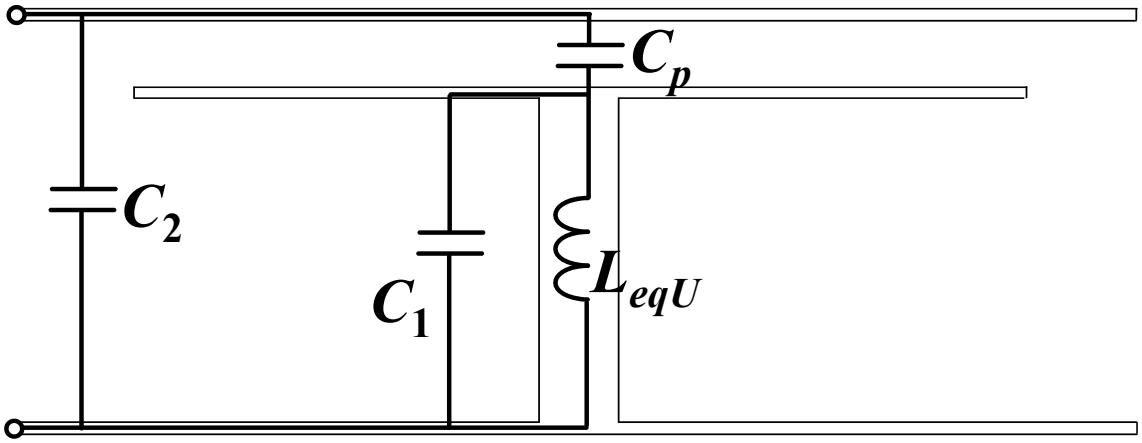

Fig. 2.26 An equivalent circuit model for unit cell of two-dimensional mushroom EBG structure for upper-bound cutoff frequency.

boundary condition of Γ point. From Fig. 2.25(a), it is shown that the magnetic field intensity on the 4 side walls has only normal component, and thus the surface current density is almost zero on the 4 side walls as shown in Fig. 2.25(b). In addition, the electric field intensity on the side walls is tangential as shown in Fig. 2.25(c). The field patterns support the boundary condition of PMC is equivalently applied on the 4 side walls at upper-bound cutoff frequency.

In order to predict the upper-bound cutoff frequency, the proposed equivalent circuit model is shown in Fig. 2.26. C_p is the parallel-plate capacitance between the top plane and patch. C_2 is the parallel-plate capacitance between top plane and bottom plane. The cavity consisting of the patch, bottom plane, and via is modeled by a parallel LC resonator comprised of C_1 and L_{eqU}. C_1 represents the parallel-plate capacitance between the patch and bottom plane. The via-plate inductance L_{eqU} can be estimated by (2.59), which is approximated by the inductance of the resonant cavity model with 4 PMC walls with a in side length and h_2 in height. Thus, the upper-bound cutoff frequency can be estimated by

$$f_U = \frac{1}{2\pi\sqrt{L_{eqU}\left(C_1 + \frac{C_p C_2}{C_p + C_2}\right)}} \tag{2.71}$$

In this case, C_1, C_2 and C_p are 25.25 pF, 4.7 pF, and 126.23 pF, respectively. The estimated L_{eqU} is 364.5 pH. Substituting the values into (2.71), we can predict the upper-bound cutoff frequency is at 1.528 GHz, which agrees well with the result from full-wave simulation 1.53 GHz. The difference between the results from the two methods is about 0.1 % only.

2.3 Summary

A method for predicting the lower- and upper-bound cutoff frequencies is proposed and applied by two physics-based models for one-dimensional and two-dimensional bandgaps, respectively. The mushroom EBG structure is taken as an example to illustrate the methodology. For the one-dimensional bandgap, we use the transmission-line sections to construct an equivalent circuit model for the unit cell of the mushroom EBG structure. We can apply periodic boundary condition to the equivalent circuit model and get the dispersion relation. The electrical lengths at lower- and upper-bound cutoff frequencies are either zero or π. It is proven that the lower- and upper-bound cutoff frequencies can be determined by the resonant frequencies of the half circuits for the symmetrical unit cells with specific boundary conditions. For the mushroom EBG structure, the lower- and upper-bound cutoff frequencies are the same as the resonant frequency of the Type-III and Type-I half resonators, respectively.

As regards two-dimensional bandgap, we also use the method extended from the one-dimensional case. For the mushroom EBG structure, the lower- and upper-bound cutoff frequencies can be determined by the resonant frequencies of the unit cell surrounded by PEC and PMC walls, respectively. Two different equivalent circuit

models associated with the lower- and upper-bound cutoff frequencies are established, respectively, and the circuit elements in the equivalent circuit models can be extracted based on resonant cavity model with corresponding boundary conditions. Such models take the 2-D distributed effect into account and can be represented by the equivalent lumped element models within the concerned bandwidth. Besides the mushroom EBG structure, the proposed method can be used to predict the bandgap of other EBG structures.

Chapter 3 Optimized Multiple Vias EBG Power/Ground Planes

In this chapter, a multiple vias EBG structure, which is the mushroom EBG structure with multiple vias, is investigated to enhance the bandwidth of the bandgap for the power/ground (P/G) noise suppression. By using four shorting vias and optimizing their arrangement, the multiple vias EBG structure presents the wider bandwidth of the bandgap comparing to the mushroom EBG structure. In addition, both the design concept and the mechanism of the bandwidth enhancement are also studied based on the optimization of vias location. Two methods are then used to predict the one- and two-dimensional bandgap. Test vehicles are manufactured on FR4 substrate to compare the measured results and the numerical ones.

3.1 Geometry and Design Concept

3.1.1 Design Concept of Multiple Vias EBG Structure

The multiple vias EBG structure considered in this chapter consists of a three-layer structure that could be embedded at any level of a multilayer PCB. The unit cell of the multiple vias EBG structure is shown in Fig. 3.1(a). The power (top) and ground (bottom) layers are solid, whereas the second layer is designed as a square patch connected to the solid ground plane by four stitching vias. The geometric parameters of the unit cell are: the side length of square unit cell a and of the patch p, the thickness between power/patch layers h_1 and between patch/ground layers h_2, and the radius of the

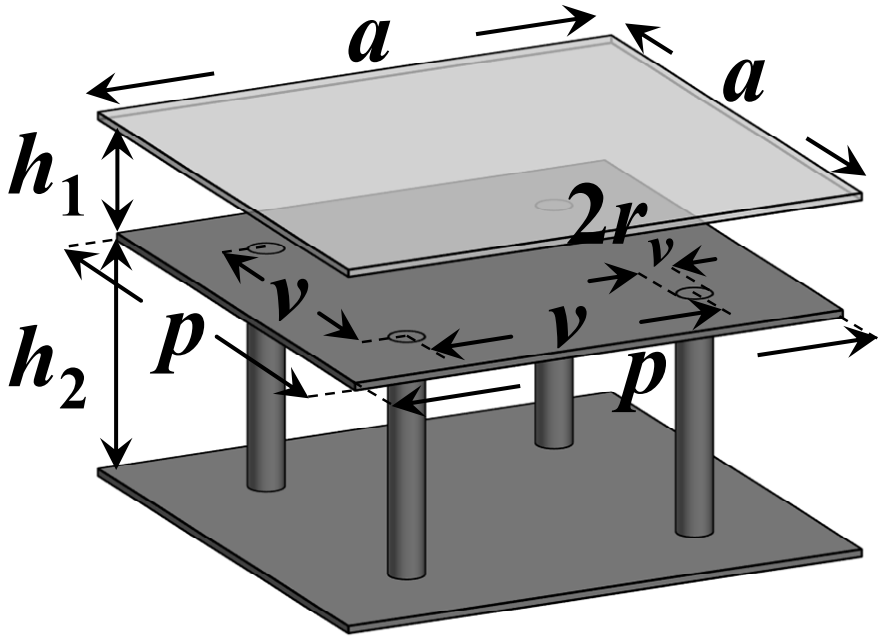

(a)

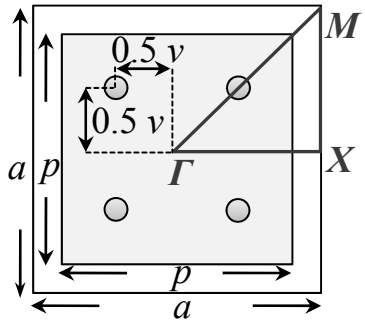

(b)

Fig. 3.1 (a) 3-D view and (b) top view of unit cell of multiple vias EBG structure.

vias r_v. The substrate is FR4-like type with relative permittivity $\varepsilon_r = 4.4$ and loss tangent $\tan\delta = 0.02$. The four vias are located on the diagonal of the patch and arranged symmetrically with respect to the center of the patch as shown in Fig. 3.1(b). To investigate the impact of the vias location on the bandwidth of the bandgap, the parameter v is set to represent the pitch between vias.

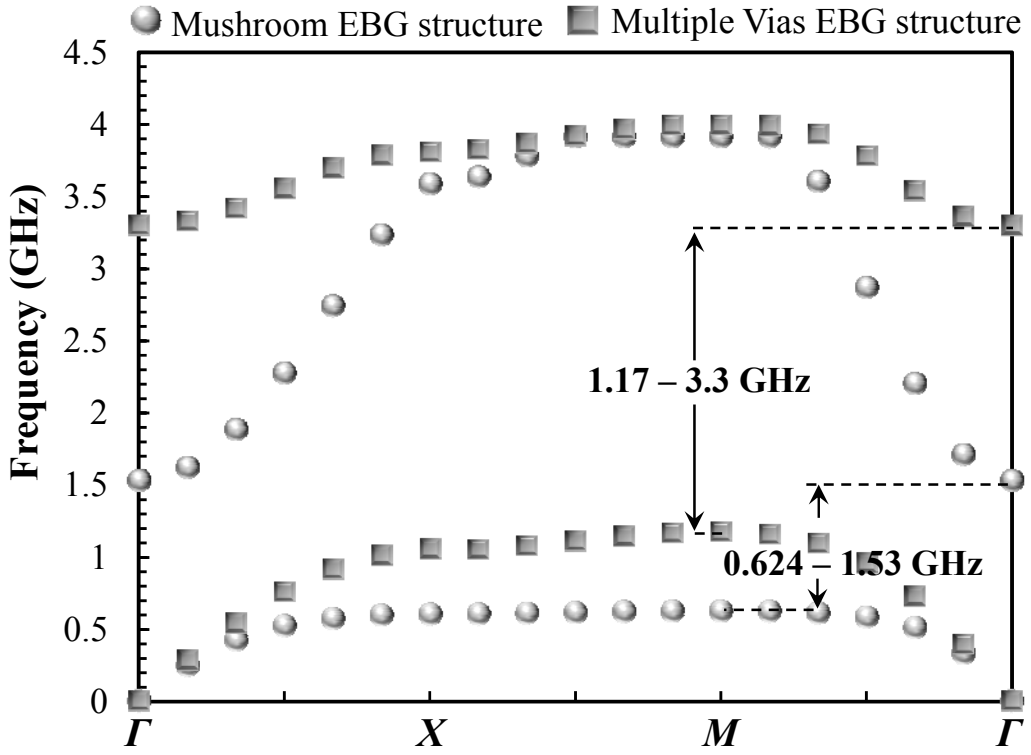

Fig. 3.2 Dispersion diagram of the multiple vias EBG structure with v = 8 mm and mushroom EBG structure.

By applying the periodic boundary condition to the unit cell, the dispersion diagram is simulated using the full-wave simulator HFSS. Fig. 3.2 shows the dispersion diagrams of the multiple vias EBG and mushroom EBG structures. The geometric parameters of the multiple vias EBG structure are designed as (a, p, r_v, h_1, h_2, v) = (20 mm, 18 mm, 0.15 mm, 0.1 mm, 0.5 mm, 8 mm). In addition, the multiple vias EBG structure and the mushroom EBG structure are with the same dimensions except the number of the vias. As shown in Fig. 3.2, the bandgaps are from 1.17 GHz to 3.3 GHz for the multiple vias EBG structure and from 0.624 GHz to 1.53 GHz for the mushroom EBG structure. The absolute bandwidths of the bandgaps formed by the multiple vias and mushroom EBG structures are 2.13 GHz and 906 MHz, respectively. The structure with multiple vias has significantly wider stopband.

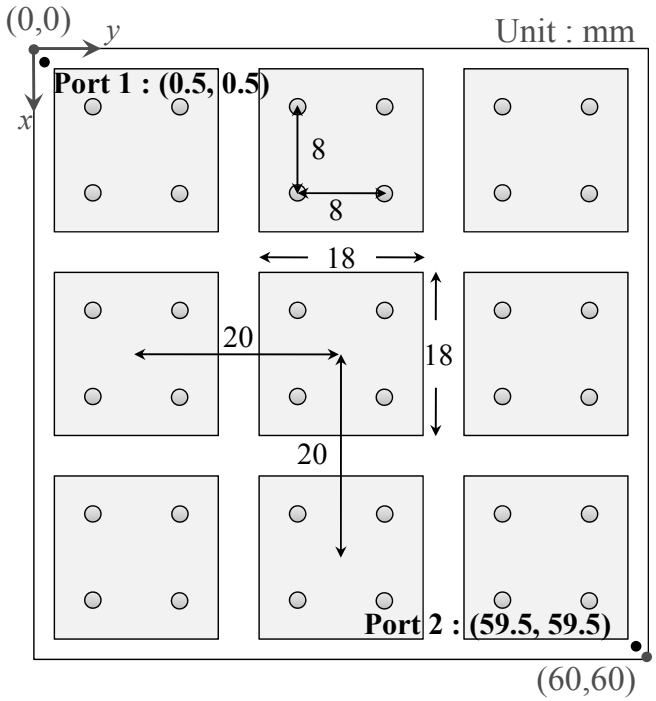

(a)

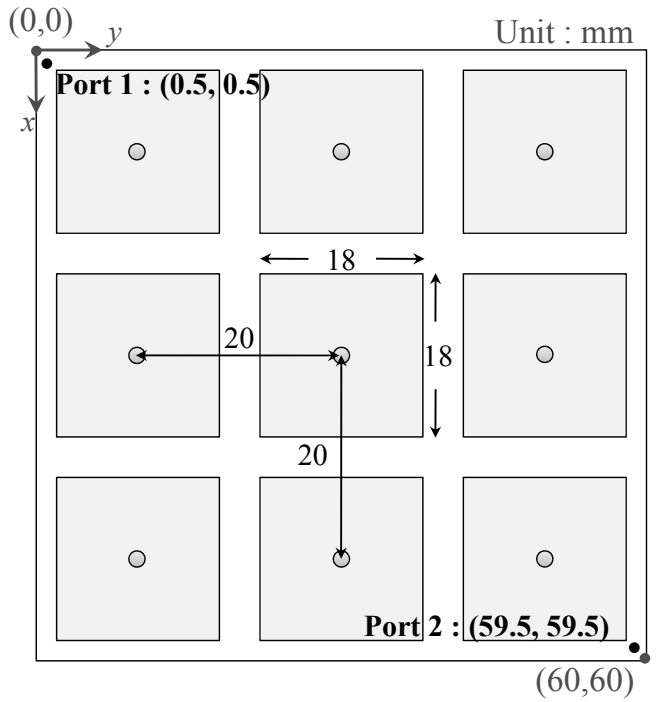

(b)

Fig. 3.3 Top views of (a) multiple vias EBG and (b) mushroom EBG P/G planes.

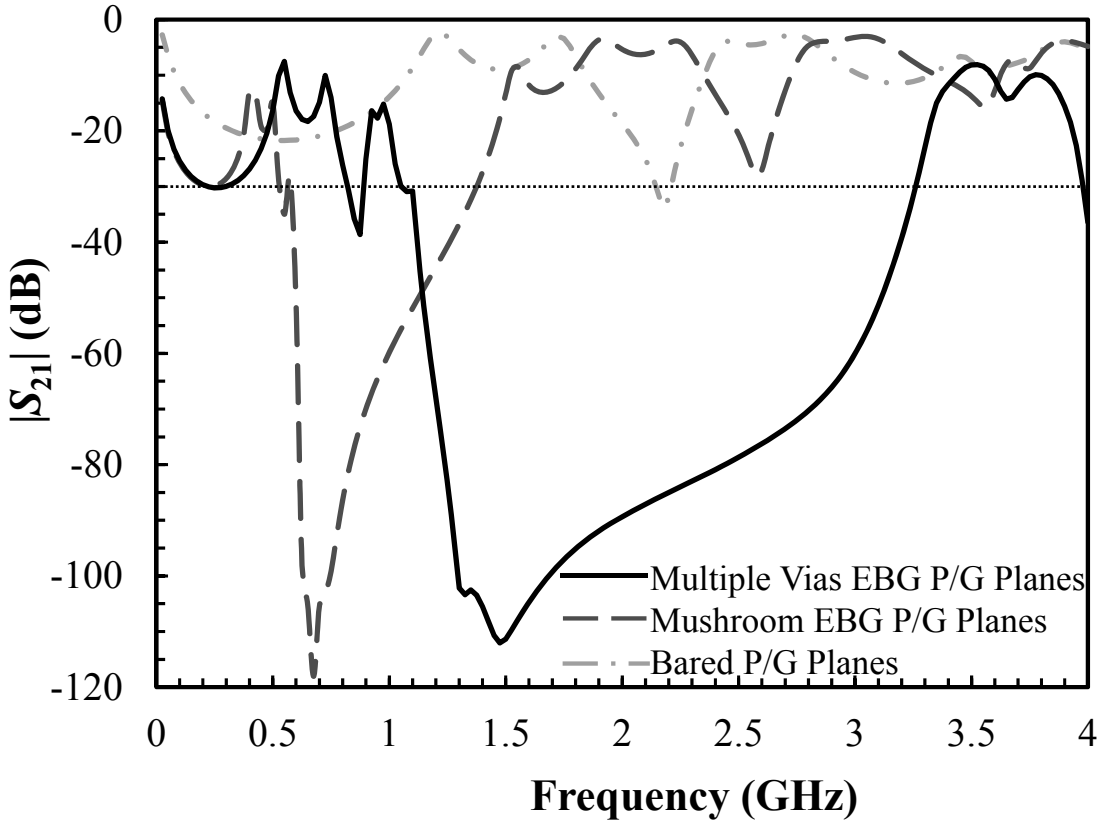

Fig. 3.4 $|S_{21}|$ of multiple vias EBG, mushroom EBG, and bared power/ground planes.

Fig. 3.3(a) and (b) show the top view of multiple vias EBG and mushroom EBG power/ground planes, respectively. Both of them consist of 3 × 3 unit cells. Two test ports are set at (0.5 mm, 0.5 mm) and (59.5 mm, 59.5 mm). The magnitude of the transfer scattering parameters S_{21} is computed as shown in Fig. 3.4. Taking -30 dB as a figure of merit of a stopband, we can find the stopband of the mushroom EBG power/ground planes is from 0.6 GHz to 1.4 GHz and that of the multiple vias EBG power/ground planes is from 1.05 GHz to 3.25 GHz. The stopbands are consistent with the bandgaps determined from the dispersion diagrams. The results of the bared power/ground planes without the EBG unit cells are also shown in this figure. It shows the coupling level can be reduced dramatically in a wider bandwidth by the multiple vias EBG power/ground planes.

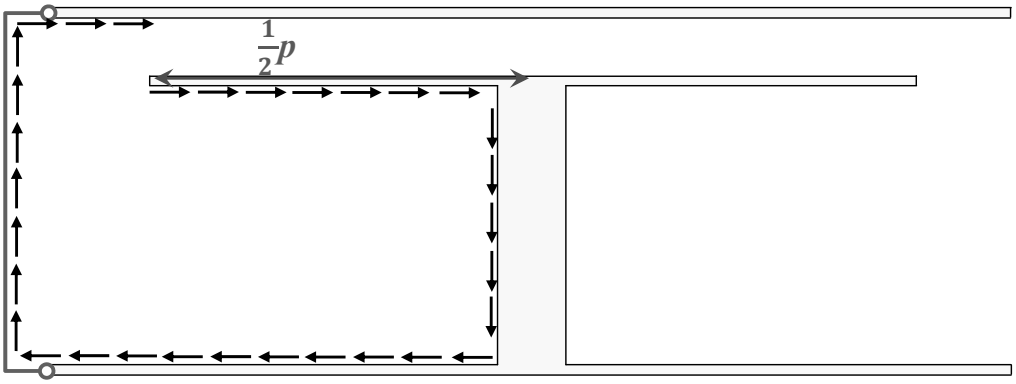

(a)

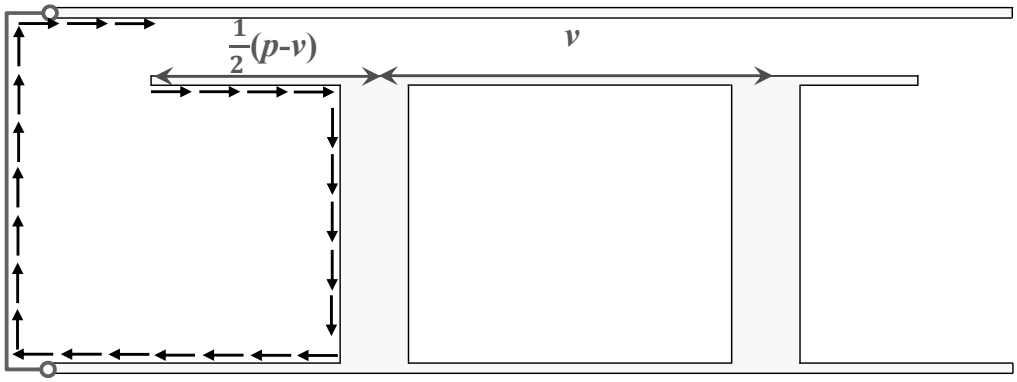

(b)

Fig. 3.5 Current path from patch, ground plane to power plane of (a) multiple vias EBG and (b) mushroom EBG structures.

The electromagnetic behavior of the two structures can be described by using the same principles. The main mechanism resulting in difference lower-bound cutoff frequencies of the multiple vias EBG and mushroom EBG structure is the effective inductance formed by the current path from the patch, ground plane to the power plane. However the mushroom EBG structure has a larger loop inductance than the multiple vias EBG structure due to the larger loop associated to the current path going from the square patch to the ground plane through the vias as described in Fig. 3.5(a) and (b). This additional inductance (larger in the case of the mushroom EBG geometry) contributes to the lower-bound cutoff frequency.

The upper-bound cutoff frequency is related to the number and position of the shorting vias between the patches and the bottom solid plane. This concept can be deduced by observing the spatial distribution of the magnitude of electrical field intensity at the upper-bound cutoff frequencies, 1.53 GHz for the mushroom EBG structure and 3.3 GHz for the multiple vias EBG structure. Firstly, the upper-bound cutoff frequencies we concerned are below the resonant frequency resulting from the half-wavelength resonance of the patch. The electrical field intensity between the top plane and patches is uniform. In addition, the separation between the top plane and patches is thin enough to have a large parallel-plate capacitance. It implies that the top solid plane and the patches can be considered virtually equipotential. Therefore, the multiple vias EBG and mushroom EBG structures are approximated as two simplified cavities with a different number of shorting vias between the two solid planes around the corresponding upper-bound cutoff frequencies.

Fig. 3.6(a) shows the distribution of the magnitude of the electrical field intensity on the bottom plane for the multiple via EBG power/ground planes at upper-bound cutoff frequency, 3.3 GHz. The structure can be simplified as a two-layer structure with the same vias arrangement as shown in Fig. 3.6(b). The resonant frequency of the simplified structure is 3.24 GHz, which is close to the upper-bound cutoff frequency. Comparing the Fig. 3.6(a) and (b), we can find that the two structures also have similar resonant pattern. Similarly, Fig. 3.7 (a) and (b) show the distribution of the magnitude of the electrical field intensity on the bottom plane for the mushroom EBG power/ground planes and corresponding simplified structure at upper-bound cutoff frequency 1.53 GHz and resonant frequency 1.49 GHz, respectively. The two structures also have similar field patterns and the close resonant frequencies.

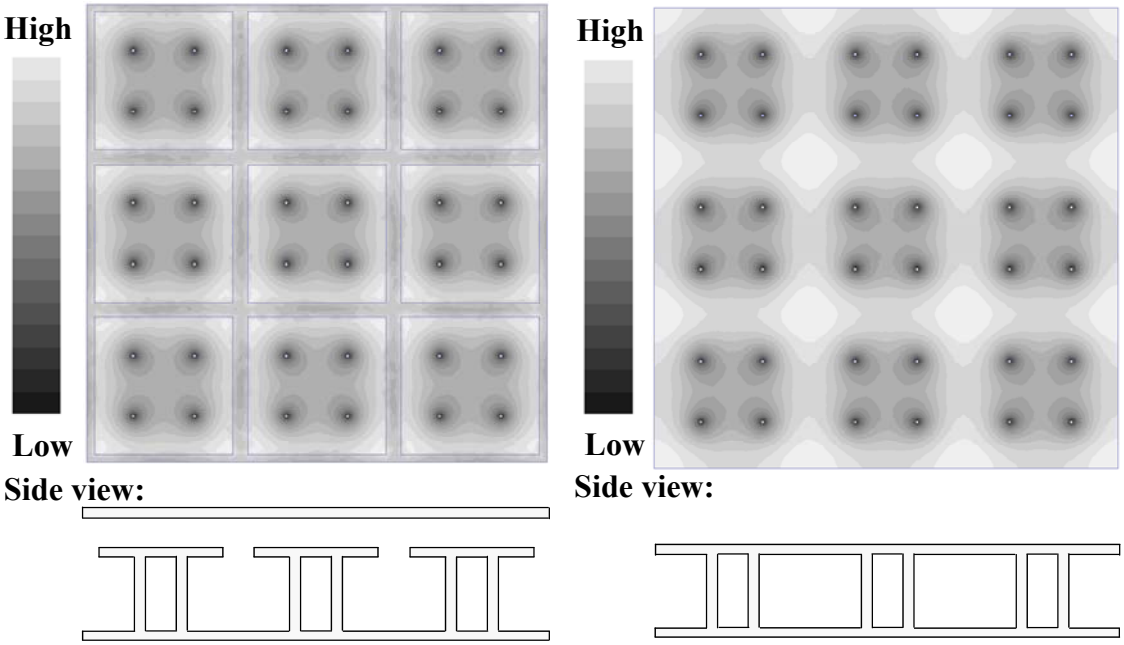

(a) (b)

Fig. 3.6 Distribution of electrical field intensity (magnitude) on bottom plane for (a) multiple vias EBG P/G planes and (b) corresponding simplified structure.

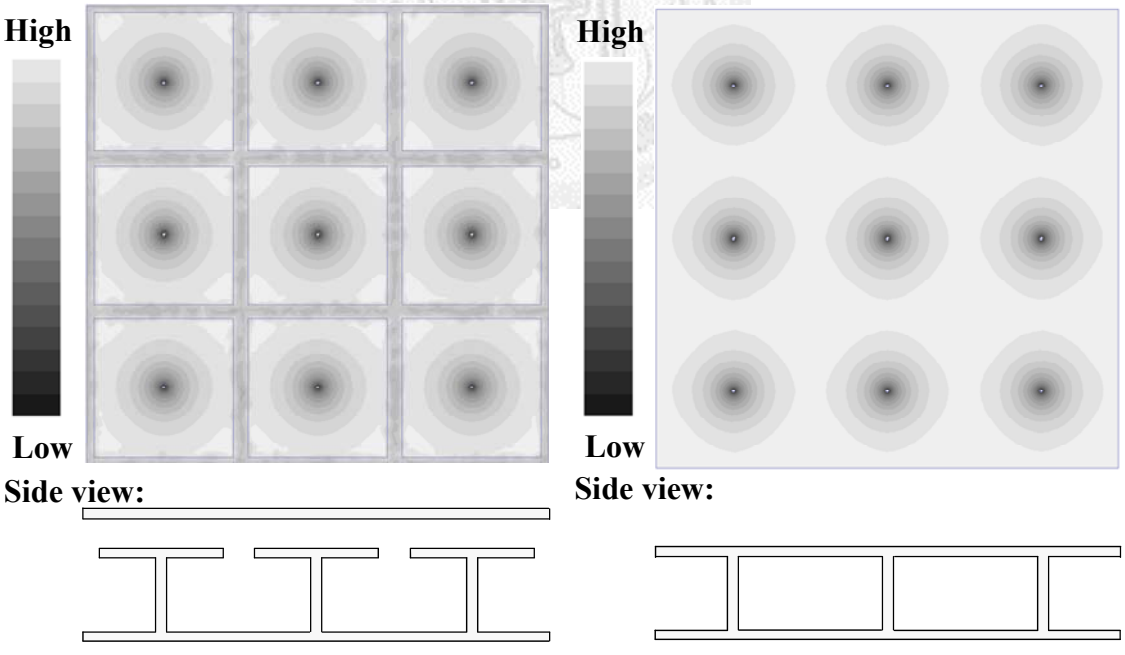

(c) (d)

Fig. 3.7 Distribution of electrical field intensity (magnitude) on bottom plane for (a) mushroom EBG P/G planes and (b) corresponding simplified structure.

Based on the comparisons of the field patterns and resonant frequencies between the original and simplified structure, it indicates that the upper-bound cutoff frequency is related to the resonance of a parallel-plate structure with the same via arrangement. Therefore, the reason why multiple vias EBG structure is with higher upper-bound cutoff frequency can be attributed to the more vias for shorting the patches and the bottom plane.

3.1.2 Optimum Design Based on Via Arrangement

In terms of design point of view, the parameter *v* that represents the distance from the center of a via to that of another closer one has an important impact on both lower- and upper-bound cutoff frequencies. Regarding lower-bound cutoff frequency, from a qualitative point of view, a decrease of *v* implies an increase in the dimension of the current loop, as shown in Fig. 3.5(b), and hence in the loop inductance of the cavity because the vias move away from the edge of the patch. This causes a shift of lower-bound cutoff frequency to lower frequency range and hence a widening of the lower-bound bandgap.

As regards upper-bound cutoff frequency, based on the above discussion, it is associated to the resonance for the equivalent cavity and hence to the size of the equivalent cavity. Fig. 3.8 shows spatial distribution of the magnitude of the electrical field intensity on the bottom plane at the corresponding upper-bound cutoff frequency of the multiple vias EBG power/ground planes with different *v*. The equivalent cavity indicated by the dashed circle in the Fig. 3.8(a) are formed among the patches for the case $v = 6$ mm. The size of the equivalent cavity reduces when *v* increases to 10 mm as shown in Fig. 3.8(b). In this case, the sizes of the equivalent cavities inside the patches and among the patches are almost the same. However, the equivalent cavity with reduced size changes to be inside the patch when *v* is 14 mm as shown in Fig. 3.8(c).

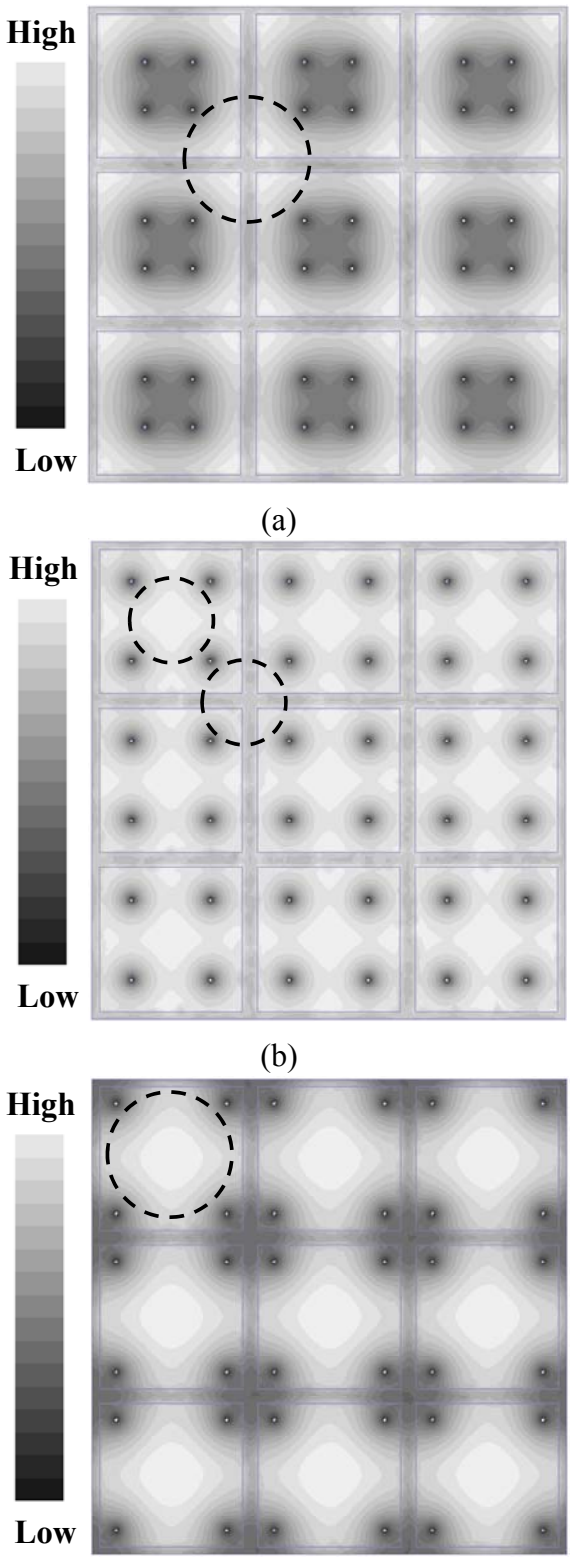

Fig. 3.8 Distribution of electrical field intensity (magnitude) on bottom plane for multiple vias EBG P/G planes with (a) v = 6 mm, (b) v =10 mm, and (c) v = 14 mm.

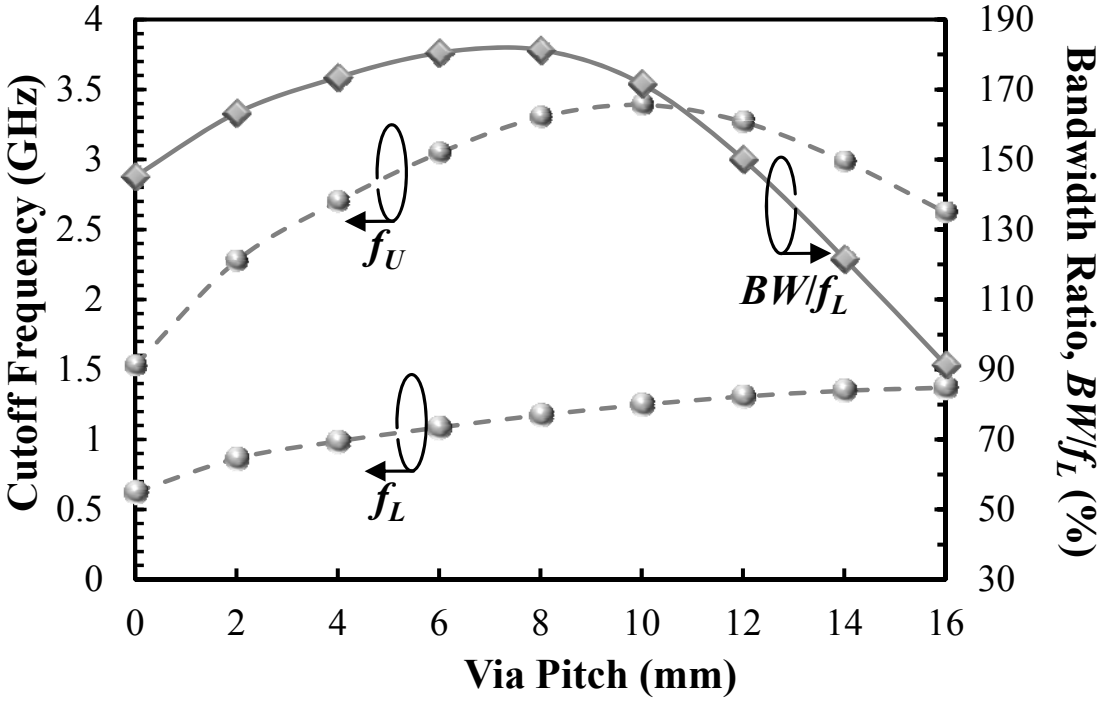

Fig. 3.9 Lower- and upper-bound cutoff frequencies and bandwidth ratio of multiple vias EBG structure with different via pitch *v*.

The upper-bound cutoff frequency is affected by the size of the equivalent cavity. It can be anticipated that the highest upper-bound cutoff frequency occurred for the multiple vias EBG structure with v = 10 mm.

Fig. 3.9 shows the lower- and upper-bound cutoff frequencies of the multiple vias EBG structure with respect to via pitch using full-wave simulation. The impact of vias position on the bandwidth can be found from this figure. The difference between lower- and upper-bound cutoff frequencies represents the bandwidth of the bandgap. The phenomenon is clearly shown that the lower-bound cutoff frequency becomes lower with smaller *v*. The lower stopband is available by moving four vias from the edge toward the center of the patch. Unfortunately, the upper-bound cutoff frequency of the multiple vias EBG structure does not always increase proportionally as the *v* is

increased. The upper-bound cutoff frequency becomes higher because of the smaller equivalent cavity formed inside the patch as v changes from 16 mm to 10 mm. However, if v keeps decreasing shorter than 10 mm, the upper-bound cutoff frequency becomes lower due to the larger equivalent cavity formed among the patches. The highest upper-bound cutoff frequency appears in the case v = 10 mm. A bandwidth ratio, defined as the ratio of the bandwidth (BW) to the lower-bound cutoff frequency (f_L), is also plotted with respect to v in the figure. The bandwidth ratio can be used to examine the bandwidths for different EBG structures when the same lower-bound cutoff frequency is desired. The cases of the four vias located neither at the edge nor at the center of the patch have the maximum bandwidth ratio for the bandgap of the multiple vias EBG structure. The maximum bandwidth ratio appears in the case v = 8 mm. As a result, to find out the parameter v of multiple vias EBG structure with maximum bandwidth ratio, a method for predicting both lower- and upper-bound cutoff frequencies has to be developed.

On the other hand, it is worth noting that the case v = 0 mm represents the mushroom EBG structure. The maximum bandwidth ratio of the multiple vias EBG and the mushroom EBG structure are 181 % and 145 %, respectively, under the assumption of the same dimension. It is worth emphasizing that not only absolute bandwidth but also bandwidth ratio is enhanced by multiple vias EBG structure.

3.2 One-Dimensional Bandgap Prediction

A case of one-dimensional multiple vias EBG structure is discussed here. An equivalent circuit model is constructed using transmission-line sections for the one-dimensional multiple vias EBG structure with different via pitch v. Two half circuits with particular boundary conditions can be used to predict the bandwidth of

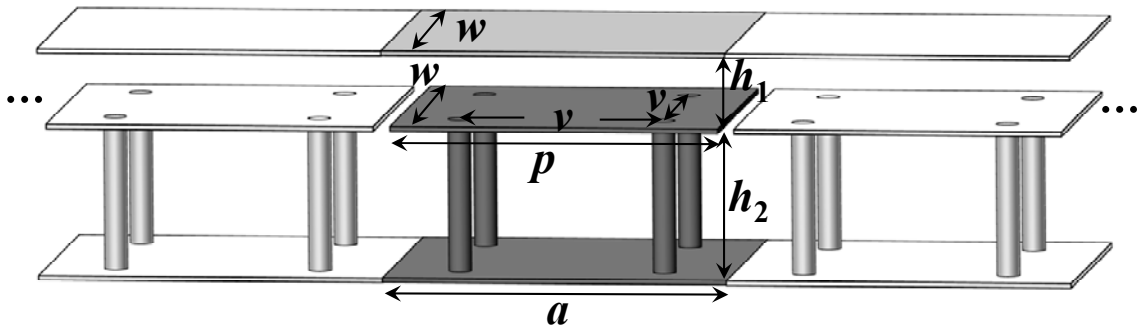

(a)

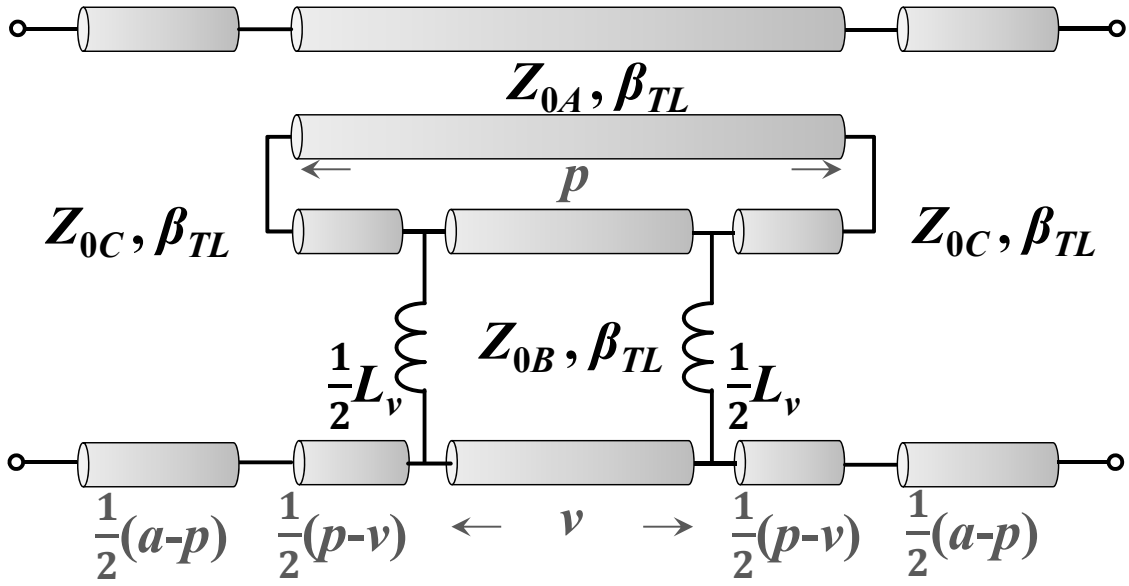

(b)

Fig. 3.10 (a) Geometry of 1-D multiple vias EBG structure and (b) corresponding equivalent circuit model.

bandgap as described in Section 2.1.2.

Fig. 3.10(a) shows the geometry of one-dimensional multiple vias EBG structure. The geometric parameters of the unit cell are: the length of the unit cell a, the width of the parallel plates w, the length of the patch p, the radius of the via r_v, the separations between the patch h_1 and the top and bottom planes h_2, and the via pitch v. The dielectric constant of the substrate is ε_r. An equivalent circuit model for the unit cell of the

multiple EBG structure is shown in Fig. 3.10(b). The concept for the equivalent circuit model of multiple vias EBG structure is similar to that of mushroom EBG structure as shown in Fig. 2.9(b). The parallel-plate pair of patch and bottom plane is divided into three transmission-line sections according to the arrangement of the vias. The two via inductors are connected at the corresponding locations. The inductance of each inductor is half of L_v, which is the inductance of single via extracted by full-wave simulation, because of the parallel connection of two vias.

The equivalent circuit model can be bisected into two identical half circuits because of the symmetry of the equivalent circuit model. The half circuit model with PEC boundary on the left side and PMC boundary on the right side can be used to estimate the lower-bound cutoff frequency. The half resonator for lower-bound cutoff frequency is shown in Fig. 3.11(a). The resonator can be divided into three parts, a short-circuited line with input impedance Z_{inCS}, an open-circuited line with input impedance Z_{inAO}, and a transmission line with input impedance Z_{inB}, which is terminated by a parallel connection of an inductor and an open-circuited line. Z_{inB} is expressed by

$$Z_{inB} = Z_{0B}\frac{Z_p + jZ_{0B}\tan\left(\beta_{TL}\frac{p-v}{2}\right)}{Z_{0B} + jZ_p\tan\left(\beta_{TL}\frac{p-v}{2}\right)} \tag{3.1}$$

, where

$$Z_p = \frac{j\omega L_v Z_{0B}\cot(\beta_{TL}\frac{v}{2})}{\omega L_v + 2Z_{0B}\cot(\beta_{TL}\frac{v}{2})}. \tag{3.2}$$

The lower-bound cutoff frequency is the solution frequency of $Z_{inCS} + Z_{inB} + Z_{inAO} = 0$,

$$jZ_{0C}\tan\left(\beta_{TL}\frac{a-p}{2}\right) + Z_{0B}\frac{Z_p + jZ_{0B}\tan\left(\beta_{TL}\frac{p-v}{2}\right)}{Z_{0B} + jZ_p\tan\left(\beta_{TL}\frac{p-v}{2}\right)} + jZ_{0A}\cot\left(\beta_{TL}\frac{p}{2}\right) = 0. \tag{3.3}$$

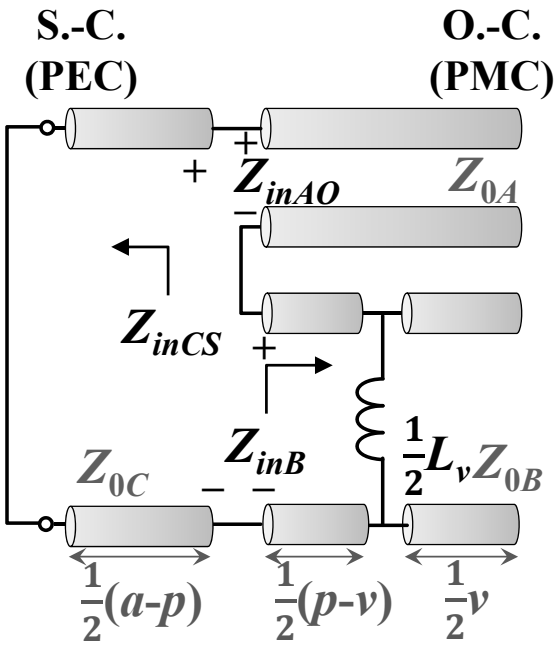

(a)

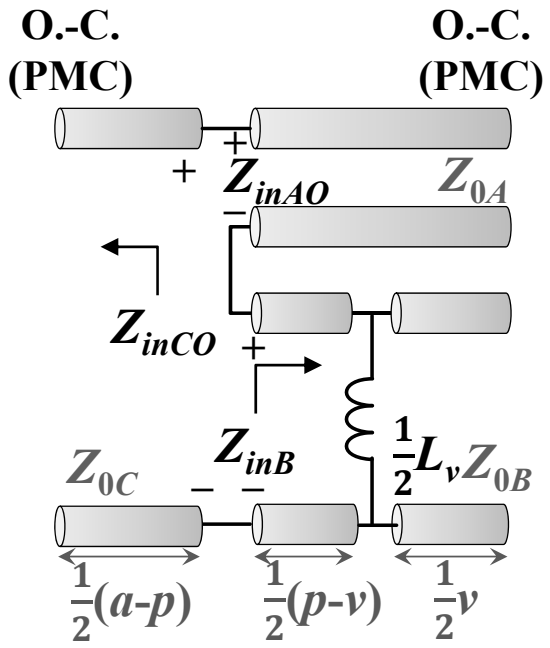

(b)

Fig. 3.11 Half resonators for (a) lower- and (b) upper-bound cutoff frequencies of one-dimensional multiple vias EBG structure.

As regards upper-bound cutoff frequency, it is the resonant frequency of the half circuit model with PMC walls on the both left and right sides. The half resonator is shown in Fig. 3.11(b). The half resonator consists of two open-circuited lines with input impedance Z_{inCO} and Z_{inAO}, respectively, and a transmission line with input impedance Z_{inB}. The resonant frequency can be determined by solving $Z_{inCO} + Z_{inB} + Z_{inAO} = 0$,

$$jZ_{0C}\cot\left(\beta_{TL}\frac{a-p}{2}\right)+Z_{0B}\frac{Z_p+jZ_{0B}\tan\left(\beta_{TL}\frac{p-v}{2}\right)}{Z_{0B}+jZ_p\tan\left(\beta_{TL}\frac{p-v}{2}\right)}+jZ_{0A}\cot\left(\beta_{TL}\frac{p}{2}\right)=0 \quad (3.4)$$

Considering the geometric parameters (a, w, p, r_v, h_1, h_2) = (20 mm, 18 mm, 18 mm, 0.15 mm, 0.1 mm, 0.5 mm), we sweep the variable v from 2 mm to 16 mm to compare the lower- and upper-bound cutoff frequencies from (3.3) and (3.4), respectively, with those from full-wave simulation. The circuit parameters are (Z_{0A}, Z_{0B}, Z_{0C}, L_v) = (1 Ω, 5 Ω, 6 Ω, 259.9 pH). The results are shown in Fig. 3.12. The agreement between the results from the derived formulas and full-wave simulation is reasonably good. The values and the trend of the lower-bound cutoff frequencies can be predicted well by solving (3.3). On the other hand, the trend of the upper-bound cutoff frequency is well predicted but the values are with fair differences. The error of lower- and upper-bound cutoff frequencies from derived formulas and full-wave simulation is shown in Fig. 3.13. The maximum errors of the lower- and upper-bound cutoff frequencies are 8.05 % and 14.8 %, respectively, for the case v = 2 mm. The case of v = 0 mm representing the mushroom EBG structure is also shown in this figure. It can be deduced that the errors of upper-bound cutoff frequency may result from the two-dimensional field distribution which is not included in this equivalent circuit model based on transmission-line sections.

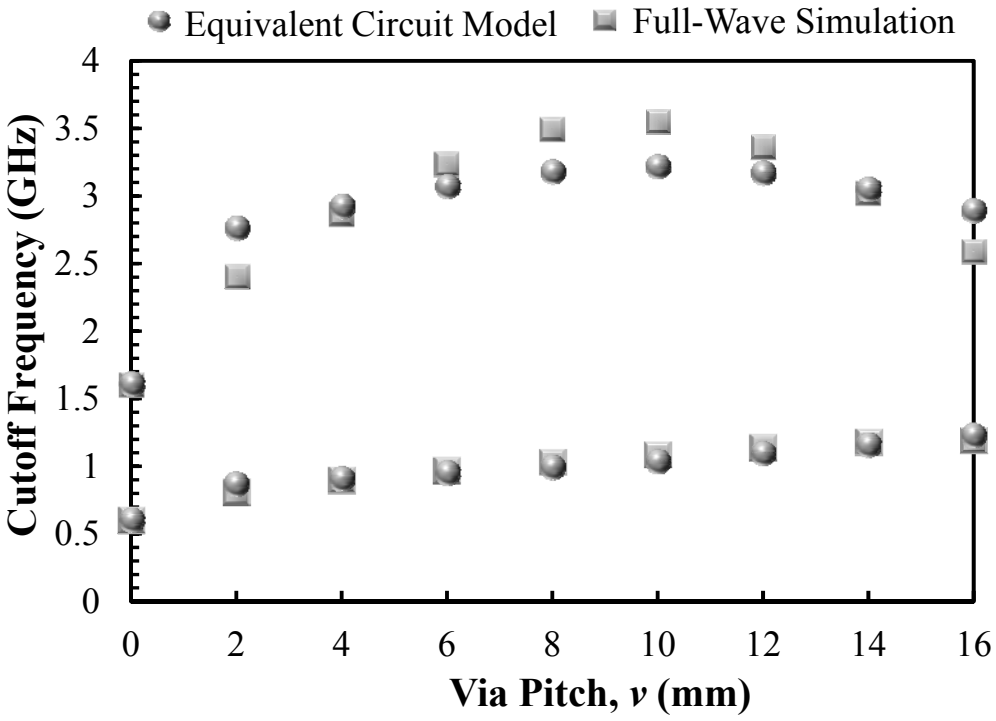

Fig. 3.12 Estimated and simulated lower- and upper-bound cutoff frequencies of 1-D multiple vias EBG structure and mushroom EBG structure (v = 0 mm).

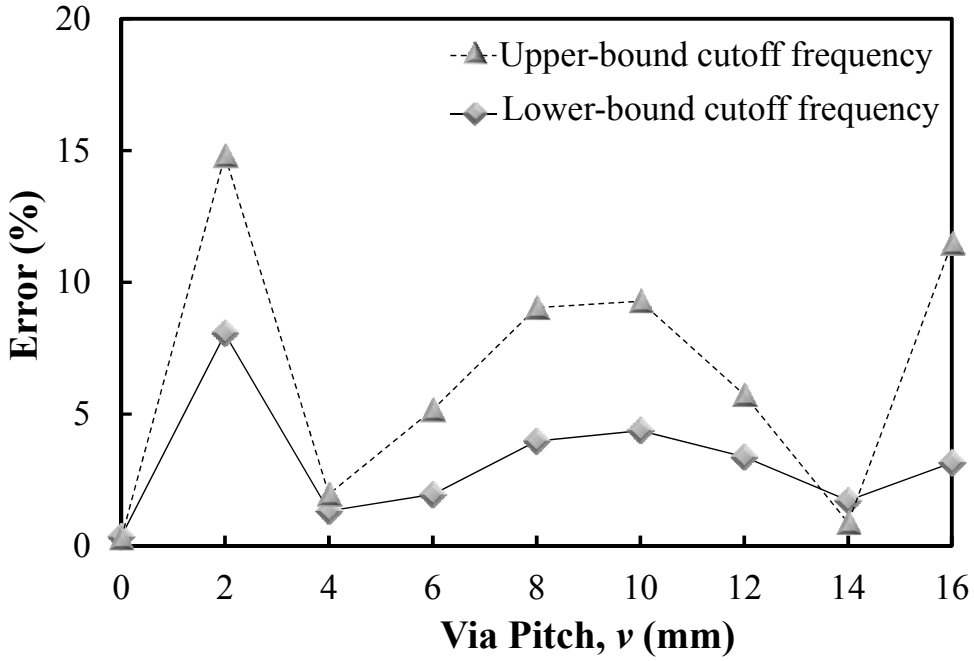

Fig. 3.13 Error of lower- and upper-bound cutoff frequencies from derived formulas and full-wave simulation.

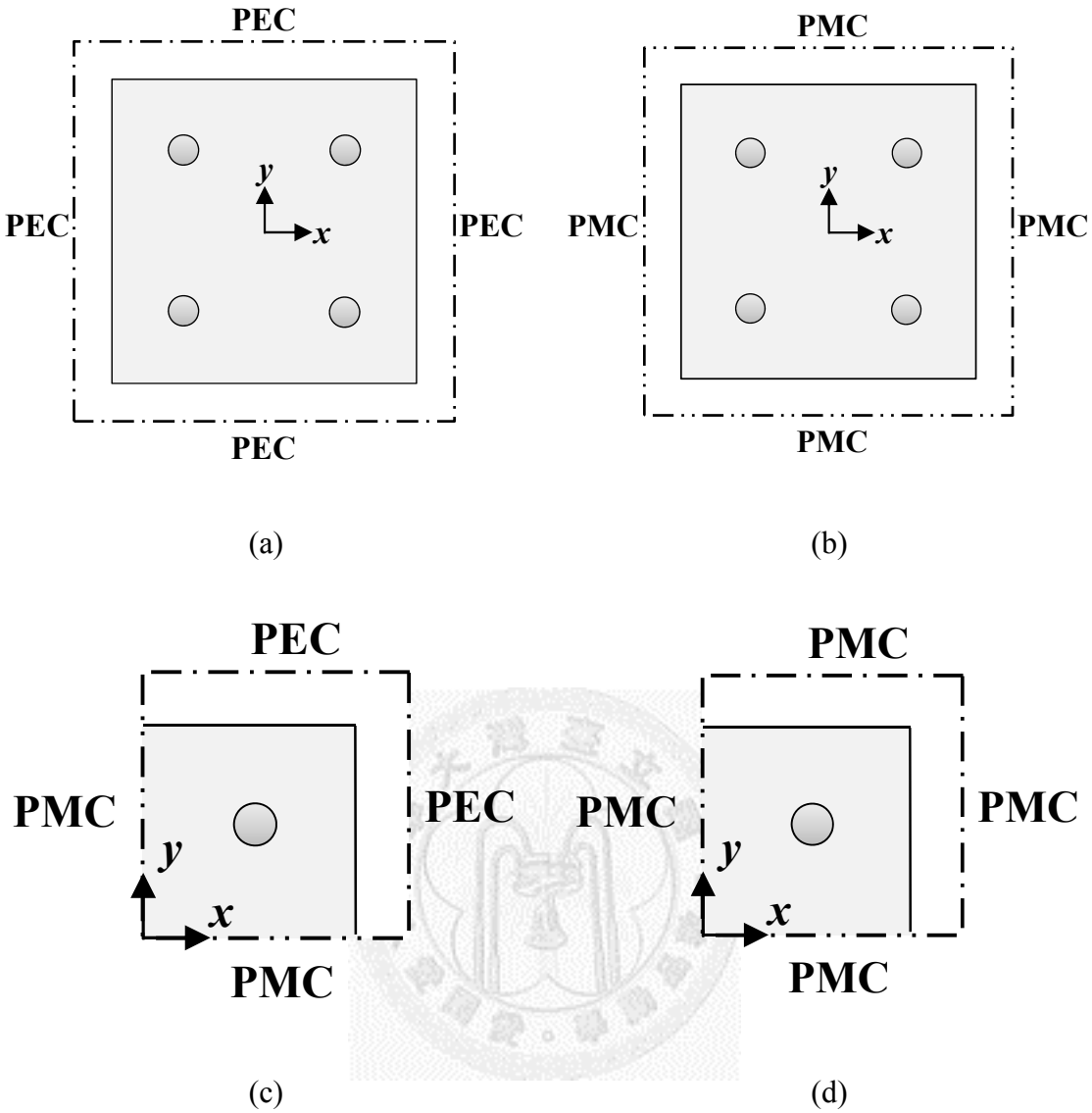

Fig. 3.14 Resonators for (a) lower- and (b) upper-bound cutoff frequencies of multiple vias EBG structure and quartered model for (c) lower- and (d) upper-bound cutoff frequencies.

3.3 Two-Dimensional Bandgap Prediction

A method to predict the bandgap of the two-dimensional multiple via EBG structure is developed in this section. As discussed in Section 2.2.3, the lower- and upper-bound cutoff frequencies can be determined as the resonant frequencies of the

unit cell with four PEC and PMC walls, respectively, around the periphery of the unit cell. Fig. 3.14 (a) and (b) show the resonators for the lower- and upper-bound cutoff frequencies, respectively. It is worth noting that the unit cell is with mirror symmetry with respect to *x*- and *y*-axis. Based on the symmetry, we can quarter the unit cell into four identical cells along the *x*- and *y*-axis. We do not need to take the whole unit cell into account. Instead, only taking the quartered model into consideration is enough for estimating the resonant frequencies. Fig. 3.14 (c) and (b) show the quartered model for the lower- and upper-bound cutoff frequencies, respectively, by applying PMC walls along the *x*- and *y*-axis. For the quartered model of the lower-bound cutoff frequency shown in Fig. 3.14 (c), there are two PMC walls along *x*- and *y*-axis and two PEC walls on the other two sides. Before predicting the lower-bound cutoff frequency, we have to develop the resonant cavity model for characterizing the equivalent circuit model of the parallel-plate structure with such boundary condition.

3.3.1 Resonant Cavity Modeling

A parallel-plate structure surrounded by two PMC walls along *x*- and *y*-axis and two PEC walls on the other two sides is considered as shown in Fig. 3.15. The cavity is with dimension P_x by P_y. The port *i* (*j*) is with side length $l_{xi,j}$ and $l_{yi,j}$ along the *x*- and *y*-direction, respectively, and located at ($T_{xi,j}$, $T_{yi,j}$). This kind of boundary condition for ϕ, *z*-directed electric field or voltage, can be expressed as

$$\begin{aligned}
&\frac{\partial \phi(x,0)}{\partial y} = 0 \qquad \text{for } 0 \le x \le P_x, \\
&\phi(x,P_y) = 0 \qquad \text{for } 0 \le x \le P_x, \\
&\frac{\partial \phi(0,y)}{\partial x} = 0 \qquad \text{for } 0 \le y \le P_y, \\
&\phi(P_x,y) = 0 \qquad \text{for } 0 \le y \le P_y.
\end{aligned} \tag{3.5}$$

The eigenfunctions for the above boundary condition are

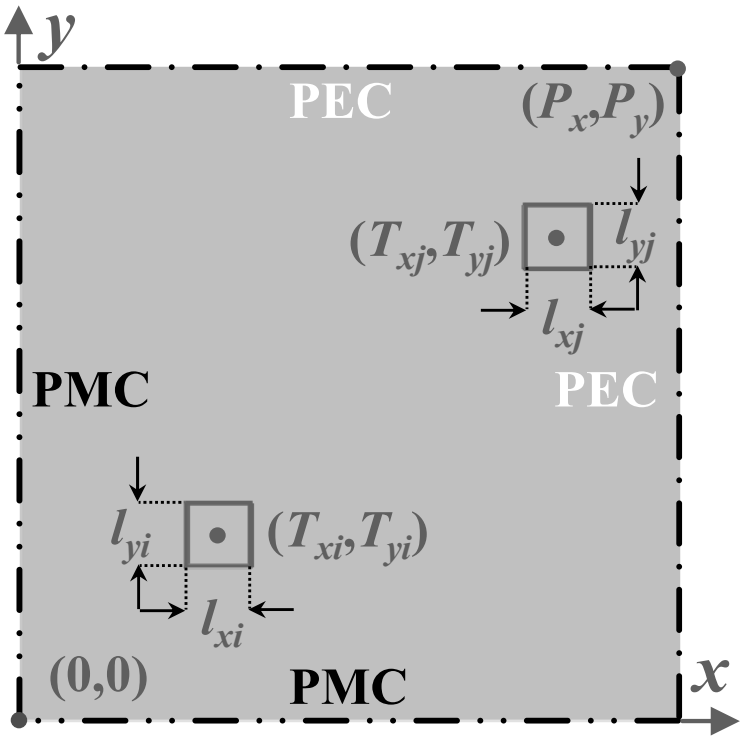

Fig. 3.15 Parallel-plate structure surrounded by two PMC walls along *x*- and *y*-axis and two PEC walls on the other two sides.

$$\phi_{mn} = \frac{C_m C_n}{\sqrt{P_x P_y}} \cos(k_m x) \cos(k_n y) \tag{3.6}$$

, where $k_m = \frac{(2m-1)\pi}{2P_x}$, $k_n = \frac{(2n-1)\pi}{2P_y}$, $C_m = C_n = \sqrt{2}$, and m and n are mode numbers (positive integers). By combing (2.41), (2.44), and (2.45), the transfer impedance Z_{ij} is derived as

$$\begin{aligned} Z_{ij} = {} & \frac{j\omega\mu d}{(l_{xi}+l_{yi})(l_{xj}+l_{yj})} \sum_{m=1}^{\infty}\sum_{n=1}^{\infty} \frac{C_m^2 C_n^2}{P_x P_y (k_m^2 + k_n^2 - k^2)} \times \\ & \cos(k_m T_{xi}) \cos(k_n T_{yi}) \cos(k_m T_{xj}) \cos(k_n T_{yj}) \times \\ & \left[l_{xi} \mathrm{sinc}(k_m \frac{l_{xi}}{2}) \cos(k_n \frac{l_{yi}}{2}) + l_{yi} \cos(k_m \frac{l_{xi}}{2}) \mathrm{sinc}(k_n \frac{l_{yi}}{2}) \right] \times \\ & \left[l_{xj} \mathrm{sinc}(k_m \frac{l_{xj}}{2}) \cos(k_n \frac{l_{yj}}{2}) + l_{yj} \cos(k_m \frac{l_{xj}}{2}) \mathrm{sinc}(k_n \frac{l_{yj}}{2}) \right]. \end{aligned} \tag{3.7}$$

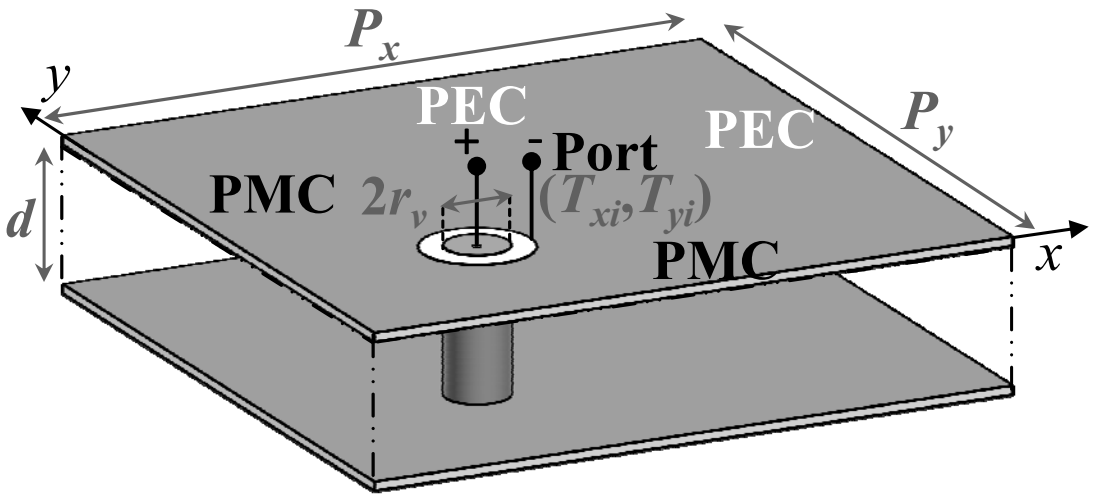

Fig. 3.16 Parallel-plate structure with a via connecting with the bottom plane surrounded by two PMC walls along *x*- and *y*-axis and two PEC walls on the other two sides.

Similarly, the self impedance Z_{ii} can be derived as

$$Z_{ii} = \frac{j\omega\mu d}{(l_{xi}+l_{yi})^2}\sum_{m=1}^{\infty}\sum_{n=1}^{\infty}\frac{C_m^2 C_n^2}{P_x P_y (k_m^2+k_n^2-k^2)}\times\left[\cos(k_m T_{xi})\cos(k_n T_{yi})\right]^2\times \left[l_{xi}\mathrm{sinc}(k_m\frac{l_{xi}}{2})\cos(k_n\frac{l_{yi}}{2})+l_{yi}\cos(k_m\frac{l_{xi}}{2})\mathrm{sinc}(k_n\frac{l_{yi}}{2})\right]^2. \quad (3.8)$$

and approximated, in the low frequency range ($k_m^2+k_n^2 \gg k^2$), as

$$\begin{aligned} Z_{ii} &\approx \frac{j\omega\mu d}{(l_{xi}+l_{yi})^2}\sum_{m=1}^{\infty}\sum_{n=1}^{\infty}\frac{C_m^2 C_n^2}{P_x P_y (k_m^2+k_n^2)}\times\left[\cos(k_m T_{xi})\cos(k_n T_{yi})\right]^2\times \\ &\left[l_{xi}\mathrm{sinc}(k_m\frac{l_{xi}}{2})\cos(k_n\frac{l_{yi}}{2})+l_{yi}\cos(k_m\frac{l_{xi}}{2})\mathrm{sinc}(k_n\frac{l_{yi}}{2})\right]^2 \\ &= j\omega L_{eq} \end{aligned} \quad (3.9)$$

, where

$$L_{eq} = \sum_{m=1}^{\infty}\sum_{n=1}^{\infty}\frac{\mu d C_m^2 C_n^2}{(l_{xi}+l_{yi})^2 P_x P_y (k_m^2+k_n^2)}\times\left[\cos(k_m T_{xi})\cos(k_n T_{yi})\right]^2\times \left[l_{xi}\mathrm{sinc}(k_m\frac{l_{xi}}{2})\cos(k_n\frac{l_{yi}}{2})+l_{yi}\cos(k_m\frac{l_{xi}}{2})\mathrm{sinc}(k_n\frac{l_{yi}}{2})\right]^2. \quad (3.10)$$

The parallel-plate structure shown in Fig. 3.16 is used to verify the accuracy of the

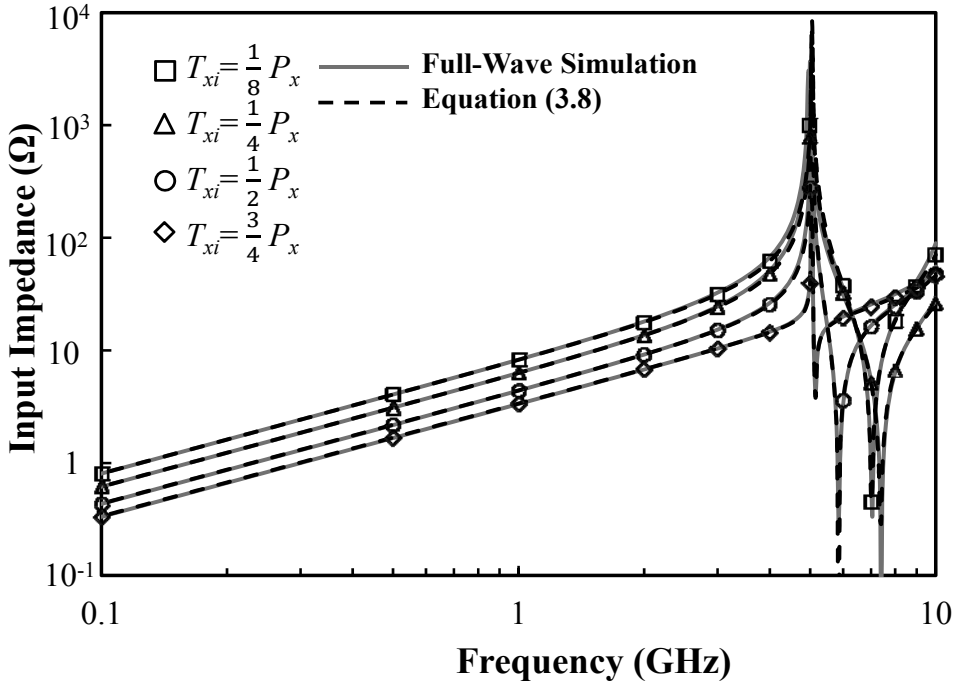

(a)

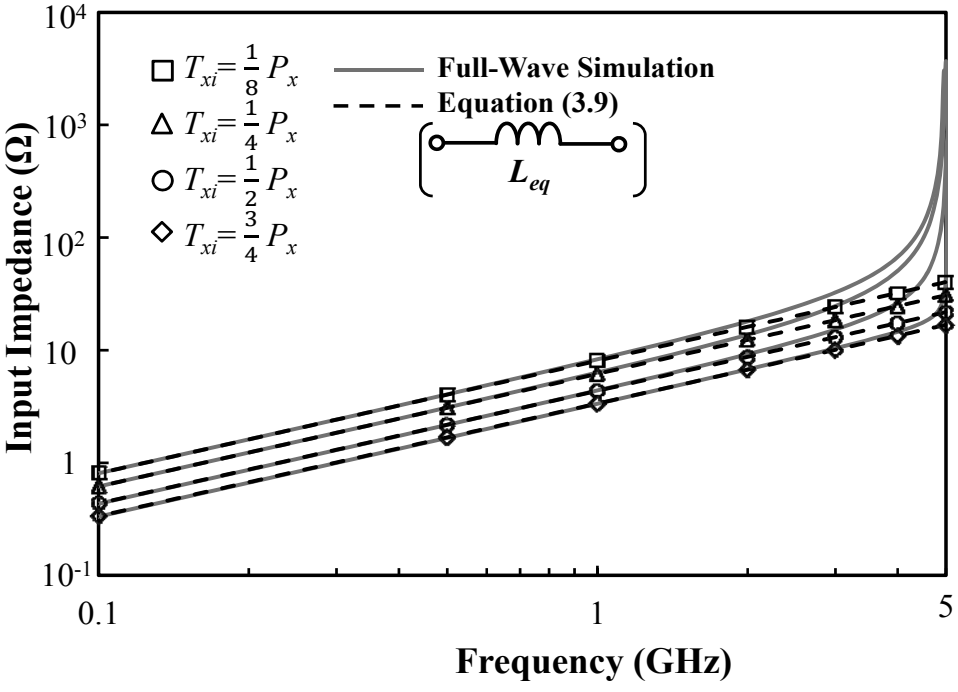

(b)

Fig. 3.17 Input impedance of parallel-plate structure shown in Fig. 3.16 (a) calculated by full-wave simulation and (3.8) and (b) approximated by (3.9).

derived formula (3.8). The geometrical parameters are $P_x = P_y = 10$ mm, $d = 0.73$ mm, and $r_v = 0.1$ mm. The location of port is the center of the via. Four cases for the via located at $T_{xi} = T_{yi} = \frac{1}{8}P_x$, $T_{xi} = T_{yi} = \frac{1}{4}P_x$, $T_{xi} = T_{yi} = \frac{1}{2}P_x$, and $T_{xi} = T_{yi} = \frac{3}{4}P_x$ are calculated by full-wave simulation, by (3.8), and by (3.9). The comparison between the results form full-wave simulation and from (3.8) is shown in Fig. 3.17(a). It indicates that the results from (3.8) agree well with those from full-wave simulation. Fig. 3.17(b) shows the comparison between the results by full-wave simulation and (3.9). It shows the formula (3.9) is a good approximation for extracting the equivalent frequency-independent inductance of the structure below the first resonant frequency 5.05 GHz. The equivalent inductance L_{eq} are 1.28, 0.98, 0.69, 0.53 nH for the cases of $T_{xi} = T_{yi} = \frac{1}{8}P_x$, $T_{xi} = T_{yi} = \frac{1}{4}P_x$, $T_{xi} = T_{yi} = \frac{1}{2}P_x$, and $T_{xi} = T_{yi} = \frac{3}{4}P_x$, respectively. The equivalent inductance becomes lower when the via moves toward the two PEC walls because of the smaller current loop.

3.3.2 Lower- and Upper-Bound Cutoff Frequencies Prediction

Fig. 3.18 (a) shows the equivalent circuit model of the quartered model of multiple vias EBG structure at lower-bound cutoff frequency. The effect of the electric field between the top plane and the embedded patch is modeled using the parallel-plate capacitance C_p calculated by

$$C_p = \frac{\varepsilon p^2}{4h_1} \tag{3.11}$$

The effect of the two-dimensional current distribution can be approximated by the equivalent inductance L_{eqL} of the parallel-plate structure shown in Fig. 3.16. The

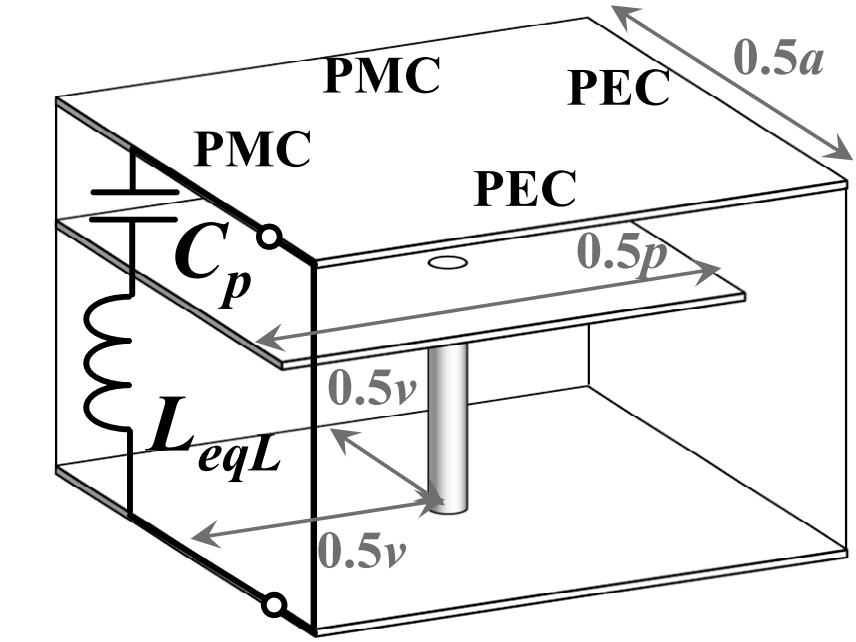

(a)

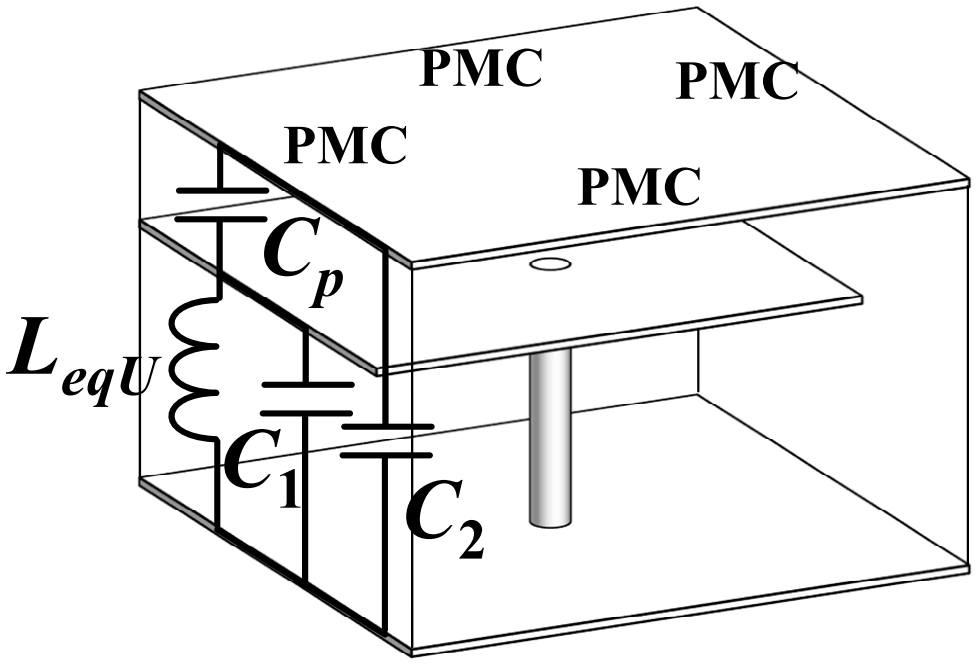

(b)

Fig. 3.18 Equivalent circuit model of quartered model for (a) lower- and (b) upper-bound cutoff frequencies.

inductance L_{eqL} can be estimated by (3.10) with $P_x = P_y = \frac{a}{2}$, $d = h_1 + h_2$, $l_{xi} = l_{yi} = \frac{\pi r_v}{2}$, and $T_{xi} = T_{yi} = \frac{v}{2}$. The lower-bound cutoff frequency can be predicted by

$$f_L = \frac{1}{2\pi\sqrt{C_p L_{eqL}}}. \tag{3.12}$$

Regarding upper-bound cutoff frequency, the equivalent circuit model of the quartered model is shown in Fig. 3.18(b). In the circuit model, C_p is the parallel-plate capacitance between the top plane and patch. C_1 and C_2 are the parallel-plate capacitance between the patch and bottom plane and between top plane and bottom plane, respectively. They can be calculated by

$$C_1 = \frac{\varepsilon p^2}{4h_2} \tag{3.13}$$

and

$$C_2 = \frac{\varepsilon(a^2 - p^2)}{4(h_1 + h_2)}. \tag{3.14}$$

The equivalent inductance L_{eqU} is approximated by the inductance of the resonant cavity model with 4 PMC walls with $P_x = P_y = \frac{a}{2}$, $d = h_2$, $l_{xi} = l_{yi} = \frac{\pi r_v}{2}$, and $T_{xi} = T_{yi} = \frac{v}{2}$ and can be estimated by (2.59). Based on the equivalent circuit model, the upper-bound cutoff frequency is calculated by

$$f_U = \frac{1}{2\pi\sqrt{L_{eqU}\left(C_1 + \frac{C_p C_2}{C_p + C_2}\right)}} \tag{3.15}$$

It is necessary to check if the derived formulas can well predict the lower- and upper-bound cutoff frequencies. Considering the geometric parameters (a, p, r_v, h_1, h_2) = (20 mm, 18 mm, 0.15 mm, 0.1 mm, 0.5 mm), we sweep the variable v from 2

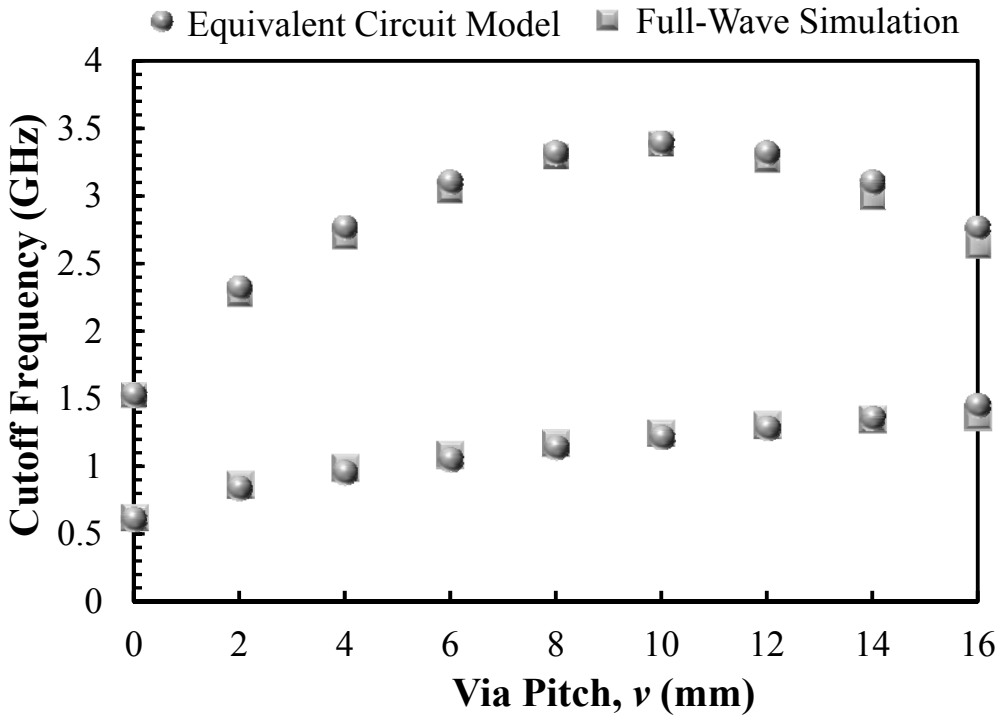

Fig. 3.19 Estimated and simulated lower- and upper-bound cutoff frequencies of 2-D multiple vias EBG structure and mushroom EBG structure (v = 0 mm).

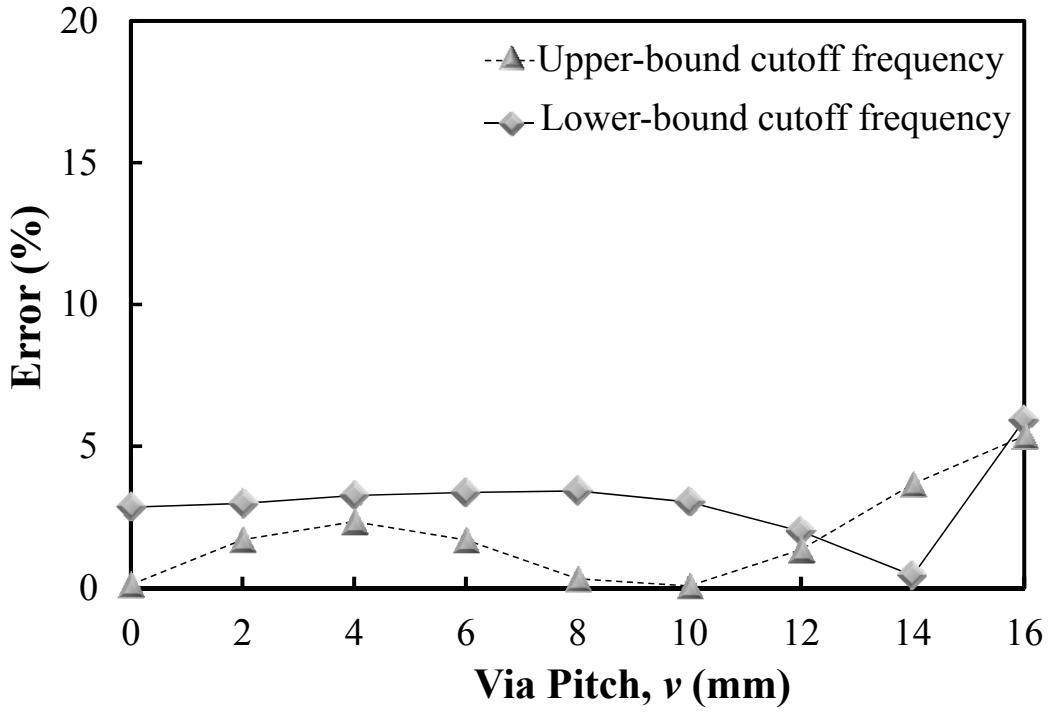

Fig. 3.20 Error of lower- and upper-bound cutoff frequencies from derived formulas and full-wave simulation.

mm to 16 mm to compare the lower- and upper-bound cutoff frequencies from (3.12) and (3.15), respectively, with those from full-wave simulation. The results are shown in Fig. 3.19. The estimated results agree well with the full-wave results. It can be found the values and trend of both lower- and upper-bound cutoff frequencies with respect to via pitch v can be well predicted. Fig. 3.20 shows the errors of the results between the derived formulas and full-wave simulation. The maximum errors of lower- and upper-bound cutoff frequencies are only 5.9 % for the former and 5.4 % for the latter. The results imply us that the resonant cavity model can well characterize the effect of the two-dimensional current distribution and give us a tool to approximate the equivalent inductance of the equivalent circuit model for multiple vias EBG structure. It shows that the method is good enough to predict the bandgap of multiple vias EBG structure and mushroom EBG structure (the case of v = 0 mm shown in Fig. 3.19 and Fig. 3.20).

3.4 Experiment Results

To verify the accuracy of the design concepts for bandwidth enhancement based on via arrangement, measured results have to be compared to numerically simulated ones. A set of test vehicles including multiple vias EBG, mushroom EBG structure, and bared board has been manufactured by using FR4 PCB fabrication. The relative permittivity of the substrate is 3.9. The bared board consists of solid power and ground planes on a dielectric substrate whose thickness is 0.6 mm. Fig. 3.21(a) shows the fabricated sample of the multiple vias EBG structure. The dimension of multiple vias EBG power/ground plane is 60 mm by 60 mm with 3 by 3 unit cells. The geometric parameters are (a, p, r_v, h_1, h_2) = (20mm, 18 mm, 0.15 mm, 0.1 mm, 0.5 mm). Two test ports are set at (2 mm, 2 mm) and (40 mm, 57 mm).

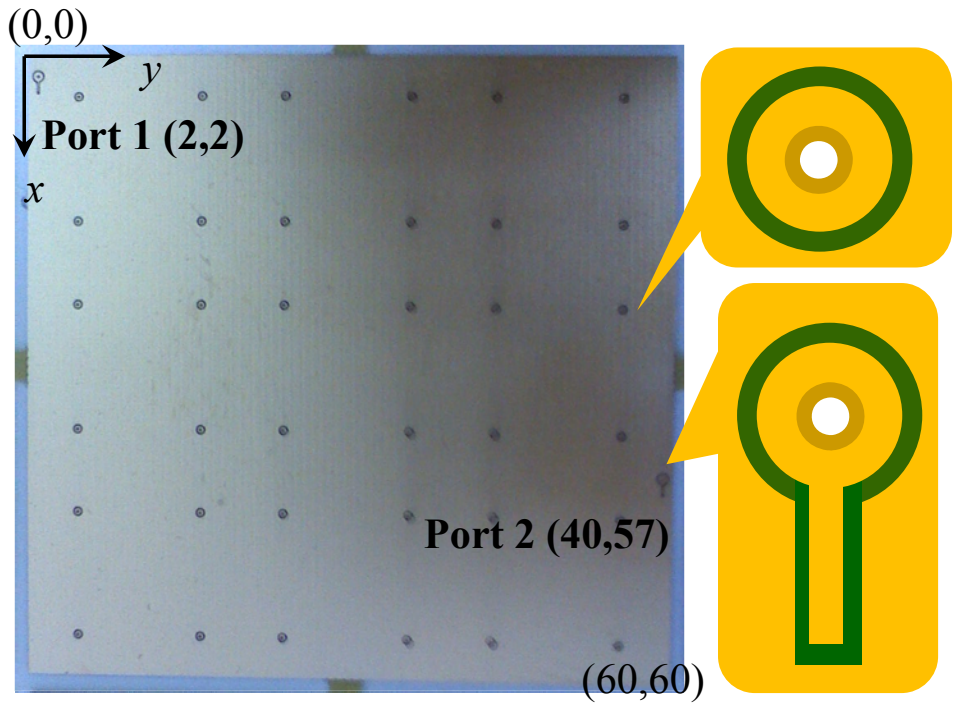

(a)

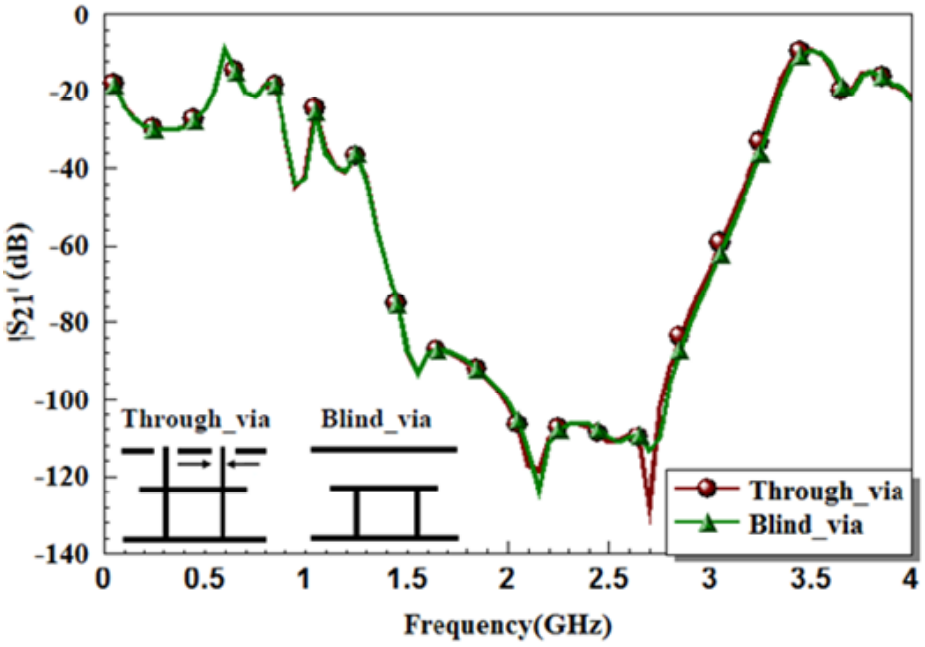

(b)

Fig. 3.21 (a) Photo of multiple vias EBG test vehicle using PTH vias fabrication. (b) Simulated *S*-parameter of multiple vias EBG structure for PTH and blind vias.

For the PCB fabrication, the vias connecting the patches to the ground plane are plated through-hole (PTH) vias instead of blind vias or buried vias because of cost considerations. However, to maintain the DC voltage level of power plane, clearances are used to isolate the power plane from the plated through-hole vias. Fig. 3.21(a) also shows the clearances and the fed-in pad. The simulation results of the multiple vias EBG structure implemented by PTH vias and blind vias are shown in Fig. 3.21 (b). It is illustrated that the two kinds of structures do not have any significant impact on the electrical properties in the frequency range of interest.

The parameter $|S_{21}|$ representing the noise coupling coefficient is measured by using an Agilent N5230A vector network analyzer and Cascade Microtech microprobes (ground-signal-ground with 350 μm pitch) on a microprobe station. Fig. 3.22 shows the simulated and measured results. The results of multiple vias EBG structure with v = 2 mm, v = 10 mm, and v = 16 mm are shown in Fig. 3.22(a). The comparisons of bared board, mushroom EBG structure, and multiple vias EBG structure with v = 8 mm are illustrated in Fig. 3.22(b). The measured data are consistent with the simulated ones. Although there is about 20 dB difference between the measured $|S_{21}|$ and the simulated one in the bandgap, the measured $|S_{21}|$ is at the level about -80 dB near the noise floor of the measurement equipment.

From the measured results, one can also note that lower-bound cutoff frequency shifts downward from 1.41 GHz to 0.91 GHz as v decreases from 16 mm to 2 mm. The upper-bound cutoff frequency of the multiple vias EBG structure with v = 10 mm is 3.48 GHz. It presents the highest upper-bound cutoff frequency than others. The accuracy of the design concept for multiple vias EBG discussed in section 3.1.2 is also confirmed.To compare the $|S_{21}|$ of multiple vias EBG structure with that of bared board, the multiple vias EBG structure power/ground plane provides over 30 dB of

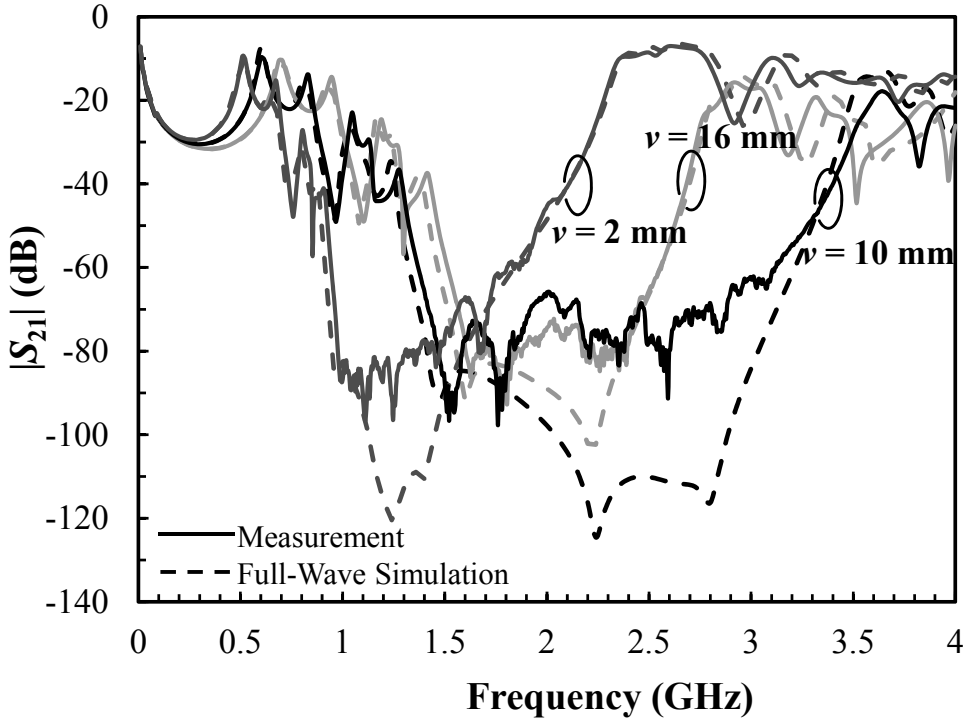

(a)

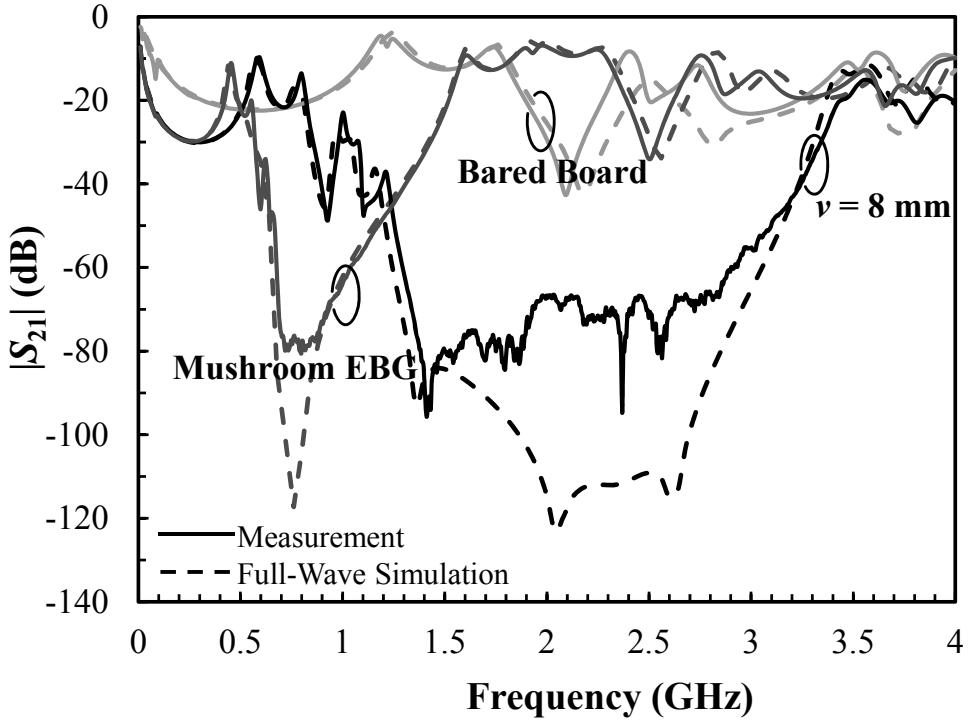

(b)

Fig. 3.22 Measured and simulated results of multiple vias EBG structure with v =1 mm, v= 5mm, and v = 8mm and (b) comparison of bared board, mushroom EBG, and multiple vias EBG structures.

noise isolation in the bandgap. Comparing the $|S_{21}|$ of multiple vias EBG structure with that of mushroom EBG structure, we can find the bandwidth ratios of multiple vias EBG structure and mushroom EBG structure are 176 % and 129 %, respectively. It is confirmed that not only absolute bandwidth but also bandwidth ratio is enhanced by multiple vias EBG structure.

3.5 Summary

In this chapter, we propose the multiple vias EBG structure and explain the mechanism of lower- and upper-bound cutoff frequencies of the EBG structure. From the comparison of multiple vias EBG and mushroom EBG structure, it is given that multiple vias EBG structure is with higher lower-bound cutoff frequency because of the smaller current loop and with higher upper-bound cutoff frequency because of the more vias to reduce the size of equivalent cavity. By sweeping the via pitch v of multiple vias EBG structure, it can be found that the highest upper-bound cutoff frequency is present for the multiple EBG structure with v = 10 mm. As regards bandwidth ratio, the maximum bandwidth ratio of the multiple vias EBG with v = 8 mm and the mushroom EBG structure are 181 % and 145 %, respectively, under the assumption of the same dimension. It is worth emphasizing that not only absolute bandwidth but also bandwidth ratio is enhanced by multiple vias EBG structure.

An equivalent circuit model with transmission-line sections is used to model the unit cell of one-dimensional multiple vias EBG structure. We derive formulas for estimating the lower- and upper-bound cutoff frequencies based on the half resonators. The error between estimated and full-wave results for upper-bound cutoff frequency is relative high because the two-dimensional current distribution is not taken into account well in the transmission-line model. Based on the resonant cavity model, the equivalent

inductance in the equivalent circuit model of quartered model can be extracted and for estimating the lower- and upper-bound cutoff frequencies. The maximum errors of lower- and upper-bound cutoff frequencies with respect to different via pitches are only 5.9 % for the former and 5.4 % for the latter. It shows that the method is good enough to predict the bandgap of multiple vias EBG structure and mushroom EBG structure. Finally, the test boards are manufactured by using FR4 PCB fabrication. The measured results agree well with the simulated ones. The design concept is verified and confirmed.

Chapter 4 Miniaturized and Stopband-Enhanced Interleaved EBG Power/Ground Planes

In this Chapter, a four-layer EBG structure with interleaved two identical patches and location-variable power/ground vias is proposed. It is based on different electromagnetic characteristics from mushroom and double-stacked EBG structures, even though the interleaved EBG structure looks like consisting of two identical mushroom structures. Using the concept of the interleaved EBG structure, both the electrical size, which is normalized to the wavelength in the substrate, and the bandwidth ratio are improved. The miniaturization (lower f_L) is achieved by additional shunt capacitance of the interleaved patches, and the bandwidth is enhanced by the optimum location of power/ground vias.

4.1 Interleaved EBG Structure

4.1.1 Geometry and Design Concept

Fig. 4.1(a) shows the unit cell of the interleaved EBG structure distributing periodically in two-dimensional direction. As shown in Fig. 4.1(b), the structure is implemented in a four-layer PCB or package substrate. The top and bottom layer is assumed the power and ground planes, respectively. In the unit cell, two patches with the same dimension are embedded between power and ground planes. In order to arrange these two patches alternately distributing in the vertical direction, one power via is used to connect the solid power plane with the embedded power patch on layer 3; the

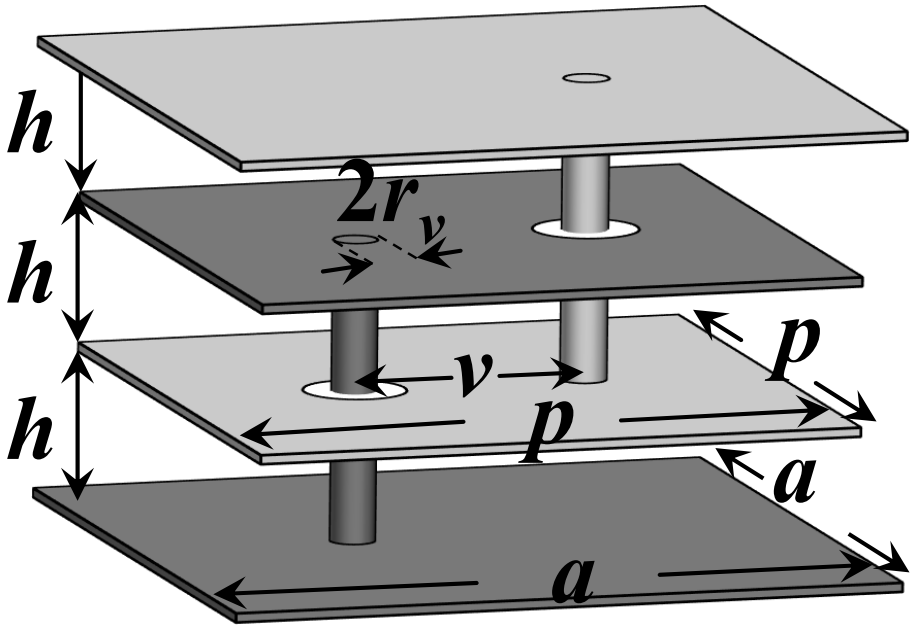

(a)

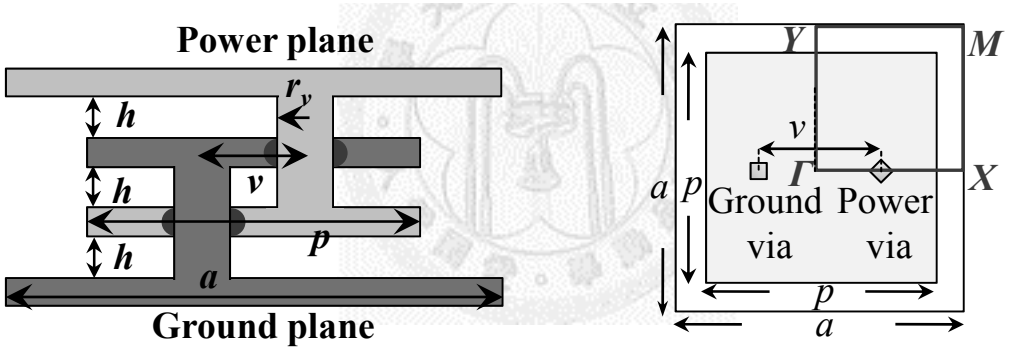

(b) (c)

Fig. 4.1 (a) Geometry of unit cell of interleaved EBG structure in (b) side view and (c) top view.

other via is used to short the solid ground plane and the embedded ground patch on layer 2.

The geometric parameters of the unit cell are: the side length of the square unit cell a, the side length of the two embedded square patches p, the center-to-center pitch of power/ground via pair v, the radius of vias r_v, and the thickness of each dielectric

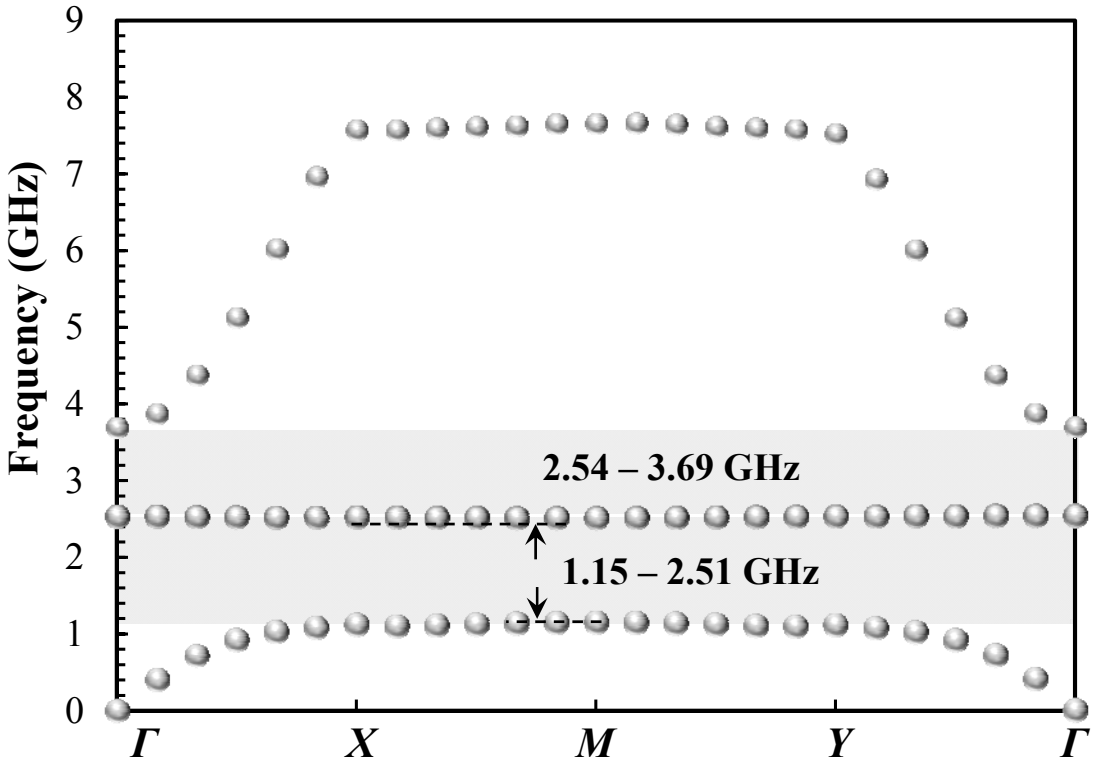

Fig. 4.2 Dispersion diagram of Interleaved EBG structure with (a, p, v, r_v, h) = (10 mm, 9.4 mm, 1 mm, 0.1 mm, 0.2 mm).

substrate h. The top view of the interleaved EBG structure is depicted in Fig. 4.1(c). In order to keep the symmetry of the unit cell, the center of the pair of the power/ground vias is anchored at the center of the patches. To assess the influence of the via location on the bandwidth of the bandgap, the parameter v is set to describe the different via arrangement.

Dispersion diagram is usually used to describe the propagation property of the periodic structure. Fig. 4.2 shows the dispersion diagram of the interleaved EBG structure with geometric parameters (a, p, v, r_v, h) = (10 mm, 9.4 mm, 1 mm, 0.1 mm, 0.2 mm), which is simulated by 3-D full-wave simulator (Ansys HFSS). The relative permittivity of the substrate is 4. As shown in Fig. 4.2, there is a wide bandgap in the

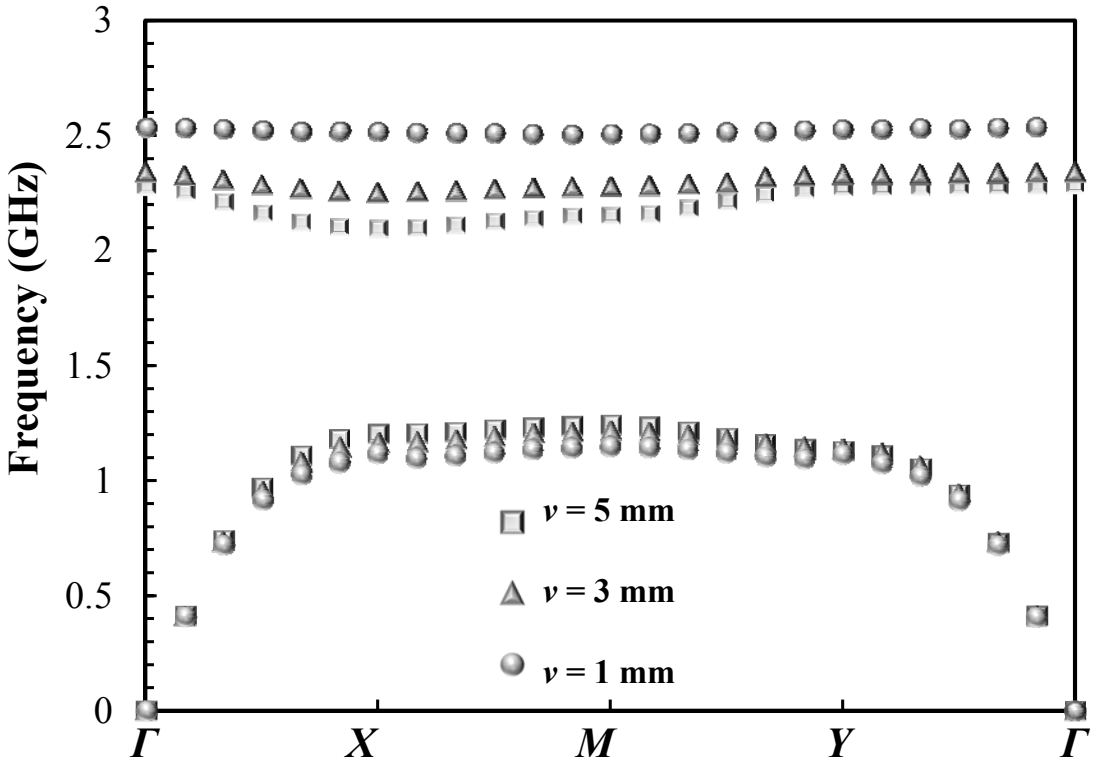

Fig. 4.3 Dispersion diagrams of interleaved EBG structures with different via pitches of 1 mm, 3 mm, and 5 mm.

frequency range from 1.15 GHz to 3.69 GHz. However, an additional propagation mode appears and divides the bandgap into two segments. The first bandgap is from 1.15 GHz to 2.51 GHz and the immediate second bandgap is from 2.54 GHz to 3.69 GHz.

To indicate the design concept of the interleaved EBG structure, Fig. 4.3 shows the dispersion diagrams of the interleaved EBG structures with different via pitches *v*. As shown in the figure, the lower-bound cutoff frequencies of the interleave EBG structures are decided by the frequencies at *M* point of the first propagation mode. They are 1.15 GHz, 1.21 GHz, and 1.24 GHz for the interleaved EBG structures with via pitches of 1 mm, 3 mm, and 5 mm, respectively. As regards upper-bound cutoff frequency, we can find that it is determined by the frequency at *X* point of the second mode. This behavior

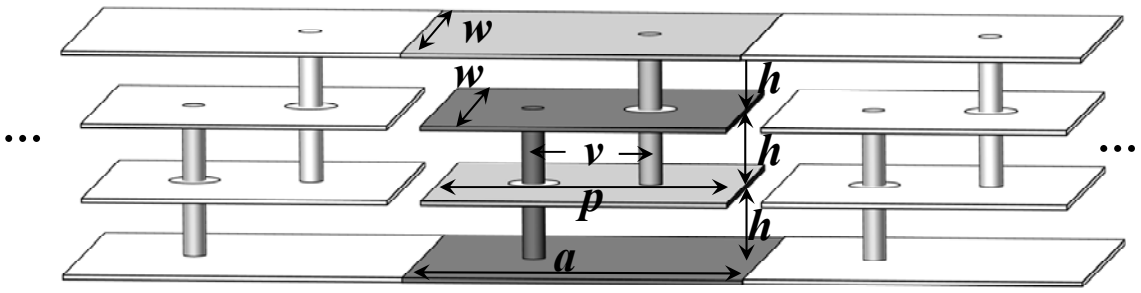

Fig. 4.4 Geometry of one-dimensional interleaved EBG structure.

is quite different from the upper-bound cutoff frequency of mushroom EBG structure, which is determined by the frequencies at Γ of the second mode. The upper-bound cutoff frequencies of the interleaved EBG structures with via pitches of 1 mm, 3 mm, and 5 mm are 2.51 GHz, 2.25 GHz, and 2.10 GHz, respectively. The ratios of the bandwidths to the lower-bound cutoff frequencies are 118.3 %, 86 %, and 69.4 % for the interleaved EBG structure with via pitches of 1 mm, 3 mm, and 5 mm, respectively. By reducing the via pitch v, the lower-bound cutoff frequency is slightly improved and the upper-bound cutoff frequency is pushed toward significantly higher band. A widest bandwidth design can be accomplished if the via pitch is kept as narrower as possible. In general, it is decided by the fabrication limitation for different substrate techniques.

4.1.2 One-Dimensional Equivalent Circuit Model and Bandgap Analysis

To analyze the bandgap mechanism of the interleaved EBG structure and understand the physical meaning, the one-dimensional case, which means the structure is repeated periodically only in one direction, is considered first and shown in Fig. 4.4. The geometric parameters are denoted as the length of the unit cell a, the length of the two embedded patches p, the width of the parallel plate w, the pitch of the power/ground vias pair v, the radius of vias r_v, and the substrate thickness of each layer h. The geometric parameters are chosen as (a, p, w, v, r_v, h) = (10 mm, 9.4 mm, 9.4 mm, 1 mm,

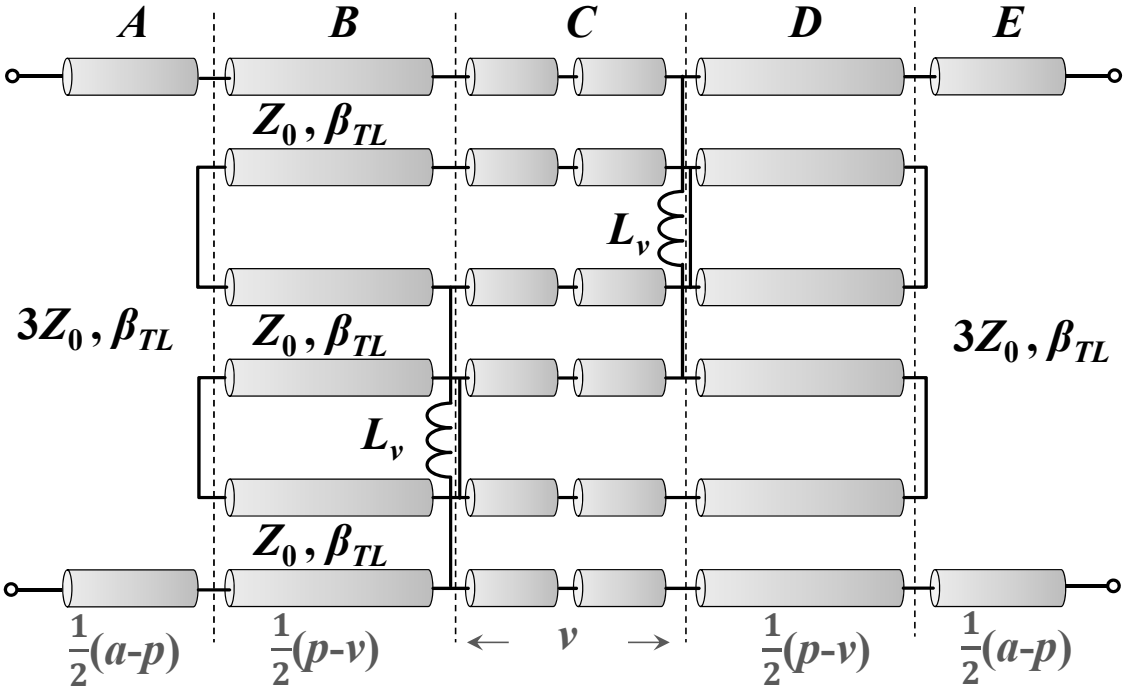

Fig. 4.5 One-dimensional equivalent circuit model of interleaved EBG structure using transmission-line sections.

0.1 mm, 0.2 mm) here. The relative permittivity of the dielectric substrate is 4.

According to the physical structure shown in Fig. 4.4, the corresponding equivalent circuit model consisting of transmission-line sections is constructed and shown in Fig. 4.5. It is divided into five parts. Part *B*, *C*, and *D* are four-layer stack-up structure. Each of them is modeled as the three transmission-line sections with characteristic impedance of Z_0 formed by adjacent metal planes. Part *A* and *E* represent a transmission-line section with characteristic impedance of $3Z_0$ formed by the power/ground parallel plates. The characteristic impedance Z_0 obtained by considering them as the parallel-plate transmission line is 4 Ω in this case. L_v, the parasitic inductance of the via extracted from full-wave simulator, is 233.6 pH.

The unit cell of the interleaved EBG structure has a rotational symmetry of 180°

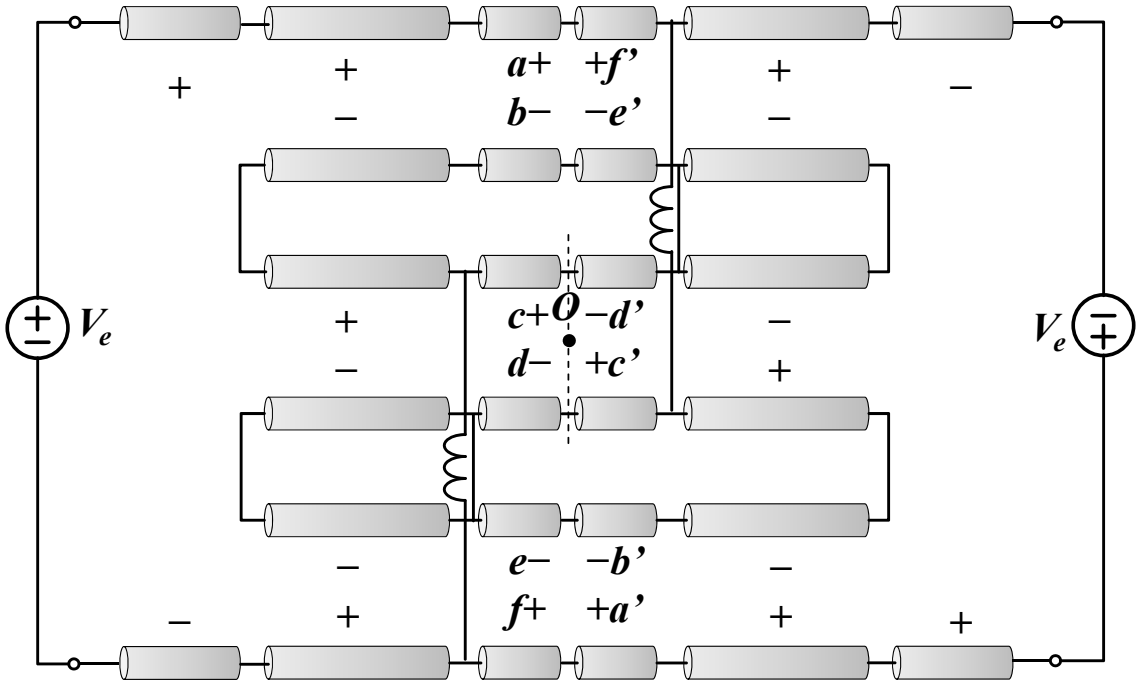

(a)

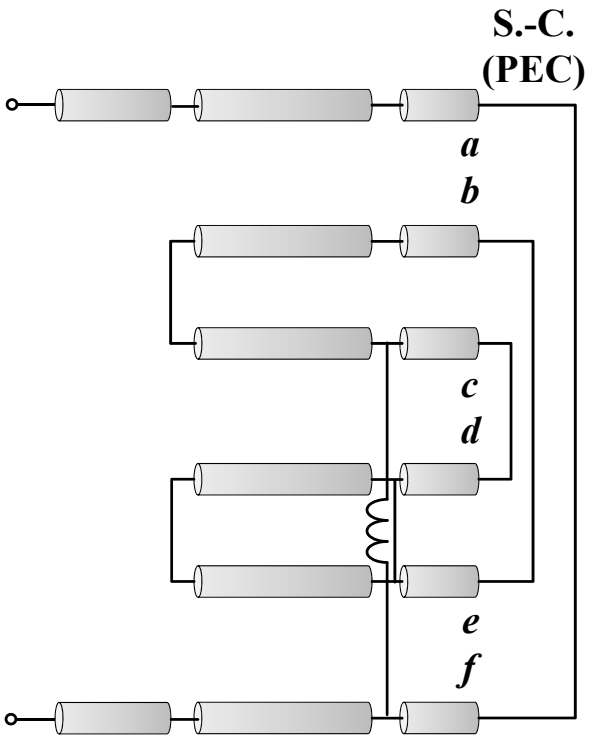

(b)

Fig. 4.6 Equivalent circuit model with (a) even-mode field pattern, which can be bisected into two identical (b) even-mode half circuits.

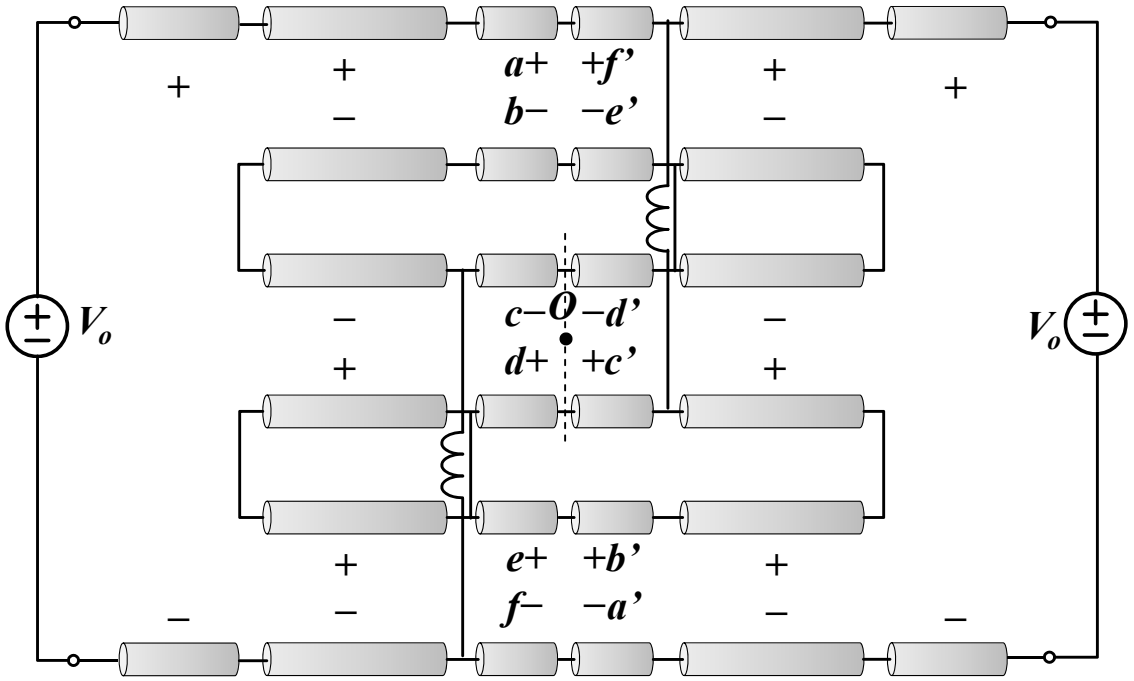

(a)

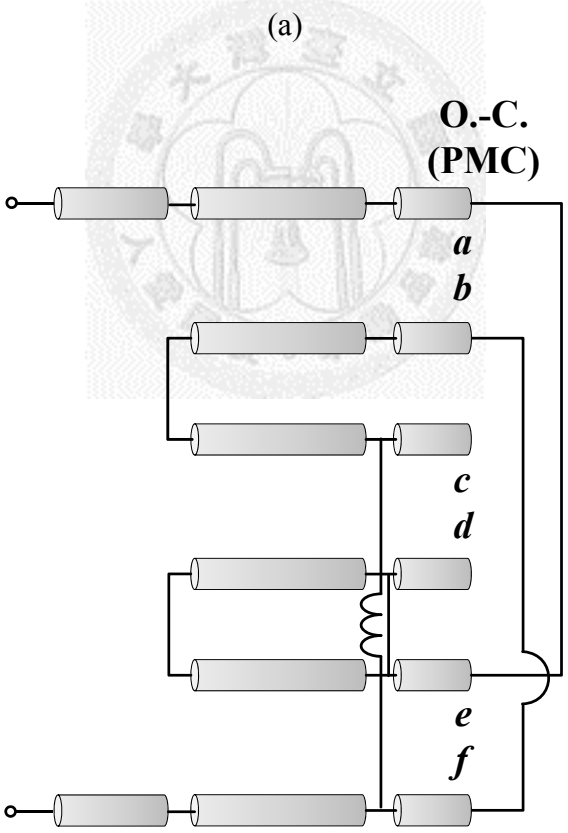

(b)

Fig. 4.7 Equivalent circuit model with (a) odd-mode field pattern, which can be bisected into two identical (b) odd-mode half circuits.

with respect to the center point *O*. As shown in Fig. 4.6(a), the points *a*, *b*, *c*, *d*, *e*, and *f* at the left side of point *O* are with rotational symmetry to the points of *a'*, *b'*, *c'*, *d'*, *e'*, and *f'* at the right of point *O*, respectively. Naturally, there are two types of eigenmodes with symmetrical (or even) and anti-symmetrical (or odd) electric potential distribution (or voltage) with respect to point *O*. Fig. 4.6(a) shows the electric potentials along the points from *a* to *f* and *a'* to *f'* for the even-mode case, and the corresponding half circuit for the even mode is shown in Fig. 4.6(b). The half circuit is formed according to the symmetrical plane crossing point *O*. In Fig. 4.6(b), the end of the conductor *c* is shorted to that of conductor *d* due to the equal voltage for *c* and *c*' (or *d* and *d*'). It is the same reason for shorting the ends of conductors *a* and *b* to those of conductors *f* and *e*, respectively. However, for the anti-symmetrical mode (or odd mode) with the field polarity shown in Fig. 4.7(a), the corresponding half circuit is shown in Fig. 4.7(b) with different boundary condition.

As discussed in Section 2.1.2, the lower- and upper-bound cutoff frequencies of the bandgap can be predicted by solving the resonant frequencies of the half circuits with proper boundary conditions. The lower-bound cutoff frequency of the interleaved EBG structure is determined by the resonant frequency of the odd-mode half circuit with short-circuited (PEC) boundary at input port. The half resonator is shown in Fig. 4.8(a). In terms of the upper-bound cutoff frequency of the interleaved EBG structure, it can be found that the cutoff frequency is decided by the resonant frequency of the even-mode half circuit with open-circuited (PMC) boundary at input port. As shown in Fig. 4.8(b), the half resonator has short-circuited (PEC) boundary on the right-hand side and open-circuited (PMC) boundary on the other side. This boundary condition is different from that of mushroom EBG structure, open-circuited (PMC) boundaries on both sides, at the upper-bound cutoff frequency. It is why the upper-bound cutoff frequency of the

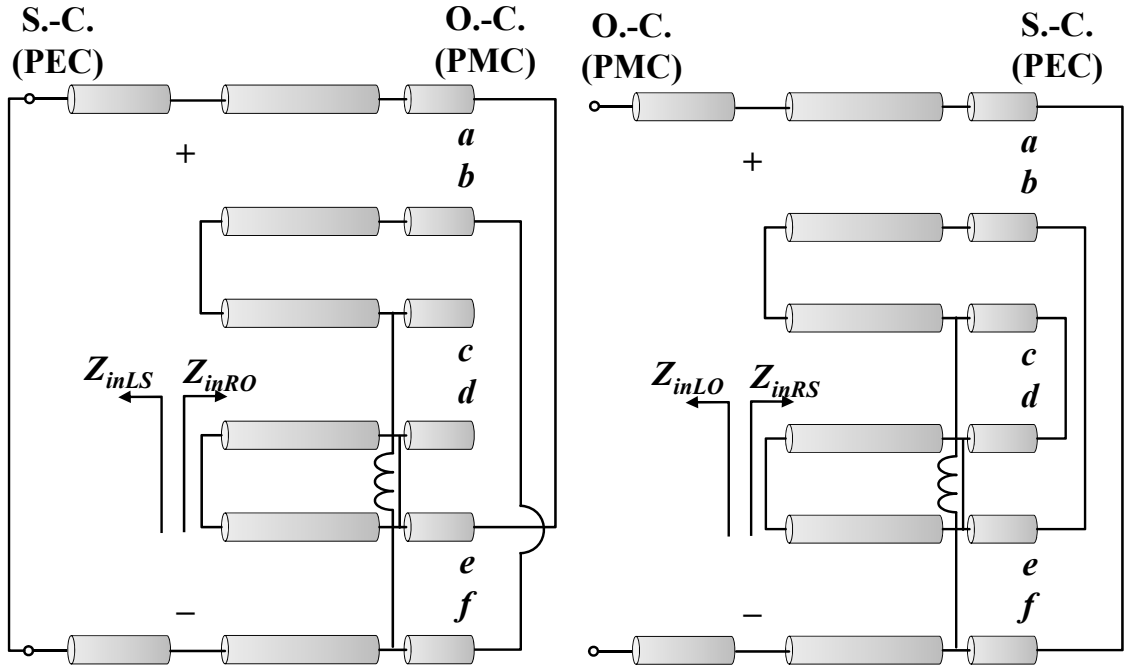

(a) (b)

Fig. 4.8 Half resonators for determining (a) lower- and (b) upper-bound cutoff frequencies of interleaved EBG structure.

interleaved EBG structure appears at the *X* point in the dispersion diagram shown in Fig. 4.3 as the above mentioned.

For the lower-bound cutoff frequency, we can use the resonant frequency of the half resonator shown in Fig. 4.8(a) to demonstrate the design concept of interleaved EBG structure for miniaturization. The resonant frequency can be obtained by solving $Z_{inRO} + Z_{inLS} = 0$. The frequency responses of impedance $|Z_{inRO}|$ and $|Z_{inLS}|$ of interleaved EBG structure are shown in Fig. 4.9 (a) using ADS. $|Z_{inLS}|$ increases monotonically from DC to 2 GHz because the short-ended transmission line is inductive. $|Z_{inRO}|$ decreases monotonically due to the capacitive behavior of the open-ended transmission line before 1.16 GHz as shown in the figure. The intersection of the impedance $|Z_{inRO}|$ and $|Z_{inLS}|$ is found at 1.15 GHz where is close to the lower-bound cutoff frequency, 1.1 GHz, solving

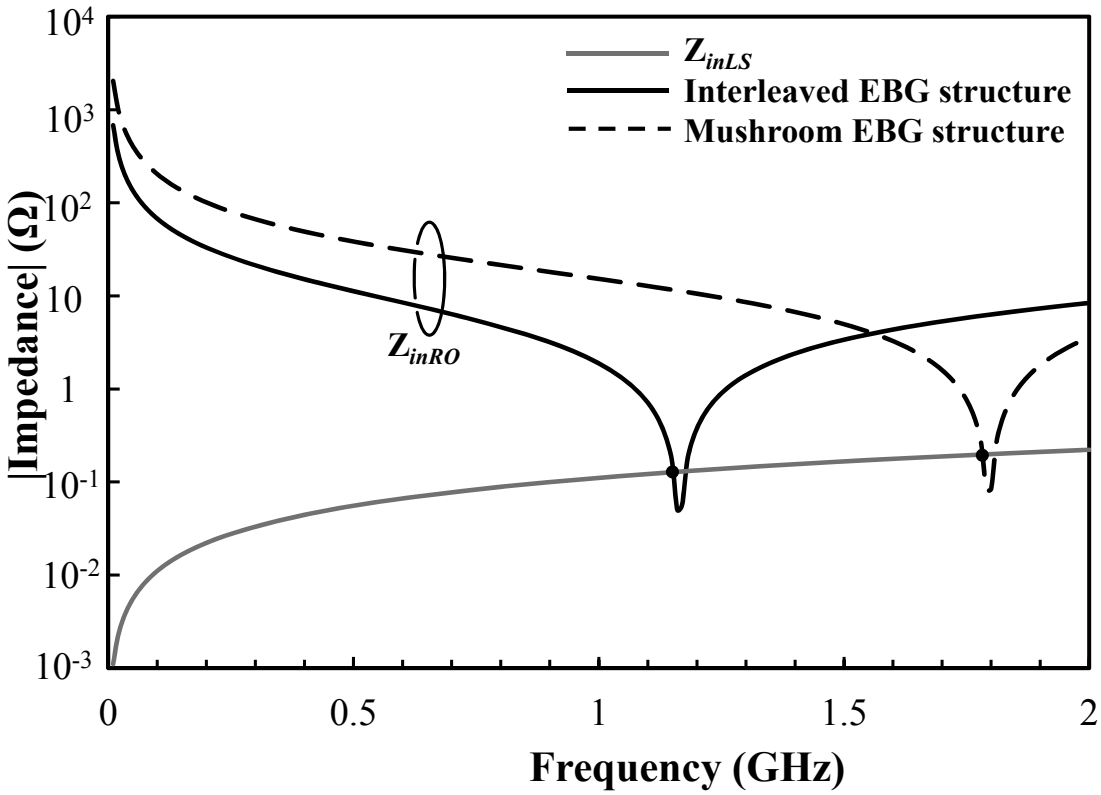

(a)

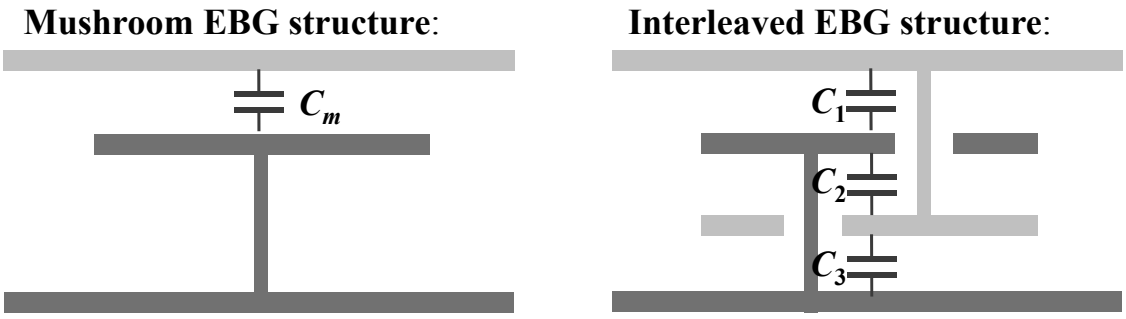

(b)

Fig. 4.9 (a) Behavior of half resonators for determining lower-bound cutoff frequency and (b) equivalent capacitance of the interleaved and mushroom EBG structure.

by full-wave simulation. The $|Z_{inRO}|$ of mushroom EBG structure with the same dimension is also shown in Fig. 4.9(a). The intersection of the impedance $|Z_{inRO}|$ and $|Z_{inLS}|$ of the mushroom EBG structure is 1.78 GHz, which is also close to the

lower-bound cutoff frequency, 1.74 GHz, solving by full-wave simulation.

It can be found the dip of $|Z_{inRO}|$ of the interleaved EBG structure is significantly lower than that of the mushroom EBG structure. Hence, the lower-bound cutoff frequency of interleaved EBG structure is lower than that of mushroom EBG structure. It is because the capacitance of the interleaved EBG structure formed by the alternate power and ground patches is three times larger than that of mushroom EBG structure. Fig. 4.9(b) shows the concept of the capacitance between the power and ground planes for the mushroom and interleaved EBG structure. It is found there are three parallel capacitors (C_1, C_2, and C_3) with total capacitance $C_1 + C_2 + C_3$ for the interleaved power/ground structure, but only one capacitor (C_m) for the mushroom EBG structure. Consequently, the lower-bound cutoff frequency is significantly decreased by the interleaved EBG structure, and thus the required layout area can be reduced.

As regards upper bound cutoff frequency, it is decided by the resonant frequency of half resonator shown in Fig. 4.8(b). Fig. 4.10 shows $|Z_{inLO}|$ and $|Z_{inRS}|$ behavior of the half resonator with different via pitches. The upper-bound cutoff frequency is the point where the inductive $|Z_{inRS}|$ and capacitive $|Z_{inLO}|$ intersect. The narrower via pitch leads to higher peak frequency, and thus higher upper-bound cutoff frequency. As shown in Fig. 4.10, the peak frequency nearly determines the intersection point, i.e., upper bound cutoff frequency, of $|Z_{inLO}|$ and $|Z_{inRS}|$. Another intuitive way to understand the effect of the via pitch on the upper-bound cutoff frequency is to see the resonant frequency of the right-hand part of the half resonator shown again in Fig. 4.11. The right-hand part of the half resonator is decomposed into two parts, part *A* and part *B*. It is shown clearly that Z_{inA} behaves inductive. The Z_{inA} is dominantly decided by series of the via inductance (L_v) and the small loop inductance (L_p) as shown in Fig. 4.11(a). It is clearly seen that Z_{inA} will become smaller as via pitch v decreases due to the reduction of L_p. In

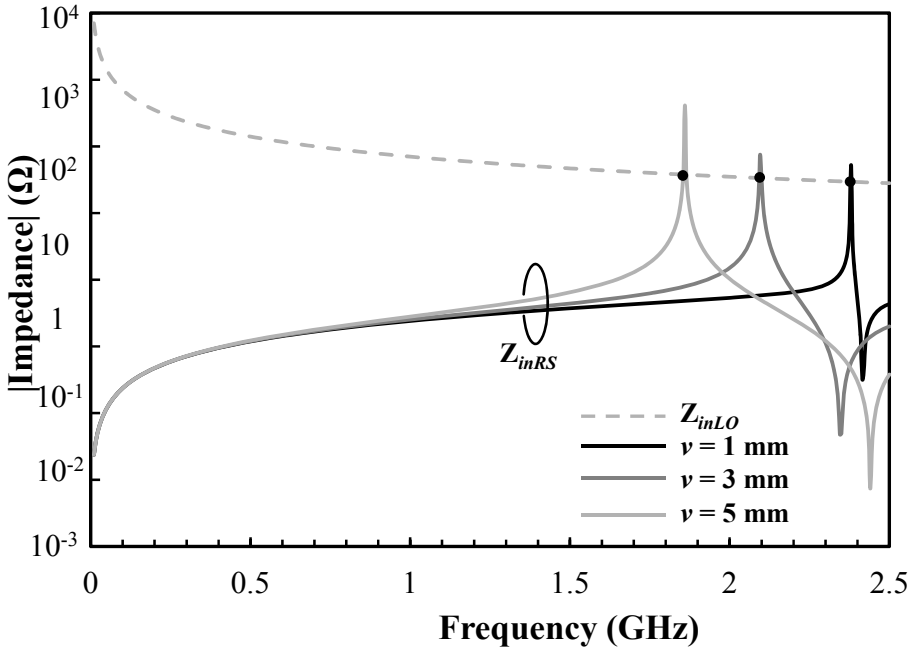

Fig. 4.10 Influence of via pitch on upper-bound cutoff frequency of interleaved EBG structure nearly determining by peak frequency of $|Z_{inRS}|$.

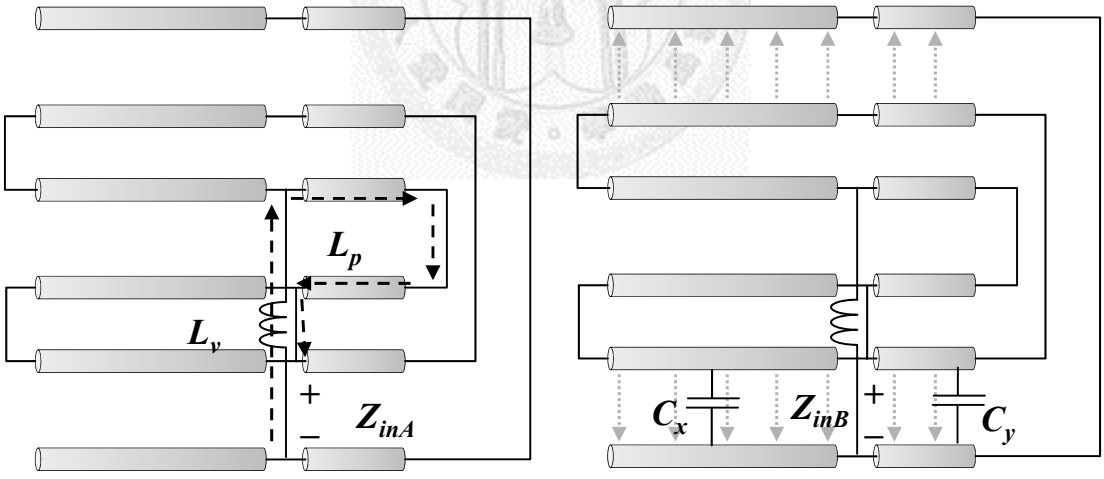

(a) (b)

Fig. 4.11 Right-hand part of half resonator for upper-bound cutoff frequency is divided into (a) part *A* and (b) part *B*.

terms of Z_{inB}, it behaves like a series connection of *LC* resonator. The capacitance

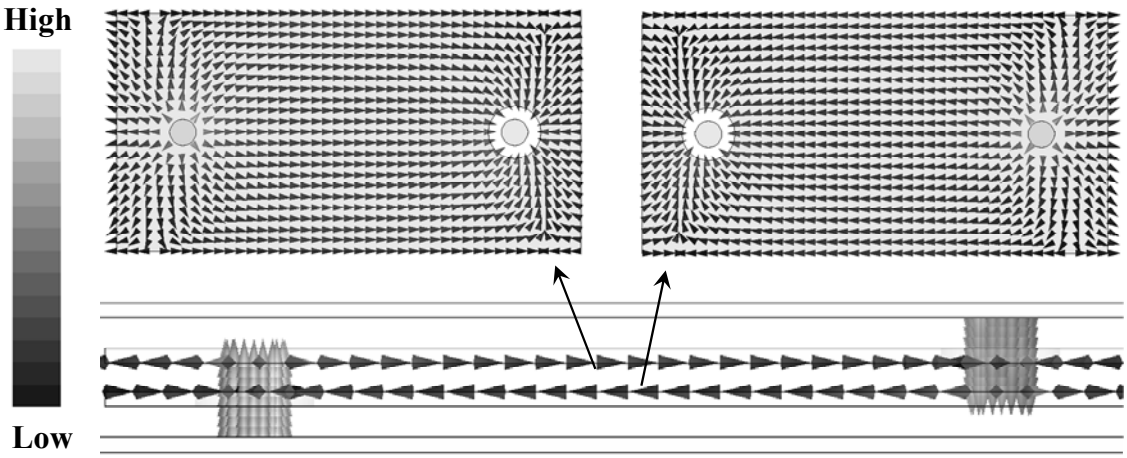

Fig. 4.12 Current distribution of interleaved EBG structure at upper-bound cutoff frequency.

results from the parallel of *Cx* and *Cy*. The equivalent series inductance is due to the via inductance. This inductance will become smaller when via pitch *v* decreases because the via becomes close to the center of the patch. Based on the above discussion, the narrowed via pitch, resulting in the decreased inductance of Z_{inA} and Z_{inB}, causes the increase of the resonant peak frequency, and thus the shift of upper-bound cutoff frequency. Fig. 4.12 shows the current distribution of an interleaved EBG structure at upper-bound cutoff frequency. It can be found that the currents on the embedded power/ground patches and power/ground vias result in a current loop. The fine pitch of power/ground vias is of benefit to reducing the size of the current loop. Thus the upper-bound cutoff frequency becomes in the higher frequency range.

To check the correctness of the equivalent circuit model and the corresponding explanation, Fig. 4.13 shows lower- and upper-bound cutoff frequencies of 1-D interleaved EBG structure from full wave simulation and proposed model. Good agreement is seen between them. The results also show that the lower-bound cutoff

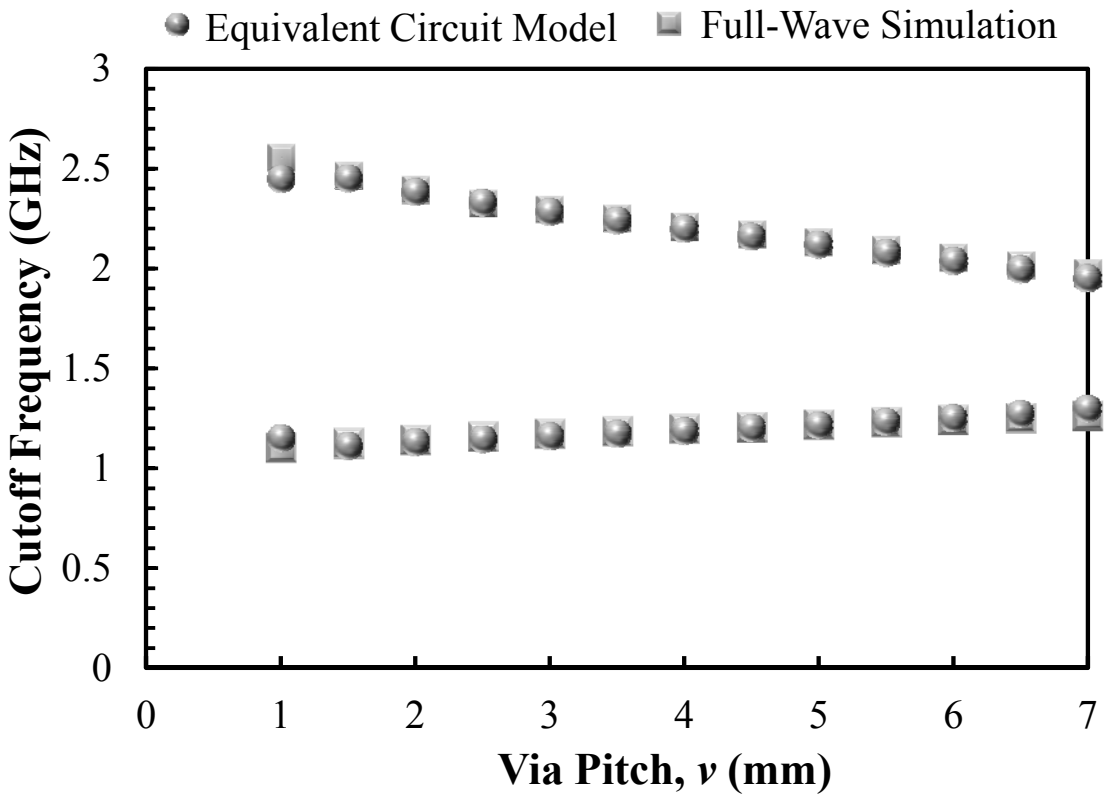

Fig. 4.13 Lower- and upper-bound cutoff frequencies of 1-D interleaved EBG structure from full wave simulation and proposed model.

frequency of the interleaved EBG structure is lower than that of mushroom EBG structure, 1.74 GHz. The enhanced bandwidth can also be achieved by narrowing the pitch of power/ground vias for interleaved EBG structure.

4.2 Interleaved EBG Structure with Multiple Pairs of Power/Ground Vias

Based on the design concept, narrowing the pitch of the power/ground vias, of the interleaved EBG structure described in the previous section, the interleaved EBG structures with multiple pairs of power/ground vias are proposed for enhancing the bandwidth. As the above mentioned, the current loop between power/ground vias

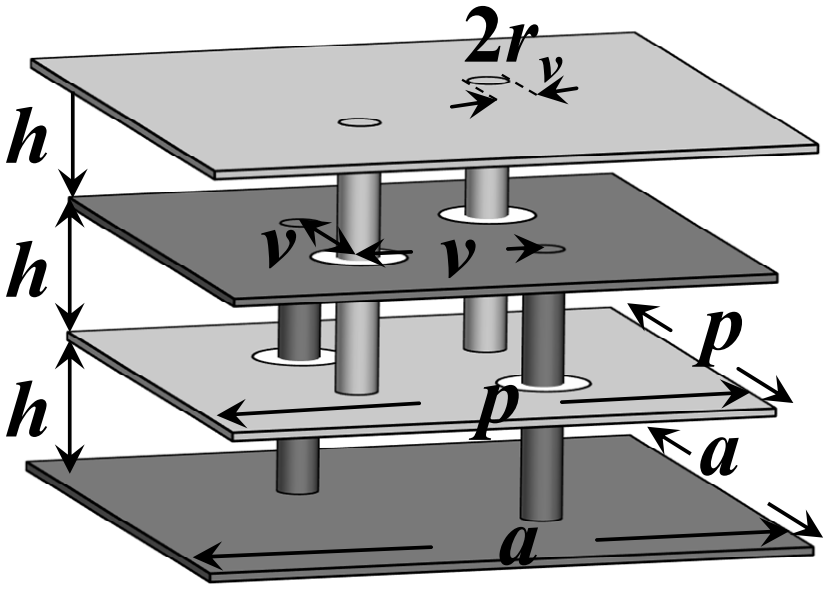

(a)

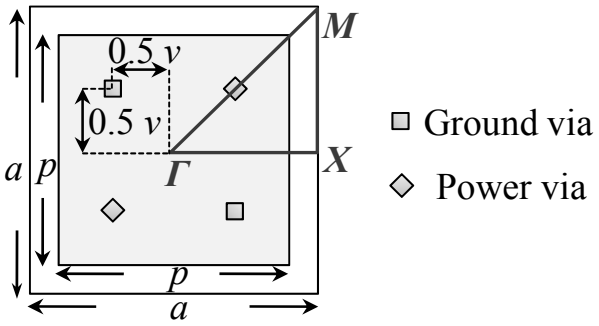

(b)

Fig. 4.14 (a) Geometry of unit cell of interleaved EBG structure with two pairs of power/ground vias in (b) top view.

contributes the equivalent inductance for upper-bound cutoff frequency. This concept implies us that we can arrange multiple pairs of power/ground vias for reducing the equivalent inductance and increasing the upper-bound cutoff frequency and bandwidth of the interleaved EBG structure.

Fig. 4.14(a) and (b) show a three-dimension view and a top view of an interleaved

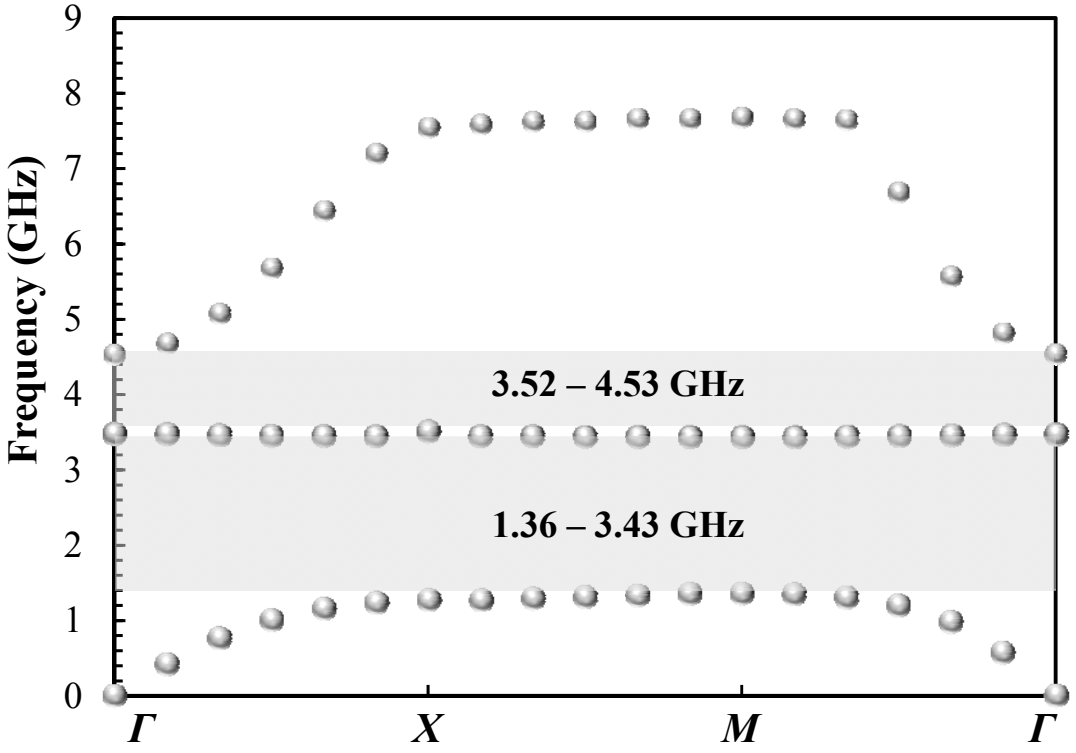

Fig. 4.15 Dispersion diagram of interleaved EBG structure with two pairs of power/ground vias. Geometric parameters are (a, p, v, r_v, h) = (10 mm, 9.4 mm, 1 mm, 0.1 mm, 0.2 mm).

EBG structure with two pairs of power/ground vias. There are two power vias to short the solid power plane to the embedded power patch and two ground vias to short the solid ground plane to the embedded ground patch. The geometric parameters of the unit cell are: the side length of the square unit cell a, the side length of the two embedded square patches p, the radius of vias r_v, and the thickness of each dielectric substrate h. The four vias are symmetrically located on the diagonals of the square patches. The pitch between each two close vias is v.

Fig. 4.15 shows the dispersion diagram of the interleaved EBG structure with two pairs of power/ground vias. In this case, the geometric parameters are (a, p, v, r_v, h) = (10 mm, 9.4 mm, 1 mm, 0.1 mm, 0.2 mm). The first bandgap is in the frequency range

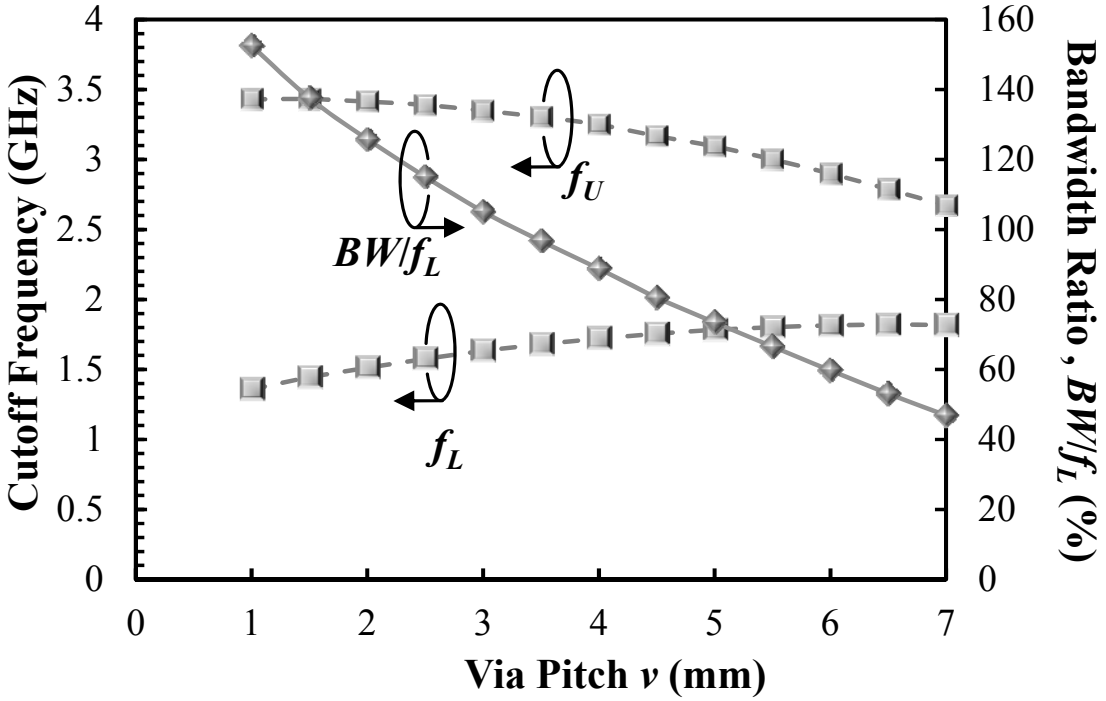

Fig. 4.16 Lower-, upper-bound cutoff frequencies and bandwidth ratio of interleaved EBG structure with two pairs of power/ground vias with respect to via pitch v.

from 1.36 GHz to 3.43 GHz. Similarly, the pitch of the power/ground vias also has a significant effect on bandwidth. Fig. 4.16 shows the lower- and upper-bound cutoff frequencies of the interleaved EBG structure with two pairs of power/ground vias with respect to the via pitch v. The trends of the cutoff frequencies are similar to the case with single pair of power/ground vias. However, the interleaved EBG structure with two pairs of power/ground vias has higher upper-bound cutoff frequency and wider bandwidth when compared with that with single pair of power/ground vias under the condition of v = 1 mm. The upper-bound cutoff frequency increases from 2.51 GHz to 3.43 GHz. The bandwidth ratios are also shown in Fig. 4.16 for different via pitches. For the case of two pairs of power/ground vias, the bandwidth ratio is 152 %, which is better than that of single pair of power/ground vias, 118.3 %.

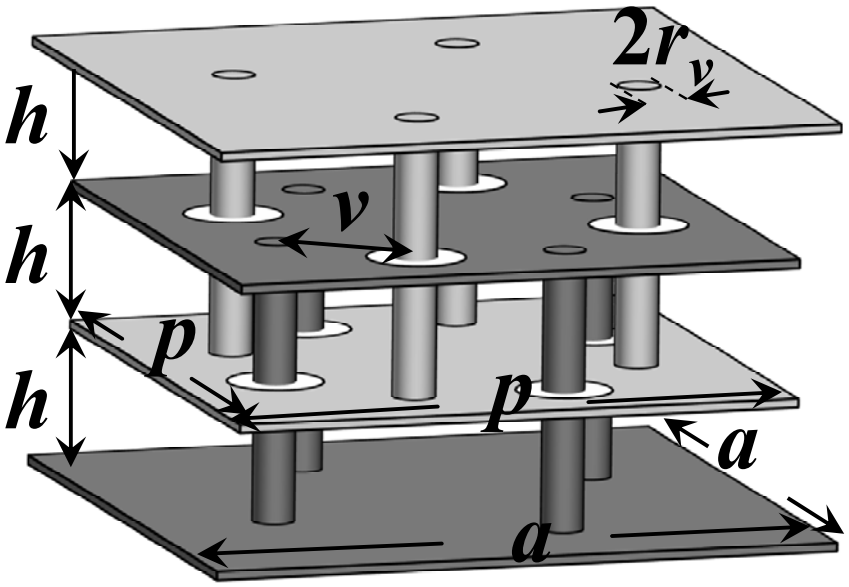

(a)

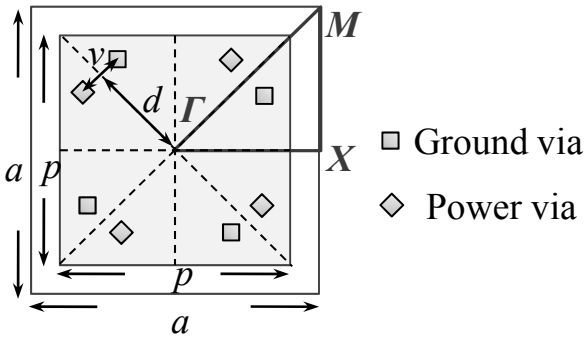

(b)

Fig. 4.17 (a) Geometry of unit cell of interleaved EBG structure with four pairs of power/ground vias in (b) top view.

Another case of the interleaved EBG structure with four pairs of power/ground vias is also porposed here. Fig. 4.17(a) and (b) show a three-dimension view and a top view of the interleaved EBG structure with four pairs of power/ground vias. In order to keep the symmetry of the unit cell, the four power/ground vias pairs are symmetrically

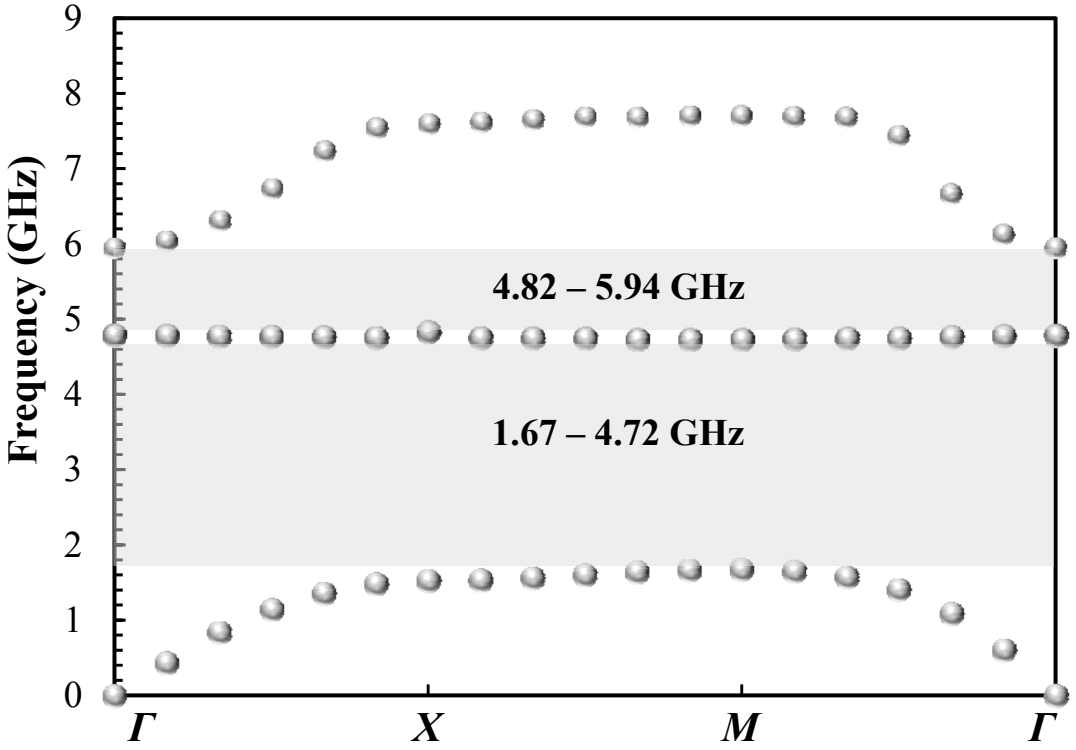

Fig. 4.18 Dispersion diagram of interleaved EBG structure with four pairs of power/ground vias. Geometric parameters are (a, p, v, r_v, h, d) = (10 mm, 9.4 mm, 1 mm, 0.1 mm, 0.2 mm, 1.2 mm).

located in the patch area. The centers of the adjacent power/ground via pairs are located on the diagonals of the quarter patches. The distance between the center of the adjacent power/ground vias pairs and that of the patch is d as shown in Fig. 4.17(b).

It can be anticipated that the fine pitch of the four pairs of power/ground vias will lead to the improvement on lower- and upper-bound cutoff frequencies. In addition to the via pitch v, the distance from the center of the patch to the center of power/ground vias pair d also has to be taken into account. Fig. 4.18 shows the dispersion diagram of the interleaved EBG structure with four pairs of power/ground vias. In this case, the geometric parameters are (a, p, v, r_v, h, d) = (10 mm, 9.4 mm, 1 mm, 0.1 mm, 0.2 mm, 1.2 mm). The first bandgap is in the frequency range from 1.67 GHz to 4.72 GHz. In

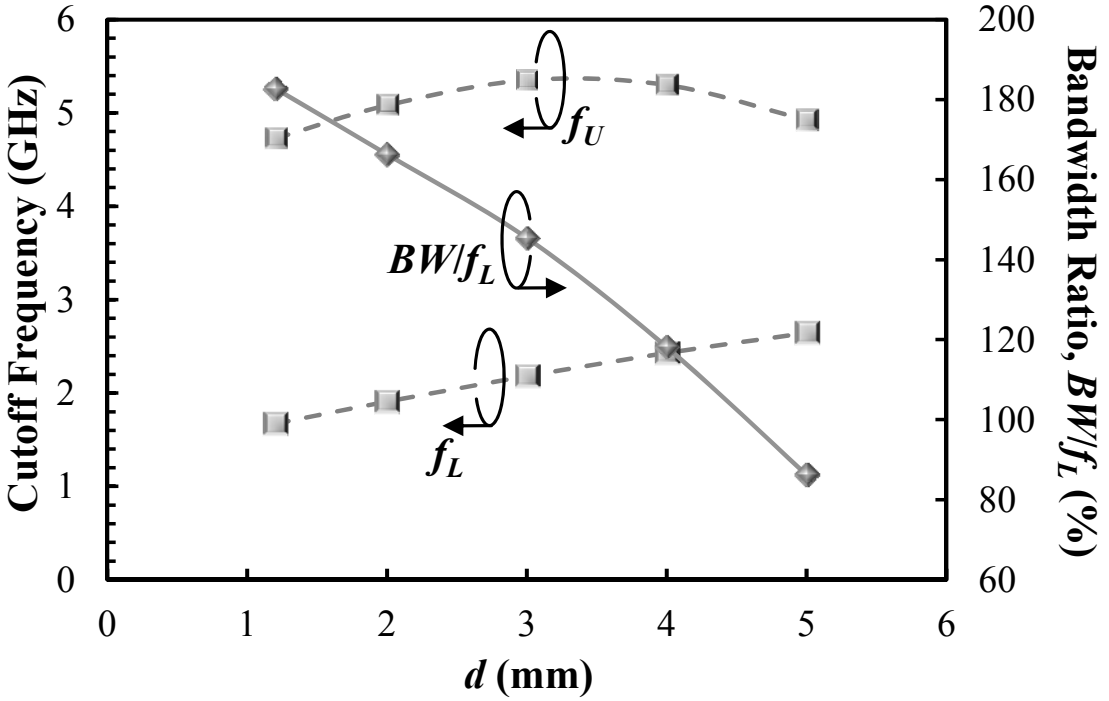

Fig. 4.19 Lower-, upper-bound cutoff frequencies and bandwidth ratio of interleaved EBG structure with four pairs of power/ground vias with respect to *d*.

this case, the eight vias are arranged around the center of the patch.

Fig. 4.19 shows lower-, upper-bound cutoff frequencies and the bandwidth ratio of the interleaved EBG structure with four pairs of power/ground vias with respect to *d*. As *d* is swept, the via pitch is invariant as 1 mm in this case. It can be found that the lower-bound cutoff frequency increases progressively as the four pairs of power/ground vias move away from the center of the patch. In terms of the upper-bound cutoff frequency, the case of d = 3 mm has highest upper-bound cutoff frequency. The bandwidth ratios with respect to *d* are also shown in this figure. The bandwidth ratio increases as *d* decreases. In the case of d = 1.2 mm, the bandwidth ratio is 183 %, which is higher than that of interleaved EBG with single and two pairs of power/ground vias.

In this section, the interleaved EBG structures with two and four pairs of

power/ground vias are proposed for enhancing the bandwidth ratio of bandgap further. As discussed in previous section, a widest bandwidth design of the interleaved EBG structure can be achieved by keeping pitch of the vias as fine as possible. However, it is decided by the limitation of substrate fabrication. Based on above discussion, if the minimum via pitch is set as 1 mm, the bandwidth ratio of the interleaved EBG structure is 118.3 %. In this situation, we still can apply the concept of the multiple pairs of power/ground vias to enhance the bandwidth ratio further under the same limit of via pitch. The bandwidth ratio is enhanced from 118.3 % to 152 % and to 183 % for the two and four pairs of power/ground vias, respectively.

4.3 Two-Dimensional Bandgap Prediction

Although the 1-D equivalent circuit model and bandgap prediction have been proposed in Section 4.1.2, the method is inappropriate for the interleaved EBG structures with multiple pairs of power/ground vias. Based on the principles deduced from the 1-D equivalent circuit model, a method to predict the bandgap of the interleaved EBG structures with multiple pairs of power/ground vias is proposed in this section.

4.3.1 Resonant Cavity Modeling with Even- and Odd-Mode Analysis

As mentioned in Section 2.2.2 and 3.3.1, we have derived the input and transfer impedances of the two-layer parallel-plate rectangular structures with three kinds of boundary conditions. They are (2.52) and (2.53) for four PMC walls, (2.63) and (2.66) for four PEC walls, and (3.7) and (3.8) for two PEC walls and two PMC walls. In this section, the even- and odd-mode analysis will be used to calculate the input impedance for other boundary conditions and other shapes.

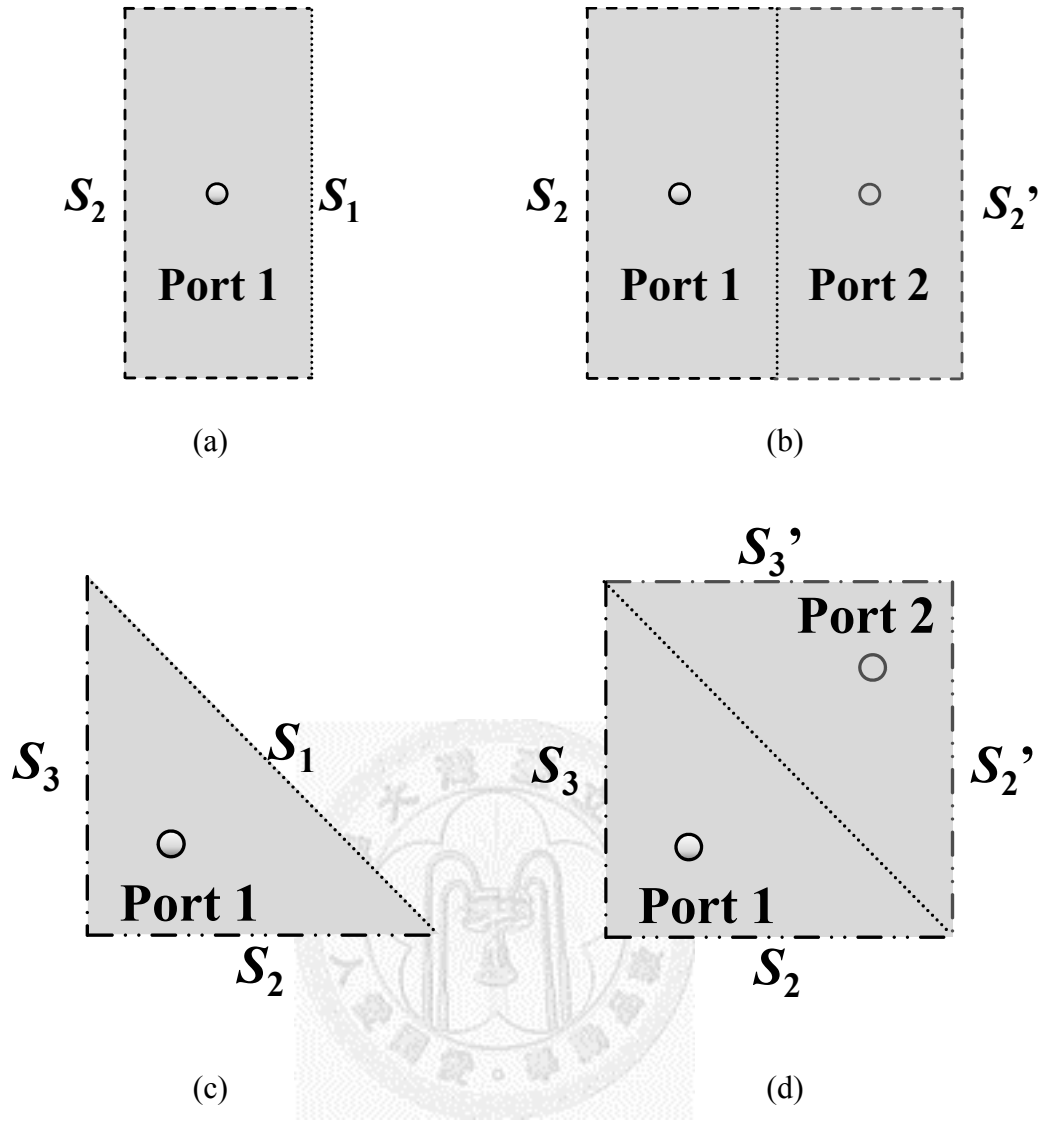

Fig. 4.20 Top views of (a) original and (b) extended rectangular structures and (c) original and (d) extended isosceles right triangle structures.

Fig. 4.20(a) shows a top view of a two-layer parallel-plate rectangular structure. One side wall is denoted as S_1 and the others are denoted as S_2. The boundary conditions on S_1 and S_2 can be different. The location of the via is the same as the location of the port 1. The input impedance from the port 1 can be derived using the procedure mentioned in Section 2.2.2. Alternatively, we can use the even- and odd-mode analysis. The structure of the original problem can be duplicated with mirror symmetry with

respect to S_1 as shown in Fig. 4.20(b) and the boundary condition on S_2' is the same as that on S_2. The extended problem is a two-port network. Based on the even- and odd-mode analysis as (2.14) and (2.15), the input impedance of the original problem will be the linear combination of the Z_{11} and Z_{21} of the extended problem. The impedance will be $Z_{11} + Z_{21}$ or $Z_{11} - Z_{21}$ if the boundary condition on S_1 is PMC or PEC walls, respectively. For example, it is supposed that the boundary conditions on S_1 and S_2 of the original problem in the Fig. 4.20(a) are PEC and PMC walls, respectively. We can use (2.52) and (2.53) to calculate the Z_{11} and Z_{21} of the extended problem shown in Fig. 4.20(b), and thus the input impedance of the original problem is the difference of the calculated Z_{11} and Z_{21}, $Z_{11} - Z_{21}$.

Based on the same concept, we can also calculate the input impedance of the two-layer parallel-plate structure in the shape of isosceles right triangle as shown in Fig. 4.20(c). The extended structure is shown in Fig. 4.20(d) by duplicating the original one with mirror symmetry with respect to S_1. In the extended problem shown in Fig. 4.20(d), the boundary conditions on S_2 and S_2' and on S_3 and S_3' are the same, respectively, and the Z_{11} and Z_{21} of the square parallel-plate structure can be calculated by (2.52) and (2.53) for four PMC walls, (2.63) and (2.66) for four PEC walls, and (3.7) and (3.8) for two PEC walls and two PMC walls. Similarly, the input impedance of the original problem shown in Fig. 4.20(c) will be $Z_{11} + Z_{21}$ or $Z_{11} - Z_{21}$ if the boundary condition on S_1 is PMC or PEC walls, respectively. It is worth noting that the input impedance can be approximated as a lumped equivalent inductance based on $k_{mn}^2 - k^2 \approx k_{mn}^2$ in the low frequency range as mentioned in Section 2.2.2 and 3.3.1.

4.3.2 Two-Dimensional Equivalent Circuit Model of Interleaved EBG Structure

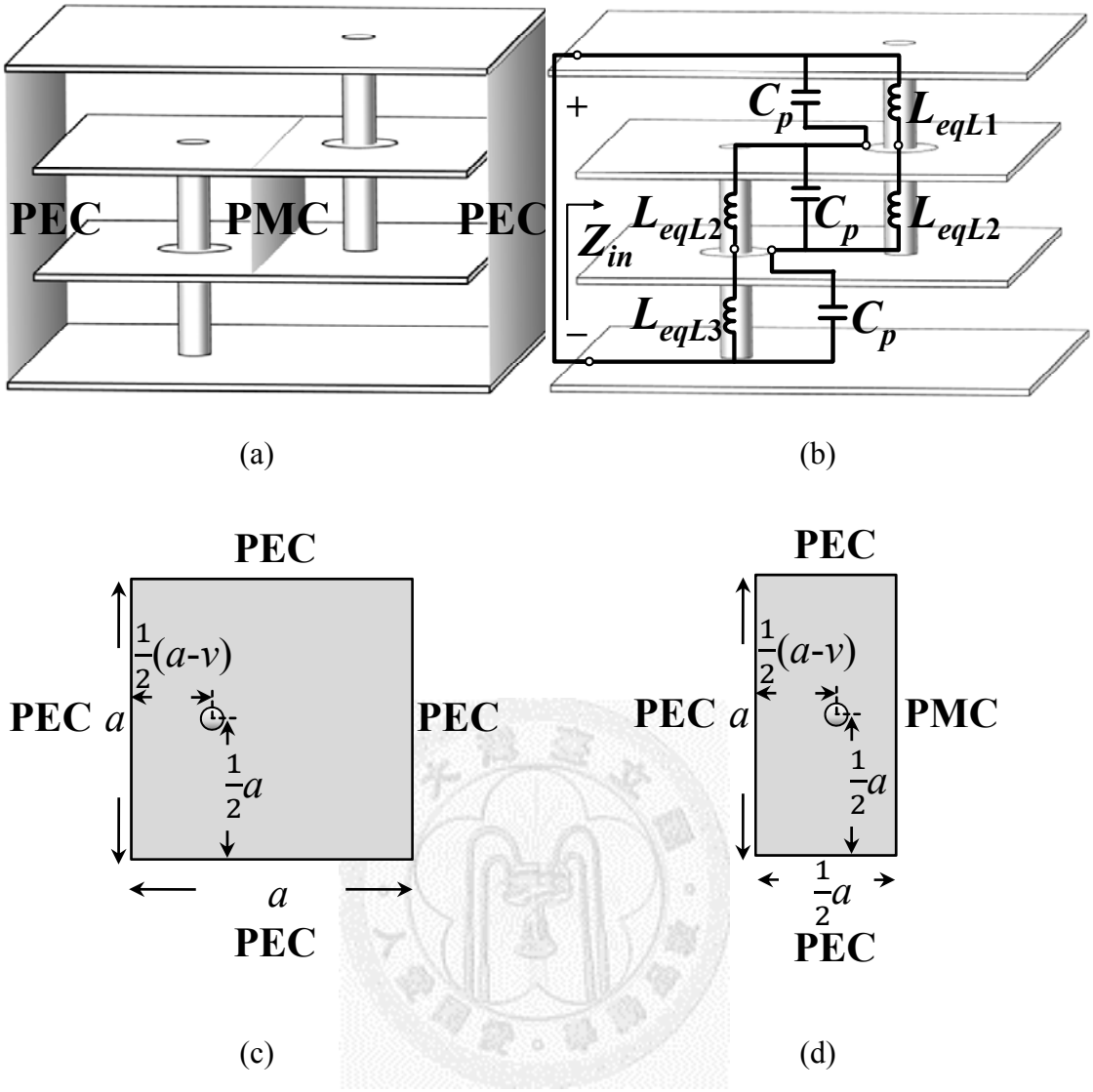

Fig. 4.21 (a) Boundary condition and (b) equivalent circuit model for lower-bound cutoff frequency of interleaved EBG structure and top views of parallel-plate structures for extraction of (c) L_{eqL1} and (d) L_{eqL2}.

Based on the bandgap analysis of the one-dimensional interleaved EBG structure described in Section 4.1.2, the boundary conditions for lower- and upper-bound cutoff frequencies as shown in Fig. 4.8(a) and (b) can be applied to the two-dimensional unit cell, respectively. For the lower-bound cutoff frequency, the boundary conditions around the periphery are four PEC walls and the boundary condition of the symmetric plane

between power and ground vias is a PMC wall as depicted in Fig. 4.21(a). According to the boundary conditions, the equivalent circuit model is constructed as shown in Fig. 4.21(b). C_p represents the parallel-plate capacitance. L_{eqL1} is the equivalent inductance of the via and parallel plates between the top and second layers. The equivalent inductance of the via and parallel plates between the third and bottom layers, L_{eqL3}, is equal to L_{eqL1} because of the symmetric structure. There are two vias between the second and third layers. Each of them is modeled by L_{eqL2}. The dimensions and boundary conditions of the parallel-plate structures for approximately extracting L_{eqL1} and L_{eqL2} are shown in Fig. 4.21(c) and (d), respectively.

The lower-bound cutoff frequency can be determined by the zero frequency of the equivalent circuit model shown in the Fig. 4.21(b). The input impedance of the equivalent circuit model Z_{in} can be calculated by Kirchhoff's voltage and current laws as

$$Z_{in} = \frac{-1 + 3C_p L_{eqL1}\omega^2 + 3C_p L_{eqL2}\omega^2}{j\omega C_p(-3 + C_p L_{eqL1}\omega^2 + C_p L_{eqL2}\omega^2)}. \tag{4.1}$$

Thus, the lower-bound cutoff frequency, the zero frequency of (4.1), can be derived as

$$f_L = \frac{1}{2\pi}\frac{1}{\sqrt{3C_p(L_{eqL1} + L_{eqL2})}}. \tag{4.2}$$

With regard to the upper-bound cutoff frequency, the boundary conditions around the periphery are four PMC walls and the boundary condition of the symmetric plane between the power and ground vias is a PEC wall. As depicted in Fig. 4.10, the four-layer structure dominates the upper-bound cutoff frequency. By ignoring the section comprised of the top and bottom layers, the four-layer structure with boundary condition for upper-bound cutoff frequency is shown in Fig. 4.22(a). According to the boundary conditions, the equivalent circuit model is established as shown in Fig. 4.22(b). Similarly, L_{eqU1}, L_{eqU2}, and L_{eqU3} are used to model the equivalent inductance of

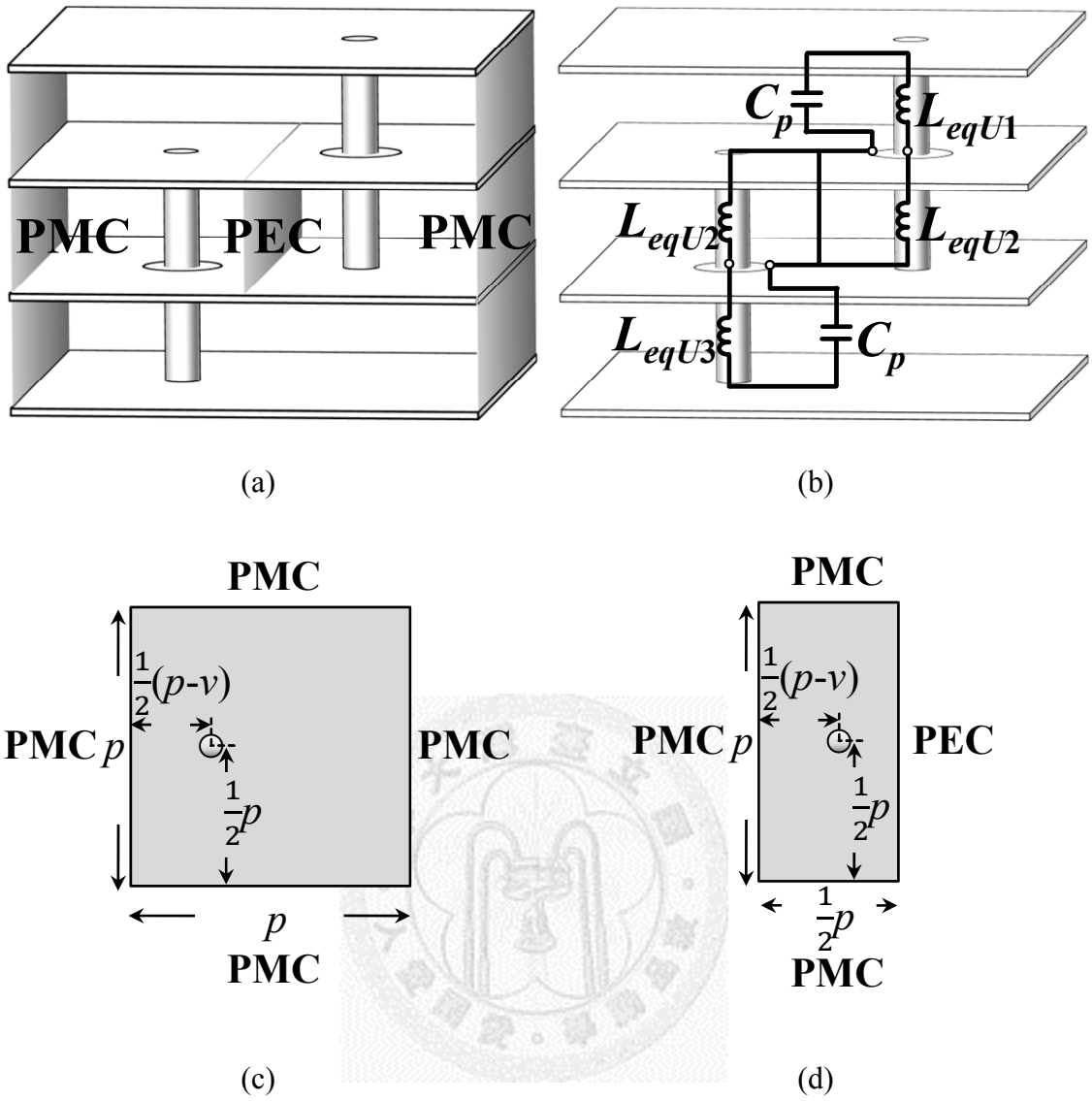

Fig. 4.22 (a) Boundary condition and (b) equivalent circuit model for upper-bound cutoff frequency of interleaved EBG structure and top views of parallel-plate structures for extraction of (c) L_{equ1} and (d) L_{equ2}.

the parallel plates between the adjacent layers. L_{equ1} and L_{equ3} are the same and can be extracted by the parallel-plate structure shown in Fig. 4.22(c). L_{equ2} is extracted by the parallel-plate structure shown in Fig. 4.22(d). The upper-bound cutoff frequency is the resonant frequency of the equivalent circuit model shown in Fig. 4.22(b) and can be calculated by

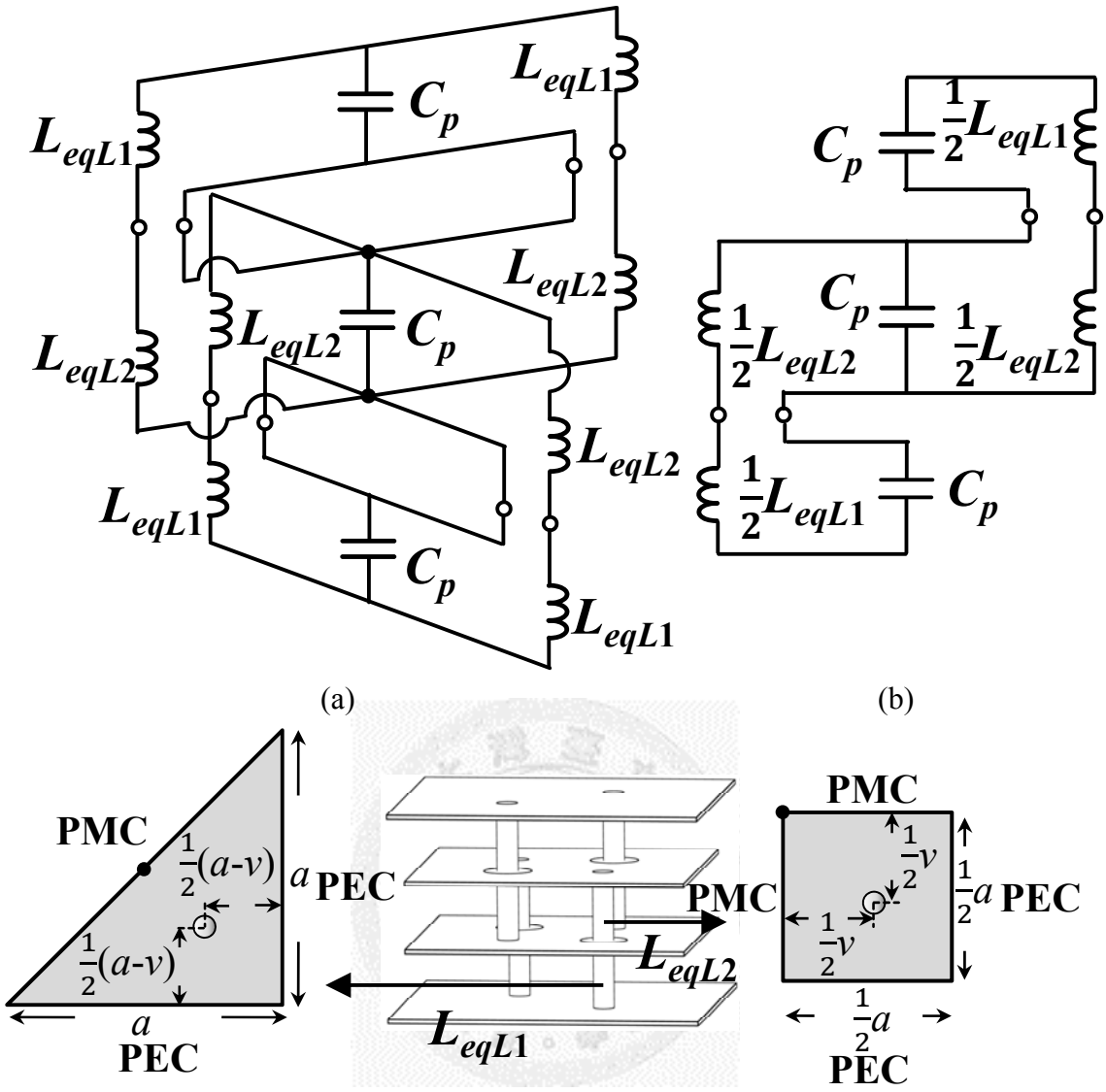

Fig. 4.23 (a) Equivalent circuit model for f_L of interleaved EBG structure with two pairs of P/G vias, (b) simplified model, and (c) top views of parallel-plate structures for extraction of L_{eqL1} and L_{eqL2}.

$$f_U = \frac{1}{2\pi\sqrt{C_p(L_{equ1} + L_{equ2})}}. \tag{4.3}$$

As regards the interleaved EBG structure with two pairs of power/ ground vias, the equivalent circuit model for lower-bound cutoff frequency is shown in Fig. 4.23(a)

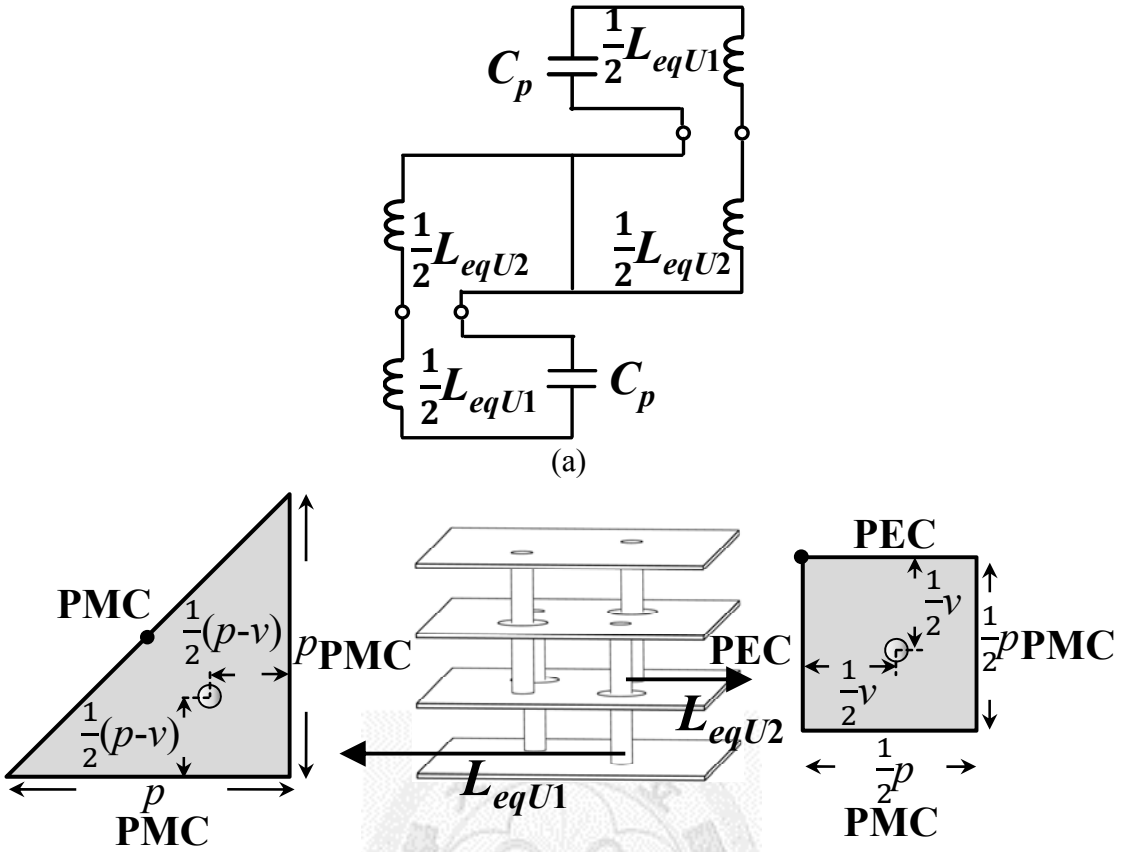

Fig. 4.24 (a) Simplified model of interleaved EBG structure with two pairs of P/G vias for f_U and (b) top views of parallel-plate structures for extraction of L_{eqU1} and L_{eqU2}.

based on the same principle. Two vias between the top and second layers and two vias between the third and bottom layers are modeled by the equivalent inductance L_{eqL1}. Four vias between the second and third layers are modeled by the equivalent inductance L_{eqL2}. The equivalent circuit model can be simplified as shown in Fig. 4.23(b). Therefore, the prototype of the simplified equivalent circuit model is similar to that shown in Fig. 4.21(b). Based on the reason, the lower-bound cutoff frequency can be determined by the zero frequency of the equivalent circuit model and can be found from (4.2) as

$$f_L = \frac{1}{\pi\sqrt{6C_p(L_{eqL1}+L_{eqL2})}}. \tag{4.4}$$

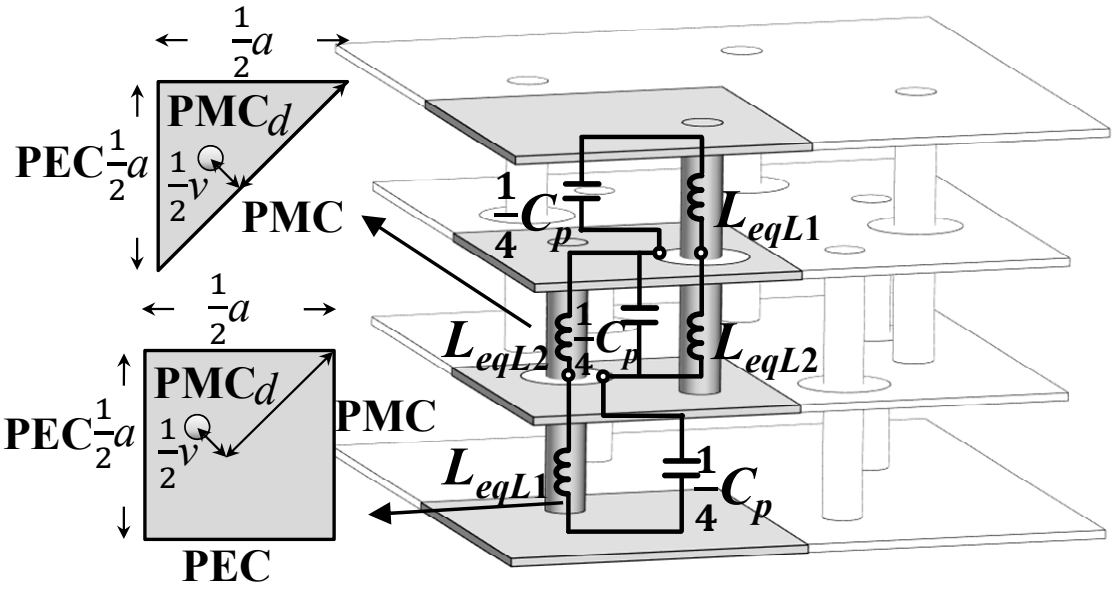

Fig. 4.25 Equivalent circuit model for f_L of interleaved EBG structure with four pairs of power/ground vias.

The top views of the parallel-plate structures for the extraction of L_{eqL1} and L_{eqL2} are shown in Fig. 4.23(c). Similarly, the simplified model for upper-bound cutoff frequency is shown in Fig. 4.24(a). The top views of the parallel-plate structures for the extraction of L_{eqL1} and L_{eqL2} are shown in Fig. 4.24(b). The upper-bound cutoff frequency can be determined by the resonant frequency of the simplified model as

$$f_U = \frac{1}{\pi\sqrt{2C_p(L_{equ1} + L_{equ2})}}. \tag{4.5}$$

As regards the interleaved EBG structure with four pairs of power/ground vias, the quartered structure is taken into account only because of the symmetry of the unit cell. The quartered structure is similar to the interleaved EBG structure with one pair of power/ground vias. The equivalent circuit model for lower-bound cutoff frequency of the quartered structure is shown in Fig. 4.25. Based on the mentioned above, the lower-bound cutoff frequency is the zero frequency of the equivalent circuit model and

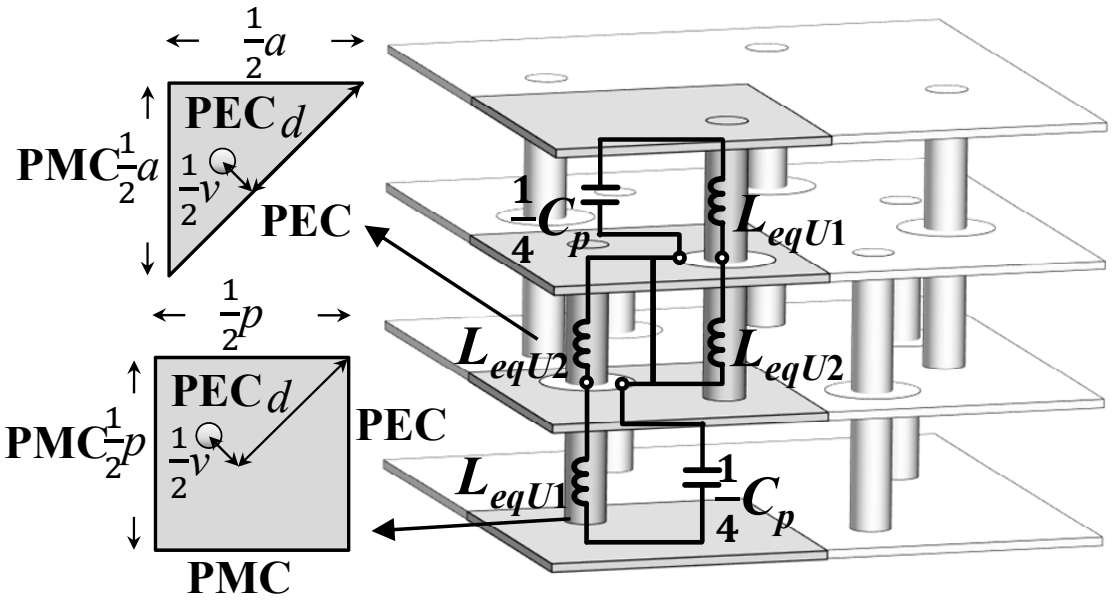

Fig. 4.26 Equivalent circuit model for f_U of interleaved EBG structure with four pairs of power/ground vias.

can be calculated by

$$f_L = \frac{1}{\pi\sqrt{3C_p(L_{eqL1} + L_{eqL2})}}. \tag{4.6}$$

Similarly, the equivalent circuit model for upper-bound cutoff frequency of the quartered structure is shown in Fig. 4.26. The upper-bound cutoff frequency can be decided by

$$f_U = \frac{1}{\pi\sqrt{C_p(L_{eqU1} + L_{eqU2})}}. \tag{4.7}$$

We have proposed the equivalent circuit models for predicting the bandgaps of the interleaved EBG structures. The bandgap predictions for the interleaved EBG structures with one, two, and four pairs of power/ground vias are calculated and shown in Fig. 4.27 (a), (b), and (c), respectively. The simulated results from HFSS are also shown in these figures. It can be found that the results from the proposed method agree well with

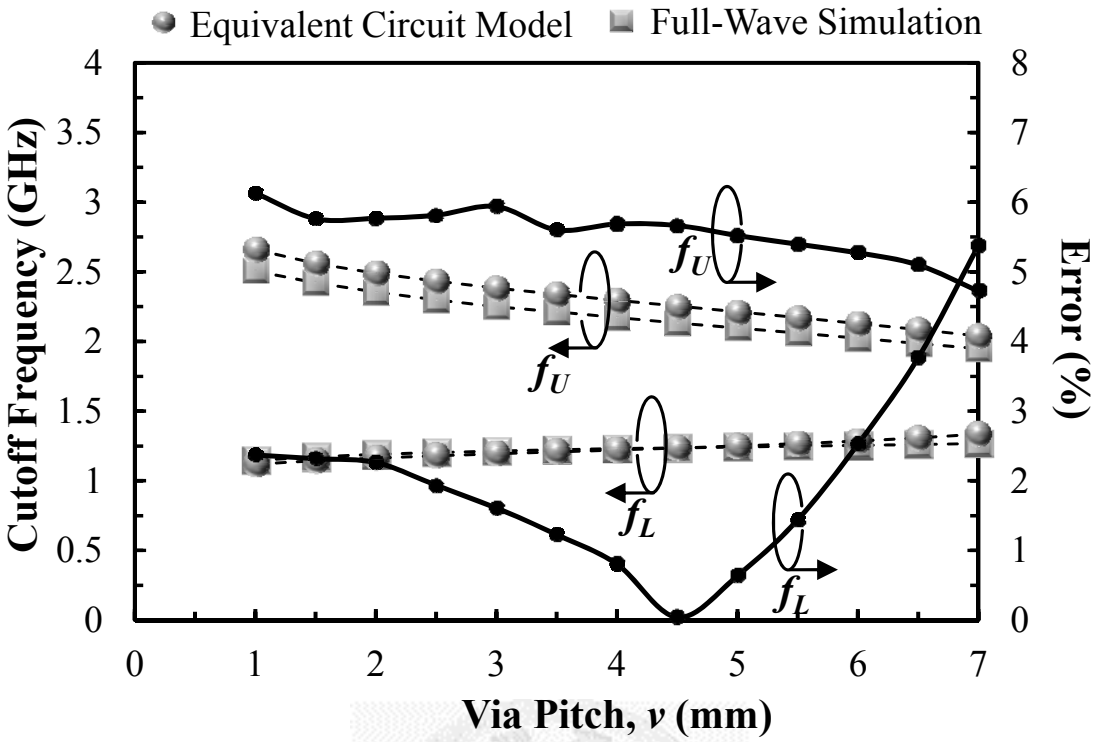
Equivalent Circuit Model
Full-Wave Simulation
Cutoff Frequency (GHz)
Error (%)
Via Pitch, v (mm)
f_U
f_L

(a)

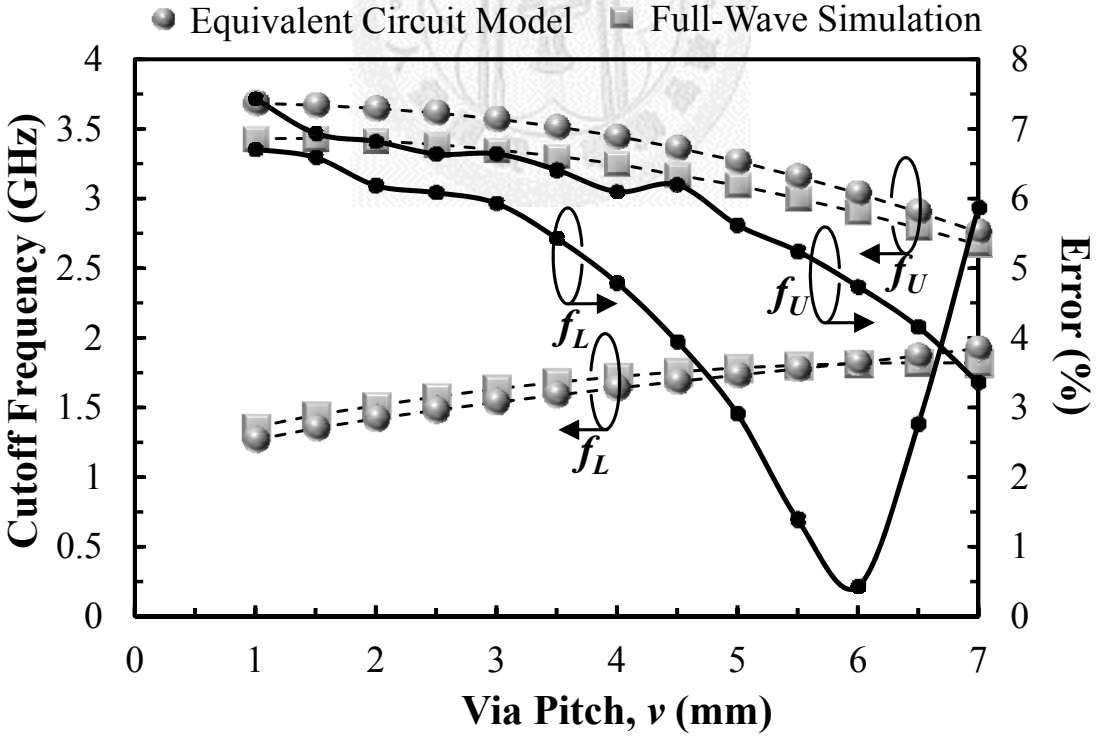
Equivalent Circuit Model
Full-Wave Simulation
Cutoff Frequency (GHz)
Error (%)
Via Pitch, v (mm)
f_U
f_L

(b)

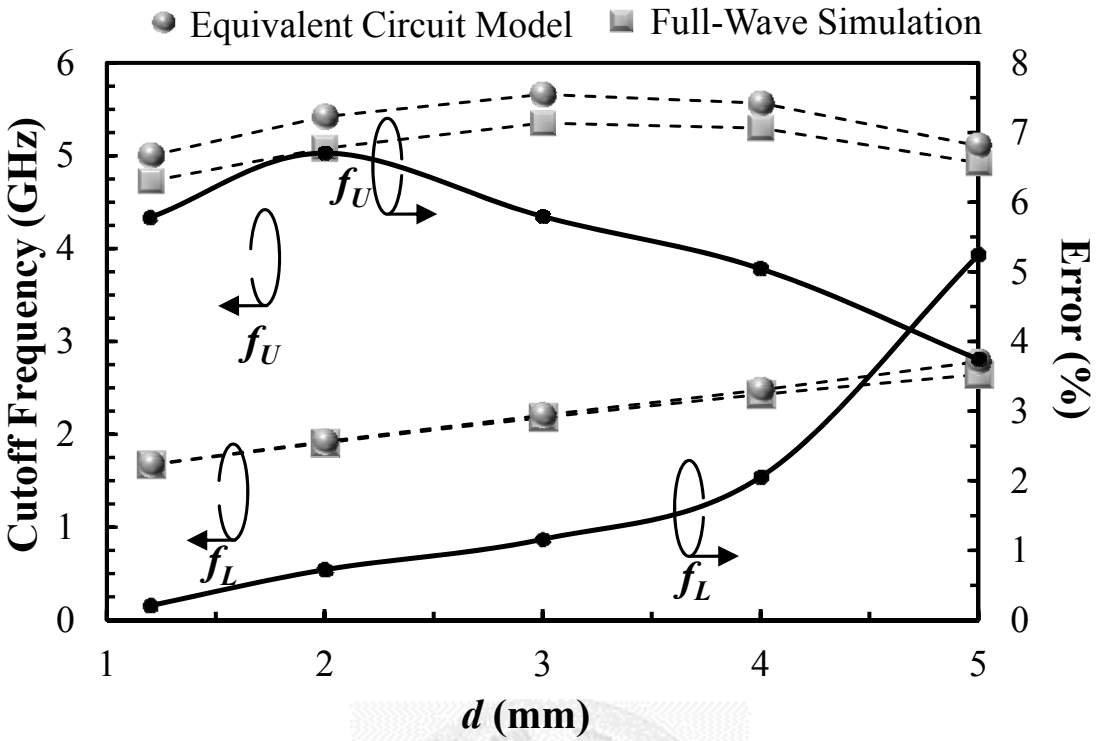

(c)

Fig. 4.27 Estimated and simulated lower-, upper-bound cutoff frequencies, and errors between the two methods for interleaved EBG structure with (a) single (b) two, and (c) four pairs of P/G vias.

those from full-wave simulations. The trends of the lower- and upper-bound cutoff frequencies can be described by the proposed predicting method. The errors between the two methods are also plotted with respect to the via pitch *v* or distance *d* in these figures. The maximum errors for lower- and upper-bound cutoff frequencies of the interleaved EBG structure with one, two, and four pairs of power/ground vias are summarized in Table 4.1. It is worth noting that the maximum error is 7.4 % for all of the cases. The proposed method provides us a useful tool for quickly predicting the bandgap with the reasonable error.

Table 4.1 Maximum errors for f_L and f_U of interleaved EBG structures

	Maximum error of f_L	Maximum error of f_U
Interleaved EBG structure (one pair of P/G vias)	5.4 %	3.1 %
Interleaved EBG structure (two pairs of P/G vias)	6.7 %	7.4 %
Interleaved EBG structure (four pairs of P/G vias)	5.2 %	6.7 %

4.4 Comparison and Measurement

4.4.1 Comparison

Fig. 4.28 shows the dispersion diagram of the interleaved EBG structure with geometric parameters (a, p, v, r_v, h) = (4 mm, 3.8 mm, 0.21 mm, 37.5 μm, 45 μm), which is simulated by 3-D full-wave simulator (Ansys HFSS). The relative permittivity of the substrate is 7.8. As shown in Fig. 4.28, the first bandgap is from 1.9 GHz to 4.54 GHz and the immediate second bandgap is from 4.56 GHz to 6.12 GHz.

For comparisons with previous works, the mushroom and double-stacked EBG structures are designed with the same substrate, stack-up layers, and size of unit cell and vias. The side views of the mushroom [35] and double-stacked EBG structures [39] are shown in Fig. 4.29(a) and (b), respectively. Fig. 4.29 (c) shows the dispersion diagrams of the two EBG structures. For the mushroom EBG structure, there is a bandgap in the range from 3.05 to 5.85 GHz. In terms of the double-stacked EBG structure, there are two bandgaps, from 2.53 to 4.79 GHz and from 7.27 to 13.26 GHz, and a passband of 2.48 GHz between them. The unit-cell length of the mushroom, double-stacked, and

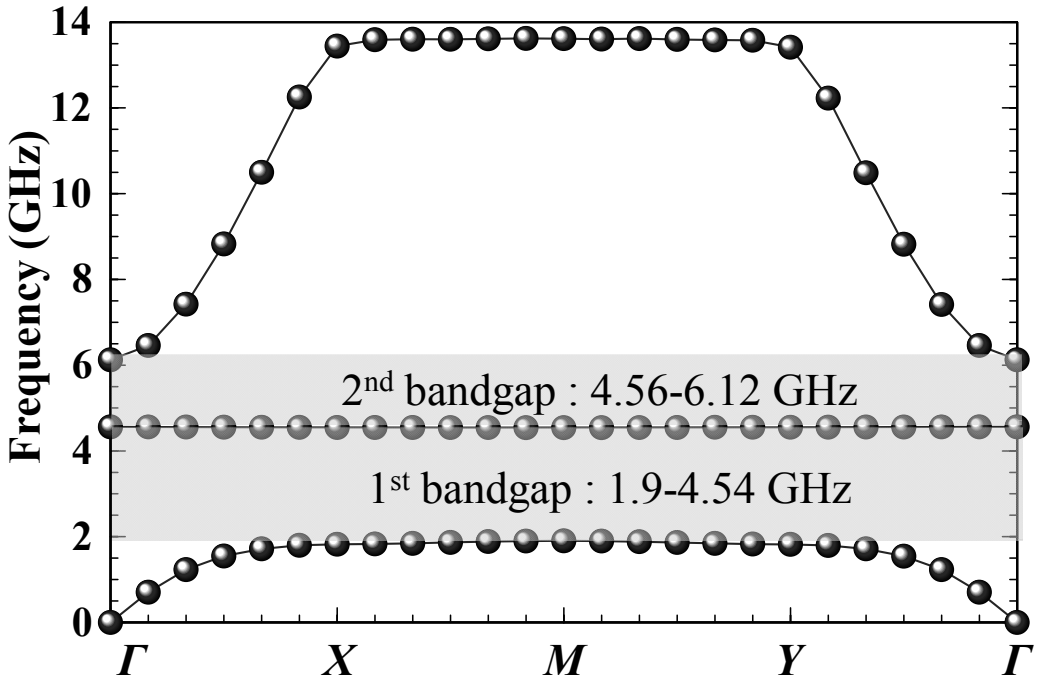

Fig. 4.28 Dispersion diagram of interleaved EBG structure with single pair of power/ground vias. The geometric parameters are (a, p, v, r_v, h) = (4 mm, 3.8 mm, 0.21 mm, 37.5 μm, 45 μm).

interleaved EBG structures are 0.114 λ_{gL}, 0.094 λ_{gL}, and 0.071 λ_{gL}, respectively, where λ_{gL} is the guided wavelength in the substrate at the first lower-bound cutoff frequency. It is shown that the interleaved EBG structure reduces the occupying area by 61.2 % and 43.6 % compared with the mushroom and double-stacked EBG structures, respectively, when the same lower-bound cutoff frequency is desired.

The bandwidth ratios are 92 %, 89.3 %, and 139 % for the mushroom, double-stacked, and interleaved (v = 0.21 mm) EBG structures. It is shown that the interleaved EBG structure enhances the bandwidth ratio of bandgap by 51.1 % and 55.7 %, compared with the mushroom and double-stacked EBG structures, respectively, when the same lower-bound cutoff frequency is desired.

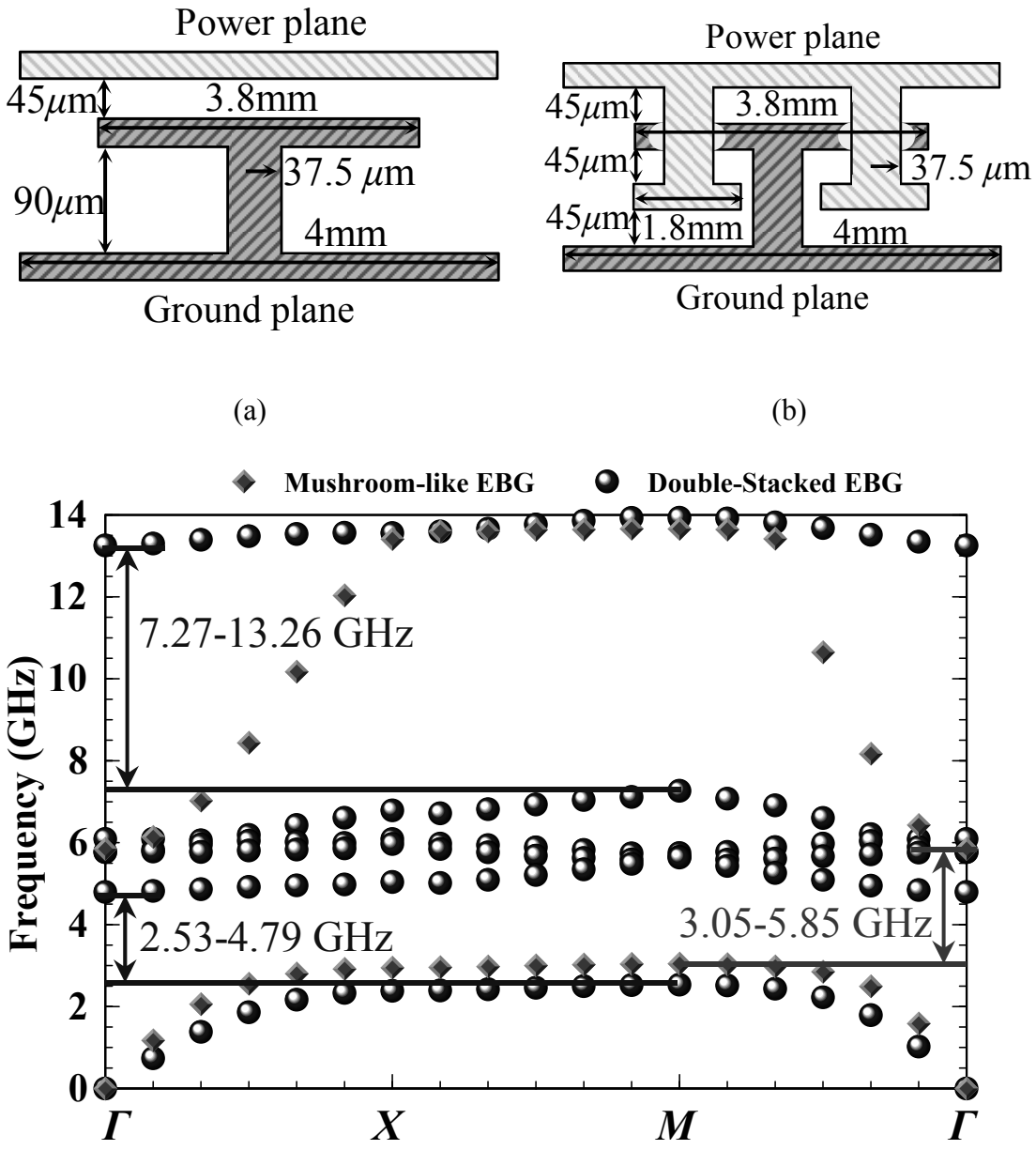

Fig. 4.29 Side views of (a) mushroom and (b) double-stacked EBG structures and (c) corresponding dispersion diagram.

As regards the interleaved EBG structure with multiple pairs of power/ground vias, two cases are considered. For the interleaved EBG structure with two pairs of power/ground vias, the geometric parameters are set as (a, p, v, r_v, h) = (4 mm, 3.8 mm,

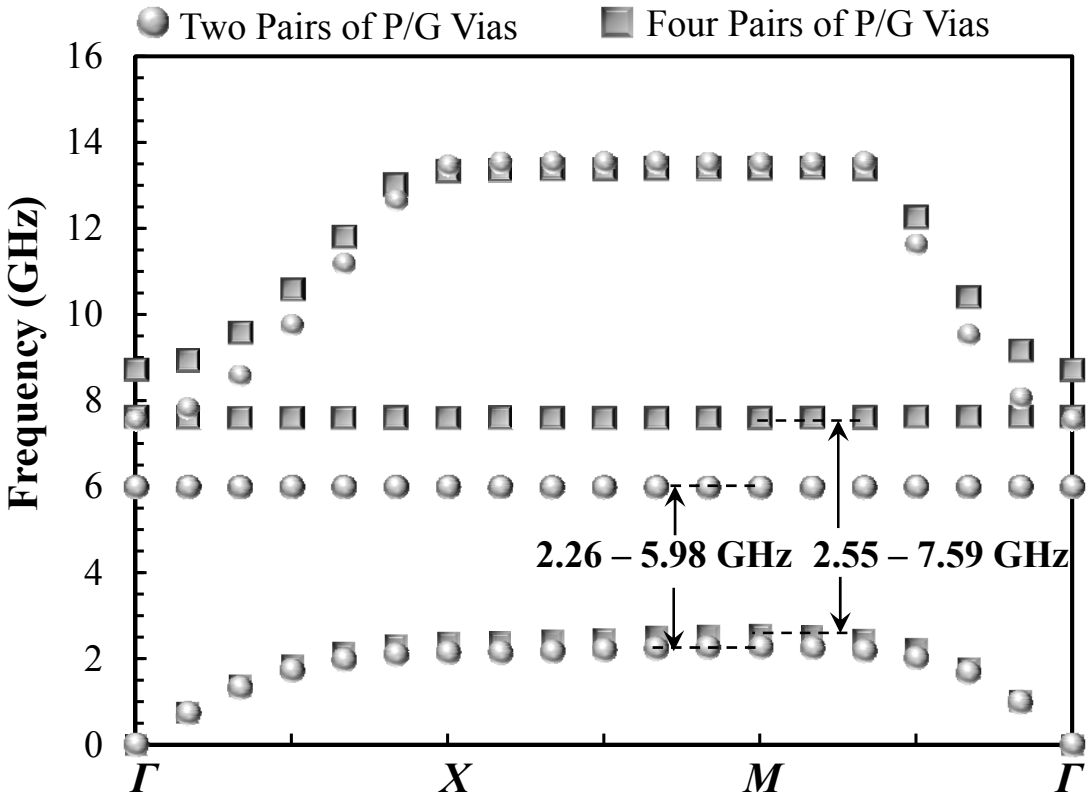

Fig. 4.30 Dispersion diagrams of interleaved EBG structure with two and four pairs of power/ground vias.

Table 4.2 Comparison of EBG structures

	Bandgap (GHz)	Unit-cell length (λ_{gL})	Bandwidth ratio (%)
Mushroom EBG structure	3.05-5.85	0.114	92
Double-stacked EBG structure	2.53-4.79	0.094	89.3
Interleaved EBG structure (one pair of P/G vias)	1.9-4.54	0.071	139
Interleaved EBG structure (two pairs of P/G vias)	2.26-5.98	0.084	165
Interleaved EBG structure (four pairs of P/G vias)	2.55-7.59	0.095	198

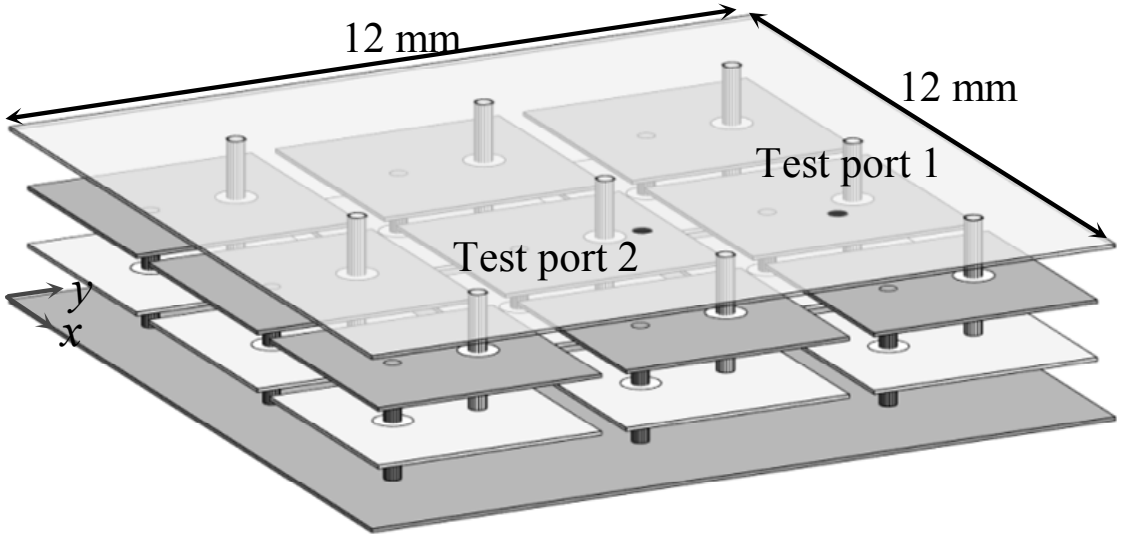

Fig. 4.31 Test board with interleaved EBG structure.

0.3 mm, 37.5 μm, 45 μm). For the interleaved EBG structure with four pairs of power/ground vias, the geometric parameters are set as (a, p, v, r_v, h, d) = (4 mm, 3.8 mm, 0.23 mm, 37.5 μm, 45 μm, 0.28 mm). The dispersion diagrams of the two cases are shown in Fig. 4.30. The unit-cell lengths of the two and four pairs of power/ground vias are 0.084 λ_{gL} and 0.095 λ_{gL}, respectively, and the bandwidth ratios of them are 165 % and 198 %, respectively. The comparison of the mushroom, double-stacked, and interleaved EBG structures are summarized in Table 4.2. The interleaved EBG structures with multiple power/ground vias have similar unit-cell length but much wider bandwidth when compared with the mushroom and double-stacked EBG structures.

4.4.2 Measurement

In order to validate the accuracy of the simulation results and demonstrate the isolation ability of the PDN with interleaved EBG structure, test boards are designed and fabricated as shown in Fig. 4.31. The 2-D interleaved EBG structure are designed in the power/ground planes with the size 12 mm × 12 mm. The structure is realized using the low-temperature co-fired ceramic (LTCC) fabrication. The relative permittivity of

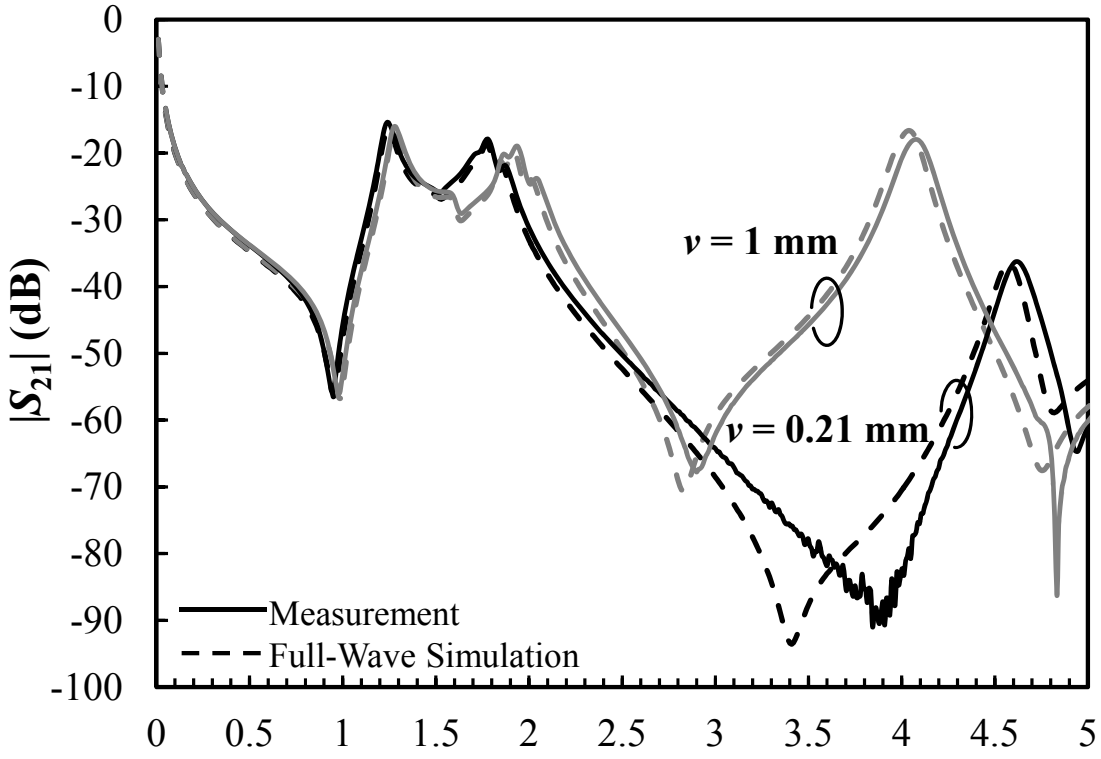

Fig. 4.32 Simulated and measured results of interleaved EBG structures with single pair of power/ground vias.

the LTCC substrate is 7.8. The geometric parameters of the unit-cell EBG test vehicles are (a, p, r_v, h) = (4 mm, 3.8 mm, 37.5 μm, 45 μm). They are the same as the aforementioned one. Four cases of the interleaved 2-D EBG structures are fabricated and measured. The pitches of single pair of power/ground vias are 0.21 mm and 1 mm. The pitch of two vias pairs is 0.3 mm. For the case of four vias pairs, the vias are arranged as v = 0.23 mm and d = 0.28 mm.

Two test ports are located at (8.8 mm, 8.8 mm) and (8.4 mm, 6 mm), respectively. The simulated and measured results of the interleaved EBG structure with single pair of power/ground vias are shown in Fig. 4.32. As expected, the lower-bound cutoff frequency is decreased from 2.08 GHz to 1.9 GHz and upper-bound cutoff frequency is increased from 4 GHz to 4.54 GHz as via pitch is reduced from 1 mm to 0.21 mm. In

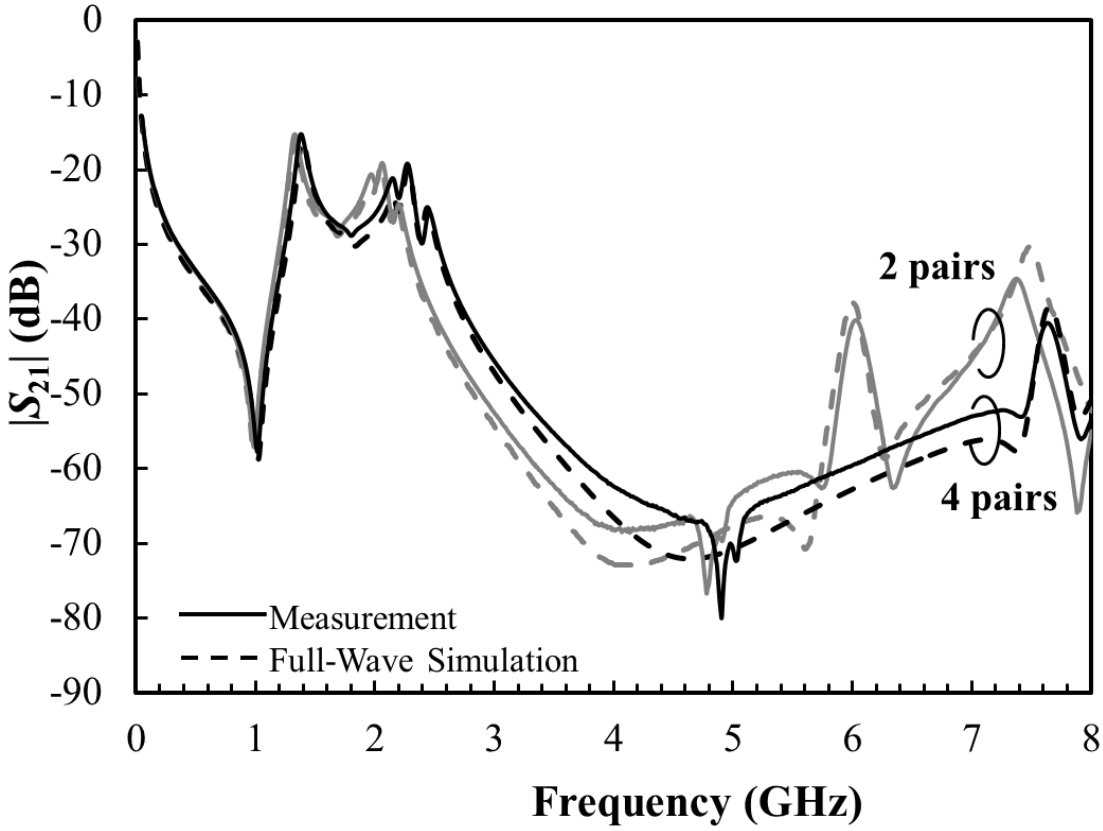

Fig. 4.33 Simulated and measured results of interleaved EBG structures with two and four pairs of power/ground vias.

general, the smallest via pitch is limited by the substrate fabrication technique. Fig. 4.33 shows the simulated and measured results of the interleaved EBG structures with two and four pairs of power/ground vias. It can be found that the first bandgap of the interleaved EBG structure with two vias pairs is from 2.26 GHz to 5.98 GHz. The bandgap of the interleaved EBG structure with four vias pairs is from 2.55 GHz to 7.59 GHz. Good agreements between the simulated and measured results validate the correctness of the design concept.

4.5 Summary

An interleaved EBG structure with wider bandwidth and smaller area has been

investigated to suppress the PDN noise. It is implemented by interleaving two identical patches between power and ground planes. An equivalent circuit model based on transmission-line sections has been constructed. By reducing the pitch of power/ground vias pair, both lower and upper bound cutoff frequencies are improved. Consequently, the extended bandwidth of bandgap can be significantly achieved. The design concept has been investigated by analyzing the corresponding mechanisms. Based on the design concept, the interleaved EBG structures with multiple pairs of power/ground vias have been also proposed to enhance the bandwidth of bandgap. The prediction method has proposed for providing us a useful tool for quickly predicting the 2-D bandgap with the reasonable error. As an example, the interleaved EBG structure with one pair of power/ground vias presents two bandgaps in the range from 1.9 GHz to 4.54 GHz and from 4.56 GHz to 6.12 GHz. The electrical size, which is normalized to the wavelength in the substrate, and bandwidth ratio are 0.071 λ_{gL} and 139 %, respectively. Compared with the size and the bandwidth of the conventional mushroom EBG structure, the interleaved EBG structure simultaneously shows substantial improvements on bandwidth of 51.1% and miniaturization of 61.2 %. With regard to the interleaved EBG structure with four pairs of power/ground vias, the bandwidth has an increase of 115.2 % wider than that of the conventional mushroom EBG structure and the required layout area can be reduced by 30.5 % simultaneously. The measured results have validated the accuracy of the simulated results and the proposed concept.

Chapter 5 Conclusion

Proposing a miniaturized and stopband-enhanced EBG structure is the main focus of this dissertation. We have developed a method to predict the lower- and upper-bound cutoff frequencies. Based on the method, physics-based models with specific boundary conditions are proposed for the unit cell of the EBG structure. The models benefit not only the prediction of the bandgap but also the understanding of the mechanism for the bandgap. Thus, we can have design concepts for achieving the improvements on the miniaturization and the enhanced bandwidth simultaneously.

In chapter 2, a method for predicting the lower- and upper-bound cutoff frequencies has been proposed for one-dimensional and two-dimensional bandgap. Instead of solving dispersion relation, the bandgaps can be determined by the resonant frequencies of the unit cells with specific boundary conditions. The method can be efficiently with the same accuracy. Based on the method, we developed two approaches for the modeling of the one- and two-dimensional unit cells, respectively. For the one-dimensional EBG structure, we have constructed an equivalent circuit model for the unit cell using transmission-line sections. In terms of the two-dimensional EBG structure, the equivalent circuit models associated with the lower- and upper-bound cutoff frequencies have been established, respectively, and the circuit elements in the equivalent circuit models can be extracted based on the derived resonant cavity models.

In chapter 3, we have proposed the multiple vias EBG structure and explained the mechanisms of lower- and upper-bound cutoff frequencies of the EBG structure. By sweeping the via pitch v of multiple vias EBG structure, it can be found that the

multiple vias EBG structure could has an optimized design for maximum bandwidth ratio. It is worth emphasizing that not only absolute bandwidth but also bandwidth ratio is enhanced by multiple vias EBG structure. In chapter 4, a novel interleaved EBG structure with wider bandwidth and smaller area has also been proposed to suppress the GBN. By reducing the pitch of power/ground vias pair, both lower- and upper-bound cutoff frequencies are improved. Consequently, the extended bandwidth of bandgap can be achieved. The design concept has been investigated by analyzing the corresponding mechanisms. Based on the design concept, the interleaved EBG structures with multiple pairs of power/ground vias have been also proposed to enhance the bandwidth of bandgap further. The 1-D equivalent circuit model of the interleaved EBG structure with one pair of power/ground vias has been constructed by using transmission-line sections and analyzed for bandgap prediction. Based on the same principle, the 2-D equivalent circuit models for quickly predicting lower- and upper-bound cutoff frequencies have been proposed for the case multiple pairs of power/ground vias. As an example, the interleaved EBG structure presents two bandgaps in the range from 1.9 GHz to 4.54 GHz and from 4.56 GHz to 6.12 GHz. The electrical size, which is normalized to the wavelength in the substrate, and bandwidth ratio are 0.071 λ_{gL} and 139 %, respectively. Compared with the size and the bandwidth of the conventional mushroom EBG structure, the interleaved EBG structure simultaneously shows substantial improvements on bandwidth of 51.1% and miniaturization of 61.2 %. With regard to the interleaved EBG structure with four pairs of power/ground vias, the bandwidth has an increase of 115.2 % wider than that of the conventional mushroom EBG structure and the required layout area can be reduced by 30.5 % simultaneously. The measured results have validated the accuracy of the simulated results and the proposed concept.

REFERENCE

[1] T.-L. Wu, H.-H. Chuang, and T.-K. Wang, “Overview of Power Integrity Solutions on Package and PCB: Decoupling and EBG Isolation,” *IEEE Trans. Electromagn. Compat.*, vol. 52, no. 2, pp. 346-356, May 2010.

[2] M. Swaminathan, J. Kim, I. Novak, and J. P. Libous, “Power Distribution Networks for System-on-Package:Status and Challenges,” *IEEE Trans. Adv. Packag.*, vol. 27, no. 2, pp. 286-300, May 2004.

[3] M. Swaminathan and E. Engin, *Power Integrity Modeling and Design for Semiconductors and Systems*, Prentice Hall, 2008.

[4] C.-Y. Hsieh, C.-D. Wang, K.-Y. Lin, and T.-L. Wu, “A power bus with multiple via ground surface perturbation lattices for broadband noise isolation: modeling and application in RF-SiP,” *IEEE Trans. Adv. Packag.*, vol. 33, no.3, pp. 582-591, Aug. 2010.

[5] J. Fan, M. Cocchini, B. Archambeault, J. L. Knighten, J. L. Drewniak, and S. Conner, “Noise coupling between signal and power/ground nets due to signal vias transitioning through power/ground plane pair,” in *Proc. IEEE Int. Symp. Electromagn. Compat.*, Detroit, MI, Aug. 18-22, 2008.

[6] T. Sudo, H. Sasaki, N. Masuda, and J. L. Drewniak, "Electromagnetic interference (EMI) of system-on-package (SOP)", *IEEE Trans. Adv. Packag.*, vol. 27, no.2, p.p. 304-314, May 2004.

[7] T.-L. Wu, S.-T. Chen, J.-N. Huang, and Y.-H. Lin, “Numerical and Experimental Investigation of Radiation Caused by the Switching Noise on the Partitioned DC Reference Planes of High Speed Digital PCB,” *IEEE Trans. Electromagn. Compat.*, vol. 46, no. 1, pp. 33-45, Feb. 2004.

[8] J. Fan, J. L. Drewniak, J. L. Knighten, N. W. Smith, A. Orlandi, T. P. Van Doren, T. H. Hubing, and R. E. DuBroff, "Quantifying SMT decoupling capacitor placement in DC power-bus design for multilayer PCBs," *IEEE Trans. Electromagn. Compat*., vol. 43, no. 4, pp. 588-599, Nov. 2001.

[9] J. Fan, W. Cui, J. L. Drewniak, T. P. Van Doren, and J. L. Knighten, "Estimating the noise mitigation effect of local decoupling in printed circuit boards," *IEEE Trans. Adv. Packag.*, vol. 25, pp. 154-165, May 2002.

[10] P. Muthana, A. E. Engin, M. Swaminathan, R. Tummala, V. Sundaram, B. Wiedenman, D. Amey, K. H. Dietz, and S. Banerji, "Design, Modeling, and Characterization of Embedded Capacitor Networks for Core Decoupling in the Package," *IEEE Trans. Adv. Packag.,* vol. 30 no. 4, pp. 809-822, Nov. 2007.

[11] P. Muthana, K. Srinivasan, A. E. Engin, M. Swaminathan, R. Tummala, V. Sundaram, B. Wiedenman, D. I. Amey, K. H. Dietz, and S. Banerji, "Improvements in Noise Suppression for I/O Circuits Using Embedded Planar Capacitors," *IEEE Trans. Adv. Packag.,* vol. 31 no. 2, pp. 234-245, May. 2008.

[12] T. Hubing, J. Chen, J. Drewniak, T. V. Doren, Y. Ren, J. Fan, and R. E. DuBroff, "Power bus noise reduction using power islands in printed circuit board designs," in *Proc. IEEE Int. Symp. Electromagn. Compat.,* Seattle, WA, Aug. 1999, pp. 1-4.

[13] J. Liang and H.-Y. D. Yang, "Radiation characteristics of a microstrip patch over an electromagnetic band-gap surface," *IEEE Trans. Antennas Propag.*, vol. 55, no. 6, pp. 1691-1697, Jun. 2007.

[14] F.-R. Yang, K.-P. Ma, Y. Qian, and T. Itoh, "A uniplanar compact photonic-bandgap (UC-PBG) structure and its applications for microwave circuit," *IEEE Trans. Microwave Theory Tech.*, vol. 47, pp. 1509-1514, Aug. 1999.

[15] D. Ahn, J. S. Park, C. S. Kim, J. Kim, Y. Qian, and T. Itoh," A design of the

low-pass filter using the novel microstrip defected ground structure," *IEEE Trans. Microw. Theory Tech.*, vol. 49, no. 1, pp. 86-93, Mar. 2001.

[16] T. Fujii and I. Ohta, "Size-reduction of coupled-microstrip 3 dB forward couplers by loading with periodic shunt capacitive stubs," in *IEEE MTT-S Int. Microw. Symp. Dig.*, Jun 2005, pp.1235-1238.

[17] J. H. Park and Y. Lee, "Improved capacitive loading method for miniaturization of 0-dB forward-wave directional couplers", *IEEE Microw. Wireless Compon. Lett.*, vol. 21, no4, pp. 191-193, Apr, 2011.

[18] D. Sievenpiper, L. Zhang, R. F. Jimenez Broas, N. G. Alex´opolous, and E. Yablonovitch, "High-Impedance Electromagnetic Surfaces with a Forbidden Frequency Band", *IEEE Trans. Microw. Theory Tech.*, vol.47, no. 11, pp.2059-2074, Nov. 1999.

[19] F. R. Yang, K. P. Ma, Y. Qian, and T. Itoh, "A novel TEM waveguide using uniplanar compact photonic-bandgap (UC-PBG) structure," *IEEE Trans. Microw. Theory Tech.*, vol. 47, pp. 2092-2098, Nov. 1999.

[20] A. Aminian, F. Yang, and Y. Rahmat-Samii, "In-phase reflection and EM wave suppression characteristics of electromagnetic bandgap ground planes," in *Proc. IEEE AP-S Int. Symp.*, Jun. 22-27, 2003, vol. 4, pp. 430-433.

[21] F. Yang and Y. Rahmat-Samii, "Microstrip antennas integrated with electromagnetic band-gap (EBG) structures: A low mutual coupling design for array applications," *IEEE Trans. Antennas Propag.*, vol. 51, no. 10, pp. 2936-2946, Oct. 2003.

[22] F. Yang and Y. Rahmat-Samii, "Mutual coupling reduction of microstrip antennas using electromagnetic band-gap structure," in *IEEE AP-S/URSI Symp. Dig.*, vol. 2, Jul. 2001, pp. 478-481.

[23] T.-L. Wu and S.-T. Chen, “A photonic crystal power/ground layer for eliminating simultaneously switching noise in high-speed circuit,” *IEEE Trans. Microw. Theory Tech.*, vol. 54, no. 8, pp. 3398-3406, Aug. 2006.

[24] G.-Z. Wu, Y.-C. Chen, and T.-L. Wu, “Design and Implementation of a Novel Hybrid Photonic Crystal Power/Ground Layer for Broadband Power Noise Suppression,” *IEEE Trans. Adv. Packag.*, vol. 33, no. 1, pp. 206-211, Feb. 2010.

[25] A. C. Scogna, T.-L. Wu, and A. Orlandi, “Noise Coupling Mitigation in PWR/GND Plane Pair by Means of Photonic Crystal Fence: Sensitivity Analysis and Design Parameters Extraction,” *IEEE Trans. Adv. Packag.*, vol. 33, no. 3, pp. 574-581, Aug. 2010.

[26] T.-L. Wu, Y.-H. Lin, and S.-T. Chen, “A Novel Power Planes With Low Radiation and Broadband Suppression of Ground Bounce Noise Using Photonic Bandgap Structures,” *IEEE Microw. Wireless Compon. Lett.*, vol. 14, no. 7, pp. 337-339, Jul. 2004.

[27] T.-L. Wu, Y.-H. Lin, T.-K. Wang, C.-C. Wang, and S.-T. Chen, “Electromagnetic bandgap power/ground planes for wideband suppression of ground bounce noise and radiated emission in high-speed circuits,” *IEEE Trans. Microw. Theory Tech.*, vol. 53, no. 9, pp. 2935-2942, Sep. 2005.

[28] J. Choi, V. Govind, and M. Swaminathan, “A novel electromagnetic bandgap (EBG) structure for mixed-signal system applications,” *in Proc. IEEE Radio Wireless Conf.*, Atlanta, GA, Sep. 2004, pp. 243-246.

[29] T.-L. Wu, Y.-H. Lin, and S.-T. Chen, “A novel power plane with super-wideband elimination of ground bounce noise on high speed circuits,” *IEEE Microw. Wireless Compon. Lett.*, vol. 15, no.3, pp. 174-176, Mar. 2005.

[30] J. Qin and O. M. Ramahi, “Ultra-wideband mitigation of simultaneous switching noise using novel planar electromagnetic bandgap structures,” *IEEE Microw. Wireless Compon. Lett.*, vol. 16, no. 9, pp. 487-489, Sep. 2006.

[31] K. H. Kim and J. E. Schutt-Aine, “Analysis and modeling of hybrid planar-type electromagnetic-bandgap structures and feasibility study on power distribution network applications,” *IEEE Trans. Microw. Theory Tech.*, vol. 56, no.1, pp. 178-186, Jan. 2008.

[32] T.-K. Wang, T.-W. Han, and T.-L. Wu, “A novel EBG power plane with stopband enhancement using artificial substrate,” *IEEE Trans. Microw. Theory Tech.*, vol. 56, no.5, pp. 1164-1171, May 2008.

[33] T.-K. Wang, C.-Y. Hsieh, H.-H. Chuang, and T.-L. Wu, “Design and modeling of a stopband-enhanced EBG structure using ground surface perturbation lattice for power/ground noise suppression,” *IEEE Trans. Microw. Theory Tech.*, vol. 57, no. 8, pp. 2047-2054, Aug. 2009.

[34] F. de Paulis, L. Raimondo, and A. Orlandi, “IR-DROP analysis and thermal assessment of planar electromagnetic bandgap structures for power integrity applications,” *IEEE Trans. Adv. Packag.*, vol. 33, no 3, pp. 617-622, Aug. 2010.

[35] R. Abhari and G. V. Eleftheriades, “Metallo-dielectric electromagnetic bandgap structures for suppression and isolation of the parallel-plate noise in high-speed circuits,” *IEEE Trans. Microw. Theory Tech.*, vol. 51, no. 6, pp. 1629-1639, Jun. 2003.

[36] T. Kamgaing and O.M. Ramahi, “A novel power plane with integrated simultaneous switching noise mitigation capability using high impedance surface,” *IEEE Microw. Wireless Compon. Lett.*, vol. 13, no. 1, pp. 21-23 Jan. 2003.

[37] Shawn D. Rogers, "Electromagnetic-bandgap layers for broad-band suppression of TEM modes in power planes," *IEEE Trans Microw. Theory Tech.*, vol. 53, no. 8, pp. 2495-2505, Aug. 2005.

[38] S. Shahparnia and O.M. Ramahi, "Simultaneous switching noise mitigation in PCB using cascaded high-impedance surfaces," *Electron. Lett.*, vol. 40, no. 2, pp. 98-100, Jan. 2004.

[39] J. Park, A.C.W. Lu, K.M. Chua, L.L. Wai, J. Lee, and J. Kim, "Double-stacked EBG structure for wideband suppression of simultaneous switching noise in LTCC-based SiP applications" *IEEE Microw. Wireless Compon. Lett.*, vol. 16, no. 9, pp. 481-483, Sept. 2006.

[40] M.-S. Zhang, Y.-S. Li, C. Jia, and L.-P. Li, "A power plane with wideband SSN suppression using a multi-via electromagnetic bandgap structure," *IEEE Microw. Wireless Compon. Lett.*, vol. 17, no. 4, pp. 307-309, April 2007.

[41] T. Kamgaing and O. M. Ramahi, "Design and modeling of high impedance electromagnetic surfaces for switching noise suppression in power planes," *IEEE Trans. Electromagn. Compat.*, vol. 47, no. 3, pp. 479-489, Aug. 2005.

[42] C.-L. Wang, G.-H. Shiue, W.-D. Guo, and R.-B. Wu, "A systematic design to suppress wideband ground bounce noise in high-speed circuits by electromagnetic-bandgap-enhanced split powers" *IEEE Trans. Microw. Theory Tech.*, vol. 54, no. 12, pp. 4209-4217, Dec. 2006.

[43] J. Lee, H. Kim, and J. Kim, "High dielectric constant thin film EBG power/ground network for broad-band suppression of SSN and radiated emissions" *IEEE Microw. Wireless Compon. Lett.*, vol. 15, no. 8, pp. 505-507, Aug. 2005.

[44] S. Shahparnia and O. M. Ramahi, “Design, implementation, and testing of miniaturized electromagnetic bandgap structures for broadband switching noise mitigation in high-speed PCBs,” *IEEE Trans. Adv. Packag.*, vol. 30, no. 2, pp. 171-179, May 2007.

[45] D.M. Pozar, *Microwave Engineering*, 2nd ed. New York: Wiley, 1998.

[46] J.-S. Hong and M. J. Lancaster, *Microstrip Filters for RF/Microwave Applications*. New York: Wiley, 2001.

[47] J. D. Joannopoulos, S. G. Johnson, J. N. Winn, and R. D. Meade, *Photonic Crystals: Molding the Flow of Light*, 2nd ed. Princeton, NJ: Princeton Univ. Press, 2008.

[48] K. Carver and J. Mink, “Microstrip antenna technology,” *IEEE Trans. Antennas Propag.*, vol. 29, no. 1, pp. 2–24, Jan. 1981.

[49] T. Okoshi, *Planar Circuits for Microwaves and Lightwaves*. Berlin, Germany: Springer-Verlag, 1985.

[50] G.-T. Lei, R. W. Techentin, P. R. Hayes, D. J. Schwab, and B. K. Gilbert, “Wave model solution to the ground/power plane noise problem,” *IEEE Trans. Instrum. Meas.*, vol. 44, pp. 300-303, Apr. 1995.

[51] J. Kim, J. Fan, A. E. Ruehli, J. Kim, and J. L. Drewniak, “Inductance calculations for plane-pair area fills with vias in a power distribution network using a cavity model and partial inductances,” *IEEE Trans. Microw. Theory Tech.*, vol. 59, no. 8, pp. 1909-1924, Aug. 2011.

[52] L. Ren, J. Kim, G. Feng, B. Archambeault, J. L. Knighten, J. Drewniak, and J. Fan, “Frequency-dependent via inductances for accurate power distribution network modeling,” in *Proc. IEEE Int. Electromagn. Compat. Symp.*, Aug. 2009, pp. 63-68.

PUBLICATION LIST

Journal Paper

1. T.-L. Wu, J. Fan, F. d. Paulis, **C.-D. Wang**, A. C. Scogna, and A. Orlandi, "Mitigation of Noise Coupling in Multilayer High-Speed PCB: State of the Art Modeling Methodology and EBG Technology," *IEICE Transactions on Communication*, Vol. E93-B, No. 07, pp. 1678-1689, July 2010.

2. C.-Y. Hsieh, **C.-D. Wang**, K.-Y. Lin, and T.-L. Wu, "A power bus with multiple via ground surface perturbation lattices for broadband noise isolation: modeling and application in RF-SiP," *IEEE Trans. Adv. Packag.*, vol. 33, no.3, pp. 582-591, Aug. 2010.

3. **C.-D. Wang**, Y.-M. Yu, F. De Paulis, A. C. Scogna, A. Orlandi, Y.-P. Chiou, and T.-L. Wu, "Bandwidth Enhancement Based on Optimized Via Location for Multiple Vias EBG Power/Ground Planes," *IEEE Trans. Compon. Packag. Manuf. Technol.*, vol. 2, no.2, pp. 332-341, Feb. 2012.

4. T.-Y. Cheng, **C.-D. Wang**, Y.-P. Chiou, and T.-L. Wu, "A New Model for Through-Silicon Vias on 3-D IC Using Conformal Mapping Method," *IEEE Microw. Wireless Compon. Lett.*, vol. 22, no. 6, pp. 303-305, Jun. 2012

5. **C.-D. Wang** and T.-L. Wu, "Model and Mechanism of Miniaturized and Stopband-Enhanced Interleaved EBG Structure for Power/Ground Noise Suppression," *IEEE Trans. Electromag. Compat.*, vol. 55, no. 1, pp. 159-167, Feb. 2013.

6. **C.-D. Wang**, Y.-J. Chang, Y.-C. Lu, P.-S. Chen, W.-C. Lo, Y.-P. Chiou, and T.-L. Wu, "ABF-Based TSV Arrays with Improved Signal Integrity on 3-D IC/Interposers: Equivalent Models and Experiments," *IEEE Trans. Compon. Packag. Manuf. Technol.*, accepted to be published.

Conference Paper

1. Y.-J. Chang, T.-Y. Zheng, H.-H. Chuang, **C.-D. Wang**, P.-S. Chen, T.-Y. Kuo, C.-J. Zhan, S-H. Wu, W.-C. Lo, Y.-C. Lu, Y.-P. Chiou, and T.-L. Wu, "Low slow-wave effect and crosstalk for low-cost ABF-coated TSVs in 3-D IC interposer," in *Proc. IEEE Electron. Compon. Technol. Conf.*, USA, May 2012, pp. 1934-1938.

2. T.-Y. Cheng, **C.-D. Wang**, Y.-P. Chiou, and T.-L. Wu, "Accuracy-improved through-silicon-via model using conformal mapping technique," in *Proc. IEEE Topical Meeting Electr. Perf. of Electron. Packag.*, pp. 189-192, October 2011.

3. **C.-D. Wang** and T.-L. Wu, "Bandwidth-enhanced EBG structure for power noise suppression in 60 GHz RF SiP," in *Proc. IEEE Int. Symp. Electromagn. Compat.*, California, USA, Jul. 2011, pp. 715-719.

4. C.-Y. Hsiao, C.-H. Huang, **C.-D. Wang**, K.-H. Liao, C.-H. Shen, C.-C. Wang, T.-L. Wu, "Mold-based compartment shielding to mitigate the intra-system coupled noise on SiP modules," in *Proc. IEEE Int. Symp. Electromagn. Compat*., California, USA, Jul. 2011, pp. 341-344.

5. C.-H. Huang, C.-Y. Hsiao, **C.-D. Wang**, T. Chen, K.-H. Liao, and T.-L. Wu, "Conformal shielding investigation for SiP modules," in *Proc. IEEE EDAPS*, Singapore, 7-9 Dec., 2010

6. **C.-D. Wang**, and T.-L. Wu, "A stopband enhanced EBG power/ground plane based on via location design," in *Proc. IEEE CPMT Symp. Japan*, Tokyo, Japan, Aug. 2010.

7. A. C. Scogna, **C.-D. Wang**, A. Orlandi, and T.-L. Wu, "Parallel-plate noise suppression using a ground surface perturbation lattice (GSPL) structure," in *Proc. IEEE Electromagn. Compat. Asia-Pacific Symp.*, Beijing, China, Apr. 2010, pp. 158-161.